

Spectroscopy and Characterization of Turbid Media Within
the Diffusion and P_3 Approximations

by

Edward L. Hull

Submitted in Partial Fulfillment
of the
Requirements for the Degree
Doctor of Philosophy

Supervised by
Professor Thomas H. Foster

Department of Physics and Astronomy
The College
Arts and Sciences

University of Rochester
Rochester, NY

1999

*To my wife Barbara,
whose patience has no apparent limit.*

Curriculum Vitae

Edward L. Hull was born in Bellefonte, Pennsylvania in 1967 and attended Franklin D. Roosevelt High School in Hyde Park, New York, where he was exposed to the intriguing world of physics by his teachers Floyd Holt and George Aaman. He was also active in the arts and performed in various musical ensembles.

In the fall of 1985 Hull enrolled at Houghton College in Houghton, New York, where he began to study music. After two years of intense effort and nominal progress, the need to forsake music as a profession was made even more plain by the exceptional musical skills of one Barbara Kinney, to whom he had taken a rather serious fancy. The two married in 1987, and Mr. Hull's studies turned once again to the sciences. He graduated from Houghton in 1989 with a Bachelor of Science degree in physics and minors in music and secondary education. Professors Duane Saufley and Frederick Trexler were particularly influential in his scientific and personal development.

In the fall of 1989, he began teaching high school physics and earth science at Sodus Senior High school in Sodus, New York. The student body selected Mr. Hull as the 1990 teacher of the year. The Hulls' daughters, Gretchen Lindsay and Abigail Waverly, were both born during his four-year stay at Sodus. During this time he also spent two summers at the University of Rochester conducting research under the auspices of a program for high school teachers sponsored by the NSF Center for Photoinduced Charge Transfer. His work was supervised by Professor Yongli Gao and Dr. Martin Aeschlimann.

Hull entered the graduate program of the Department of Physics and Astronomy at the University of Rochester in the fall of 1994, and was awarded a Department of Defense fellowship. He served as a graduate teaching assistant under Professors Paul

Tipton and Lynne Orr and was the winner of the Department's 1995 Graduate Teaching award. He began thesis research in the laboratory of Dr. Thomas H. Foster in 1995 and earned a Master of Arts degree in Physics in 1997. He became a doctoral candidate later that year and completed his thesis research in 1999.

Mr. Hull has been a member of the American Physical Society, the Optical Society of America, and the American Society for Photobiology.

Acknowledgements

My research at the University of Rochester has been made possible by the help of many people to whom I am gratefully indebted.

Dr. Thomas H. Foster has served as my thesis advisor for the duration of my graduate studies. It has truly been a privilege to be a graduate student in his laboratory. Advising graduate students is no small task, and I am very appreciative of the time and thought he has invested in introducing me to our scientific community, discussing scientific issues, training me in the process of scientific writing, and shaping my approach to laboratory research. It is difficult to imagine growing more as a scientist in another lab. Dr. Foster has also allowed me time to investigate issues which were interesting to me but perhaps not of immediate importance to the lab as a whole. I am grateful for this flexibility and for his respect for my family commitments. The research described in this thesis was funded by Professor Foster's grants from the USPHS (#CA68409) and the Whitaker Foundation.

Irene Georgakoudi, Mike Nichols, John Larkin, Jarod Finlay and Soumya Mitra were all graduate students in Professor Foster's lab during my time there. Mike Nichols introduced me to the lab, scientific computing, and much of the experimental apparatus used in my research. Irene Georgakoudi and John Larkin have been good friends as well as scientific comrades; it is a pleasure to acknowledge many fruitful discussions with them. Irene's baklava deserves a word of special recognition. Jarod and Soumya are relative newcomers to the lab and have both been very helpful to me in the past few hectic months. B.J. Marleau worked as an undergraduate for two summers in Dr. Foster's group and made the diffusing plates which are now ubiquitous in the lab.

David Conover, a research associate in the Department of Radiology, has contributed significantly to the work described in these pages. Mr. Conover machined and fabricated several of the fiber optic probes used with our equipment and assisted the data collection for the material described in Chapter 5. He has also helped with a variety of other technical issues and has often contributed valuable insights that have helped to refine experimental designs and analysis techniques.

Members of the lab of Professor Russell Hilf have also been important in my scientific development. Mr. Scott Gibson has helped me to understand various matters related to the biology of my experiments and, jokes about cubical tumors notwithstanding, has exhibited exemplary patience in coping with the physicists Dr. Foster continues to send his way. Mr. Jim Havens was responsible for tumoring and animal maintenance and also taught me various animal handling techniques.

It has been a particular pleasure to engage in discussions with colleagues in the medical optics community. I spent the summer of 1997 as a visitor in the lab of Dr. Arjun Yodh at the University of Pennsylvania in Philadelphia. Professor Yodh exposed me to the techniques and instrumentation of frequency-domain tissue spectroscopy. I had beneficial discussions with his students David Boas, Xingde Li, and Joe Culver. I have also been helped on numerous occasions by members of the lab of Dr. Michael Patterson at McMaster University in Hamilton, Ontario, Canada. Professor Patterson and his colleagues Jody Bruulsema, Joe Hayward, and Tom Farrell all offered useful advice on various experimental issues.

In the Department of Physics and Astronomy, Dr. Lynne Orr has generously given computing time on numerous occasions. I also had helpful discussions with Dr. Orr, Dr. Tom Ferbel, and Dr. Paul Tipton. Barbara Warren in the office of graduate studies has been extremely kind and helpful to me over the past four years and

deserves an extra measure of thanks.

I would like to thank my parents and parents-in-law for financial support and emotional encouragement during the time taken to complete this work. Finally, I thank my family: Barbara, Gretchen and Abigail Hull. They have patiently endured many nights of work and time away from home during my time as a graduate student. Without their love and support, this document would most certainly not exist.

Abstract

Noninvasive measurement of tissue optical properties has become an area of increasing interest in recent years. Because such measurements have the potential to provide a wide range of clinically useful information, techniques for determining tissue optical properties from straightforward measurements are of considerable importance.

In this thesis, the diffusion approximation to the radiative transport equation is applied to radially-resolved measurements of the reflectance emitted from highly scattering media interrogated by a normally-incident pencil beam. Solutions to the photo-diffusion equation are considered which express the reflectance as a function of the tissue absorption and transport scattering coefficients. The expressions are then fitted to measured reflectance data in order to extract these optical properties as fitting parameters. The expressions are evaluated through a series of Monte Carlo experiments.

The design and testing of a steady-state reflectance spectrometer is described, and it is demonstrated that the diffusion-theory solutions can be used to determine absorption and scattering coefficients of turbid media from experimental reflectance data to accuracies of 10% or better when medium optical properties are within the regime of validity of the diffusion approximation. These techniques are applied to studies of tissue-simulating phantoms containing human red blood cells and to measurements of the hemoglobin oxygenation status of subcutaneous rodent mammary tumors.

Optical diffusion theory is only valid when the tissue transport scattering coefficient is much greater than the absorption coefficient. In cases where absorption and scattering are comparable in magnitude, new theoretical models are needed for

accurate quantitation of optical properties. The P_3 approximation to the radiative transport equation is used to develop such a model. Approximate P_3 boundary conditions for semi-infinite media are derived, and a simple model of optical beams suitable for small source-detector separations is proposed. It is demonstrated that the resulting reflectance expressions can be used to accurately extract optical properties from experimental measurements of media with transport albedos as small as 0.59, a value which is typical of tissue in the visible region of the spectrum. The potential for reflectance spectroscopy in the visible to provide information about mitochondrial cytochrome oxidation status is assessed experimentally.

Finally, a steady-state technique for localizing buried sources of luminescence is developed, and it is shown that the method determines the depth of a buried spherical fluorescent bulb to ± 1 mm accuracy for source depths as large as 40 mm. A sensitivity analysis is performed to investigate the stability of the technique with respect to errors in initial estimates of the medium optical properties. The corrupting effects of nonspecifically localized lumiphore are considered theoretically, and limits are placed on the effective optical contrast required for practical implementation of the technique.

TABLE OF CONTENTS

| | |
|--|-----------|
| Curriculum Vitae | iii |
| Acknowledgments | v |
| Abstract | viii |
| Table of Contents | x |
| List of Tables | xiv |
| List of Figures | xv |
| List of Symbols | xx |
| | |
| 1 Introduction and Overview | 1 |
| 1.1 A brief introduction to tissue optical properties | 1 |
| 1.1.1 Tissue scattering | 2 |
| 1.1.2 Tissue absorption | 5 |
| 1.2 Overview of the thesis | 9 |
| References | 11 |
| | |
| 2 Radiative Transport Theory: the Diffusion, P_1, and P_3 | |
| Approximations | 15 |
| 2.1 The transport equation and the P_N approximation | 15 |

| | | |
|-------|---|----|
| 2.2 | The P_1 approximation | 19 |
| 2.3 | The diffusion approximation | 21 |
| 2.4 | The P_3 approximation | 22 |
| 2.5 | Considerations for applying the P_3 approximation to tissue spectroscopy | 31 |
| 2.6 | Boundary conditions | 40 |
| 2.6.1 | Marshak conditions and semi-infinite Green's functions in the diffusion approximation | 42 |
| 2.6.2 | Marshak conditions and semi-infinite Green's functions in the P_3 approximation | 45 |
| 2.7 | Reflectance expressions | 49 |
| 2.7.1 | Diffusion approximation | 49 |
| 2.7.2 | P_3 approximation | 52 |
| 2.8 | Representation of beams | 57 |
| | References | 63 |

3 Validation of Theoretical Reflectance Expressions with

| | | |
|-------|--|-----------|
| | Analysis of Simulated and Experimental Data | 66 |
| 3.1 | Introduction | 66 |
| 3.2 | Monte Carlo evaluation of the fitting functions | 66 |
| 3.2.1 | Sensitivity to minimum source-detector separation | 68 |
| 3.2.2 | Sensitivity to maximum source-detector separation | 84 |
| 3.3 | Broadband steady-state reflectance spectrometer | 86 |
| 3.3.1 | Instrument | 86 |
| 3.3.2 | Data reduction | 90 |

| | | |
|----------|---|------------|
| 3.4 | Phantom studies | 94 |
| 3.4.1 | Partial diffusion theory solution | 95 |
| 3.4.2 | Full diffusion theory solution | 104 |
| 3.4.3 | P_3 solution | 109 |
| 3.5 | Summary | 116 |
| | References | 117 |
| | | |
| 4 | Quantitative Near-infrared Spectroscopy of Tissue-simulating Phantoms Containing Erythrocytes and Mitochondria | 118 |
| 4.1 | Introduction | 118 |
| 4.2 | Materials and methods | 122 |
| 4.2.1 | Phantom preparation | 122 |
| 4.2.2 | Spectral analysis techniques | 123 |
| 4.2.2.1 | Least squares fitting | 123 |
| 4.2.2.2 | Singular value decomposition | 124 |
| 4.2.2.3 | Computation and verification of hemoglobin oxygen saturation | 126 |
| 4.3 | Results and discussion | 127 |
| 4.3.1 | Hemoglobin reference spectra | 127 |
| 4.3.2 | Spectroscopy of erythrocytes; verification of reported saturations | 129 |
| 4.3.3 | SVD background estimation | 136 |
| 4.3.4 | Comparison with discrete wavelength techniques | 140 |
| 4.4 | Spectroscopy of phantoms containing hemoglobin and mitochondria | 146 |

| | | |
|----------|--|------------|
| 4.5 | Conclusions | 156 |
| | References | 158 |
| 5 | Carbogen-induced Changes in Rat Mammary Tumor | |
| | Oxygenation Reported by Near-infrared Spectroscopy | 164 |
| 5.1 | Introduction | 164 |
| 5.2 | Materials and methods | 166 |
| | 5.2.1 Spectroscopy | 166 |
| | 5.2.2 Animals and tumors | 168 |
| 5.3 | Results | 168 |
| 5.4 | Discussion | 177 |
| | Appendix | 181 |
| | References | 184 |
| 6 | Localization of Luminescent Inhomogeneities in Turbid | |
| | Media with Spatially Resolved Measurements of CW | |
| | Diffuse Luminescence Emittance | 188 |
| 6.1 | Introduction | 188 |
| 6.2 | Theory | 191 |
| 6.3 | Experimental methods and results | 193 |
| 6.4 | Monte Carlo evaluation of the fitting algorithm | 204 |
| 6.5 | Limitations imposed by background luminescence | 213 |
| 6.6 | Discussion and conclusions | 220 |
| | References | 225 |
| 7 | Conclusions | 229 |

LIST OF TABLES

| | | |
|-----|---|-----|
| 2.1 | Parameters A , C_ϕ , and C_j for various refractive index mismatches and detector types | 51 |
| 2.2 | Parameters $k_1 - k_6$ for various refractive index mismatches and detector types | 56 |
| 3.1 | Actual and fitted MnTPPS concentrations: DT_{full} solution | 110 |
| 6.1 | Actual and fitted values of z_0 and μ_{eff} obtained from fits to experimental diffuse luminescence emittance data | 202 |
| 6.2 | Actual and fitted source depths for various effective contrast ratios and source depths | 219 |

LIST OF FIGURES

| | | |
|------|---|----|
| 1.1 | Scattering properties of rat liver | 3 |
| 1.2 | Phase functions for various human tissues | 6 |
| 1.3 | Representative tissue absorption spectra | 8 |
| | | |
| 2.1 | Infinite slab geometry | 27 |
| 2.2 | Diffusion and P_3 attenuation coefficients | 32 |
| 2.3 | Asymptotic attenuation coefficients: Diffusion, P_3 , and P_5 approximations . | 33 |
| 2.4 | Infinite medium absorbed fluence comparison | 35 |
| 2.5 | Illustration of first-order similarity relations | 37 |
| 2.6 | Parameters γ and δ for the Henyey-Greenstein phase function | 39 |
| 2.7 | Dipole source arrangement for the extrapolated boundary condition | 44 |
| 2.8 | Partial-current and extrapolated boundary conditions comparison | 46 |
| 2.9 | Diffusion and P_3 extrapolation lengths | 48 |
| 2.10 | Comparison of various diffusion theory reflectance expressions | 53 |
| 2.11 | Geometry for calculation of reflectance in the P_3 approximation | 55 |
| 2.12 | Comparison of diffusion and P_3 reflectance expressions: $\mu_a=0.01 \text{ mm}^{-1}$ | 58 |
| 2.13 | Comparison of diffusion and P_3 reflectance expressions: $\mu_a=1.0 \text{ mm}^{-1}$ | 59 |
| 2.14 | Comparison of various beam representations | 61 |

| | | |
|------|--|-----|
| 3.1 | Data sets used in Monte Carlo evaluation of reflectance expressions | 70 |
| 3.2 | Fitted optical properties for DT_{full} , DT_{flux} , and P_3 solutions: $\mu_a=0.01 \text{ mm}^{-1}$ and $n_{rel} = 1.4$ | 72 |
| 3.3 | χ_v^2 for DT_{full} , DT_{flux} , and P_3 solutions: $\mu_a=0.01 \text{ mm}^{-1}$ and $n_{rel} = 1.4$ | 73 |
| 3.4 | Fitted optical properties for DT_{full} , DT_{flux} , and P_3 solutions: $\mu_a=0.01 \text{ mm}^{-1}$ and $n_{rel} = 1.0$ | 75 |
| 3.5 | χ_v^2 for DT_{full} , DT_{flux} , and P_3 solutions: $\mu_a=0.01 \text{ mm}^{-1}$ and $n_{rel} = 1.0$ | 76 |
| 3.6 | Fitted optical properties for DT_{full} , DT_{flux} , and P_3 solutions: $\mu_a=0.5 \text{ mm}^{-1}$ and $n_{rel} = 1.4$ | 78 |
| 3.7 | χ_v^2 for DT_{full} , DT_{flux} , and P_3 solutions: $\mu_a=0.5 \text{ mm}^{-1}$ and $n_{rel} = 1.4$ | 79 |
| 3.8 | Summary of fitted absorption coefficients: DT_{full} and P_3 solutions | 81 |
| 3.9 | Summary of fitted transport scattering coefficients: DT_{full} and P_3 solutions | 83 |
| 3.10 | Optical property error contours for DT_{full} and P_3 solutions: $\mu_a=0.5 \text{ mm}^{-1}$. . . | 85 |
| 3.11 | Steady-state reflectance spectrometer | 87 |
| 3.12 | Circular probe head | 88 |
| 3.13 | Reconstructed MnTPPS absorption spectra: DT_{flux} solution | 96 |
| 3.14 | Fitted MnTPPS concentrations: DT_{flux} solution | 98 |
| 3.15 | 1.25% Liposyn-II® scattering spectrum: DT_{flux} solution | 101 |
| 3.16 | Reconstructed transport scattering spectra of polystyrene spheres: DT_{flux} solution | 103 |
| 3.17 | Reconstructed water absorption spectrum: DT_{full} solution | 105 |
| 3.18 | Effects of changing the internal reflection parameter: DT_{full} solution | 107 |
| 3.19 | Reconstructed MnTPPS absorption spectra: DT_{full} solution | 108 |
| 3.20 | Reconstructed MnTPPS absorption spectrum: P_3 solution vs. DT_{full} solution | 112 |

| | | |
|------|---|-----|
| 3.21 | Reconstructed polystyrene spheres transport scattering spectrum: P ₃ solution vs. DT _{full} solution | 113 |
| 3.22 | Summary of fitted MnTPPS concentrations: P ₃ vs. DT _{full} solutions | 115 |
| 4.1 | Comparison of SSDRS hemoglobin absorption spectra with spectra from the literature | 128 |
| 4.2 | Fits to background-corrected SSDRS hemoglobin absorption spectra | 130 |
| 4.3 | Fitted oxy-, deoxy- and total hemoglobin concentrations from a phantom containing polystyrene spheres and red cells | 131 |
| 4.4 | Fitted Hill curve for background-corrected hemoglobin absorption spectra | 133 |
| 4.5 | Fits to SSDRS hemoglobin spectra not corrected for background absorption | 134 |
| 4.6 | Fitted Hill curves for background-corrected and non-background-corrected SSDRS spectra | 135 |
| 4.7 | Simulated background absorption spectrum | 137 |
| 4.8 | Singular value decomposition analysis example | 139 |
| 4.9 | Fitted Hill curves for background-corrected and background- contaminated data | 141 |
| 4.10 | Comparison of SSDRS hemoglobin saturations with discrete wavelength algorithms: background-corrected data | 143 |
| 4.11 | Comparison of SSDRS hemoglobin saturations with discrete wavelength algorithms: background-contaminated data. | 145 |
| 4.12 | Oxidized and reduced mitochondrial absorption spectra in the visible and near- infrared | 149 |

| | | |
|------|--|-----|
| 4.13 | Mitochondrial difference spectra: near IR | 151 |
| 4.14 | Mitochondrial difference spectra: visible | 152 |
| 4.15 | Sample fitted absorption spectra from a mixed mitochondria/ red cells phantom | 154 |
| 4.16 | Hemoglobin oxygen saturation and mitochondrial oxidation status as a function of pO_2 | 155 |
| 5.1 | Illustration of in vivo reflectance probe | 167 |
| 5.2 | Sample SSDRS absorption spectra from an R3230AC tumor: room air vs. carbogen inhalation | 169 |
| 5.3 | SVD analysis of in vivo absorption spectra | 171 |
| 5.4 | Hemoglobin oxygen saturations and concentrations before, during, and after carbogen breathing | 173 |
| 5.5 | Carbogen-induced change in HbO_2 saturation vs. change in total Hb concentration | 174 |
| 5.6 | Carbogen-induced change in HbO_2 saturation vs. initial HbO_2 saturation | 176 |
| 6.1 | Dipole approximation for the emittance from a buried point source | 192 |
| 6.2 | Experimental apparatus for fluorescence excitation and detection | 195 |
| 6.3 | Representative experimental diffuse fluorescence emittance data | 198 |
| 6.4 | Fitted depths of buried sources vs. actual source depths | 199 |
| 6.5 | Fitted values of μ_{eff} as a function of source depth | 201 |
| 6.6 | Fluorescence emittance data from two buried sources | 203 |
| 6.7 | $1/\chi^2$ surfaces as a function of μ_{eff} and z_0 for three different source depths . | 206 |

| | | |
|------|--|-----|
| 6.8 | Contours of constant χ^2 for $z_0=10.0$ mm for various extrapolated boundary positions | 208 |
| 6.9 | Error in fitted source depth as a function of assumed extrapolated boundary position | 210 |
| 6.10 | Error in fitted source depth as a function of the fitted value of μ_{eff} | 211 |
| 6.11 | Ratio of emittance intensity from a 6-mm diameter luminescent inclusion to that of the bulk medium as a function of the inclusion depth | 216 |
| 6.12 | Simulated background-contaminated luminescence emittance data | 218 |

LIST OF SYMBOLS

| Symbol | Description |
|--------------------|---|
| Y_{lm} | Spherical harmonics |
| P_l | Legendre ploynomial |
| μ_a | Absorption coefficient |
| μ_s | Scattering coefficient |
| μ_s' | Reduced (or "transport") scattering coefficient |
| μ_t | Total interaction coefficient ($\mu_t = \mu_a + \mu_s$) |
| μ_t' | Reduced total interaction coefficient ($\mu_t' = \mu_a + \mu_s'$) |
| μ_t^m | $\mu_a + \mu_s (1-g_m)$ |
| a | Albedo [$a = \mu_s/(\mu_a + \mu_s)$] |
| a' | Reduced albedo [$a' = \mu_s'/(\mu_a + \mu_s')$] |
| μ_{eff} | Effective attenuation coefficient ($\mu_{\text{eff}} = [3\mu_a\mu_t']^{1/2}$) |
| D | Steady-state diffusion coefficient [$D = 1/(3\mu_t')$] |

| | |
|-----------------------------|--|
| S | Source function |
| σ_{lm} | Moments of the source distribution, spherical harmonics expansion |
| q_m | Moments of the source distribution in a medium with planar symmetry |
| $f(\hat{s} \cdot \hat{s}')$ | Scattering phase function |
| g_l | Moments of the scattering phase function |
| g | Used alone = scattering anisotropy |
| γ | $(1-g_2)/(1-g_1)$ |
| δ | $(1-g_3)/(1-g_1)$ |
| L | Radiance |
| ϕ_{lm} | Moments of the radiance, spherical harmonics expansion |
| φ_m | Moments of the radiance in a medium with planar symmetry |
| ψ_m | Moments of the radiance in a medium with spherical symmetry |
| Φ | Optical fluence (equivalent to $\phi_{0,0}$ and φ_0 and ψ_0) |
| Φ_G | Green's function for the fluence |
| Φ_{G_∞} | Green's function for the fluence in an infinite medium |
| \mathbf{j} | Flux |
| EBC | Extrapolated boundary condition |
| PCBC | Partial-current boundary condition |

| | |
|------------------|---|
| η | Cosine of the angle between the z axis and the observation direction \hat{s} . |
| ξ | Cosine of the angle between \hat{r} and the observation direction \hat{s} |
| v^+ | Transient P_3 attenuation coefficient |
| $v^-, v_{P_3}^-$ | Asymptotic P_3 attenuation coefficient |
| $v_{P_5}^-$ | Asymptotic P_5 attenuation coefficient |
| $h_l(v_j)$ | Function which relates the expansion coefficient of the l^{th} moment of the radiance to the coefficient of the zeroth moment (the fluence). |
| z_0 | Depth of buried source |
| E | Emittance |

CHAPTER 1

Introduction and Overview

1.1 A brief introduction to tissue optical properties

In recent years, substantial theoretical and experimental efforts have been directed toward development of accurate, noninvasive techniques for measurement of tissue optical properties. A relatively recent review of optical methods in biology has been published by Chance [1]. Optical properties frequently of interest include the tissue absorption (μ_a) and scattering (μ_s) coefficients and the scattering anisotropy (g) [2,3], which is defined as the average cosine of the scattering angle. Because the scattering cross section of most tissues is tens ($\lambda \approx 400$ nm) to thousands ($\lambda \approx 800$ nm) of times larger than the absorption cross section, noninvasive and quantitatively accurate spectroscopy of thick tissues remains a challenging problem. Such measurements have the potential, however, to provide important diagnostic information such as hemoglobin oxygenation status [4], blood glucose level [5,6], concentrations of exogenously administered drugs such as sensitizers used in photodynamic therapy [7,8], and the concentration and oxidation status of several other important endogenous chromophores [9 – 11]. Low-resolution tomographic imaging of tissue optical properties has also become a field of intense interest. Many researchers are presently working toward near-infrared (NIR) optical tomography of the breast [12] and brain [13]. Such images have the potential to provide early detection of hematoma (brain) and cancer (breast), as well as relatively

inexpensive functional imaging [14].

1.1.1 Tissue scattering

The scattering properties of a wide variety of tissue samples have been studied by many researchers using an assortment of measurement techniques. Reference [3] provides an extensive table of such measurements. One example is provided in Figure 1.1, which depicts measurements by Parsa et al. [15] of the scattering coefficient (upper panel) and the scattering anisotropy (lower panel) of rat liver in the 350 nm–2.2 μm wavelength range. The authors used an inverse adding-doubling algorithm [16] in conjunction with measurements of the total diffuse reflectance, diffuse transmittance, and collimated transmittance obtained with a single integrating sphere. The figure depicts the average of measurements from 11 different thin tissue sections. The magnitude of the scattering coefficient is one notable feature; in the visible and NIR spectral regions, μ_s ranges from approximately 17 mm^{-1} ($\lambda=500$ nm) to 7 mm^{-1} ($\lambda=1000$ nm). These values are typical of those reported for a wide variety of tissue types. For nearly all sampled wavelengths, the scattering anisotropy is in the range $0.8 \leq g \leq 0.9$, indicating that scattering is predominantly forward-directed. This is also representative of many tissues.

The exact origin of the scattering properties of tissues remains a topic of current research [17], but it is generally agreed that mitochondria are one of the most significant scattering centers in many mammalian tissues. Mitochondria are the cellular organelles responsible for the production of ATP, and are typically ellipsoidal in shape, having major and minor axis lengths on the order of 1 μm and 0.5 μm [18]. Beauvoit et al. measured the reduced scattering coefficient of several transplantable rodent tumors and normal tissues by time-domain transmission spectroscopy and found

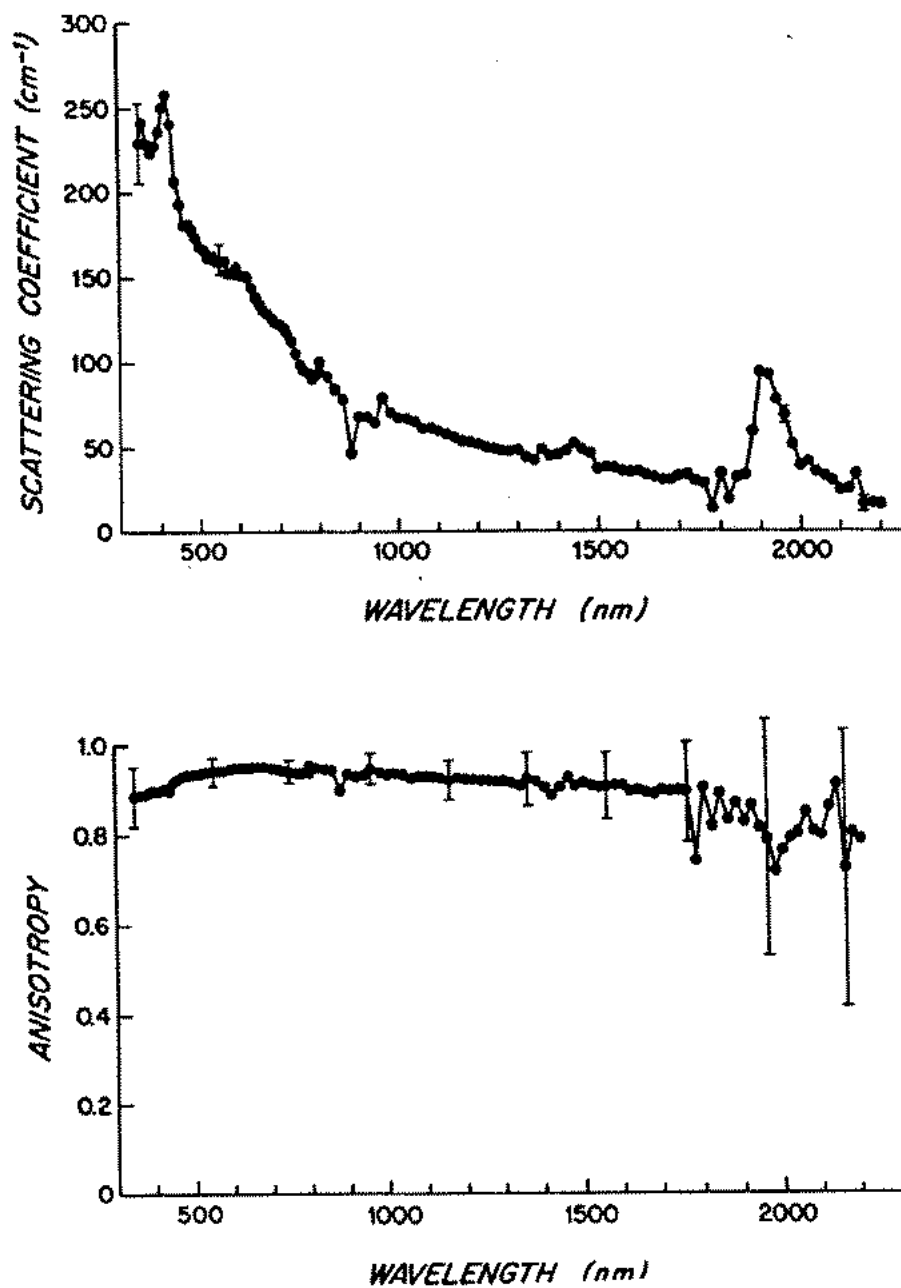


Figure 1.1 The scattering coefficient (upper panel) and scattering anisotropy (lower panel) of thin sections of excised rat liver. Data are from Parsa et al. [15].

a strong correlation between the magnitude of μ_s' and the mitochondrial protein content of these tissues [19]. This was particularly true for liver and brain, tissues which are rich in mitochondria.

The size of tissue scatterers can be roughly estimated by the wavelength dependence of the tissue scattering coefficient. In the case of Rayleigh scattering, which holds in the limit of scatterer sizes much smaller than an optical wavelength, $\mu_s'(\lambda)$ exhibits a λ^{-4} dependence. As the scatterer size increases, the wavelength dependence of the scattering coefficient becomes less pronounced; for refractive index mismatches relevant to biological tissue, $\mu_s'(\lambda)$ is approximately proportional to λ^{-1} for 0.2 μm -diameter scatterers and to $\lambda^{-0.4}$ for 1.0 μm -diameter scatterers, as calculated by Mie scattering theory [20]. Using this type of analysis, Nilsson et al. found that effective scatterer sizes in liver were consistent with mitochondria being the dominant scatterer [21].

Although mitochondria are important tissue scattering centers, other structures can also serve as efficient optical scatterers. For example, Saidi et al. have demonstrated that, in neonatal skin, the optical scattering coefficient correlates with the size and density of collagen fibers [22]. These authors demonstrated that the scattering coefficient of neonatal skin could be modeled effectively by the superposition of a term computed by Mie theory for cylindrical scatterers having a size and number density comparable to that of the tissue collagen fibers and a second term accounting for the presence of Rayleigh scattering. Another elegant study by Perelman et al. found that a small fraction of the light reflected by epithelial tissues in the visible and near-infrared exhibits a wavelength-dependent amplitude periodicity [23]. They demonstrated that this periodic structure originates from back-reflection by cell nuclei, and were able to infer the distribution of nuclear sizes by analyzing the wavelength

dependence of this reflectance signal.

The angular dependence of tissue scattering is also an important issue. Figure 1.2 illustrates measurements by Marchesini et al. [24] of the normalized scattering phase function of excised samples of human liver, lung, and uterine smooth muscle. The scattering phase function $P(\cos \theta)$ is a probability density function which describes the probability for an incident photon to scatter through a deflection angle between θ and $\theta + d\theta$. For all tissues depicted in this plot, it is evident that the scattering is very forward-directed. The average cosine of the scattering angle is in the range of 0.84 (liver) to 0.88 (lung). This highly anisotropic, forward-directed scattering is again consistent with the hypothesis that the primary scatterers are structures such as mitochondria, which have a size on the order of an optical wavelength. Another interesting feature of this plot is the gradual increase in the scattering probability for $\theta \geq 110^\circ$. This positive slope at large values of θ suggests the contribution of a $\cos^2(\theta)$ term to the phase function, a functional form that is associated with Rayleigh scattering.

1.1.2 Tissue absorption

The absorption coefficient of tissue is dominated by hemoglobin in the visible wavelength range and by hemoglobin and water in the near infrared (NIR). Figure 1.3 illustrates the absorption spectra of oxyhemoglobin, deoxyhemoglobin and water in these spectral regions. The near IR hemoglobin spectra are from Wray et al. [25], the visible hemoglobin spectra are from Zijlstra et al. [26], and the water spectrum is from Kou et al. [27]. The magnitudes of the absorption coefficients assume a hemoglobin concentration of 50 μM and an 80% volume fraction of water. Several interesting features are evident, including the well-known fact that the absorption spectrum of

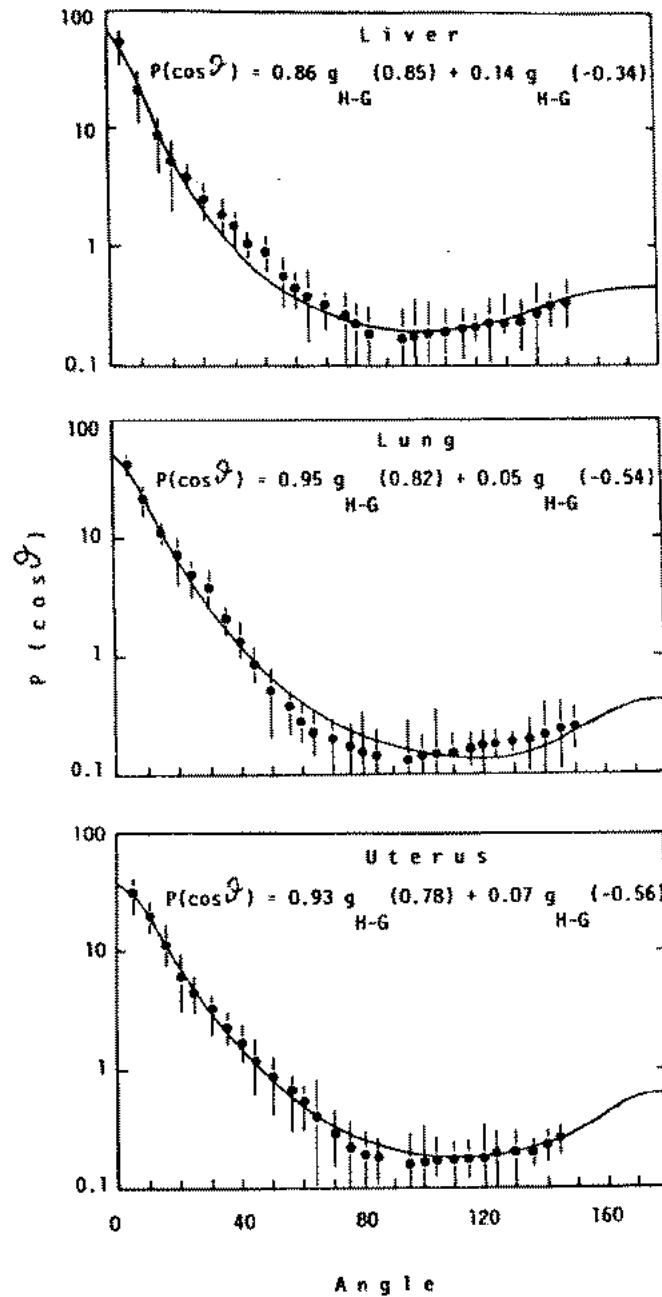


Figure 1.2 Scattering phase functions ($P(\cos \theta)$) of excised human liver (upper panel), lung (center panel), and uterine smooth muscle (bottom panel). The phase function is a probability density function describing the probability for a photon to scatter through a deflection angle between θ and $\theta + d\theta$. Each experimental data set has been fitted to a normalized sum of two Henyey-Greenstein (g_{H-G}) phase functions. The argument of g_{H-G} is the scattering anisotropy. Data are from Marchesini et al. [24].

hemoglobin changes dramatically upon binding of oxygen. This spectral shift is the basis for optical hemoglobin oximetry. In addition, a pronounced “valley” exists between the absorption bands of hemoglobin which dominate the visible wavelengths and the near IR absorption bands of water. This region of low absorption around $650 \text{ nm} \leq \lambda \leq 850 \text{ nm}$ has been called the “therapeutic window,” because light in this wavelength range can penetrate on the order of centimeters into tissue. This wavelength region is commonly exploited in applications which are based on optical diffusion theory. Finally, it is important to note the magnitude of the absorption coefficient relative to the magnitude of the scattering coefficient in the visible and near IR. The fact that μ_s dominates μ_a by a factor of ~ 1000 in the near IR is the basis for optical diffusion theory, which is presented in detail in Chapter 2. In the visible, μ_s is typically on the order of 20 times μ_a , and diffusion theory does not apply.

While hemoglobin and water are the principal absorbers in tissue, there are other interesting chromophores which contribute to the tissue absorption spectrum. Mitochondrial cytochromes, for example, exhibit absorption spectra which are sensitive to their oxidation status and can potentially provide a wealth of information about the local cellular environment [18,28]. In fact, Jöbsis, who is generally regarded as the founder of near IR spectrophotometry of tissue, identified hemoglobin and cytochrome aa_3 as the principal absorbers in reflectance spectra of cat brain [29]. Fat also provides a near IR absorption signal which is significant for some tissues, particularly the breast [30].

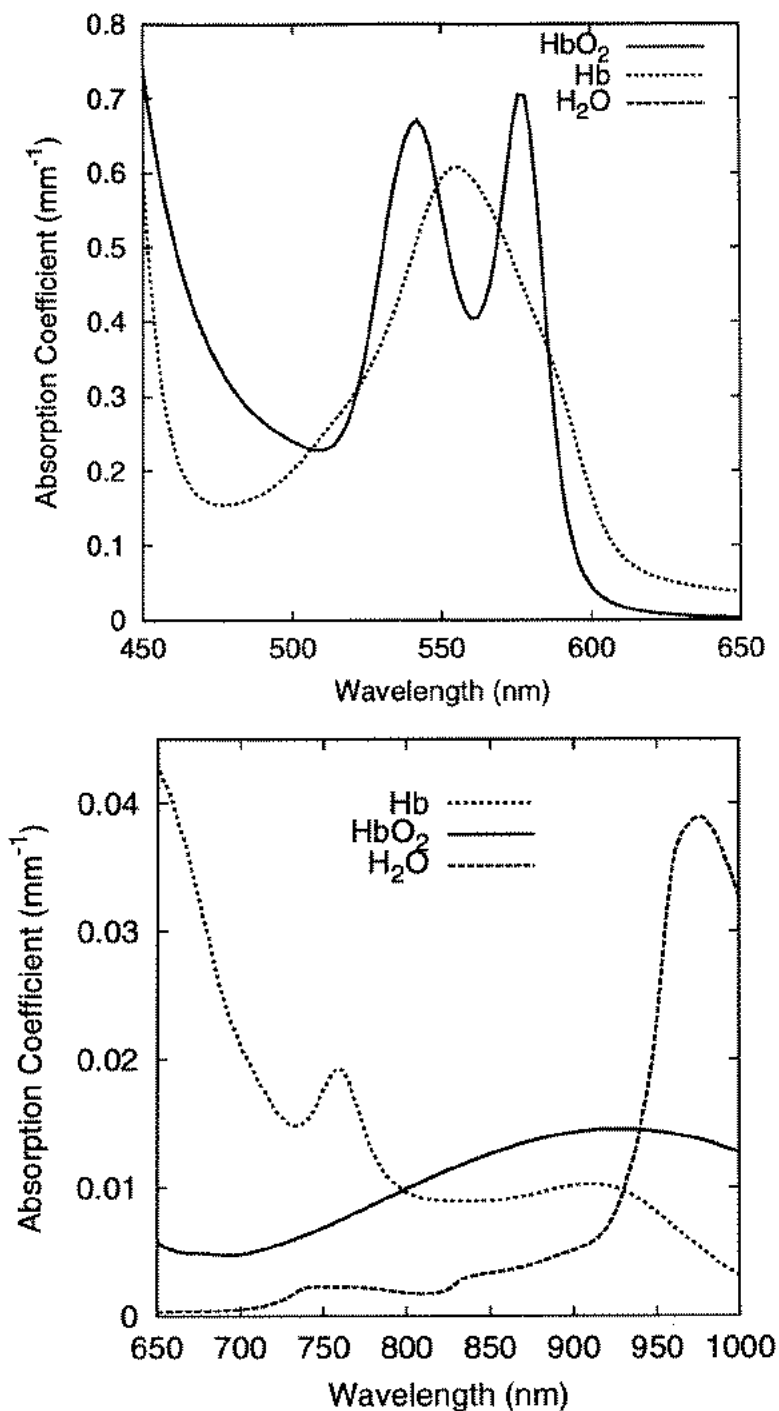


Figure 1.3 Absorption spectra of hemoglobin and water typical of tissue in the visible (upper panel) and near-IR (lower panel). The hemoglobin absorption coefficients were calculated by assuming a concentration of 50 μM , and the water spectrum was computed assuming 80% water by volume. Hemoglobin spectra are from Wray et al [25] (near IR), and Zijlstra et al. [26]. The water spectrum is from Kou et al. [27].

1.2 Overview of the thesis

In Chapter 2, the theoretical framework of light transport in tissue is presented in the context of the P_N approximation to the radiative transport equation. The derivation of the theory of optical diffusion and associated boundary conditions is an outline of work done by others and is essential for a thorough understanding of the remaining chapters. The derivation of the Green's function for the transport equation in the P_3 approximation and the associated boundary conditions, reflectance expressions, and dipole beam representation is work which is original to this thesis.

In Chapter 3, the P_3 and diffusion theory reflectance expressions derived in Chapter 2 are fitted to Monte Carlo simulated data in order to assess the range of validity of the various theoretical expressions and the accuracy of tissue optical properties which are extracted as fitting parameters. The design, implementation, and testing of a diffuse reflectance spectrometer is also described, and the instrument is used to perform quantitative spectroscopy of highly scattering tissue-simulating phantoms. Portions of Chapter 3 have been previously published [31,32], and joint authorship with M.G. Nichols and T.H. Foster is gratefully acknowledged. In addition, portions of Section 3.4.1 appeared in Dr. Nichols's PhD thesis [33].

Chapter 4 presents experiments which test the accuracy and validity of hemoglobin spectroscopy performed with the instrument described in Chapter 3. An analysis of the proper basis spectra for near-IR hemoglobin oximetry is presented, and it is demonstrated that the spectroscopic techniques developed in Chapters 2 and 3 can be implemented to give quantitatively accurate hemoglobin absorption spectra. An analysis technique is developed which facilitates hemoglobin spectroscopy in the presence of weakly absorbing but uncharacterized absorbing species. The contents of

Chapter 4 have been published [31]; joint authorship with M.G. Nichols and T.H. Foster is again acknowledged.

In Chapter 5, the analysis techniques developed in Chapter 4 are applied to in-vivo measurements of hemoglobin oxygenation status in a subcutaneous rodent tumor model. The effects of inspired carbogen (5% CO₂, 95% O₂) on the measured hemoglobin oxygen saturation and total hemoglobin concentration are studied, and it is demonstrated that carbogen inhalation results in a general elevation of hemoglobin saturation in the R3230AC tumor line used in this study. The contents of Chapter 5 have been published [34] with D. Conover and T.H. Foster as co-authors.

In Chapter 6, the diffusion-theory Green's function developed in Chapter 2 is implemented in a slightly different context. The expression is recast to express the emittance from a luminescent point source buried in scattering medium. This expression is fit to experimental measurements of the emittance from a spherical fluorescent inhomogeneity to reconstruct the depth of the inclusion and the effective attenuation coefficient of the scattering medium. These experiments were designed to test the ability of a steady-state technique to accurately localize sources of fluorescence and/or phosphorescence in deep tissues. An analysis of the sensitivity of the technique to the medium optical properties is presented. The corrupting effects of nonspecifically localized lumiphore are also considered, and suggestions are made with regard to potential future applications of this technique. With the exception of Section 6.5, the contents of Chapter 6 have also been published [35], and co-authorship with M.G. Nichols and T.H. Foster is once again gratefully acknowledged.

References

1. B. Chance, "Optical method," *Ann. Rev. Biophys. Biophys. Chem.* **20**, 1-28 (1991).
2. A.J. Welch and M.J.C. van Gemert, *Optical-Thermal Response of Laser-Irradiated Tissue* (Plenum Press, New York, 1995), pp. 275-303.
3. W. Cheong, S.A. Prahl, and A.J. Welch, "A review of the optical properties of biological tissues," *IEEE J. Quan. Elec.* **26**, 2166-2185 (1990).
4. E.M. Sevick, B. Chance, J. Leigh, S. Nioka, and M. Maris, "Quantitation of time-resolved and frequency-resolved optical spectra for the determination of tissue oxygenation," *Anal. Biochem.* **195**, 330-351 (1991).
5. J.T. Bruulsema, J.E. Hayward, T.J. Farrell, M.S. Patterson, L. Heinemann, M. Berger, T. Koschinsky, J. Sandahl-Christiansen, H. Orskov, M. Essenpreis, G. Schmelzeisen-Redeker, and D. Böcker, "Correlation between blood glucose concentration in diabetics and noninvasively measured tissue optical scattering coefficient," *Opt. Lett.* **22**, 190-192 (1997).
6. M. Kohi, M. Essenpreis, and M. Cope, "The influence of glucose concentration upon the transport of light in tissue-simulating phantoms," *Phys. Med. Biol.* **40**, 1267-1287 (1995).
7. M.S. Patterson, B.C. Wilson, J.W. Feather, D.M. Burns, and W. Pushka, "The measurement of dihematoporphyrin ether concentration in tissue by reflectance spectrophotometry," *Photochem. Photobiol.* **46**, 337-343 (1987).
8. R.A. Weersink, J.E. Hayward, K.R. Diamond, and M.S. Patterson, "Accuracy of noninvasive in vivo measurements of photosensitizer uptake based on a diffusion model of reflectance spectroscopy," *Photochem. Photobiol.* **66**, 326-335 (1997).
9. M. Cope and D.T. Delpy, "System for long-term measurement of cerebral blood and tissue oxygenation on newborn infants by near-infrared transillumination," *Med. Biol. Eng. Comput.* **26**, 289-294 (1988).

10. B. Chance, M.T. Dait, T. Zhang, T. Hamaoka, and F. Hagerman, "Recovery from exercise-induced desaturation in the quadriceps muscles of elite competitive rowers," *Am. J. Physiol.* **262**, C766-C775(1992).
11. W. Bank and B. Chance, "Diagnosis of mitochondrial diseases by near infrared spectroscopy (NIRS)," in *Optical Tomography, Photon Migration, and Spectroscopy of Tissue and Model Media: Theory, Human Studies, and Instrumentation*, B. Chance and R. R. Alfano, eds., **Proc. SPIE 2389**, 829-834 (1995).
12. S. Fantini, S.A. Walker, M.A. Franceschini, M. Kaschke, P.M. Schlag, and K.T. Moesta, "Assessment of the size, position, and optical properties of breast tumors in vivo by noninvasive optical methods," *Appl. Opt.* **37**, 1982-1989 (1998).
13. S.R. Hintz, W.F. Cheong, J.P. VanHouten, D.K. Stevenson, and D.A. Benaron, "Bedside imaging of intracranial hemorrhage in the neonate using light: comparison with ultrasound, computed tomography, and magnetic resonance imaging," *Pediatr. Res.* **45**, 54-59 (1999).
14. A. Villringer and B. Chance, "Non-invasive optical spectroscopy and imaging of human brain function," *Trends Neurosci.* **20**, 435-442 (1997).
15. P. Parsa, S.L. Jacques, and N.S. Nishioka, "Optical properties of rat liver between 350 and 2200 nm," *Appl. Opt.* **28**, 2325-2330 (1989).
16. A.J. Welch and M.J.C. van Gemert, *Optical-Thermal Response of Laser-Irradiated Tissue* (Plenum Press, New York, 1995), pp. 101-125.
17. J.M. Schmitt and G. Kumar, "Optical scattering properties of soft tissue: a discrete particle model," *Appl. Opt.* **37**, 2788-2797 (1998).
18. D. Voet and J.G. Voet, *Biochemistry* (John Wiley & Sons, New York, 1995), Chapter 20.
19. B. Beauvoit, S.M. Evans, T.W. Jenkins, E.E. Miller, and B. Chance, "Correlation between the light scattering and the mitochondrial content of normal tissues and transplantable rodent tumors," *Anal. Biochem.* **226**, 167-174 (1995).

20. J.R. Mourant, J.P. Freyer, A.H. Hielscher, A.A. Eick, A. Shen, and T.M. Johnson, "Mechanisms of light scattering from biological cells relevant to noninvasive tissue diagnostics," *Appl. Opt.* **37**, 3586-3593 (1998).
21. A.M.K. Nilsson, C. Sturesson, D.L. Liu, and S. Andersson-Engels, "Changes in spectral shape of tissue optical properties in conjunction with laser-induced thermotherapy," *Appl. Opt.* **37**, 1256-1267 (1998).
22. I.S. Saidi, S.L. Jacques, and F.K. Tittel, "Mie and Rayleigh modeling of visible-light scattering in neonatal skin," *Appl. Opt.* **34**, 7410-7419 (1995).
23. L.T. Perelman, V. Backman, M. Wallace, G. Zonios, R. Manoharan, A. Nusrat, S. Shields, M. Seiler, C. Lima, T. Hamano, I. Itzkan, J. VanDam, J.M. Crawford, and M.S. Feld, "Observation of periodic fine structure in reflectance from biological tissue: a new technique for measuring nuclear size distribution," *Phys. Rev. Lett.* **80**, 627-630 (1998).
24. R. Marchesini, A. Bertoni, S. Andreola, E. Melloni, and A.E. Sichirollo, "Extinction and absorption coefficients and scattering phase functions of human tissues in vitro," *Appl. Opt.* **28**, 2318-2324 (1989).
25. S. Wray, M. Cope, D.T. Delpy, J.S. Wyatt, and E.O.R. Reynolds, "Characterization of the near-infrared absorption spectra of cytochrome aa_3 and hemoglobin for the noninvasive monitoring of cerebral oxygenation," *Biochim. Biophys. Acta* **933**, 184-192 (1988).
26. W.G. Zijlstra, A. Buursma, and W.P. Meeuwssen-van der Roest, "Absorption spectra of human fetal and adult oxyhemoglobin, de-oxyhemoglobin, carboxyhemoglobin, and methemoglobin," *Clin. Chem.* **37/9**, 1633-1638 (1991).
27. L.H. Kou, D. Labrie, and P. Chylek, "Refractive indexes of water and ice in the 0.65 μ m to 2.5 μ m spectral range," *Appl. Opt.* **32**, 3531-3540 (1993).
28. B. Chance, "Spectrophotometry of intracellular respiratory pigments," *Science* **120**, 767-775 (1954).

29. F.F. Jöbsis, J.H. Keizer, J.C. LaManna, and M. Rosenthal, "Reflectance spectrophotometry of cytochrome aa_3 in vivo," *J. Appl. Physiol.* **43**, 858-872 (1977).
30. J.B. Fishkin, O. Coquoz, E.R. Anderson, M. Brenner, and B.J. Tromberg, "Frequency-domain photon migration measurements of normal and malignant tissue optical properties in a human subject," *Appl. Opt.* **36**, 10-20 (1997).
31. E.L. Hull, M.G. Nichols, and T.H. Foster, "Quantitative broadband near-infrared spectroscopy of tissue- simulating phantoms containing erythrocytes," *Phys. Med. Biol.* **43**, 3381-3404 (1998).
32. M.G. Nichols, E.L. Hull, and T.H. Foster, "Design and testing of a white-light, steady-state diffuse reflectance spectrometer for determination of optical properties of highly scattering systems," *Appl. Opt.* **36**, 93-104 (1997).
33. M.G. Nichols, "Transport of Oxygen and Light in Model Tumor Systems," PhD dissertation (University of Rochester, Rochester, NY, 1996).
34. E.L. Hull, D.L. Conover, and T.H. Foster, "Carbogen-induced changes in rat mammary tumour oxygenation reported by near infrared spectroscopy," *Br. J. Cancer* **79**, 1709-1716 (1999).
35. E.L. Hull, M.G. Nichols, and T.H. Foster, "Localization of luminescent inhomogeneities in turbid media with spatially resolved measurements of cw diffuse luminescence emittance," *Appl. Opt.* **37**, 2755-2765 (1998).

CHAPTER 2

Radiative Transport Theory: the Diffusion, P_1 , and P_3 Approximations

2.1 The transport equation and the P_N approximation

A widely-accepted theoretical description of light propagation in biological tissues is the Boltzmann transport equation [1,2], which describes the transport of light in a homogeneous scattering and absorbing system:

$$\frac{1}{c} \frac{\partial L(\mathbf{r}, \hat{s}, t)}{\partial t} = -\nabla \cdot L(\mathbf{r}, \hat{s}, t) \hat{s} - \mu_t L(\mathbf{r}, \hat{s}, t) + \mu_s \int_{4\pi} L(\mathbf{r}, \hat{s}', t) f(\hat{s}, \hat{s}') d\Omega' + S(\mathbf{r}, \hat{s}, t) \quad (2.1)$$

where L is the radiance at position \mathbf{r} in direction \hat{s} at time t , with dimensions of power per unit area per unit solid angle, and c is the speed of light in the scattering medium. The scattering coefficient μ_s has dimensions of inverse length and is equal to the scattering cross section of an individual scatterer multiplied by the volume density of scatterers. The scattering mean free pathlength is given by the inverse of μ_s . The total interaction coefficient μ_t is given by the sum of the scattering and absorption coefficients ($\mu_t \equiv \mu_a + \mu_s$), and the scattering phase function $f(\hat{s}, \hat{s}')$ is a probability density function describing the probability for a photon traveling in direction \hat{s}' to scatter into direction \hat{s} . The source distribution is represented by $S(\mathbf{r}, \hat{s}, t)$, and has dimensions of power per unit volume per unit solid angle. The transport equation is a

conservation equation for the radiance at any given volume element of phase space located at position \mathbf{r} and observed from direction \hat{s} . The term on the left hand side represents the time rate of change of the radiance, and the right hand side describes the processes which can result in a decrease (flux along the direction \hat{s} , absorption within the volume element, or scattering out of direction \hat{s}) or increase (scattering into direction \hat{s} from any other direction \hat{s}' or the introduction of photons by sources) in the radiance. The transport equation is a heuristic description of light transport, treating photons as particles undergoing random elastic collisions or absorption events. Coherence and polarization effects are ignored in this representation of the equation of transport.

Because it is difficult to obtain analytic solutions to this integro-differential equation except for the most straightforward geometries and source distributions, such as infinite media and plane wave illumination, various strategies have been developed for arriving at approximate solutions. The P_N approximation is one standard technique. The outline of the P_N approximation presented here has been adapted from several sources, primarily Ishimaru [1], Case and Zweifel [2], Davison [3] and Boas [4]. In the P_N approximation, the angular quantities in Equation 2.1 are expanded in spherical harmonics Y_{lm} . The radiance and source terms are expanded as:

$$L(\mathbf{r}, \hat{s}, t) = \sum_{l=0}^N \sum_{m=-l}^l \sqrt{\frac{2l+1}{4\pi}} \phi_{lm}(\mathbf{r}, t) Y_{lm}(\hat{s}) \quad (2.2)$$

and

$$S(\mathbf{r}, \hat{s}, t) = \sum_{l=0}^N \sum_{m=-l}^l \sqrt{\frac{2l+1}{4\pi}} \sigma_{lm}(\mathbf{r}, t) Y_{lm}(\hat{s}) \quad , \quad (2.3)$$

where ϕ_{lm} and σ_{lm} are the moments of the radiance and source distribution, respectively.

The ϕ_{0m} and ϕ_{1m} are related to two more familiar quantities known as the fluence and the photon flux (or current density). The fluence is the isotropic component of the radiance, defined by

$$\begin{aligned}\Phi &= \int_{4\pi} L(\mathbf{r}, \hat{\mathbf{s}}, t) d\Omega \\ &= \sum_{l=0}^{\infty} \sum_{m=-l}^l \phi_{lm} \int_{4\pi} \sqrt{\frac{2l+1}{4\pi}} Y_{lm}(\hat{\mathbf{s}}) d\Omega \\ &= \phi_{0,0} \quad .\end{aligned}\tag{2.4}$$

The flux is the linearly anisotropic component of the radiance and is defined by

$$\begin{aligned}\mathbf{j}(\mathbf{r}, t) &= \int_{4\pi} L(\mathbf{r}, \hat{\mathbf{s}}, t) \hat{\mathbf{s}} d\Omega \\ &= \sum_{l=0}^{\infty} \sum_{m=-l}^l \phi_{lm} \int_{4\pi} \sqrt{\frac{2l+1}{4\pi}} Y_{lm}(\hat{\mathbf{s}}) [\sin\theta\cos\phi\hat{x} + \sin\theta\sin\phi\hat{y} + \cos\theta\hat{z}] d\Omega \\ &= \sqrt{\frac{4\pi}{3}} \sum_{l=0}^{\infty} \sum_{m=-l}^l \phi_{lm} \int_{4\pi} \sqrt{\frac{2l+1}{4\pi}} Y_{lm}(\hat{\mathbf{s}}) \left[\sqrt{\frac{1}{2}} (-Y_{1,1}^*(\hat{\mathbf{s}}) + Y_{1,-1}^*(\hat{\mathbf{s}})) \hat{x} \right. \\ &\quad \left. -i \sqrt{\frac{1}{2}} (+Y_{1,1}^*(\hat{\mathbf{s}}) + Y_{1,-1}^*(\hat{\mathbf{s}})) \hat{y} + Y_{1,0}^*(\hat{\mathbf{s}}) \hat{z} \right] d\Omega \\ &= \sqrt{\frac{1}{2}} (-\phi_{1,1} + \phi_{1,-1}) \hat{x} - i \sqrt{\frac{1}{2}} (\phi_{1,1} + \phi_{1,-1}) \hat{y} + \phi_{1,0} \hat{z} \quad .\end{aligned}\tag{2.5}$$

It can be seen that the cartesian components of the flux are given by linear combinations of the $\phi_{1,m}$ terms in Equation 2.2.

Under the assumption that the scattering amplitude is dependent on the scattering angle and independent of the spatial location in the medium and the direction $\hat{\mathbf{s}}$ of the incident beam, the phase function f may be expanded in a series of Legendre polynomials in the scattering angle:

$$f(\hat{s} \cdot \hat{s}') = \sum_{l=0}^N \frac{2l+1}{4\pi} g_l P_l(\hat{s} \cdot \hat{s}') \quad (2.6)$$

where P_l is a Legendre polynomial of order l . The phase function is normalized, so $g_0 = 1$, and g_1 is the average cosine of the scattering angle, or the “scattering anisotropy”, which is typically denoted simply g . The phase function most commonly employed for modeling tissue scattering in medical optics is the Henyey-Greenstein phase function [5], which is given by

$$f(\hat{s} \cdot \hat{s}') = f(\cos \theta) = \frac{1}{4\pi} \frac{1 - g^2}{[1 + g^2 - 2g \cos \theta]} \quad (2.7)$$

It is interesting to note that, for the Henyey-Greenstein phase function, $g_l = g_1^l$. Thus, all higher-order moments of the Henyey-Greenstein phase function are determined from the first moment. This is somewhat restrictive and does not allow for an accurate representation of some phase functions which have actually been measured in biological tissues [6-8]. Bevilacqua et al. have recently proposed two new hybrid phase functions which allow more accurate modeling of scattering distributions likely to be encountered in tissue [9].

The P_N approximation is obtained by truncating the expansions in Equations 2.2, 2.3, and 2.6 at $l=N$, where N is the order of the approximation. The resulting set of coupled differential equations may then be solved to determine the corresponding moments of the radiance. Higher-order approximations more accurately model increased anisotropy in the radiance, which is encountered near sources and boundaries, and more precisely predict the attenuation of radiation far from sources. Smaller albedos ($a = \mu_s/(\mu_a + \mu_s)$) require increasingly higher orders of approximation

for correct prediction of the attenuation coefficient.

2.2 The P_1 approximation

In the P_1 approximation, the radiance, source term, and phase function, respectively, may each be written as the sum of an isotropic term and a linearly anisotropic term:

$$L(\mathbf{r}, \hat{s}, t) = \frac{1}{4\pi} \Phi(\mathbf{r}, t) + \frac{3}{4\pi} \mathbf{j}(\mathbf{r}, t) \cdot \hat{s} \quad , \quad (2.8)$$

$$S(\mathbf{r}, \hat{s}, t) = \frac{1}{4\pi} S_0(\mathbf{r}, t) + \frac{3}{4\pi} \mathbf{S}_1(\mathbf{r}, t) \cdot \hat{s} \quad , \quad (2.9)$$

and

$$f(\hat{s} \cdot \hat{s}') = \frac{1}{4\pi} + \frac{3}{4\pi} g_1 \hat{s} \cdot \hat{s}' \quad , \quad (2.10)$$

where S_0 and \mathbf{S}_1 are related to the monopole and dipole moments of the source distribution in a manner analogous to the relationships in Equations 2.4 and 2.5.

After Equations 2.8, 2.9, and 2.10 are substituted into Equation 2.1, integration over all solid angles yields a partial differential equation in Φ and \mathbf{j} :

$$\frac{1}{c} \frac{\partial}{\partial t} \Phi(\mathbf{r}, t) + \mu_a \Phi(\mathbf{r}, t) + \nabla \cdot \mathbf{j}(\mathbf{r}, t) = S_0(\mathbf{r}, t) \quad . \quad (2.11)$$

Another such equation may be obtained by multiplying Equation 2.1 by \hat{s} and again integrating over all solid angles:

$$\frac{1}{c} \frac{\partial}{\partial t} \mathbf{j}(\mathbf{r}, t) + (\mu_s' + \mu_a) \mathbf{j}(\mathbf{r}, t) + \frac{1}{3} \nabla \Phi(\mathbf{r}, t) = \mathbf{S}_1(\mathbf{r}, t) \quad . \quad (2.12)$$

Equations 2.11 and 2.12 may then be decoupled, yielding an equation in Φ alone:

$$\begin{aligned}
-D \nabla^2 \Phi(\mathbf{r}, t) + c \mu_a \Phi(\mathbf{r}, t) + \frac{\partial \Phi(\mathbf{r}, t)}{\partial t} + \frac{3D}{c} \left[\mu_a \frac{\partial \Phi}{\partial t} + \frac{1}{c} \frac{\partial^2 \Phi}{\partial t^2} \right] = \\
c S_0(\mathbf{r}, t) - 3D \nabla \cdot \mathbf{S}_1(\mathbf{r}, t) + \frac{3D}{c} \frac{\partial S_0}{\partial t} \quad ,
\end{aligned}
\tag{2.13}$$

where D is the photon diffusion coefficient ($D = c/[3(\mu_a + \mu_s')]$, with $\mu_s' = \mu_s(1-g)$). Equation 2.13 constitutes the P_1 approximation to the radiative transport equation.

Note that in the P_1 approximation, the scattering coefficient always appears multiplied by the factor $1-g$. This product is referred to as the “reduced” or “transport” scattering coefficient. The fact that μ_s always enters the P_1 approximation in this manner indicates that, in situations where the P_1 approximation is valid, the highly anisotropic, forward-directed scattering typical of tissues may be modeled as a case in which scattering is isotropic, but with the scattering cross section reduced by a factor of $1-g$. Therefore, when working in the P_1 approximation, it is customary to describe a medium in terms of its “reduced” optical properties, defined by:

$$\begin{aligned}
\mu_s' &= \mu_s(1-g) \\
\mu_t' &= \mu_a + \mu_s' \\
a' &= \mu_s' / (\mu_s' + \mu_a) \quad ,
\end{aligned}
\tag{2.14}$$

where μ_t' is the reduced total attenuation coefficient and a' is the reduced albedo. Another quantity frequently of interest is the transport mean free path (mfp'), which is the inverse of μ_t' . The description of optical transport using these reduced optical properties is an application of the similarity principle and has been discussed in detail by Wyman et al. [10,11] and Star et al. [12].

2.3 The diffusion approximation

The time-dependent photo-diffusion equation is obtained when the last term on the right-hand side and the last two terms on the left-hand side of Equation 2.13 are dropped. The validity of this assumption can be seen by considering a sinusoidally modulated source so that the fluence $\Phi(\mathbf{r},t)$ can be expressed as $\Phi(\mathbf{r}) \exp(-i\omega t)$. The time derivatives can then be replaced by $-i\omega$, and the terms in question can be ignored if $3D\omega/c^2 \ll 1$, which is equivalent to $c\mu_s'/\omega \gg 1$, implying that the transport scattering frequency must be much larger than the modulation frequency [13]. The remaining expression is the time-dependent photo-diffusion equation:

$$-D \nabla^2 \Phi(\mathbf{r},t) + c\mu_a \Phi(\mathbf{r},t) + \frac{\partial}{\partial t} \Phi(\mathbf{r},t) = c S_0(\mathbf{r},t) - 3D \nabla \cdot \mathbf{S}_1(\mathbf{r},t) \quad . \quad (2.15)$$

Again assuming an isotropic source, the steady-state components of Equation 2.15 yield the steady-state photo-diffusion equation,

$$D' \nabla^2 \Phi(\mathbf{r}) - \mu_a \Phi(\mathbf{r}) = -S_0(\mathbf{r}) \quad . \quad (2.16)$$

Note that the equation has been re-scaled by dividing through by c , so the steady-state diffusion coefficient now has dimensions of length (conventional in the literature) and is given by $D' = (3(\mu_a + \mu_s'))^{-1}$. Hereafter D will be used to denote the “steady-state” diffusion coefficient. In the steady state, again assuming only isotropic sources, Equation 2.12 yields an exact corollary to Fick’s law for photon diffusion:

$$\mathbf{j}(\mathbf{r}) = -D \nabla \Phi(\mathbf{r}) \quad . \quad (2.17)$$

To a good approximation, Equation 2.17 is also valid in the frequency domain for modulation frequencies smaller than ~ 1 GHz [14]. Note also that, in the steady state,

there is no distinction between the P_1 and diffusion approximations.

The diffusion approximation is generally valid if the transport albedo is large (≈ 1), the scattering is not extremely anisotropic (i.e., g_1 is less than approximately 0.99), and at source-detector separations greater than 1 transport mean free path. An excellent discussion of the different regimes of validity of the P_1 and diffusion approximations has been published by Fishkin et al. [13].

The Green's function of the time-independent diffusion equation assuming a homogeneous infinite medium is well-known [15] and is given by

$$\Phi_G(r) = \frac{1}{4\pi D} \frac{e^{-\mu_{\text{eff}} r}}{r}, \quad (2.18)$$

where μ_{eff} is the effective attenuation coefficient, defined by $\mu_{\text{eff}} = (3\mu_a(\mu_a + \mu_s'))^{-1/2}$. It is important to recognize that Equation 2.18 is the Green's function for the *fluence* in the diffusion approximation. The Green's function for the *radiance* is obtained by substituting the expression in Equation 2.18 into Equations 2.17 and 2.8.

2.4 The P_3 approximation

The P_3 approximation to the transport equation is obtained by truncating the expansions in Equations 2.2, 2.3, and 2.6 at the level of $l = 3$. As the P_1 equation resulted in set of 4 coupled, first-order, linear partial differential equations corresponding to the scalar and three cartesian components of Equations 2.11 and 2.12, the P_3 approximation yields a set of 16 such equations. In general, the P_N approximation generates a set of $(N+1)^2$ coupled equations. To derive the Green's function to Equation 2.1 in the P_3 approximation for the case of an isotropic, cw point

source in an infinite, spherically symmetric medium, we consider first the simpler case of a slab source of infinite extent in an infinite medium. We then take the limiting form of that solution as the thickness of the slab approaches zero and transform the result to a spherically symmetric geometry using standard transport theory techniques.

In an infinite slab geometry, the radiance is dependent only on the z coordinate and η , where η is the cosine of the angle between the z axis and \hat{s} ($\eta \equiv \hat{z} \cdot \hat{s}$). In this case, the radiance, source term, and scattering phase function from Equation 2.1 may be expanded:

$$\begin{aligned} L(z, \eta) &= \sum_{m=0}^3 \frac{2m+1}{4\pi} \varphi_m(z) P_m(\eta) \\ S(z, \eta) &= \sum_{m=0}^3 \frac{2m+1}{4\pi} q_m(z) P_m(\eta) \\ f(\hat{s} \cdot \hat{s}') &= \sum_{m=0}^3 \frac{2m+1}{4\pi} g_m P_m(\hat{s} \cdot \hat{s}') \quad , \end{aligned} \quad (2.19)$$

where P_m is a Legendre polynomial of order m and φ_m and q_m are the moments of the radiance and the source distribution, respectively. Inserting Equations 2.19 into Equation 2.1, multiplying by $P_l(\eta)$, and integrating over all solid angles yields the following set of first-order linear partial differential equations [2]:

$$\frac{1}{2l+1} \left[l \frac{\partial}{\partial z} \varphi_{l-1} + (l+1) \frac{\partial}{\partial z} \varphi_{l+1} \right] + (\mu_t - \mu_s g_l) \varphi_l = q_l \quad . \quad (2.20)$$

The first four of these equations (ignoring moments for which $l \geq 3$) are:

$$\begin{aligned}
\mu_a \varphi_0 + \varphi_1' &= q_0 \\
\frac{1}{3} \varphi_0' + \mu_t^{(1)} \varphi_1 + \frac{2}{3} \varphi_2' &= q_1 \\
\frac{1}{5} \varphi_1' + \mu_t^{(2)} \varphi_2 + \frac{3}{5} \varphi_3' &= q_2 \\
\frac{1}{7} \varphi_2' + \mu_t^{(3)} \varphi_3 &= q_3
\end{aligned} \tag{2.21}$$

where primes denote differentiation, $\mu_t^{(l)} \equiv \mu_a + \mu_s (1 - g_l)$, and $\mu_t^{(0)} = \mu_a$. These equations could, in principle, be decoupled to obtain a single 4th order partial differential equation in the fluence (φ_0), but, since we seek a complete expression for the radiance in the P_3 approximation, we take the approach of solving Equations 2.21 directly. Considering source-free regions initially and noting that the equations are first-order and linear, we seek (four) simple-exponential solutions to the homogeneous version of Equations 2.21. Assuming a solution for φ_l of the form

$$\varphi_l(z) = \sum_{j=0}^3 A_{lj} e^{v_j z} \quad , \tag{2.22}$$

and substituting into Equations 2.21 yields, for each j ,

$$v \left[(l+1) A_{l+1} + l A_{l-1} \right] + (2l + 1) \mu_t^{(l)} A_l = 0 \quad (l = 0 \dots 3). \tag{2.23}$$

Nontrivial solutions for v may be determined by requiring the determinant of the coefficients in Equations 2.23 to vanish,

$$\begin{vmatrix}
\mu_a & v & 0 & 0 \\
v & 3 \mu_t^{(1)} & 2 v & 0 \\
0 & 2 v & 5 \mu_t^{(2)} & 3 v \\
0 & 0 & 3 v & 7 \mu_t^{(3)}
\end{vmatrix} = 0 \quad , \tag{2.24}$$

which gives the four possible values of v_j :

$$v = \pm v^+ = \pm \left[\frac{\beta + \sqrt{\beta^2 - \gamma}}{18} \right]^{1/2} \quad (2.25)$$

and

$$v = \pm v^- = \pm \left[\frac{\beta - \sqrt{\beta^2 - \gamma}}{18} \right]^{1/2}, \quad (2.26)$$

where

$$\beta \equiv 27 \mu_a \mu_t^{(1)} + 28 \mu_a \mu_t^{(3)} + 35 \mu_t^{(2)} \mu_t^{(3)} \quad (2.27)$$

and

$$\gamma \equiv 3780 \mu_a \mu_t^{(1)} \mu_t^{(2)} \mu_t^{(3)}. \quad (2.28)$$

These results agree with those of Star [16] and Boas [17], whose notation is used here.

The various A_{l_j} are determined by solving Equations 2.23. They are found to be related to A_{0_j} by functions of the medium optical properties $h_l(v_j)$:

$$\begin{aligned} A_{1_j} &= A_{0_j} h_1(v_j); & h_1(v_j) &\equiv \left(-\frac{\mu_a}{v_j} \right) \\ A_{2_j} &= A_{0_j} h_2(v_j); & h_2(v_j) &\equiv \left(-\frac{1}{2} + \frac{3\mu_a \mu_t^{(1)}}{2v_j^2} \right) \\ A_{3_j} &= A_{0_j} h_3(v_j); & h_3(v_j) &\equiv \left(-\frac{9\mu_a \mu_t^{(1)}}{14\mu_t^{(3)} v_j} + \frac{3v_j}{14\mu_t^{(3)}} \right). \end{aligned} \quad (2.29)$$

Thus, the radiance in source-free regions of media with planar symmetry is

given by

$$L(z, \eta) = \sum_{l=0}^3 \frac{2l+1}{4\pi} \varphi_l(z) P_l(\eta) \quad , \quad (2.30)$$

with $\varphi_l(z)$ given by Equation 2.22, attenuation coefficients v_l given by Equations 2.25 and 2.26, and constants A_{l_j} defined by Equation 2.29. The A_{0_j} are four constants to be determined by the source distribution and boundary conditions.

We now solve for the radiance generated by a slab of infinite extent and finite width $2b$ (Figure 2.1) containing a homogeneous distribution of isotropic sources. We then take the limit as the slab width goes to zero, the source strength (q_0) goes to infinity, and the product $2q_0b$ remains equal to unity (i.e., unit source strength per unit area).

In the interior region ($|z| \leq b$), all possible values of v (i.e., $\pm v^\pm$) are permissible, while in the exterior region ($|z| > b$), only solutions which decay to zero as $z \rightarrow \infty$ (i.e., $-v^\pm$) are allowed. Requiring symmetry with respect to the $z=0$ axis and noting that the $h_l(v_j)$ are of odd parity with respect to v for odd l and even parity with respect to v for even l , we obtain for the interior region:

$$\begin{aligned} \varphi_{0_{in}}(x) &= E \cosh(z v^-) + F \cosh(z v^+) \\ \varphi_{1_{in}}(x) &= E h_1(v^-) \sinh(|z v^-|) + F h_1(v^+) \sinh(|z v^+|) \\ \varphi_{2_{in}}(x) &= E h_2(v^-) \cosh(z v^-) + F h_2(v^+) \cosh(z v^+) \\ \varphi_{3_{in}}(x) &= E h_3(v^-) \sinh(|z v^-|) + F h_3(v^+) \sinh(|z v^+|) \quad . \end{aligned} \quad (2.31)$$

In the exterior region we have

$$\begin{aligned} \varphi_{0_{out}}(x) &= C \exp(-v^-(|z|-b)) + D \exp(-v^+(|z|-b)) \\ \varphi_{1_{out}}(x) &= C h_1(-v^-) \exp(-v^-(|z|-b)) + D h_1(-v^+) \exp(-v^+(|z|-b)) \\ \varphi_{2_{out}}(x) &= C h_2(-v^-) \exp(-v^-(|z|-b)) + D h_2(-v^+) \exp(-v^+(|z|-b)) \\ \varphi_{3_{out}}(x) &= C h_3(-v^-) \exp(-v^-(|z|-b)) + D h_3(-v^+) \exp(-v^+(|z|-b)) \quad . \end{aligned} \quad (2.32)$$

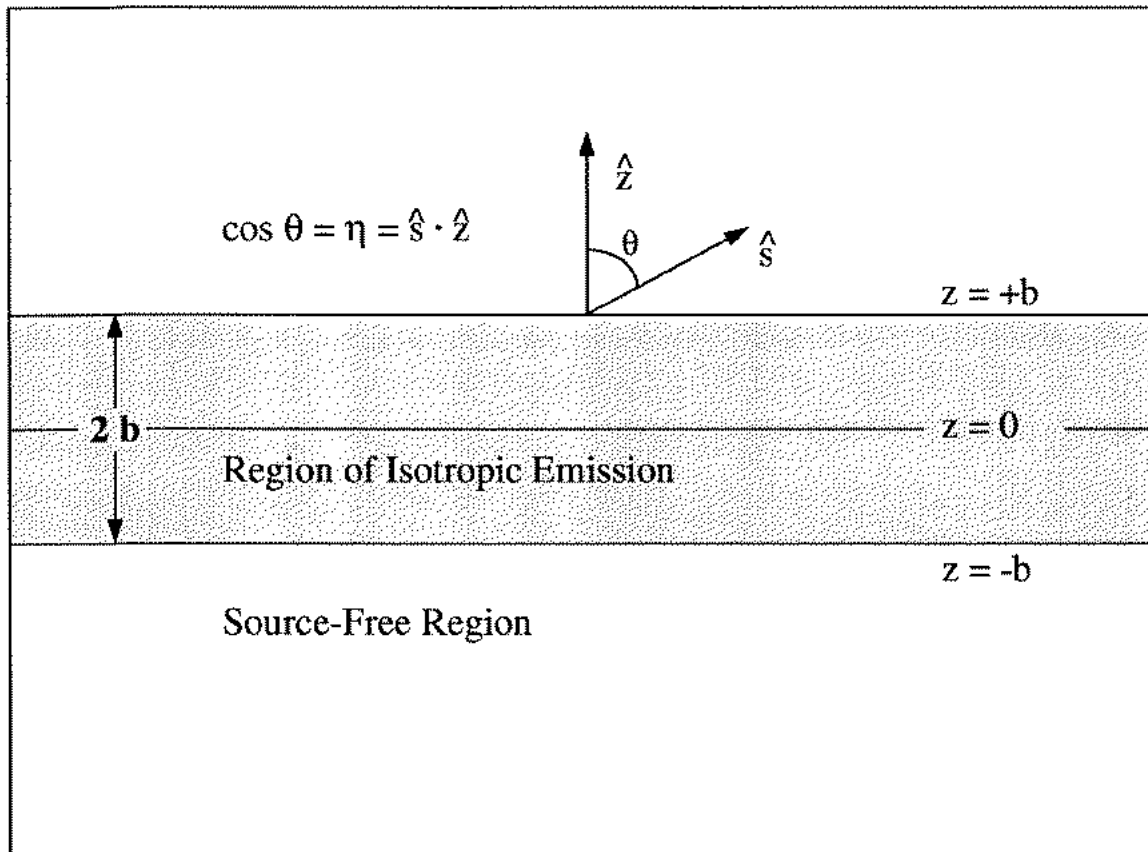


Figure 2.1 The infinite slab geometry used in the derivation of the P_3 Green's function.

The constants of interest are C and D, which describe the radiance external to the source region. To obtain a solution, we require continuity of each moment of the radiance (φ_0 , φ_1 , φ_2 , and φ_3) at the boundaries $z=\pm b$ [3]. In addition, for the case of the interior region, we must add to the general solutions of the homogeneous equations (above) particular solutions to the inhomogeneous equations. The solution of Equations 2.21, assuming an isotropic source ($q_l = 0$ for $l \geq 1$) is

$$\begin{aligned}\varphi_0(z, \mu) &= \frac{q_0}{\mu_a} \\ \varphi_l(z, \mu) &= 0 \quad (l > 0) .\end{aligned}\tag{2.33}$$

Thus, we solve the system of equations

$$\begin{aligned}\varphi_{0_{in}}(\pm b) + \frac{q_0}{\mu_a} &= \varphi_{0_{out}}(\pm b) \\ \varphi_{1_{in}}(\pm b) &= \varphi_{1_{out}}(\pm b) \\ \varphi_{2_{in}}(\pm b) &= \varphi_{2_{out}}(\pm b) \\ \varphi_{3_{in}}(\pm b) &= \varphi_{3_{out}}(\pm b)\end{aligned}\tag{2.34}$$

for the coefficients C and D. The result is

$$\begin{aligned}C &= \frac{b v^{-3} (3\mu_a \mu_t^{(1)} - v^{+2}) q_0}{3 \mu_a^2 \mu_t^{(1)} (1+b v^-) (v^{-2} - v^{+2})} \\ D &= \frac{b v^{+3} (3\mu_a \mu_t^{(1)} - v^{-2}) q_0}{3 \mu_a^2 \mu_t^{(1)} (1+b v^+) (v^{+2} - v^{-2})} .\end{aligned}\tag{2.35}$$

Taking the limit as $b \rightarrow 0$, $q_0 \rightarrow \infty$, $2q_0 b = 1$, we obtain

$$C = \frac{v^{-3} (3\mu_a \mu_t^{(1)} - v^{+2})}{6 \mu_a^2 \mu_t^{(1)} (v^{-2} - v^{+2})}$$

$$D = \frac{v^{+3} (3\mu_a \mu_t^{(1)} - v^{-2})}{6 \mu_a^2 \mu_t^{(1)} (v^{+2} - v^{-2})} .$$
(2.36)

Thus, in an infinite homogeneous medium, the P_3 Green's function for the fluence originating from an infinite plane source is

$$\psi_0(z) = C \exp(-v^- z) + D \exp(-v^+ z) ,$$
(2.37)

with C and D defined in Equation 2.36 and v^- and v^+ defined in Equations 2.25 and 2.26. The flux in this case is in the \hat{z} direction, and the magnitude of the flux is given by ϕ_1 . Higher-order moments of the radiance may be determined using Equations 2.19, 2.22, and 2.29.

To transform these results to spherically-symmetric geometries, we note several general results of transport theory. First, the fluence in a spherically symmetric medium, $\psi_{0_{sp}}(r)$, is related to the fluence in a medium with planar symmetry, $\phi_{0_{pl}}(z)$, in the following manner [2]:

$$\psi_{0_{sp}}(r) = -\frac{1}{2\pi r} \frac{d}{dr} [\phi_{0_{pl}}(r)] .$$
(2.38)

Second, in spherically symmetric geometries, the radiance can depend only on $r = |\mathbf{r}|$ and the angle between \hat{r} and the observation direction \hat{s} . In the P_N approximation, the radiance may therefore be expressed

$$L(r, \hat{s}) = \sum_{l=0}^N \frac{2l+1}{4\pi} \psi_l(r) P_l(\hat{r} \cdot \hat{s}) \quad . \quad (2.39)$$

Furthermore, the moments of the radiance in a medium with spherical symmetry, ψ_l , are known to be of the form [18]

$$\psi_l(r) = \sum_{j=0}^N B_j h_l(v_j) Q_l(v_j r) \quad , \quad (2.40)$$

where B_j are constants determined by the source distribution and boundary conditions, $h_l(v_j)$ are identical to the functions defined in Equation 2.29 for the case of planar symmetry, and the functions $Q_l(x)$ are defined by the recursion relation

$$Q_l(x) = Q_{l-2}(x) - \frac{2l-1}{x} Q_{l-1}(x) \quad . \quad (2.41)$$

The first two Q_l are given by

$$\begin{aligned} Q_0(x) &= \frac{e^x}{x} \\ Q_1(x) &= \left(1 - \frac{1}{x}\right) \frac{e^x}{x} \quad . \end{aligned} \quad (2.42)$$

The Green's function for the fluence in a spherically-symmetric medium in the P_3 approximation is therefore obtained by applying Equation 2.38 to Equation 2.37, which gives the result

$$\begin{aligned} \psi_0(r) &= \left(\frac{-C(v^-)^2}{2\pi} \right) \frac{\exp(-v^- r)}{(-v^- r)} + \left(\frac{-D(v^+)^2}{2\pi} \right) \frac{\exp(-v^+ r)}{(-v^+ r)} \\ &= C' Q_0(-v^- r) + D' Q_0(-v^+ r) \quad . \end{aligned} \quad (2.43)$$

Higher-order moments of the radiance are obtained by substituting C' and D' from Equation 2.43, the $Q_l(x)$ defined in Equations 2.41 and 2.42, and the $h_l(v_j)$ defined in

Equation 2.29 into Equation 2.40. The result is the P_3 Green's function for the radiance originating from isotropic point source in an infinite medium:

$$L(r, \hat{s}) = \sum_{l=0}^3 \frac{2l+1}{4\pi} \left[C' h_l(-v^-) Q_l(-v^- r) + D' h_l(-v^+) Q_l(-v^+ r) \right] P_l(\hat{s} \cdot \hat{r}) \quad (2.44)$$

2.5 Considerations for applying the P_3 approximation to tissue spectroscopy

In the P_3 approximation, there are two possible magnitudes for the attenuation coefficient: v^+ and v^- (Equations 2.25 and 2.26). The solution associated with v^+ contributes significantly only at source-detector separations $\lesssim 2$ transport mean free paths and is known as the “transient” solution. The solution associated with v^- dominates at large source-detector separations and is known as the “asymptotic” solution. Figure 2.2 is a plot of v^+ , v^- , and μ_{eff} (the diffusion theory attenuation coefficient) as a function of the transport albedo assuming $\mu_s = 10.0 \text{ mm}^{-1}$, Henyey-Greenstein scattering and a scattering anisotropy (g) of 0.9. The corresponding value of the absorption coefficient is indicated on the top axis. Note that v^- is approximately equal to μ_{eff} for large albedos where diffusion theory would be expected to be valid, and deviates increasingly from μ_{eff} as the albedo decreases. Thus, smaller albedos require correspondingly higher-order approximations to the transport equation in order to adequately model optical attenuation far from sources.

The striking degree of improvement offered by the P_3 approximation is evident in Figure 2.3, which is a plot of the asymptotic attenuation coefficients of the diffusion approximation (μ_{eff}), the P_3 approximation ($v_{P_3}^-$), and the P_5 approximation ($v_{P_5}^-$) as a function of the transport albedo for the scattering conditions described above. While

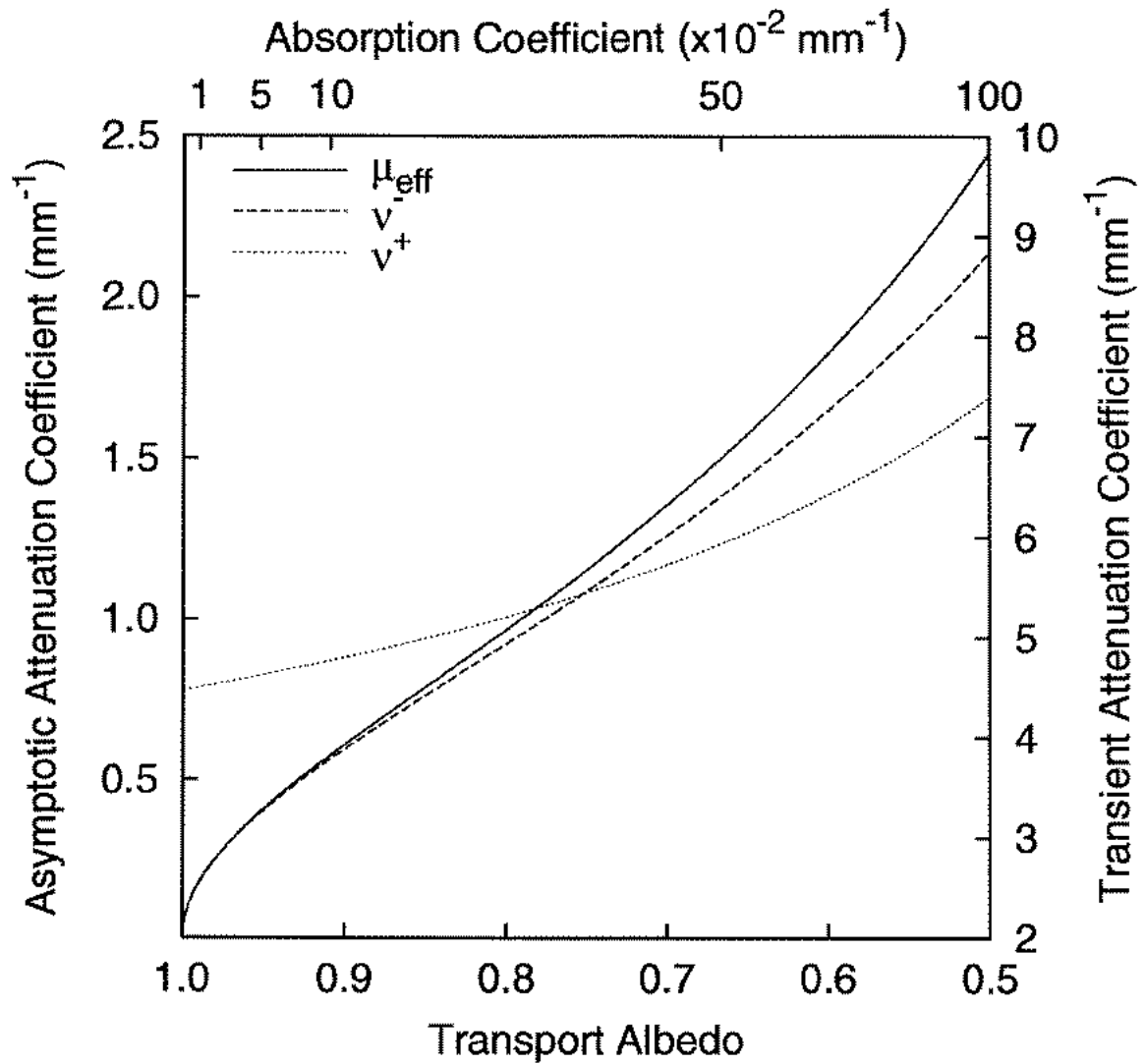


Figure 2.2 The P_3 transient attenuation coefficient (v^+), asymptotic attenuation coefficient (v), and μ_{eff} (the diffusion-theory attenuation coefficient) as a function of the transport albedo assuming $\mu_s = 10.0 \text{ mm}^{-1}$, Henyey-Greenstein scattering and a scattering anisotropy (g) of 0.9. The corresponding value of the absorption coefficient is indicated on the top axis.

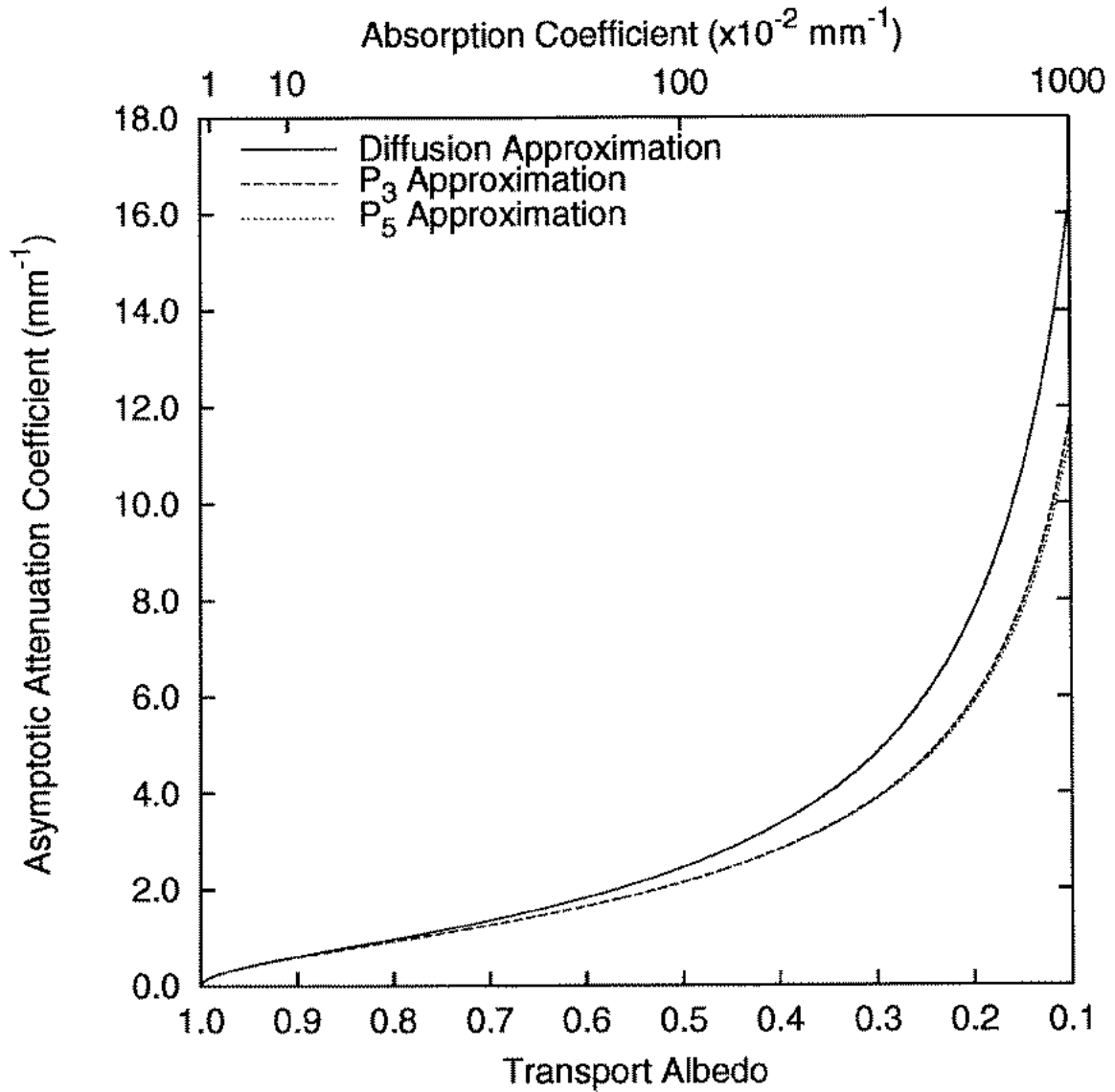


Figure 2.3 The asymptotic attenuation coefficients of the diffusion approximation (μ_{eff}), the P₃ approximation (ν_{P_3}), and the P₅ approximation (ν_{P_5}) as a function of the transport albedo for the scattering conditions used to generate Figure 2.2.

the P_3 and diffusion solutions agree to within 1% only for $a' \geq 0.95$, 1% agreement between the P_3 and P_5 solutions is maintained for a much larger range of albedos ($a' \geq 0.25$), suggesting that the P_3 approximation should be accurate for the full range of tissue optical properties likely to be encountered throughout the visible and near-IR regions of the spectrum. Note also that the terminal slopes of the three lines plotted in Figure 2.3 indicate the degree to which the various approximations approach Beer's Law in the limit of $a' \rightarrow 0$, corresponding to a purely absorbing medium. In this case, the asymptotic attenuation coefficient should approach μ_a , resulting in an infinite terminal slope. A 63% correction is achieved in moving from the diffusion to the P_3 approximation (asymptotic coefficients of $1.73\mu_a$ and $1.16\mu_a$, respectively), while the P_5 result yields an additional 10% correction ($\tilde{\nu}_{P_5} = 1.06\mu_a$).

Figure 2.4 depicts the results of Monte Carlo simulations of isotropic point sources in infinite media. The data points are the absorbed fluence as a function of r , the distance from the source. Also shown are the diffusion theory solution for the fluence (dotted lines), the asymptotic P_3 solution for the fluence (contribution from ν^- only, dashed lines), and the total P_3 solution for the fluence (contributions from ν^+ and ν^- , solid lines). In panel a, the medium optical properties were $\mu_a=0.01 \text{ mm}^{-1}$, $\mu_s=10.0 \text{ mm}^{-1}$, $g=0.9$ ($\mu_s'=1.00 \text{ mm}^{-1}$, $a'=0.99$). For this simulation, the diffusion theory solution and the asymptotic P_3 solutions are identical. In panel b, the optical properties were $\mu_a=1.00 \text{ mm}^{-1}$, $\mu_s=10.0 \text{ mm}^{-1}$, $g=0.9$ ($\mu_s'=1.00 \text{ mm}^{-1}$, $a'=0.5$). It is clear that the P_3 solution estimates the asymptotic attenuation coefficient much more accurately than diffusion theory for low albedos. For large source-detector separations and large albedos, the P_3 and diffusion solutions are equivalent as expected. At short source-detector separations, however, the transient P_3 solution substantially improves the theoretical prediction of the fluence.

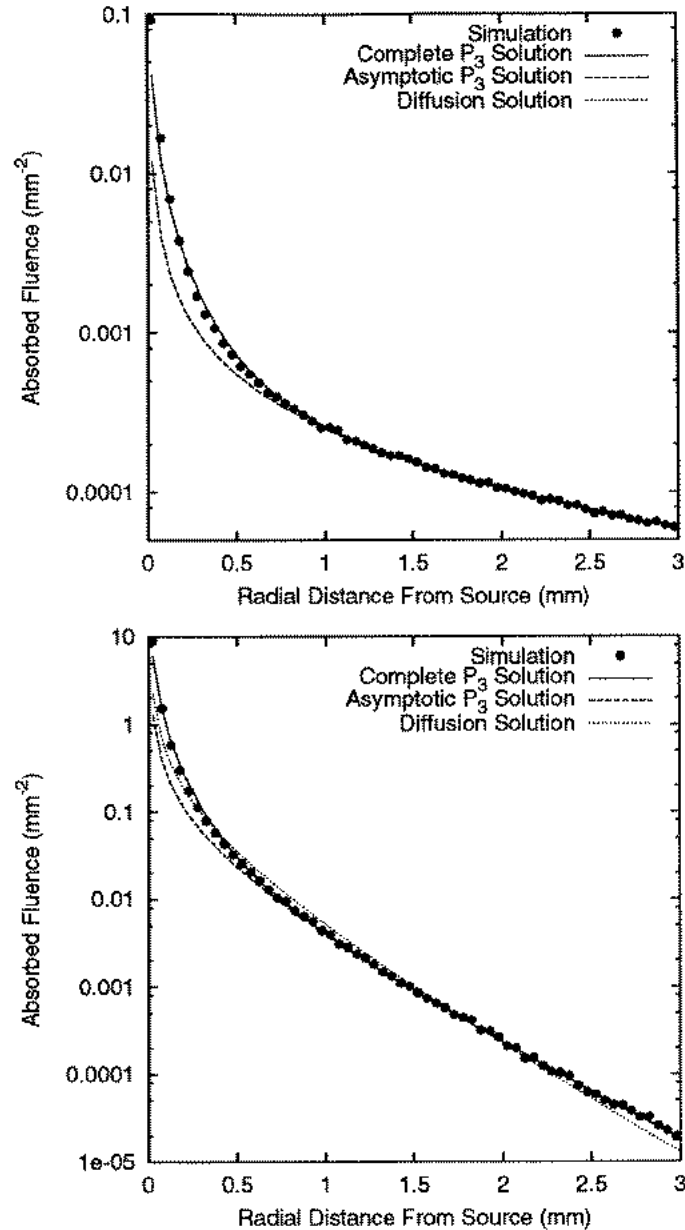


Figure 2.4: Results of Monte Carlo simulations of isotropic point sources in infinite media. Data points are the absorbed fluence as a function of r , the distance from the source. Also shown are the diffusion theory solution for the fluence (dotted lines), the asymptotic P_3 solution for the fluence (contribution from v only, dashed lines), and the total P_3 solution for the fluence (contributions from v^+ and v^- , solid lines). In the upper panel, the medium optical properties were $\mu_a=0.01 \text{ mm}^{-1}$, $\mu_s=10.0 \text{ mm}^{-1}$, $g=0.9$. For this simulation, the diffusion theory solution and the asymptotic P_3 solutions are identical. In the lower panel, the optical properties were $\mu_a=1.00 \text{ mm}^{-1}$, $\mu_s=10.0 \text{ mm}^{-1}$, $g=0.9$.

It is interesting to compare the Green's functions for the fluence and the corresponding expressions for the photon flux in the diffusion and P_3 approximations. In the diffusion approximation, the fluence (ψ_0) and the magnitude of the flux (ψ_1) are related through Fick's Law:

$$\psi_1(r) = -D \left| \nabla \psi_0(r) \right| . \quad (2.45)$$

In the P_3 approximation, the magnitude of the flux (ψ_1) is given by:

$$\begin{aligned} \psi_1(r) &= C' h_1(-v^-) Q_1(-v^- r) + D' h_1(-v^+) Q_1(-v^+ r) \\ &= C' \left(\frac{\mu_a}{v^-} \right) \left(1 - \frac{1}{(-v^- r)} \right) \frac{e^{-v^- r}}{(-v^- r)} + D' \left(\frac{\mu_a}{v^+} \right) \left(1 - \frac{1}{(-v^+ r)} \right) \frac{e^{-v^+ r}}{(-v^+ r)} \\ &= - \left(\frac{\mu_a}{(v^-)^2} \right) \nabla Q_0(-v^- r) - \left(\frac{\mu_a}{(v^+)^2} \right) \nabla Q_0(-v^+ r) \\ &\neq -k \left| \nabla \psi_0(r) \right| , \end{aligned} \quad (2.46)$$

where k is an arbitrary constant. Notice that, in the P_3 approximation, there is not a single diffusion coefficient which relates the flux to the gradient of the fluence. However, each *term* in the fluence expression (Equation 2.43) is related by Fick's Law to a *corresponding* term in the flux expression via an associated diffusion coefficient. The diffusion coefficient associated with the transient solution is $\mu_a/(v^+)^2$, and the diffusion coefficient associated with the asymptotic solution is $\mu_a/(v^-)^2$. Thus, the Green's function for the fluence in the P_3 approximation can be considered as the sum of two diffusion-theory Green's functions with different diffusion coefficients.

A significant simplification of the P_3 Green's function is possible when certain approximate relationships exist among the moments of the scattering phase function. This simplification is illustrated in Figure 2.5, which depicts Monte Carlo computations of the reflectance generated from a pencil beam incident on a semi-infinite medium for

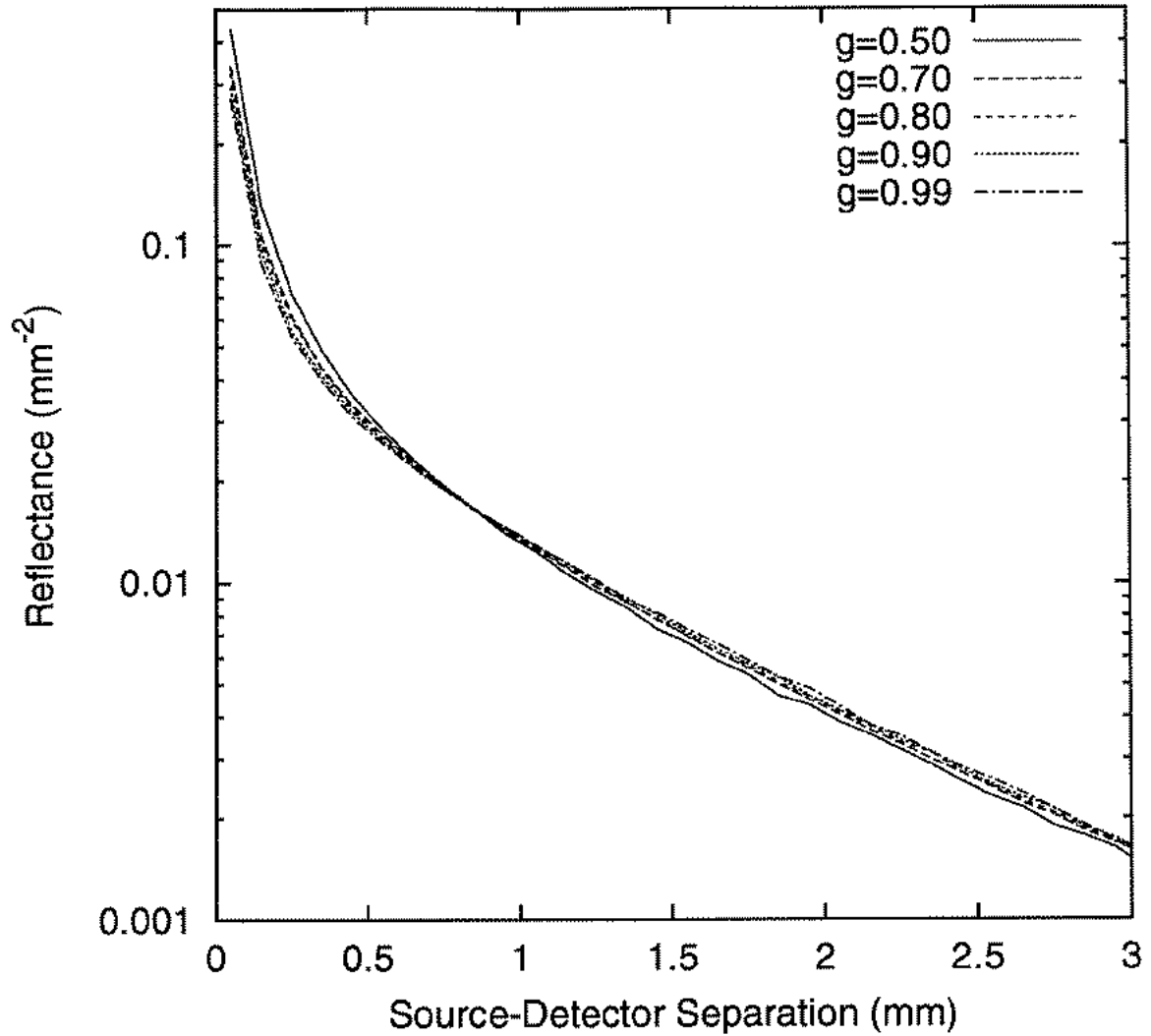


Figure 2.5 The reflectance generated from a pencil beam incident on a semi-infinite medium for which $\mu_a=0.1 \text{ mm}^{-1}$ and $\mu_s'=1.00 \text{ mm}^{-1}$. Data were generated by Monte Carlo simulation. Five different cases, all using Henyey-Greenstein scattering, are shown: $g=0.99$, 0.90 , 0.80 , 0.70 , and 0.50 . For the full range of source-detector separations, the results for $g \geq 0.7$ are nearly indistinguishable.

which $\mu_a=0.1 \text{ mm}^{-1}$ and $\mu_s'=1.00 \text{ mm}^{-1}$. Five different cases, all using Henyey-Greenstein scattering, are shown: $g=0.99, 0.90, 0.80, 0.70$, and 0.50 . For the full range of source-detector separations, the results for $g \geq 0.7$ are nearly indistinguishable. Similar behavior occurs for transport albedos in the range $0.5 \leq a' \leq 0.99$ (data not shown). These results suggest that, while the second- and third-order moments of the radiance are required to accurately represent the reflectance for cases of small source-detector separations and/or large absorption coefficients, a first-order similarity relation still exists under certain circumstances. When this is the case, the radiance can still be expressed as a function of μ_a and μ_s' only, despite that fact that diffusion theory is not valid.

This similarity relation exists when the dimensionless parameters γ and δ , defined by $\gamma=(1-g_2)/(1-g_1)$ and $\delta=(1-g_3)/(1-g_1)$, are relatively constant with respect to changes in g . An example is provided in Figure 2.6, which depicts γ and δ as a function of g_1 for the Henyey-Greenstein phase function. In the range $0 \leq g_1 \leq 1$, γ increases from 1 to 2 and δ increases from 1 to 3. However, in the range $0.7 \leq g_1 \leq 0.99$, $\gamma=1.85 \pm 0.15$ ($\pm 8\%$ variation) and $\delta=2.6 \pm 0.4$ ($\pm 15\%$ variation). Thus, in the theoretical development of the previous section, for scattering anisotropies in the range $0.70 \leq g \leq 0.99$, we may replace occurrences of $\mu_s(1-g_2)$ with $\gamma\mu_s'$ (using $\gamma=1.85$) and occurrences of $\mu_s(1-g_3)$ with $\delta\mu_s'$ (using $\delta=2.6$) and expect to accurately model the radiance in the P_3 approximation as a function of only μ_a and μ_s' . This simplification is significant because it allows extraction of μ_a and μ_s' as fitting parameters without detailed knowledge of the scattering phase function. Interestingly, Bevilacqua has deduced from Monte Carlo simulations that, for media with optical properties relevant to diffusion theory, the reflectance close to sources depends on μ_s' and γ [9]. The solution presented here gives the functional form of this dependence.

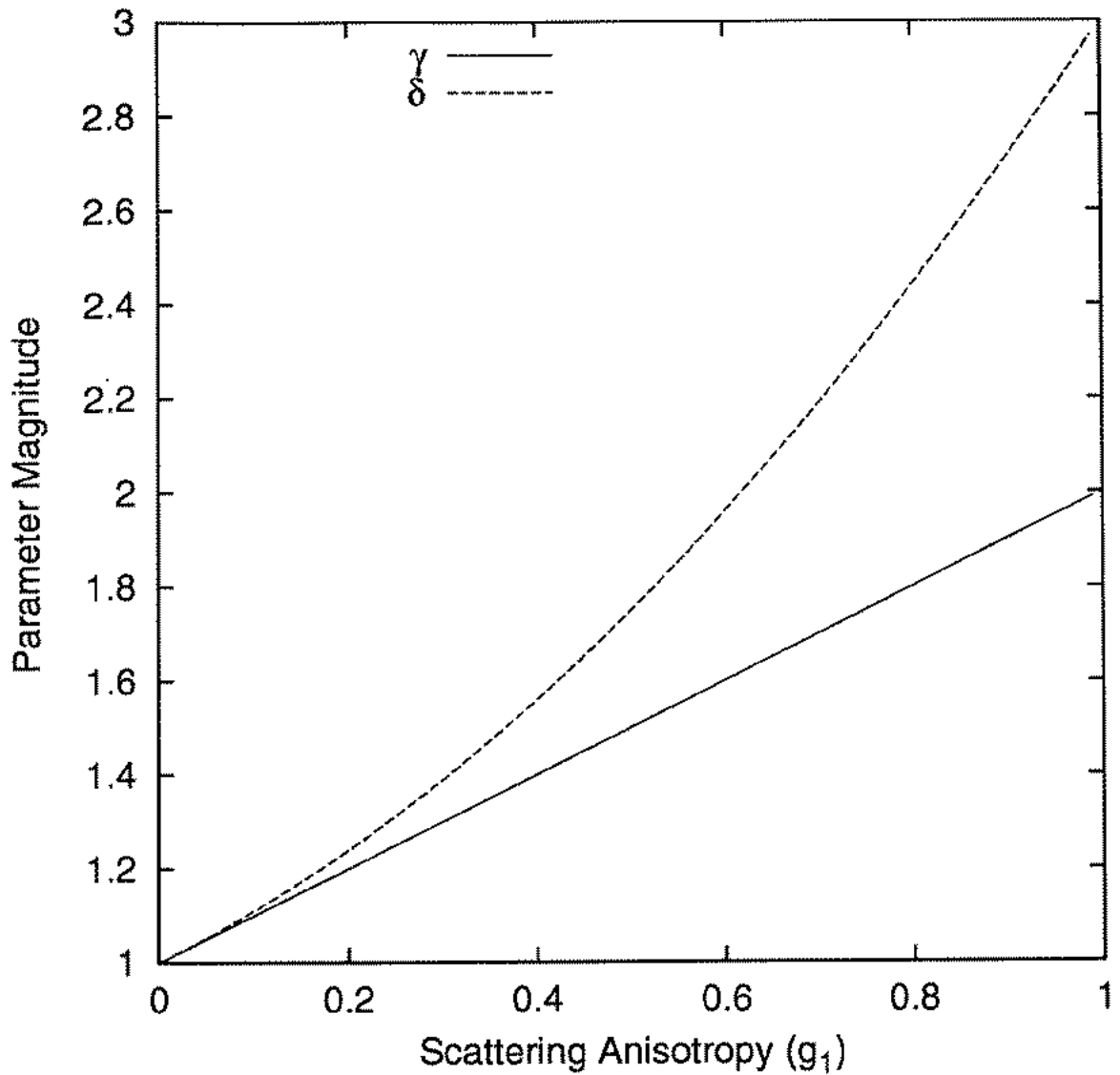


Figure 2.6 The parameters γ and δ (defined by $\gamma=(1-g_2)/(1-g_1)$ and $\delta=(1-g_3)/(1-g_1)$) as a function the scattering anisotropy for the Henyey-Greenstein phase function. The magnitudes of γ and δ vary significantly over the full range of g_1 . However, in the range $0.7 \leq g_1 \leq 0.99$, $\gamma=1.85 \pm 0.15$ ($\pm 8\%$ variation) and $\delta=2.6 \pm 0.4$ ($\pm 15\%$ variation).

The values of γ and δ which optimize this simplified P_3 theory for the Henyey-Greenstein phase function do not necessarily optimize it for spectroscopy of tissue. For example, the phase functions measured by Marchesini et al. for human liver, lung, and uterus which were presented in Chapter 1 have fitted values of $\gamma=2.25, 2.91, \text{ and } 2.56$, respectively. The corresponding values of δ are 3.00, 4.04, and 3.56. These larger values of γ and δ reflect the fact that the measured phase functions have a Rayleigh-like contribution at large scattering angles which is not modeled by the Henyey-Greenstein phase function. Since experimentally measured phase functions of other isolated tissue samples [7] and cells in suspension [6] also exhibit this behavior, it is likely that estimates of γ and δ can be obtained which optimize the simplified P_3 theory for spectroscopy of a wide variety of tissues.

2.6 Boundary Conditions

To obtain solutions for the radiance emitted from a semi-infinite medium bounded by a non-scattering half space, appropriate boundary conditions must be prescribed at the interface. Consider first the case of a boundary between turbid and non-scattering media having equal refractive indices. In this case, assuming no external sources, the physically correct boundary condition to impose is

$$L(\mathbf{r}, \hat{\mathbf{s}}) = 0 \quad (\hat{\mathbf{s}} \cdot \hat{\mathbf{n}} \leq 0) \quad , \quad (2.47)$$

where $\hat{\mathbf{n}}$ is the outward-directed normal to the surface of the scattering medium. This condition simply requires that radiance incident on the boundary from within the scattering medium cannot re-enter the medium. Any photon incident on the boundary must proceed undeviated into the non-scattering medium. This condition is

inconsistent with the P_N approximation, however, since it prescribes a precise value for the radiance at the surface for all observation directions $\hat{s} \cdot \hat{n} \leq 0$. This is equivalent to an infinite number of boundary conditions, and only $(N+1)/2$ conditions may be imposed at a boundary in the P_N approximation.

Approximate boundary conditions are therefore needed, and one of two strategies is generally adopted. First, one can set the radiance equal to zero for $(N+1)/2$ prescribed observation directions \hat{s} on the boundary. These are known as the Mark boundary conditions [2,3,18]. Another set of conditions was developed by Robert Marshak in 1947 in the context of neutron transport theory [3,18]. The Marshak boundary conditions require the radiance at each boundary to be orthogonal to $(N+1)/2$ polynomials in $\hat{s} \cdot \hat{n}$ which span the range $-1 \leq (\hat{s} \cdot \hat{n}) \leq 1$. A natural choice for such a basis set is the Legendre polynomials. The Marshak boundary conditions for the P_N approximation are therefore expressed

$$\int_{\hat{s} \cdot \hat{n} \leq 0} L(\mathbf{r}, \hat{s}) P_l(\hat{s} \cdot \hat{n}) d\Omega = 0 \quad (l = 1, 3, 5 \dots N) \quad (2.48)$$

One advantage of this scheme is that the first order Marshak condition is

$$\int_{\hat{s} \cdot \hat{n} \leq 0} L(\mathbf{r}, \hat{s}) (\hat{s} \cdot \hat{n}) d\Omega = 0 \quad , \quad (2.49)$$

which sets the diffuse fluence entering the scattering medium from the boundary equal to zero in an average sense. It has been demonstrated that the Marshak conditions are superior to the Mark conditions for the P_N approximation when $n \leq 5$ [3]. Therefore, only the Marshak conditions are considered here.

In the case of an index-mismatched boundary, a fraction of the radiance incident

on the boundary from the scattering medium will be reflected back into the scattering medium. That fraction is determined by the Fresnel reflection coefficient for unpolarized light. In this case, the Marshak conditions are modified to the form

$$\int_{\hat{s} \cdot \hat{n} \leq 0} L(\mathbf{r}, \hat{s}) P_l(\hat{s} \cdot \hat{n}) d\Omega = \int_{\hat{s} \cdot \hat{n} \geq 0} R(\cos^{-1}(\hat{s} \cdot \hat{n})) L(\mathbf{r}, \hat{s}) P_l(\hat{s} \cdot \hat{n}) d\Omega \quad (l = 1, 3, 5 \dots N), \quad (2.50)$$

where $R(\cos^{-1}(\hat{s} \cdot \hat{n}))$ is the Fresnel reflection coefficient for radiation incident on the boundary from direction \hat{s} .

2.6.1 Marshak conditions and semi-infinite Green's functions in the diffusion approximation

Substituting the expansion of the radiance in the diffusion approximation (Equation 2.8) into Equation 2.50 with $l=1$ and invoking Fick's Law (Equation 2.17) reduces the first-order Marshak condition to the form [14,19]

$$\psi'_0 \Big|_{z=0} = \frac{1}{2AD} \psi_0 \Big|_{z=0}, \quad (2.51)$$

where A is a dimensionless parameter called the internal reflection coefficient. The value of A depends on the refractive index mismatch and may be calculated by numerical integration of functions involving the Fresnel reflection coefficient [14] or by approximate methods [20,19]. The quantity $2AD$ is known as the extrapolation length and is discussed in detail by Aronson [21]. Equation 2.51 defines the normal derivative of the fluence in terms of the absolute magnitude of the fluence and is known as the "partial-current" boundary condition. This condition specifies that the slope of the fluence at the boundary is such that the fluence linearly extrapolates to zero a distance $2AD$ from the physical boundary. This observation motivates the commonly-invoked

“extrapolated” boundary condition, which simply requires the fluence to be zero on a fictitious boundary, displaced a distance $z_b = 2AD$ from the physical boundary.

The Green’s function of the diffusion equation for semi-infinite media satisfying the extrapolated boundary condition (EBC) may be constructed by the method of images. For a point source located at cylindrical coordinates ($\rho=0$, $z=z_0$), the extrapolated boundary condition is satisfied by introducing a negative image source equidistant from the extrapolated boundary at ($\rho=0$, $z=-(z_0+2z_b)$), thereby forcing the fluence to zero at $z=-z_b$. This arrangement is illustrated schematically in Figure 2.7. In this case, the fluence in the medium and on the boundary is given by

$$\begin{aligned} \Phi_{G_{EBC}}(\rho, z) &= \Phi_{G_\infty}(r_1(\rho, z)) - \Phi_{G_\infty}(r_2(\rho, z)) \\ &= \frac{1}{4\pi D} \left(\frac{\exp[-\mu_{eff}(\rho^2 + [z - z_0]^2)^{1/2}]}{(\rho^2 + [z - z_0]^2)^{1/2}} - \frac{\exp[-\mu_{eff}(\rho^2 + [z + z_0 + 2z_b]^2)^{1/2}]}{(\rho^2 + [z + z_0 + 2z_b]^2)^{1/2}} \right) \end{aligned} \quad (2.52)$$

where Φ_{G_∞} is the infinite-medium Green’s function (Equation 2.18) and r_1 and r_2 are the distances to the source and image points, as illustrated in Figure 2.7.

The Green’s function of the diffusion equation which rigorously satisfies the partial-current boundary condition (PCBC) for semi-infinite media was first published by Bryan [22], who also exploited the method of images. For a source at ($\rho=0$, $z=z_0$), the solution has the following form:

$$\begin{aligned} \Phi_{G_{PCBC}}(\rho, z) &= \frac{1}{4\pi D} \left(\frac{\exp[-\mu_{eff}(\rho^2 + [z - z_0]^2)^{1/2}]}{(\rho^2 + [z - z_0]^2)^{1/2}} + \frac{\exp[-\mu_{eff}(\rho^2 + [z + z_0]^2)^{1/2}]}{(\rho^2 + [z + z_0]^2)^{1/2}} \right. \\ &\quad \left. - \frac{2}{z_b} \int_0^\infty \exp(-l/z_b) \frac{\exp[-\mu_{eff}(\rho^2 + [z + z_0 + l]^2)^{1/2}]}{(\rho^2 + [z + z_0 + l]^2)^{1/2}} dl \right). \end{aligned} \quad (2.53)$$

The first term on the right hand side of Equation 2.53 is the response function (Φ_{G_∞}) for

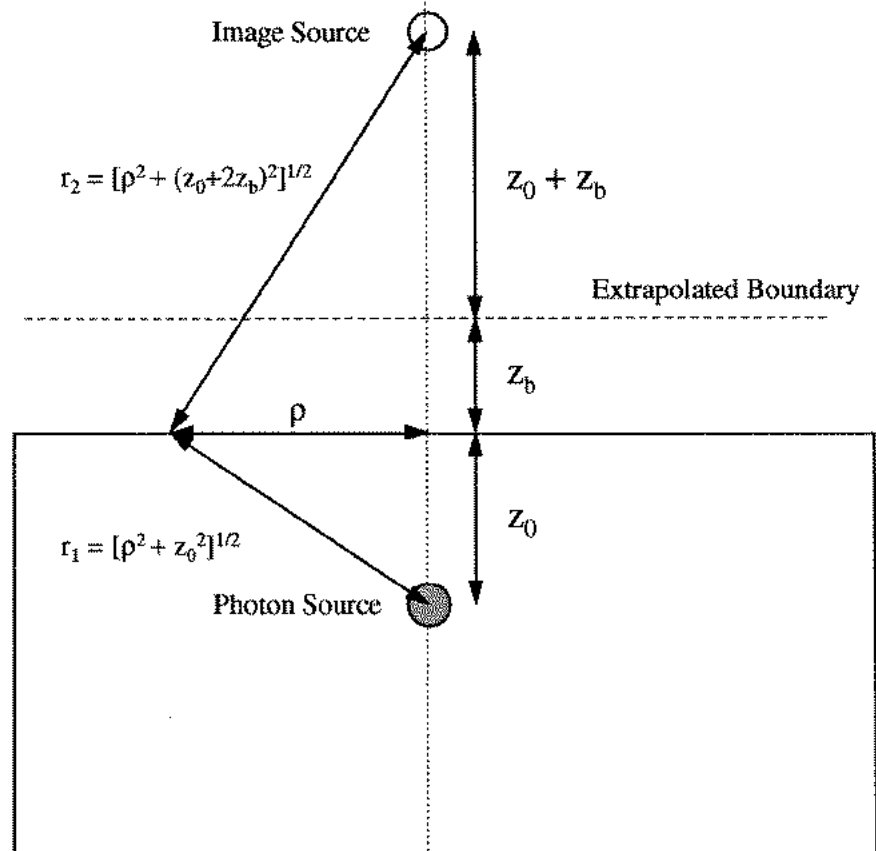


Figure 2.7 Dipole source arrangement for the extrapolated boundary condition.

the point source, the second term is Φ_{G_e} for a positive image source equidistant from the physical boundary ($\rho=0, z=-z_0$), and the third term is the response function for an exponentially-damped line of negative image sources extending from $z=-z_0$ to $z=-\infty$. The geometric center of this line of sources is located at $z=z_0+z_b$. Figure 2.8 provides a schematic comparison of the image source distributions of the partial-current and extrapolated boundary conditions.

It is interesting to compare the Green's functions of the rigorous partial-current boundary condition and the approximate extrapolated boundary condition. In both cases, an overall -1 image charge is placed opposite the physical boundary from the point source. Haskell et al. have determined that, with respect to an origin at $z=0$, the extrapolated and partial-current source distributions have the same dipole and quadrupole moments and differ only in octupole and higher moments [14]. In other words, using only two image sources, each of magnitude -1, the best possible approximation to the infinite line of sources in the partial-current image configuration is obtained when one image is placed directly on top of the positive image at $z=-z_0$ (thereby canceling it), and the remaining -1 image source is placed at $z=-(z_0+2z_b)$.

2.6.2 Marshak conditions and semi-infinite Green's functions in the P_3 approximation

In the P_3 approximation, two conditions are required at an interface. In the Marshak scheme, these conditions are:

$$\int_{\hat{s}\cdot\hat{n}\leq 0} L(\mathbf{r},\hat{s}) P_l(\hat{s}\cdot\hat{n}) d\Omega = \int_{\hat{s}\cdot\hat{n}\geq 0} R(\cos^{-1}(\hat{s}\cdot\hat{n})) L(\mathbf{r},\hat{s}) P_l(\hat{s}\cdot\hat{n}) d\Omega \quad (l = 1,3). \quad (2.54)$$

If Equation 2.44 is substituted into Equations 2.54, two boundary conditions may be

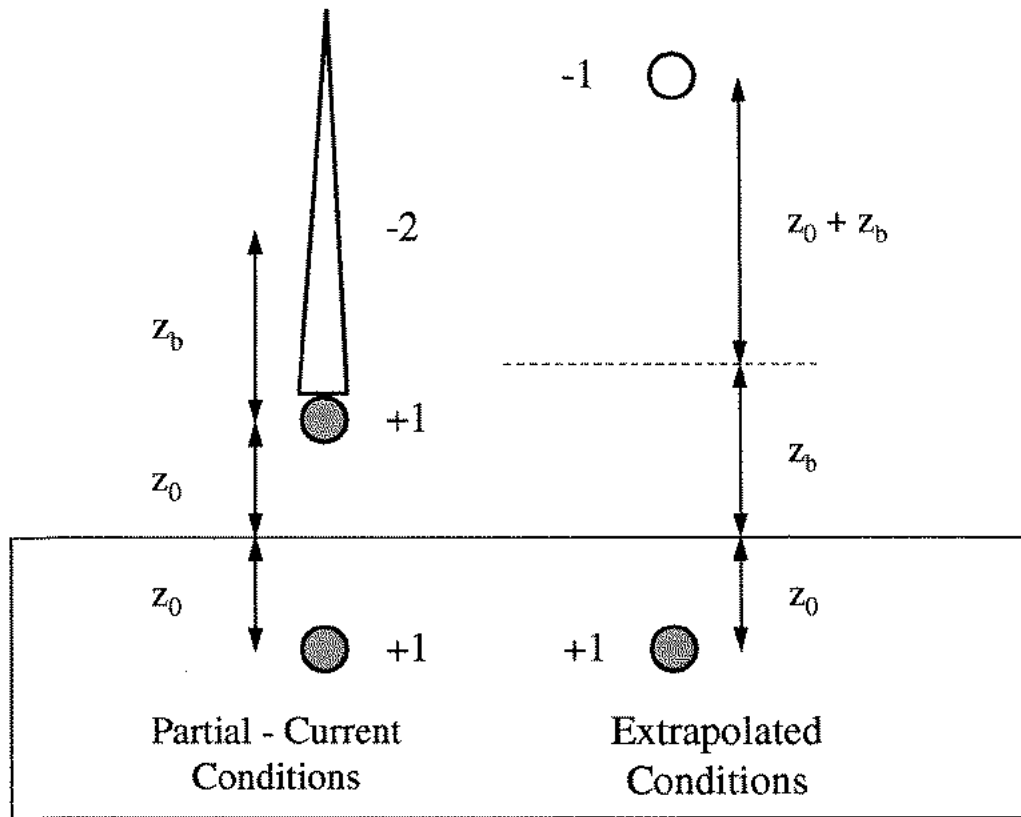


Figure 2.8 A comparison of the image source distributions for the partial-current and extrapolated boundary conditions. Adapted from Haskell et al., ref. [14].

generated which, after further simplification, relate the fluence at the boundary to its first three normal derivatives. In principle, the Green's function satisfying the P_3 fourth-order differential equation for the fluence could be solved subject to this pair of boundary conditions.

In this work, a simpler strategy is adopted. Because the Green's function for the fluence is the sum of two diffusion-theory Green's functions, approximate boundary conditions for the P_3 approximation may be obtained by satisfying diffusion-theory boundary conditions for the asymptotic and transient solutions individually. In other words, an isotropic point source at $z=z_0$ is treated as two separate sources. The source associated with the asymptotic solution must satisfy diffusion-theory boundary conditions with an extrapolation length of $z_{b_{asympt.}} = -2AD_{asympt.}$, and the source associated with the transient solution must satisfy diffusion-theory boundary conditions with an extrapolation length of $z_{b_{trans.}} = -2AD_{trans.}$. Figure 2.9 depicts extrapolation lengths as a function of μ_a for the asymptotic and transient P_3 solutions as well as the diffusion theory extrapolation length. For these calculations, a relative refractive index mismatch of 1.4 and Henyey-Greenstein scattering with $\mu_s=10.0$ and $g=0.9$ were assumed. The extrapolation length for the transient solution is much smaller than the asymptotic extrapolation length, as one might intuitively expect. It is also interesting that, for increasing μ_a (decreasing albedo) $z_{b_{asympt}}$ decreases while $z_{b_{trans}}$ increases.

The drawback to this approach is that it does not properly satisfy boundary conditions for the higher-order terms in the radiance. However, it will be demonstrated that this solution yields excellent agreement with experimental data, suggesting that the boundary condition is not especially sensitive to these terms.

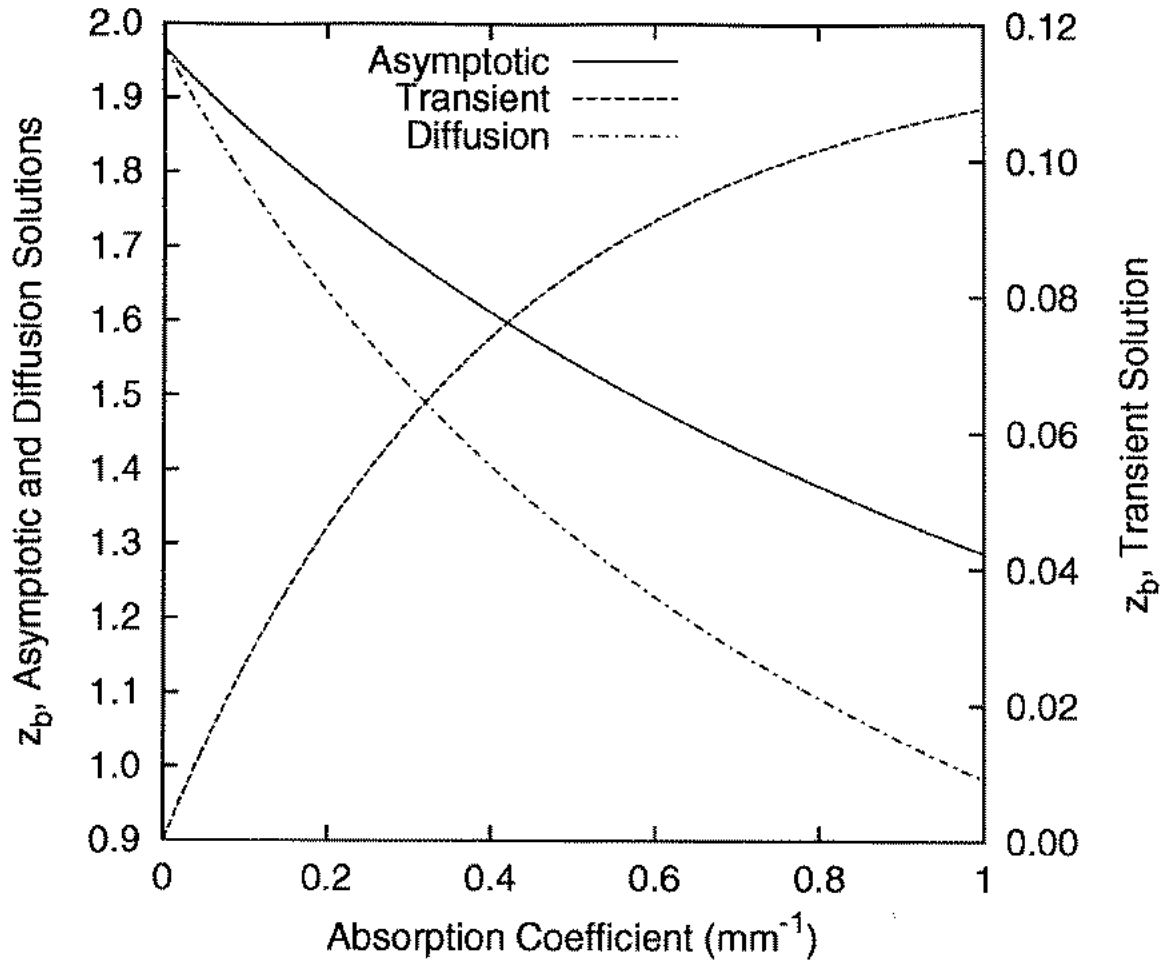


Figure 2.9 Extrapolation lengths as a function of μ_a for the asymptotic (left axis) and transient (right axis) P_3 solutions. The diffusion-theory extrapolation length is also plotted on the left axis. A relative refractive index mismatch of 1.4 and Henyey-Greenstein scattering with $\mu_s=10.0$ and $g=0.9$ were assumed .

2.7 Reflectance Expressions

The expressions for the radiance derived in the preceding sections may be used to calculate the optical power collected by a detector (the “reflectance”) at an interface between scattering and non-scattering media. In this section we consider exact and approximate expressions for the reflectance in the diffusion and P_3 approximations. For the diffusion approximation, we consider EBC solutions exclusively, since others [23] have shown that the EBC solutions give results which are in better agreement with experimental data than the PCBC solution.

2.7.1 Diffusion approximation

In the past, several investigators have equated the reflectance in the diffusion approximation to the z -component of the photon flux across the tissue-air interface [15,24,25]. This technique gives the result

$$\begin{aligned} R(\rho; z_0) &= -D \nabla \Phi_{G_{EBC}}(\rho, \mathbf{z}; z_0) \cdot (-\hat{\mathbf{z}})|_{z=0} \\ &= \frac{1}{4\pi} \left[z_0 \left(\mu_{eff} + \frac{1}{r_1} \right) \frac{\exp(-\mu_{eff} r_1)}{r_1^2} + (z_0 + 2z_b) \left(\mu_{eff} + \frac{1}{r_2} \right) \frac{\exp(-\mu_{eff} r_2)}{r_2^2} \right], \end{aligned} \quad (2.55)$$

where $R(\rho; z_0)$ is the reflectance at a radial distance ρ from an isotropic source buried at depth z_0 in a semi-infinite medium, $\hat{\mathbf{z}}$ is the outward-directed normal at the tissue surface, $\Phi_{G_{EBC}}$ is the Green’s function in Equation 2.52, and r_1 and r_2 are as defined in Figure 2.7.

A more correct expression for the reflectance is obtained by determining the portion of the radiance which is transmitted across the boundary:

$$R_{detected}(\rho; z_0) = \int_{\Omega_{detector}} T_{Fresnel}(\cos^{-1}(\hat{s} \cdot \hat{n})) L(\mathbf{r}, \hat{s}; z_0) \hat{n} \cdot \hat{s} d\Omega \quad , \quad (2.56)$$

where \hat{n} is the outward normal, $\cos^{-1}(\hat{n} \cdot \hat{s})$ specifies the angle of incidence on the tissue-air interface, and $\Omega_{detector}$ is the solid angle subtended by the detector. When the expression for the radiance in the diffusion approximation (Equation 2.5) is substituted in Equation 2.56, again assuming extrapolated boundary conditions, the result is

$$R_{detected}(\rho; z_0) = C_{\Phi} \Phi_{G_{EBC}}(\rho; z_0) + C_j j_{z_{EBC}}(\rho; z_0) \quad , \quad (2.57)$$

where $\Phi_{G_{EBC}}$ is the Green's function for the fluence (Equation 2.52), $j_{z_{EBC}}$ is the z-component of the flux described by Equation 2.55, and C_{Φ} and C_j depend upon the numerical aperture and refractive index of the detector as well as the relative refractive index mismatch at the interface. A summary of values of C_{Φ} and C_j for various refractive indices and detector numerical apertures is provided in Table 2.1.

Equation 2.57 presents an interesting dilemma in that the relative weighting of the contributions of the fluence and the flux to the reflectance is a function of the numerical aperture of the detector. In order to overcome this difficulty, one might be tempted to reason that, since the partial-current boundary condition (Equation 2.51) requires the fluence and flux to be proportional to one another at the boundary, the functional form of $R(\rho)$ will be given equally well by the expression for the fluence (Equation 2.52) or the expression for the flux (Equation 2.55), as long as normalized measurements are made. In practice, however, the radial dependence of the fluence and flux solutions at the boundary differs, and the expression in Equation 2.57 most closely represents the emittance from a buried isotropic source. This is an indication that the partial-current boundary condition is, in fact, only an approximation to the physically correct condition. This is demonstrated in Figure 2.10, in which the data

| | $n_{\text{detector}} = 1.0$ $n_{\text{rel}} = 1.4$ $NA_{\text{detector}} = 1$ | $n_{\text{detector}} = 1.46$ $n_{\text{rel}} = 1.4$ $NA_{\text{detector}} = 0.22$ | $n_{\text{detector}} = 1.0$ $n_{\text{rel}} = 1.0$ $NA_{\text{detector}} = 1$ | $n_{\text{detector}} = 1.46$ $n_{\text{rel}} = 1.33$ $NA_{\text{detector}} = 0.22$ |
|------------|---|---|---|--|
| A | 2.95 | 2.95 | 1.00 | 2.52 |
| C_{ϕ} | 0.1178 | 0.0062 | 0.25 | 0.0068 |
| C_j | 0.3056 | 0.0184 | 0.50 | 0.0203 |

Table 2.1 Values of the internal reflection coefficient (A), C_{ϕ} , and C_j for various relative refractive index mismatches, detector refractive indices, and detector numerical apertures.

points depict the emittance calculated by Monte Carlo simulation of a buried isotropic point source ($z_0=0.99$ mm) in a semi-infinite medium with optical properties of $\mu_a=0.01$ mm^{-1} , $\mu_s'=1.00$ mm^{-1} , and $n=1.4$. The solid line in Figure 2.10 is the reflectance calculated by Equation 2.57. This solution is not normalized; its absolute magnitude exactly matches the data for $\rho \geq 2.0$ mm. The dashed line is the reflectance computed by Equation 2.55, (the flux component only) normalized to the data at $\rho=10.0$ mm. The dotted line is the reflectance computed by Equation 2.52 (the fluence component only) normalized to the data at $\rho=10.0$ mm. The shapes of these two approximate solutions are different, and neither captures the shape of the actual emittance as well as the reflectance computed by Equation 2.57.

2.7.2 P_3 approximation

In the case of the P_3 approximation, we must apply Equation 2.56 to the distribution of sources found to most appropriately model the reflectance for a buried isotropic point source. Here the procedure is outlined for a single point source; a similar calculation must be carried out for each of the image sources employed in a given solution. The radiance originating from a point source in an infinite medium in the P_3 approximation is given by Equation 2.44. We therefore compute

$$R(\rho; z_0) = \int_{\Omega_{\text{detector}}} T_{\text{Fresnel}}(\theta) \cos(\theta) \left[\sum_{l=0}^3 \frac{2l+1}{4\pi} \psi_l(\rho; z_0) P_l(\xi) \right] \sin(\theta) d\theta d\phi, \quad (2.58)$$

where

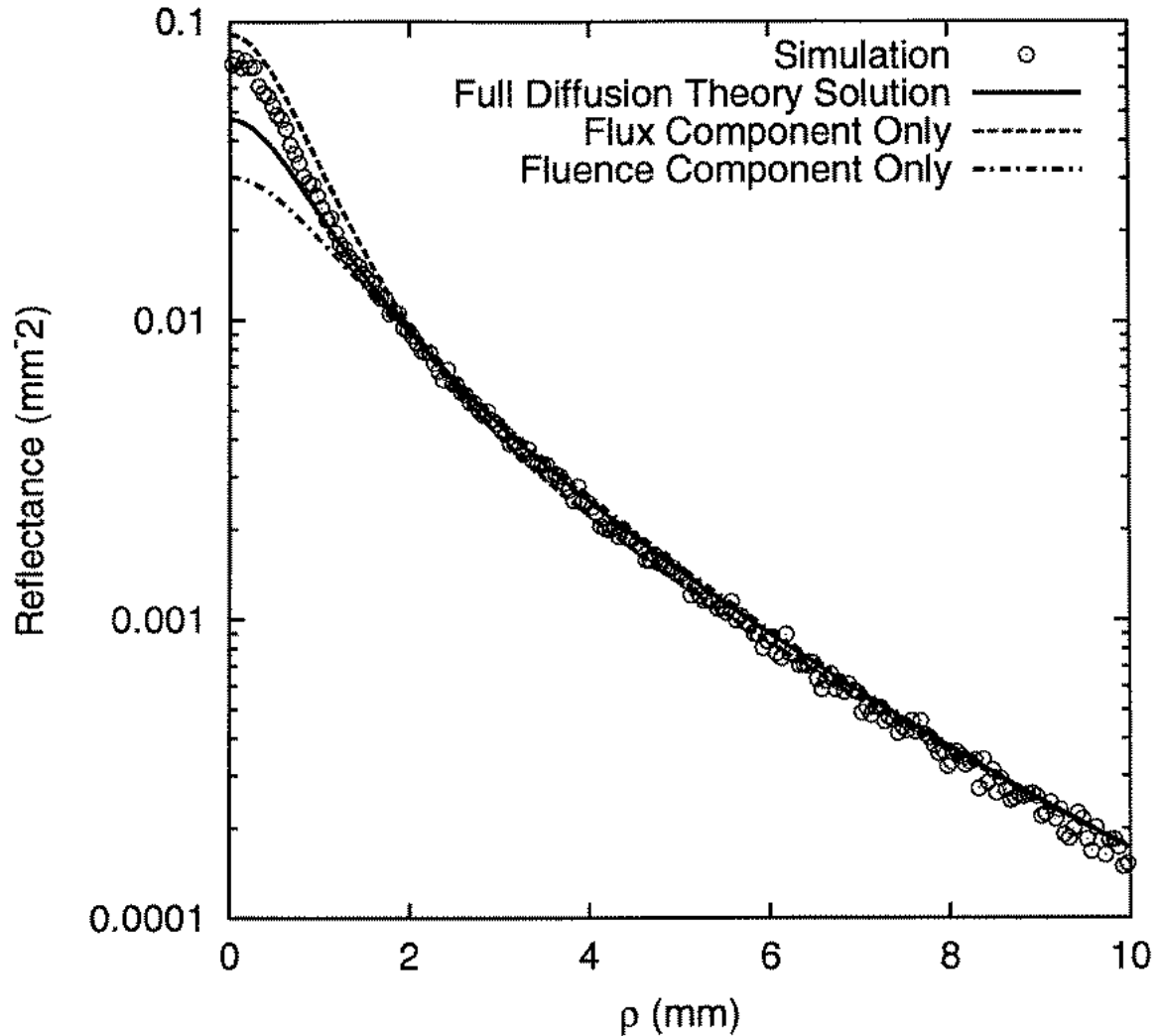


Figure 2.10 The reflectance calculated by Monte Carlo simulation from a buried isotropic point source ($z_0=0.99$ mm) in a semi-infinite medium with optical properties of $\mu_a=0.01$ mm^{-1} , $\mu_s'=1.00$ mm^{-1} , and $n=1.4$. The solid line is the full diffusion theory solution for the reflectance calculated by Equation 2.57. This solution is not normalized. The dashed line is the reflectance computed by Equation 2.55, (the flux component only) normalized to the data at $\rho=10.0$ mm. The dotted line is the reflectance computed by Equation 2.52 (the fluence component only), also normalized to the data at $\rho=10.0$ mm.

$$\begin{aligned}
\xi &= \hat{s} \cdot \hat{r} \\
&= (\sin\theta \cos\phi \hat{x} + \sin\theta \sin\phi \hat{y} + \cos\theta \hat{z}) \cdot \left(-\frac{z_0}{\sqrt{\rho^2 + z_0^2}} \hat{z} + \frac{\rho}{\sqrt{\rho^2 + z_0^2}} \hat{y} \right) \\
&= \frac{-z_0 \cos\theta}{\sqrt{\rho^2 + z_0^2}} + \frac{\rho \sin\theta \sin\phi}{\sqrt{\rho^2 + z_0^2}} ,
\end{aligned} \tag{2.59}$$

for each real or image source. The various coordinates and unit vectors in Equations 2.58 and 2.59 are illustrated in Figure 2.11. This leads to an expression of the form

$$R(\rho; z_0) = \sum_{l=0}^3 \frac{2l+1}{4\pi} \psi_l(\rho; z_0) S_l(\rho; z_0) , \tag{2.60}$$

where

$$\begin{aligned}
S_0(\rho; z_0) &= k_1 \\
S_1(\rho; z_0) &= k_2 \left(\frac{z_0}{(\rho^2 + z_0^2)^{1/2}} \right) \\
S_2(\rho; z_0) &= k_3 \left(\frac{3z_0^2}{2(\rho^2 + z_0^2)^{1/2}} \right) + k_4 \left(\frac{3\rho^2}{2(\rho^2 + z_0^2)^{1/2}} \right) - k_1 \left(\frac{1}{2} \right) \\
S_3(\rho; z_0) &= k_5 \left(\frac{5z_0^3}{2(\rho^2 + z_0^2)^{3/2}} \right) + k_6 \left(\frac{15z_0\rho^2}{2(\rho^2 + z_0^2)^{3/2}} \right) - k_2 \left(\frac{3z_0}{2(\rho^2 + z_0^2)^{1/2}} \right) .
\end{aligned} \tag{2.61}$$

The various k_n in Equations 2.61 depend upon the numerical aperture of the detector and the refractive index mismatch. Table 2.2 provides values of k_n for two detectors: a 2π detector (NA = 1.0) and an optical fiber with NA=0.22 and core refractive index of 1.46. Relative index mismatches of 1.4 (typical of tissue) and 1.33 (water) are considered.

The P_3 Green's function for the reflectance is contrasted with the diffusion theory Green's function in Figures 2.12 and 2.13. Figure 2.12 presents the same data shown

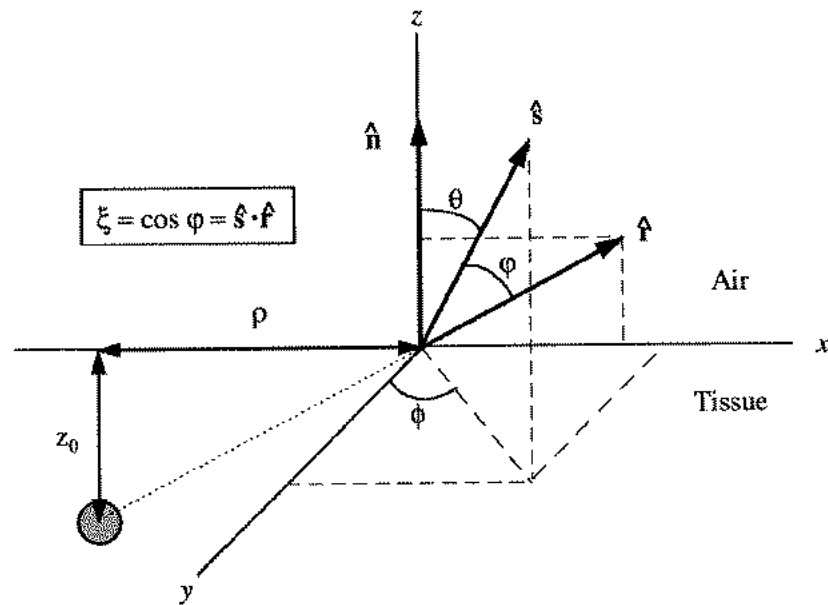


Figure 2.11 Coordinates and unit vectors used in the calculation of the reflectance in the P_3 approximation.

| | $n_{\text{detector}} = 1.0$ $n_{\text{tissue}} = 1.4$ $NA_{\text{detector}} = 1$ | $n_{\text{detector}} = 1.46$ $n_{\text{tissue}} = 1.4$ $NA_{\text{detector}} = 0.22$ | $n_{\text{detector}} = 1.0$ $n_{\text{tissue}} = 1.33$ $NA_{\text{detector}} = 1$ | $n_{\text{detector}} = 1.46$ $n_{\text{tissue}} = 1.33$ $NA_{\text{detector}} = 0.22$ |
|-------|--|--|---|---|
| k_1 | 1.480 | 0.0775 | 1.659 | 0.0858 |
| k_2 | 1.280 | 0.0771 | 1.407 | 0.0852 |
| k_3 | 1.117 | 0.0766 | 1.208 | 0.0846 |
| k_4 | 0.985 | 0.0761 | 1.049 | 0.0840 |
| k_5 | 0.181 | 0.0005 | 0.225 | 0.0006 |
| k_6 | 0.148 | 0.0005 | 0.179 | 0.0006 |

Table 2.2 Coefficients of the terms in Equations 2.61 for various detector types and refractive index mismatches.

in Figure 2.10. The solid line is the P_3 prediction for the reflectance using extrapolated boundary conditions as described above. The dashed line is the complete diffusion theory solution. The diffusion theory solution deviates from the data significantly for $\rho < 1.0$ mm, while the P_3 solution captures the reflectance for the full range of ρ . Figure 2.13 depicts Monte Carlo data for the same scattering conditions as Figure 2.12 but with $z_0 = 0.5$ mm and $\mu_s = 1.0$ ($a' = 0.5$). In addition to significant deviation at small ρ , the diffusion solution overestimates the asymptotic attenuation for this case because of the low albedo. In contrast, the P_3 solution captures the data extremely well for all ρ . For both of the data sets in Figures 2.12 and 2.13, the P_3 solution using partial-current boundary conditions is identical to the solution using extrapolated boundary conditions and is therefore not shown.

2.8 Representation of beams

To the extent that first-order similarity relations are valid, a pencil beam incident on a semi-infinite scattering medium can be modeled as an infinite line of isotropic sources located at the sites of initial scattering events. The strength of this line source is attenuated according to $\exp(-\mu_t' z)$, and, assuming unit initial beam intensity, the total integrated source strength (or monopole moment) is equal to a' (the transport albedo). This distribution is expressed

$$S(z) = a' \mu_t' e^{-\mu_t' z} . \quad (2.62)$$

It is often desirable to represent incident beams in terms of simpler source distributions. In this chapter, Green's functions for the radiance and the reflectance generated by isotropic point sources have been developed. We therefore seek

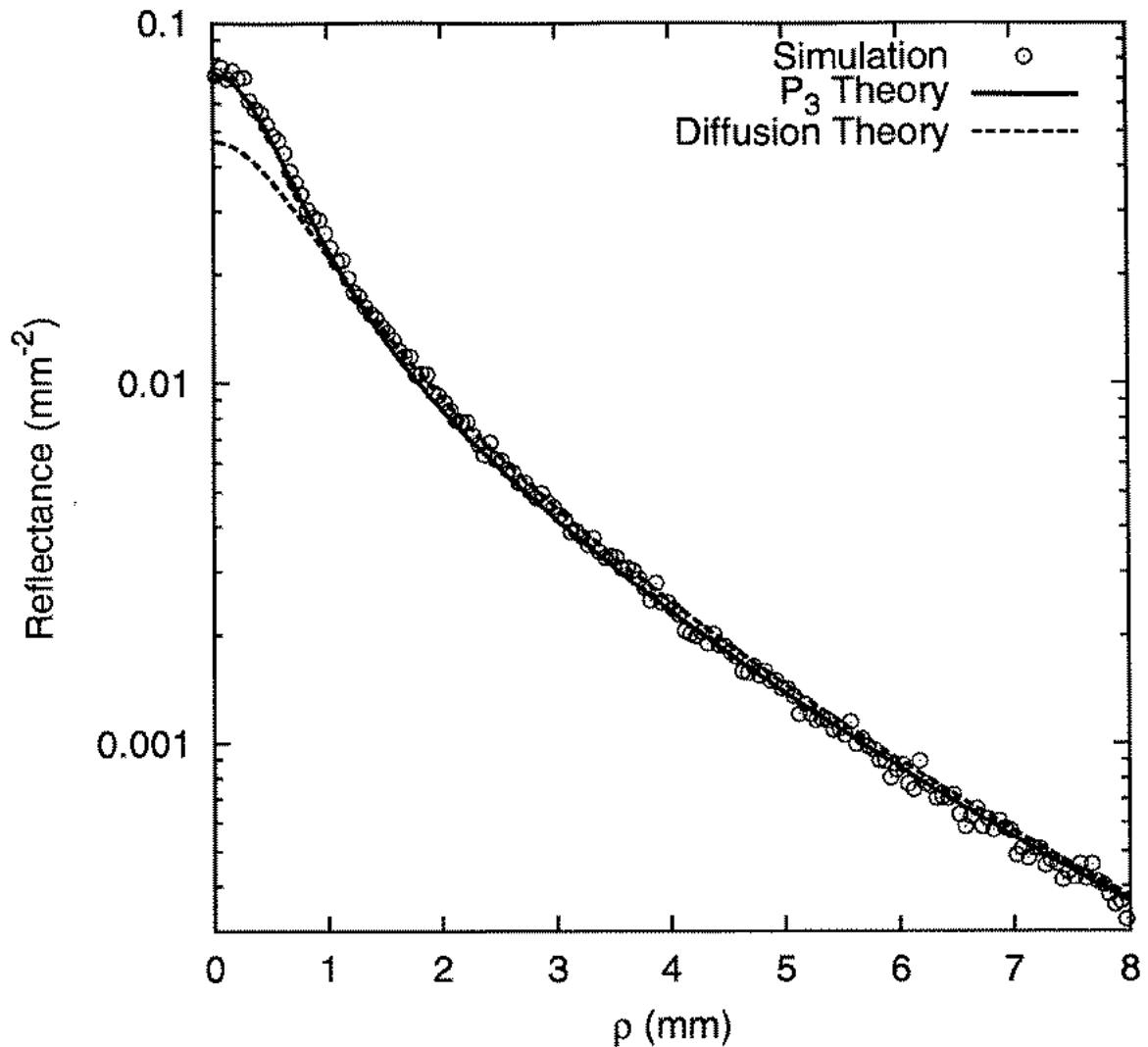


Figure 2.12 Reflectance data generated by Monte Carlo simulation (points) for an isotropic point source at $z_0=0.99$ mm in a semi-infinite medium having optical properties of $\mu_a=0.01$ mm^{-1} , $\mu_s=10.0$ mm^{-1} , and $g=0.9$ ($a'=0.99$) with Henyey-Greenstein scattering. The solid line is the P_3 prediction for the reflectance computed using Equation 2.60. The dashed line is the complete diffusion theory solution (Equation 2.57).

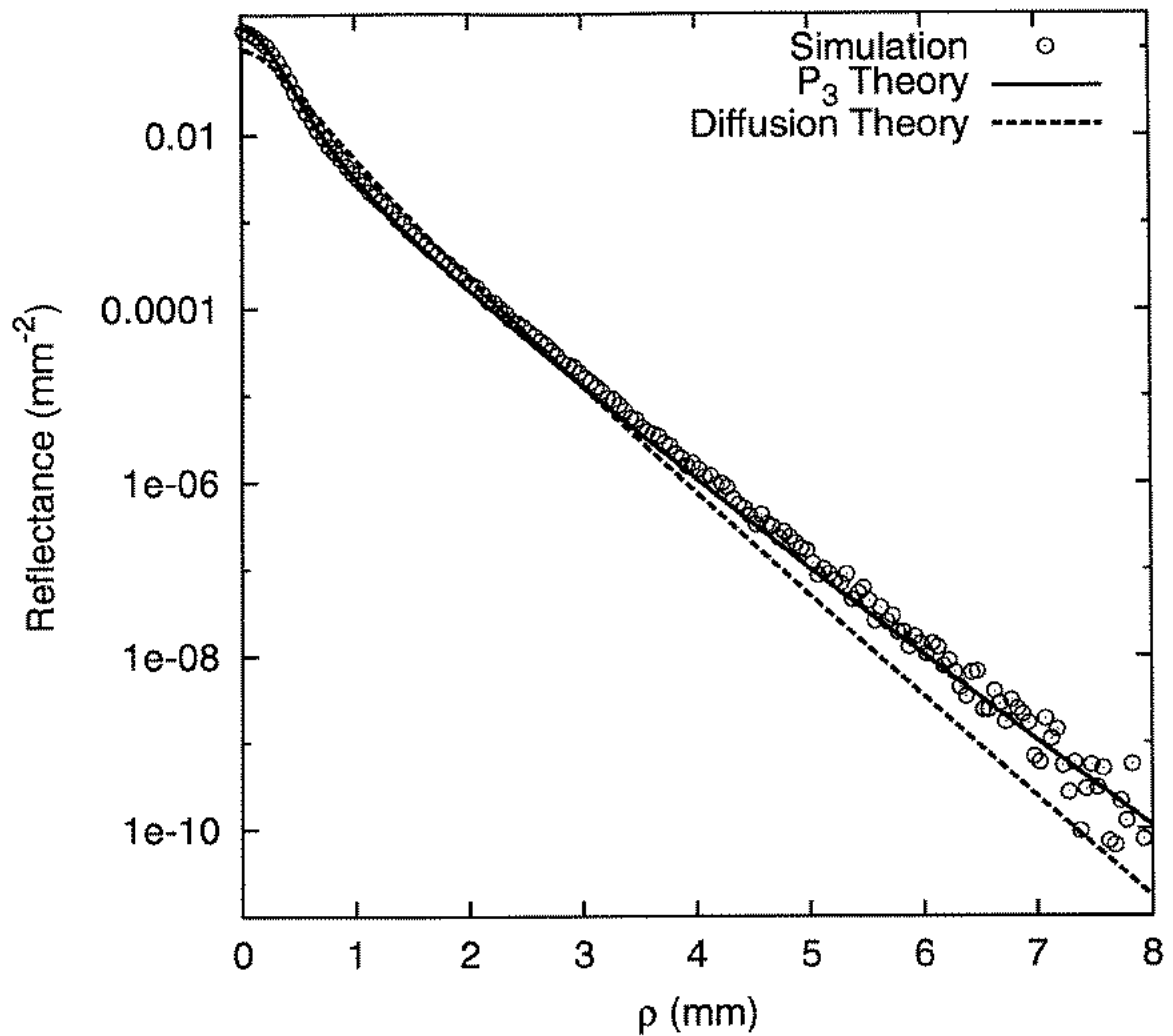


Figure 2.13 Reflectance data generated by Monte Carlo simulation (points) for an isotropic point source at $z_0=0.5$ mm in a semi-infinite medium having optical properties of $\mu_a=1.1$ mm^{-1} , $\mu_s=10.0$ mm^{-1} , and $g=0.9$ ($a'=0.5$) with Henyey-Greenstein scattering. The solid line is the P_3 prediction for the reflectance computed using Equation 2.60. The dashed line is the complete diffusion theory solution (Equation 2.57).

distributions of point sources which have the same dipole moment (or the same dipole and quadrupole moments) with respect to an origin at the air-tissue interface as the distribution in Equation 2.62.

To satisfy the dipole moment, a single point source of magnitude a' is required. In order to determine its location, we solve

$$\int_0^{\infty} z a' \mu_t' e^{-\mu_t' z} dz = \int_0^{\infty} z a' \mu_t' \delta(1-z_0) dz \quad (2.63)$$

for the effective source depth (z_0). The result is $z_0=1/\mu_t'$, which is the standard diffusion theory representation of a collimated beam [14,23]. To satisfy both the dipole and quadrupole moments, two sources are required. If the sources have equal magnitudes, we solve:

$$\begin{aligned} \int_0^{\infty} z a' \mu_t' e^{-\mu_t' z} dz &= \int_0^{\infty} z a' \mu_t' \frac{1}{2} (\delta(1-z_{0_1}) + \delta(1-z_{0_2})) dz \\ \int_0^{\infty} z^2 a' \mu_t' e^{-\mu_t' z} dz &= \int_0^{\infty} z^2 a' \mu_t' \frac{1}{2} (\delta(1-z_{0_1}) + \delta(1-z_{0_2})) dz \end{aligned} \quad (2.64)$$

for z_{0_1} and z_{0_2} , and obtain $z_{0_1}=2/\mu_t'$ and $z_{0_2}=0$. Thus a source at a depth of two transport mean free paths and a second source of equal magnitude placed directly on the physical boundary satisfy the dipole and quadrupole moments of the distribution in Equation 2.62.

A comparison of these beam models is provided in Figure 2.14, which is a plot of the reflectance generated by a Monte Carlo simulation of a pencil beam normally incident on a semi-infinite medium having optical properties of $\mu_a=1.00 \text{ mm}^{-1}$, $\mu_s=10.0 \text{ mm}^{-1}$, and $g=0.9 \text{ mm}^{-1}$. The solid line is the 2-source beam model, calculated using the

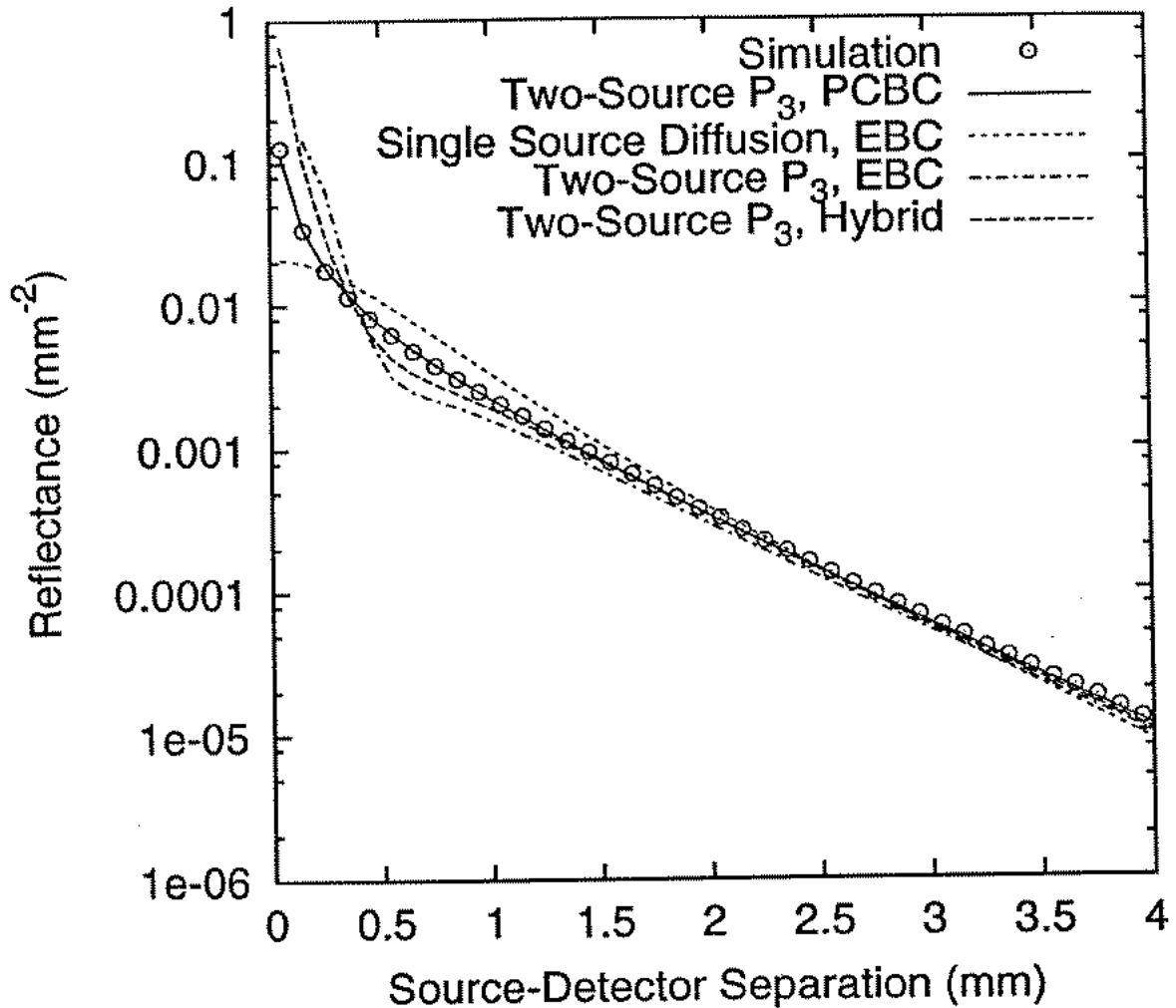


Figure 2.14 Monte Carlo simulation of the reflectance generated by a pencil beam normally incident on a semi-infinite medium having optical properties of $\mu_a=0.50 \text{ mm}^{-1}$, $\mu_s=10.0 \text{ mm}^{-1}$, and $g=0.9 \text{ mm}^{-1}$ (\bullet). The solid line is the 2-source beam model, calculated using the P_3 Green's function and partial-current boundary conditions. The dash-dotted line is the 2-source beam model, calculated using the P_3 Green's function and extrapolated boundary conditions. The line with long dashes is the 2-source beam model, calculated using the hybrid Green's function described in the text and extrapolated boundary conditions. The line with short dashes is the standard single-source diffusion theory solution. This solution deviates more significantly for larger ρ . A small range of ρ is plotted here to emphasize the behavior near $\rho=0$.

P_3 Green's function and partial-current boundary conditions. The dash-dotted line is the 2-source beam model calculated with the P_3 Green's function and extrapolated boundary conditions. The line with long dashes is a hybrid Green's function obtained by using the diffusion-theory Green's function, but with μ_{eff} replaced by v and D replaced by $\mu_a/(v)^2$. The line with short dashes is the standard single-source diffusion theory solution. It is interesting that in the P_3 approximation the partial-current boundary conditions give better agreement with the data than the extrapolated boundary conditions. This solution is very time-consuming to compute, however, and does not lend itself easily to incorporation into a fitting algorithm. For this reason, the hybrid Green's function, which also gives good agreement with the data, is used as an initial P_3 fitting function in Chapter 3.

References

1. A. Ishimaru, *Wave Propagation and Scattering in Random Media* (Oxford University Press, Oxford, UK, 1997), Chapter 7.
2. K.M. Case and P.F. Zweifel, *Linear Transport Theory* (Addison-Wesley, Reading, MA, 1967), Chapter 2.
3. B. Davison, *Neutron Transport Theory* (Oxford University Press, London, 1958), Chapter 10-Chapter 12.
4. D.A. Boas, "Diffuse Photon Probes of Structural and Dynamical Properties of Turbid Media: Theory and Biomedical Applications," PhD dissertation (University of Pennsylvania, Philadelphia, PA, 1996).
5. L.G. Henyey and J.L. Greenstein, "Diffuse radiation in the galaxy," *Astrophys. J.* **93**, 70-83 (1941).
6. J.R. Mourant, J.P. Freyer, A.H. Hielscher, A.A. Eick, A. Shen, and T.M. Johnson, "Mechanisms of light scattering from biological cells relevant to noninvasive tissue diagnostics," *Appl. Opt.* **37**, 3586-3593 (1998).
7. S.T. Flock, B. Wilson, and M.S. Patterson, "Total attenuation coefficients and scattering phase functions of tissues and phantom materials," *Med. Phys.* **14**, 835-841 (1987).
8. R. Marchesini, A. Bertoni, S. Andreola, E. Melloni, and A.E. Sichirollo, "Extinction and absorption coefficients and scattering phase functions of human tissues in vitro," *Appl. Opt.* **28**, 2318-2324 (1989).
9. F. Bevilacqua, "Local Optical Characterization of Biological Tissues In Vitro and In Vivo," PhD dissertation (École Polytechnique Fédérale de Lausanne, Lausanne, Switzerland, 1998).

10. D.R. Wyman, M.S. Patterson, and B.C. Wilson, "Similarity relations for anisotropic scattering in Monte Carlo simulations of deeply penetrating neutral particles," *J. Comput. Phys.* **81**, 137-150 (1989).
11. D.R. Wyman and M.S. Patterson, "A discrete method for anisotropic angular scattering in Monte Carlo simulations," *J. Comput. Phys.* **76**, 414-425 (1988).
12. W.M. Star, P.A. Marijnissen, and M.J.C. VanGemert, "Light dosimetry in optical phantoms and in tissues: I. Multiple flux and transport theory," *Phys. Med. Biol.* **33**, 437-454 (1988).
13. J.B. Fishkin, S. Fantini, M.J. vandeVen, and E. Gratton, "Gigahertz photon density waves in a turbid medium: theory and experiments," *Phys. Rev. E* **53**, 2307-2319 (1996).
14. R.C. Haskell, L.O. Svaasand, T. Tsay, T. Feng, M.S. McAdams, and B.J. Tromberg, "Boundary conditions for the diffusion equation in radiative transfer," *J. Opt. Soc. Am. A* **11**, 2727-2741 (1994).
15. T.J. Farrell, M.S. Patterson, and B.C. Wilson, "A diffusion theory model of spatially resolved, steady-state diffuse reflectance for the noninvasive determination of tissue optical properties in vivo," *Med. Phys.* **19**, 879-888 (1992).
16. W.M. Star, "Comparing the P_3 approximation with diffusion theory and with Monte Carlo calculations of light propagation in a slab geometry," *SPIE Institute Series IS5*, 146-154 (1989).
17. D.A. Boas, H. Liu, M.A. O'Leary, B. Chance, and A.G. Yodh, "Photon migration within the P_3 approximation," in *Optical tomography, photon migration, and spectroscopy of tissue and model media: theory, human studies, and instrumentation*, B. Chance and R. R. Alfano, eds., Proc. SPIE **2389**, 240-247 (1995).
18. A.M. Weinberg and E.P. Wigner, *The Physical Theory of Neutron Chain Reactors* (University of Chicago Press, Chicago, IL, 1958), pp. 272-278.

19. M. Keijzer, W.M. Star, and P.R. Storchi, "Optical diffusion in layered media," *Appl. Opt.* **27**, 1820-1824 (1988).
20. R.A.J. Groenhuis, H.A. Ferwerda, and J.J.T. Bosch, "Scattering and absorption of turbid materials determined from reflection measurements, 1: Theory," *Appl. Opt.* **22**, 2456-2462 (1983).
21. R. Aronson, "Boundary conditions for diffusion of light," *J. Opt. Soc. Am. A* **12**, 2532-2539 (1995).
22. G.H. Bryan, "An application of the method of images to the conduction of heat," *Proc. London Math. Soc.* **22**, 424-430 (1891).
23. A. Kienle and M.S. Patterson, "Improved solutions of the steady-state and the time-resolved diffusion equations for reflectance from a semi-infinite turbid medium," *J. Opt. Soc. Am. A* **14**, 246-254 (1997).
24. A.H. Hielscher, S.L. Jacques, L. Wang, and F.K. Tittel, "The influence of boundary conditions on the accuracy of diffusion theory in time-resolved reflectance spectroscopy of biological tissue," *Phys. Med. Biol.* **40**, 1957-1975 (1995).
25. M.G. Nichols, E.L. Hull, and T.H. Foster, "Design and testing of a white-light, steady-state diffuse reflectance spectrometer for determination of optical properties of highly scattering systems," *Appl. Opt.* **36**, 93-104 (1997).

CHAPTER 3

Validation of Theoretical Reflectance Expressions with Analysis of Simulated and Experimental Data

3.1 Introduction

This chapter presents experimental and numerical evaluation of the theoretical expressions derived in Chapter 2 for the reflectance emitted from a semi-infinite turbid medium irradiated by a pencil beam. In Section 3.2, the accuracy of optical properties returned by fitting these expressions to Monte-Carlo simulated data is investigated for various ranges of source-detector separations and medium optical properties. A broadband steady-state reflectance spectrometer has been designed and constructed for collection of experimental reflectance data from tissues and other highly scattering media. The instrument and associated data reduction techniques are presented in Section 3.3. Data collected from tissue-simulating phantoms are analyzed in Section 3.4, and the advantages and limitations of each expression are summarized in Section 3.5.

3.2 Monte Carlo evaluation of the fitting functions

When evaluating the theoretical reflectance expressions derived in Chapter 2, it is important to consider several questions. First, what is the range of optical properties

which can be accurately extracted from fitting each expression to reflectance data? Second, what are the minimum and maximum source-detector separations required for accurate quantitation of μ_a and μ_s ? Third, if a given expression returns optical properties which are inaccurate in an absolute sense, is it still useful for measuring *relative* changes in medium optical properties? Finally, how sensitive is each theoretical expression to the exact details of the experimental probe, the scattering phase function, and the exact incident beam profile?

To investigate these issues, simulated radially-resolved reflectance data sets were generated from Monte Carlo calculations performed with the variance reduction algorithm of Wang et al. [1]. The reflectance was binned in either 0.1 or 0.3 mm-wide concentric annular rings centered around a normally incident pencil beam. The standard error in the reflectance signal was also scored in order to estimate accurately the statistical uncertainty in the reflectance. The number of photon packets propagated was dependent on the width of the detection bins and the simulated optical properties and was generally determined by allowing the simulation to continue until the smallest uncertainty in the simulated data was comparable to that of the shot-noise limitation inherent in our 16-bit experimental detector. The actual number of packets launched ranged from 300,000 to 6,000,000. All photons exiting the tissue surface were scored, therefore the effective detector numerical aperture was 1.0. The Henyey-Greenstein phase function with $g=0.9$ was used to model scattering, and, unless stated otherwise, a tissue refractive index of 1.4 was used.

Since the instrument to be described in Section 3.3 is not capable of absolute reflectance measurements, all of the data analyzed in this section were normalized to the signal at a prescribed reference location, denoted ρ_{norm} . For this reason, all of the

fitting functions were also normalized; functions of the form

$$R_{norm}(\rho) = \frac{R(\rho)}{R(\rho_{norm})} \quad (3.1)$$

were fit to the data, where the numerator is the reflectance expression under investigation and the denominator is that expression evaluated at $\rho = \rho_{norm}$.

Because diffusion theory is only valid for source-detector separations larger than approximately 1 mfp', the diffusion theory reflectance expressions model the incident beam as a single isotropic point source buried at a depth of one transport mean free path. This beam representation will be used to test both diffusion-theory Green's functions for the reflectance derived in Section 2.7.1. For the P_3 reflectance expression, the dipole beam representation is coupled with the hybrid diffusion- P_3 Green's function described in Section 2.8. This Green's function was adopted for initial testing purposes because of its computational efficiency. The following labeling conventions will be adopted: DT_{full} will denote the diffusion theory expression using the complete diffusion theory Green's function, DT_{flux} will denote the diffusion theory expression using the Green's function which incorporates only the photon flux at the boundary, and P_3 will denote the P_3 expression. Since extrapolated boundary conditions are used exclusively in this chapter, the explicit "EBC" notation is omitted.

3.2.1 Sensitivity to minimum source-detector separation

To examine the sensitivity and accuracy of the various reflectance expressions to the radial position of the first detection fiber, ρ_{min} , multiple fits of each theory were made to individual Monte Carlo data sets while ρ_{min} was varied from 0.15 mm to some maximum value. For all fits described in this section, a Levenberg-Marquadt nonlinear

least-squares algorithm was used within the commercial software package MATLAB®, and the solutions were normalized to the radial position of the first included detection fiber, so $\rho_{\text{norm}} = \rho_{\text{min}}$. This strategy forces the fitted solution to agree exactly with the experimental data at ρ_{min} , and the fitted optical properties are therefore somewhat sensitive to the precision of the reflectance at this radial location. Three different sets of optical properties were investigated. The first simulation set used $\mu_a=0.01 \text{ mm}^{-1}$, $\mu_s'=1.00 \text{ mm}^{-1}$, and $n_{\text{rel}}=1.4$; the second used $\mu_a=0.01 \text{ mm}^{-1}$, $\mu_s'=1.00 \text{ mm}^{-1}$, and $n_{\text{rel}}=1.0$; and the final set used $\mu_a=0.50 \text{ mm}^{-1}$, $\mu_s'=1.00 \text{ mm}^{-1}$, and $n_{\text{rel}}=1.4$. These data sets are depicted in Figure 3.1. The coefficients of the various boundary- and detector-sensitive parameters in the fitting functions (A , C_ϕ and C_j for the diffusion-theory solutions and $k_1 - k_6$ for the P_3 solution) were selected according to Tables 2.1 and 2.2.

Results for simulated optical properties of $\mu_a=0.01 \text{ mm}^{-1}$, $\mu_s'=1.00 \text{ mm}^{-1}$, and $n_{\text{rel}}=1.4$ are depicted in Figure 3.2. The radial position of the most remote detection fiber, ρ_{max} , was 20.0 mm for all fits depicted in this figure. The upper panel illustrates the fitted values of μ_a as a function of ρ_{min} for the DT_{full} (solid circles and solid line), the DT_{flux} (open circles and dashed line), and the P_3 (solid squares and dotted line) expressions. The horizontal line indicates the value of μ_a used in the simulation. The same point and line styles are used in the lower panel, which depicts the fitted values of μ_s' . The χ_v^2 goodness-of-fit statistic is presented in Figure 3.3.

Several interesting features may be noticed in Figures 3.2 and 3.3. First, fitting to data sets containing the smallest ρ_{min} resulted in the greatest errors in both the absorption and transport scattering coefficients. Although this is true for all of the fitting functions, the failure at small values of ρ_{min} is particularly evident for the diffusion-theory solutions. The returned absorption coefficient is systematically lower

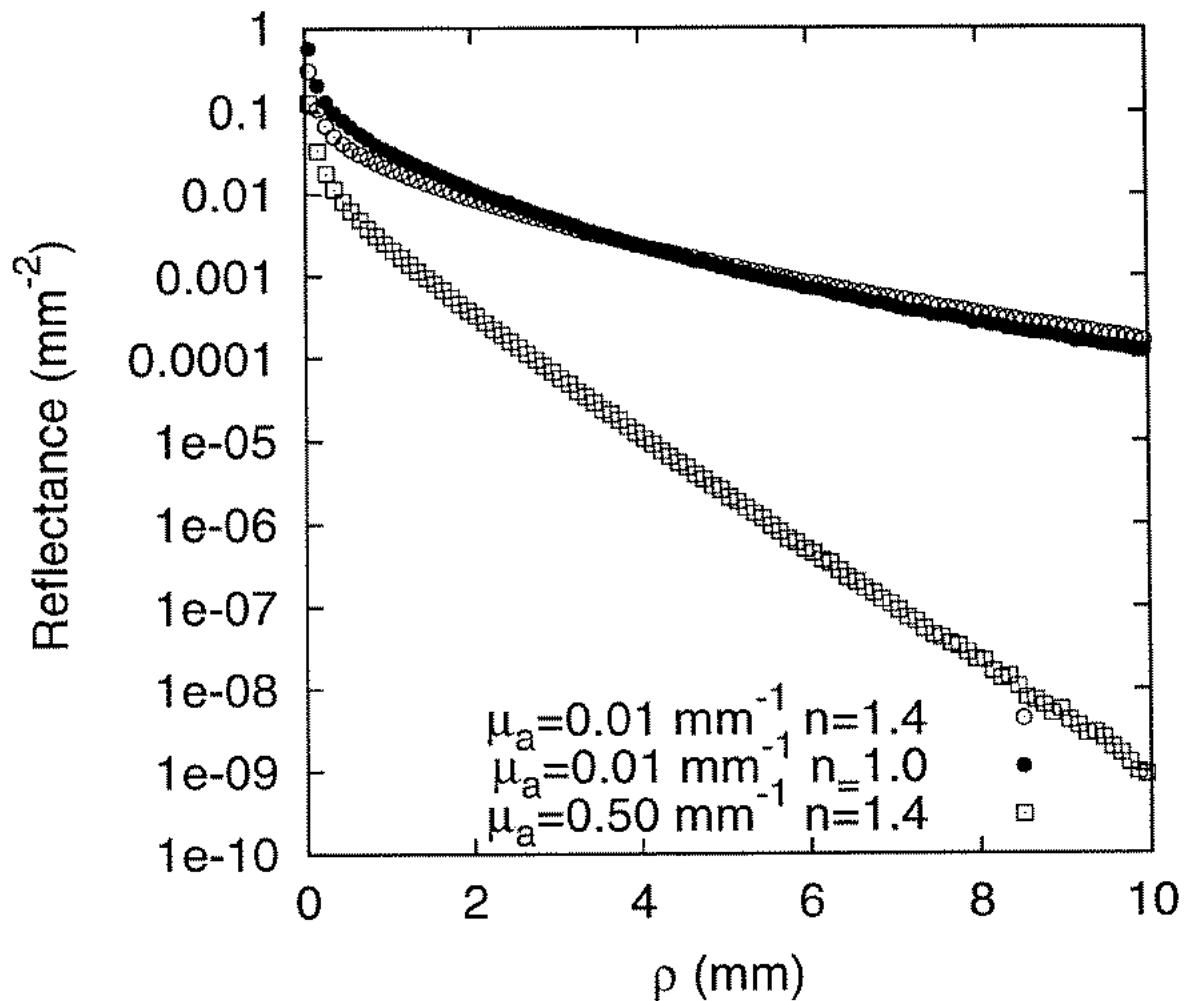


Figure 3.1 The reflectance data sets used for the sensitivity analyses presented in Section 3.1. Each simulation set assumed Henyey-Greenstein scattering with $\mu_s' = 1.00$ and $g = 0.9$.

than the actual value used in the Monte Carlo simulation, and the transport scattering coefficient is returned systematically high. This failure occurs because diffusion theory is unable to account for the non-diffuse component of the reflectance that is encountered for these small source-detector separations. As ρ_{\min} increases, the fractional error in the returned optical properties rapidly decreases for the DT_{full} solution, reaching a minimum near zero for $\rho_{\min} \approx 0.7$ mm (0.7 mfp'), after which μ_a is systematically high and μ_s' is systematically low. For minimum source-detector separations from 1.2 mm to 2 mm (1.2 to 2.0 mfp'), the error in the returned optical properties is relatively constant and much smaller than the error encountered with the smallest source-detector separations. For this range of ρ_{\min} , the transport scattering and absorption coefficients are accurate to $\pm 5\%$. The DT_{flux} solution performs poorly for all ρ_{\min} . This is because of the excessively large slope in this solution at small values of ρ , a deviation which was illustrated in Figure 2.10. The location of the sharp transition near $\rho_{\min} = 1.5$ mm is sensitive to statistical fluctuations in the reflectance data and is further evidence of the relative instability of this solution. The P_3 solution generally yields the most accurate fitted coefficients throughout the full range of ρ_{\min} but also deviates significantly from the actual values for ρ_{\min} less than approximately 0.5 mm. This deviation probably results from the fact that the hybrid diffusion- P_3 Green's function is not as accurate as the complete Green's function in this range of source-detector separations.

It is interesting to observe that, while the fitted optical properties for the DT_{full} and P_3 solutions are relatively constant for $\rho_{\min} \approx 1.0$ to 3.0 mm, increasing ρ_{\min} beyond approximately 3.0 mm results in increased error in and coupling between the fitted values of μ_a and μ_s' . This occurs because, when $\mu_s' \gg \mu_a$, the magnitude of the

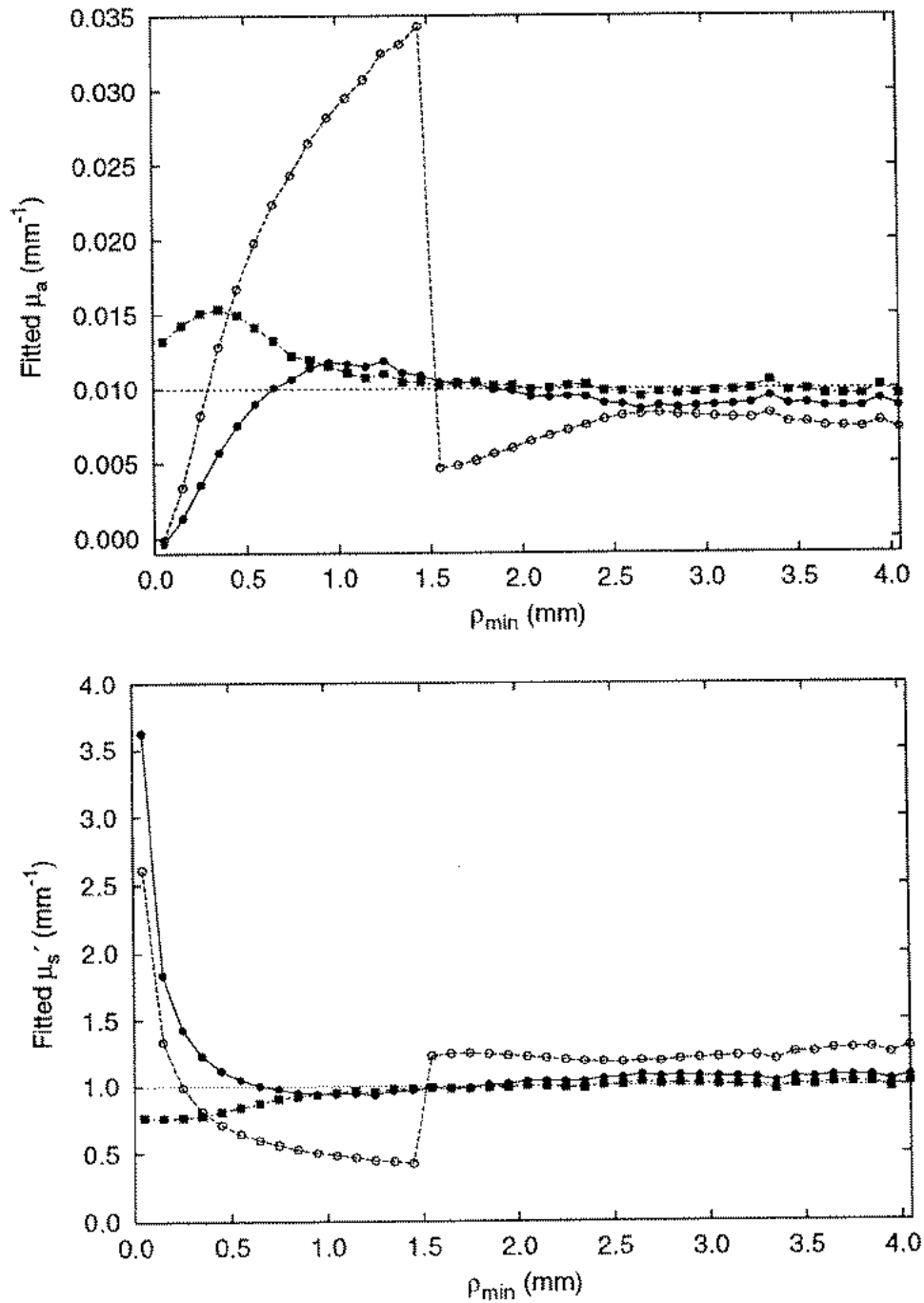


Figure 3.2 Values of μ_a (upper panel) and μ_s' (lower panel) resulting from fits of the DT_{full} (solid circles and solid lines), DT_{flux} (open circles and dashed lines), and P_3 (solid squares and dotted lines) solutions to simulated reflectance data for a medium with optical properties of $\mu_a=0.01 \text{ mm}^{-1}$, $\mu_s'=1.00 \text{ mm}^{-1}$, and $n_{\text{rel}}=1.4$.

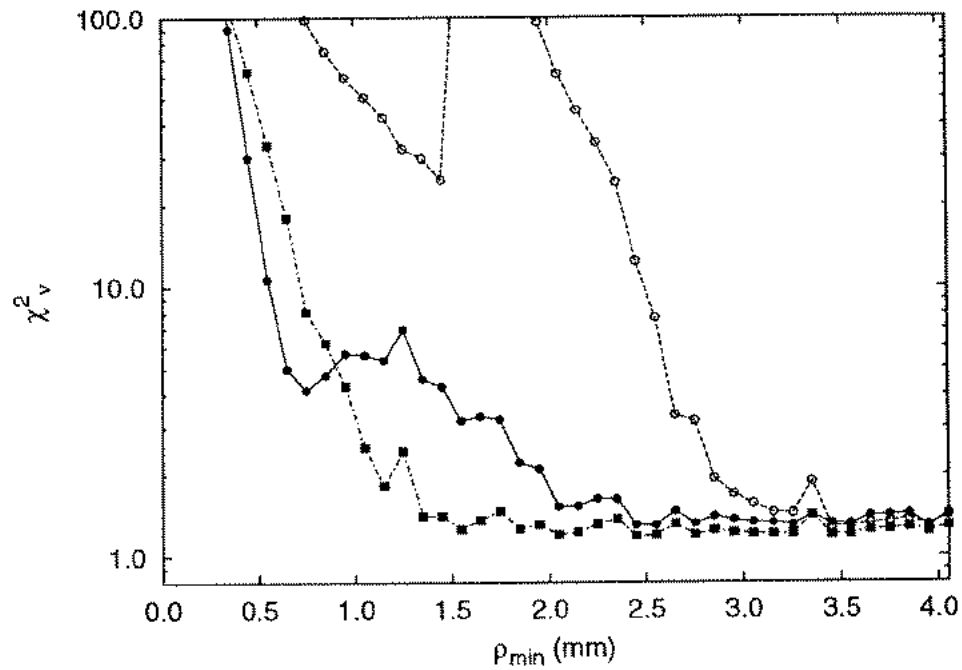


Figure 3.3 Values of the χ_v^2 goodness-of-fit statistic resulting from fits of the DT_{full} (solid circles and solid line), DT_{flux} (open circles and dashed line), and P_3 (solid squares and dotted line) reflectance expressions to simulated reflectance data for a medium with optical properties of $\mu_a=0.01 \text{ mm}^{-1}$, $\mu_s'=1.00 \text{ mm}^{-1}$, and $n_{ref}=1.4$. The fitted optical properties are illustrated in Figure 3.2.

reflectance at source-detector separations less than a few transport mean free paths is determined primarily by the transport scattering coefficient, μ_s' , since the short optical pathlengths traversed by the photons do not allow for appreciable absorption. For $\rho \gg \text{mfp}'$, the reflectance decreases exponentially at a rate governed by μ_{eff} . Since this parameter involves the product of the optical coefficients, it is not sufficient for unique determination of μ_s' and μ_a . For these reasons, experimental data sets containing the diffuse reflectance measured at small as well as large radial distances from the incident beam are required in order to uniquely separate the two optical coefficients. If all of the detectors are situated at radial distances from the source where absorption effects are significant, the ability to independently obtain μ_s' is impaired, resulting in poor discrimination between μ_a and μ_s' . The symmetry in the curves of the returned optical properties confirms that the errors in μ_a and μ_s' are highly correlated: when the returned transport scattering coefficient is low, the absorption coefficient is returned high, so the overall estimate of μ_{eff} is preserved.

Figures 3.4 and 3.5 present the same analysis depicted in Figures 3.2 and 3.3 for a medium with an index-matched boundary ($n_{\text{rel}}=1.0$). Figure 3.1 shows that the index-matched reflectance data increase more drastically near $\rho=0$ than do the index-mismatched data. Given the shape of the DT_{flux} solution, one might expect it to perform better under these circumstances, and that is in fact the case. Figure 3.4 illustrates that both diffusion-theory solutions give comparable results for the index-matched case, with μ_a and μ_s' accurate to $\pm 5\%$ for $1.2 \leq \rho_{\text{min}} \leq 3.0$ mm. Interestingly, the P_3 solution performs less well under these conditions. The reason for this is not entirely clear but is again likely to be associated with the approximations involved with the hybrid fitting function.

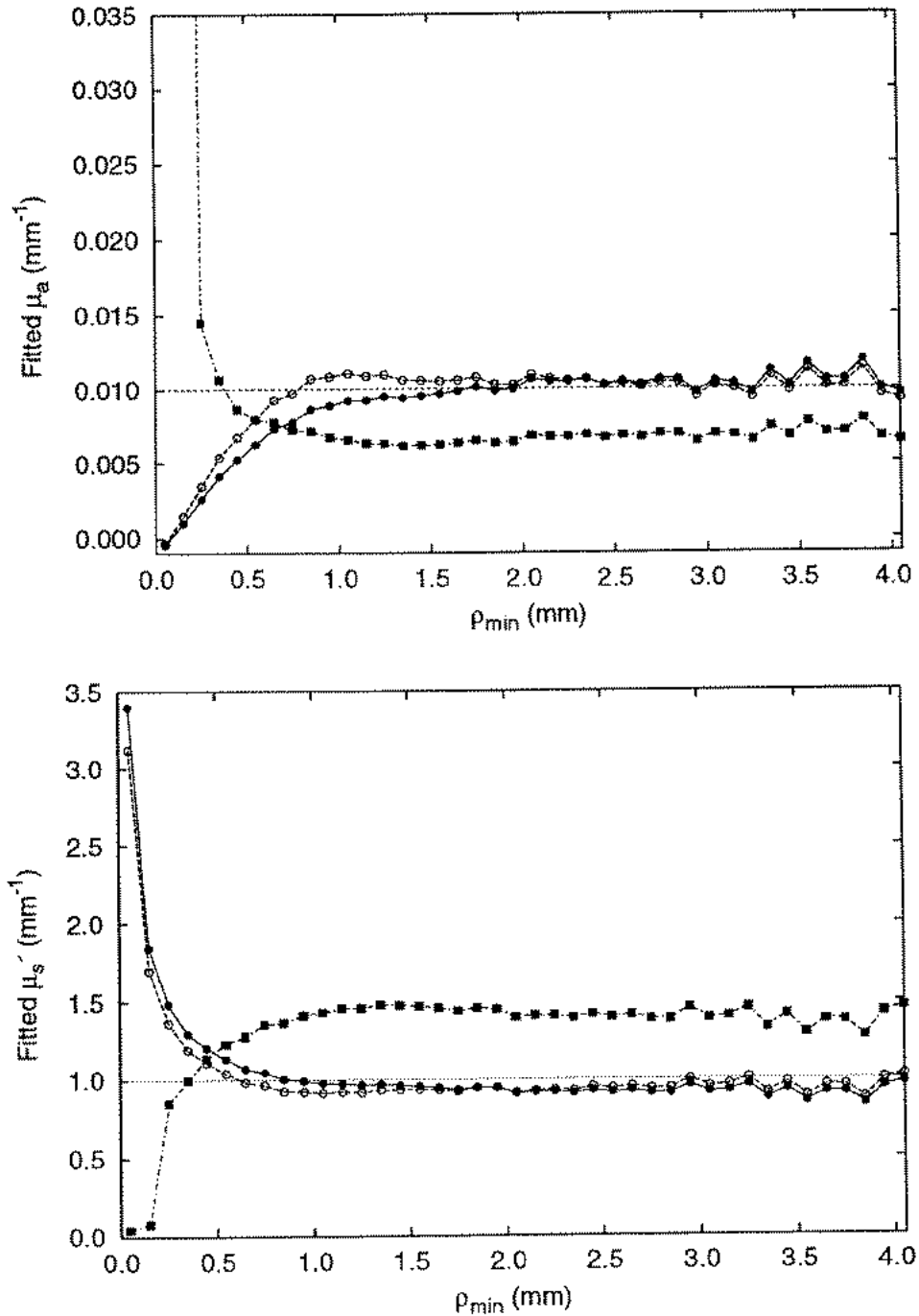


Figure 3.4 Values of μ_a (upper panel) and μ_s' (lower panel) resulting from fits of the DT_{full} (solid circles and solid lines), DT_{flux} (open circles and dashed lines), and P_3 (solid squares and dotted lines) solutions to simulated reflectance data for a medium with optical properties of $\mu_a=0.01 \text{ mm}^{-1}$, $\mu_s'=1.00 \text{ mm}^{-1}$, and $n_{\text{rel}}=1.0$.

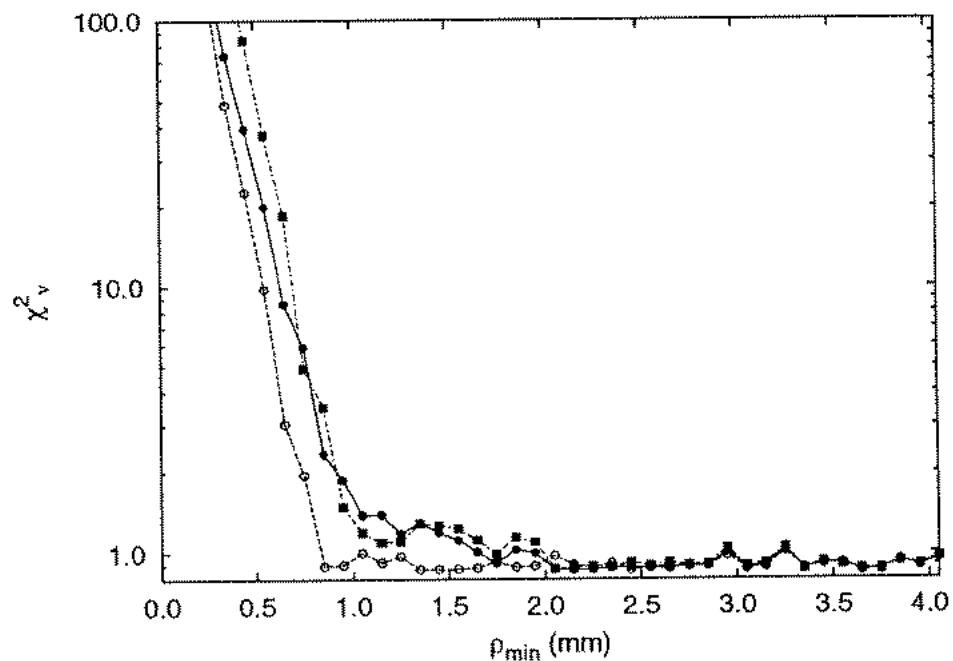


Figure 3.5 Values of the χ_v^2 goodness-of-fit statistic resulting from fits of the DT_{full} (solid circles and solid line), DT_{flux} (open circles and dashed line), and P_3 (solid squares and dotted line) solutions to simulated reflectance data for a medium with optical properties of $\mu_a=0.01 \text{ mm}^{-1}$, $\mu_s'=1.00 \text{ mm}^{-1}$, and $n_{ref}=1.0$. The fitted optical properties are illustrated in Figure 3.4.

Figures 3.6 and 3.7 present the same analysis depicted in Figures 3.2 and 3.3 for a medium with $\mu_a=0.5 \text{ mm}^{-1}$ and $\mu_s'=1.00 \text{ mm}^{-1}$. These optical properties are not within the regime of validity of standard diffusion theory but are suggestive of those which might be encountered in tissue in the visible region of the spectrum (Figures 1.1 and 1.3). The value of ρ_{\max} was fixed at 5.45 mm, and ρ_{\min} was varied from 0.15 mm to 2.05 mm. This range of ρ_{\min} was selected because, for this data set, the reflectance becomes simple-exponential in v by $\rho \approx 2.0 \text{ mm}$ (Figure 3.1). The transition to simple-exponential decay in the reflectance at a rate defined by the asymptotic attenuation coefficient occurs at increasingly smaller values of ρ as the absorption coefficient increases. As discussed above, this transition defines the regions of ρ which are most sensitive to scattering ($\rho < \rho_{\text{transition}}$) and absorption ($\rho > \rho_{\text{transition}}$).

For this simulated data set, the diffusion-theory solutions result in large errors in the fitted optical properties. The exact value of the fitted coefficients also depends sensitively on the value of ρ_{\min} . Near $\rho_{\min} \approx 1.7 \text{ mm}$, both diffusion-theory solutions also demonstrate a marked transition in the sign of the error in the fitted values of μ_a and μ_s' . The exact value of ρ_{\min} at which this transition occurs is a function of statistical fluctuations in the data and the medium optical properties, so it is perhaps impossible to predict the optimum value of ρ_{\min} for which diffusion theory could be made most valid. In addition, it can be seen that χ^2 is significantly larger for the diffusion-theory solutions than for the P_3 solution throughout the range of ρ_{\min} shown here, indicating a general lack of agreement between the diffusion expressions and the data. In contrast, the P_3 solution gives good agreement with the data and estimates of optical properties which are accurate to within $\pm 10\%$ for $0.5 \leq \rho_{\min} \leq 2.05 \text{ mm}$. This illustrates that quantitative optical spectroscopy of tissue in the visible region of the spectrum,

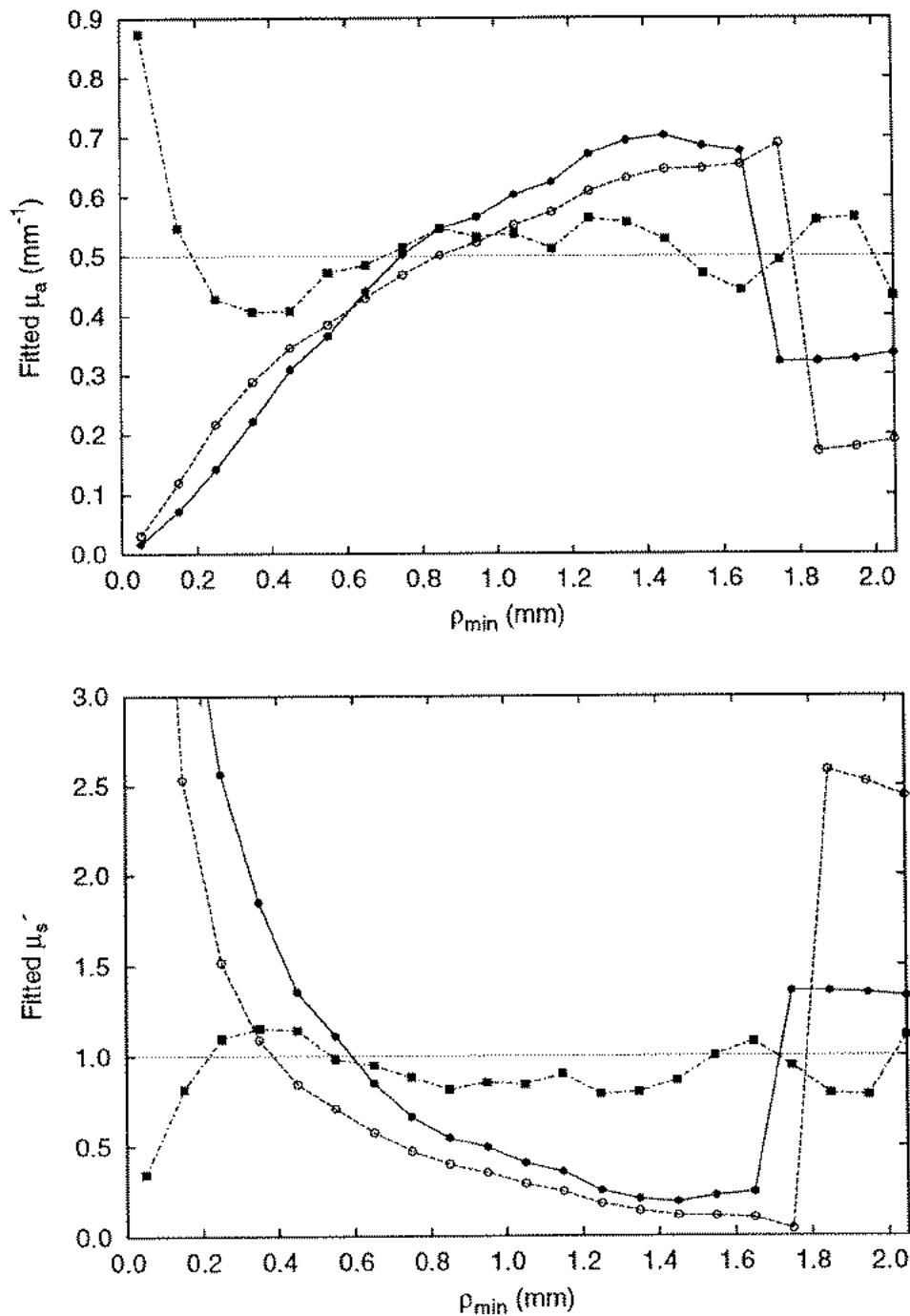


Figure 3.6 Values of μ_a (upper panel) and μ_s' (lower panel) resulting from fits of the DT_{full} (solid circles and solid lines), DT_{flux} (open circles and dashed lines), and P_3 (solid squares and dotted lines) reflectance expressions to simulated reflectance data for a medium with optical properties of $\mu_a = 0.50 \text{ mm}^{-1}$, $\mu_s' = 1.00 \text{ mm}^{-1}$, and $n_{\text{rel}} = 1.4$.

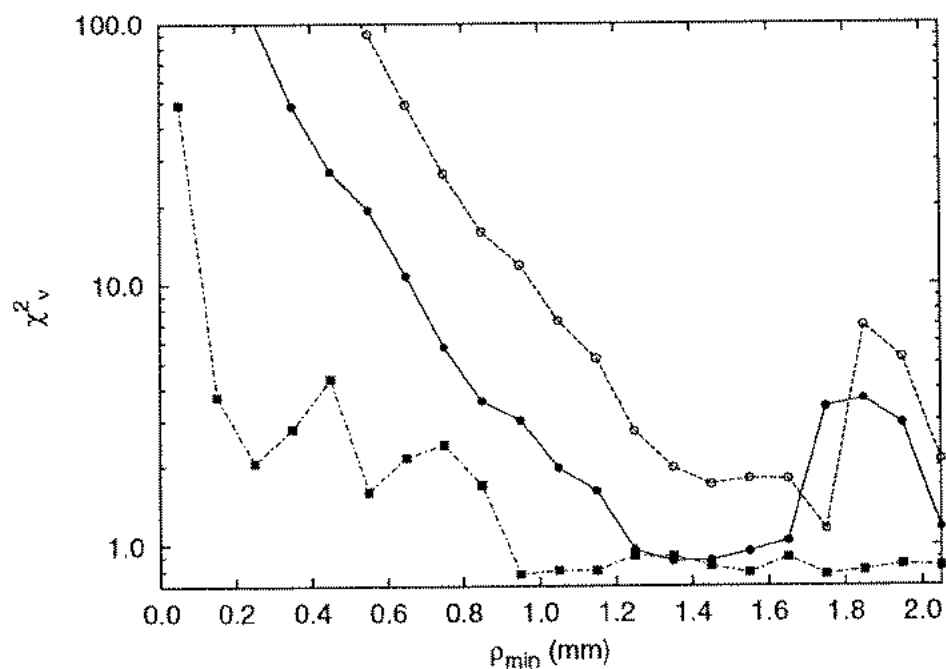


Figure 3.7 Values of the χ^2_v goodness-of-fit statistic resulting from fits of the DT_{full} (solid circles and solid line), DT_{max} (open circles and dashed line), and P_3 (solid squares and dotted line) reflectance expressions to simulated reflectance data for a medium with optical properties of $\mu_a=0.50 \text{ mm}^{-1}$, $\mu_s'=1.00 \text{ mm}^{-1}$, and $n_{rel}=1.4$. The fitted optical properties are illustrated in Figure 3.6.

where μ_a is of the order of 0.5 mm^{-1} and μ_s' is on the order of 1.0 mm^{-1} , is not possible within the diffusion approximation but can be accomplished within the P_3 approximation.

A summary of fits to a series of index-mismatched Monte Carlo data sets is presented in Figures 3.8 and 3.9. In these simulations, μ_s' was equal to 1.00 mm^{-1} and μ_a ranged from 0.0001 mm^{-1} to 5.0 mm^{-1} . This is a roughly physiologic range of μ_a for tissue in the wavelength range $400 \leq \lambda \leq 950 \text{ nm}$, although the absorption coefficient is not likely to be greater than 1.0 mm^{-1} for most tissues. Figure 3.8 depicts the reconstructed absorption coefficient as a function of the actual absorption coefficient, and the diagonal line indicates the line of exact agreement between fitted and actual absorption coefficients. Figure 3.9 depicts the reconstructed scattering coefficients, and the horizontal line at 1.00 mm^{-1} represents the actual scattering coefficient used in the simulations. In both figures, the open circles represent the DT_{full} solution with $\rho_{\text{min}}=1.65 \text{ mm}$, the open triangles represent the DT_{flux} solution with $\rho_{\text{min}}=1.65 \text{ mm}$, and the solid squares represent the P_3 solution with $\rho_{\text{min}}=0.45 \text{ mm}$. These values of ρ_{min} were selected based on Figures 3.2 – 3.7 and gave the most accurate optical properties for each expression when considered over the full range of simulated optical properties. The value of ρ at which the statistical uncertainty in the reflectance data became $\geq 10\%$ was used for ρ_{max} and varied from 20.0 mm to 3.0 mm .

Examination of Figure 3.8 reveals that, once an apparent lower detectability threshold of approximately 0.0005 mm^{-1} is reached, μ_a is reconstructed by the DT_{full} expression to an accuracy of 10% or better for $0.005 \leq \mu_a \leq 0.025 \text{ mm}^{-1}$. For absorption coefficients larger than 0.025 mm^{-1} , the DT_{full} expression overestimates μ_a in a progressively more significant fashion until a sudden transition to underestimation

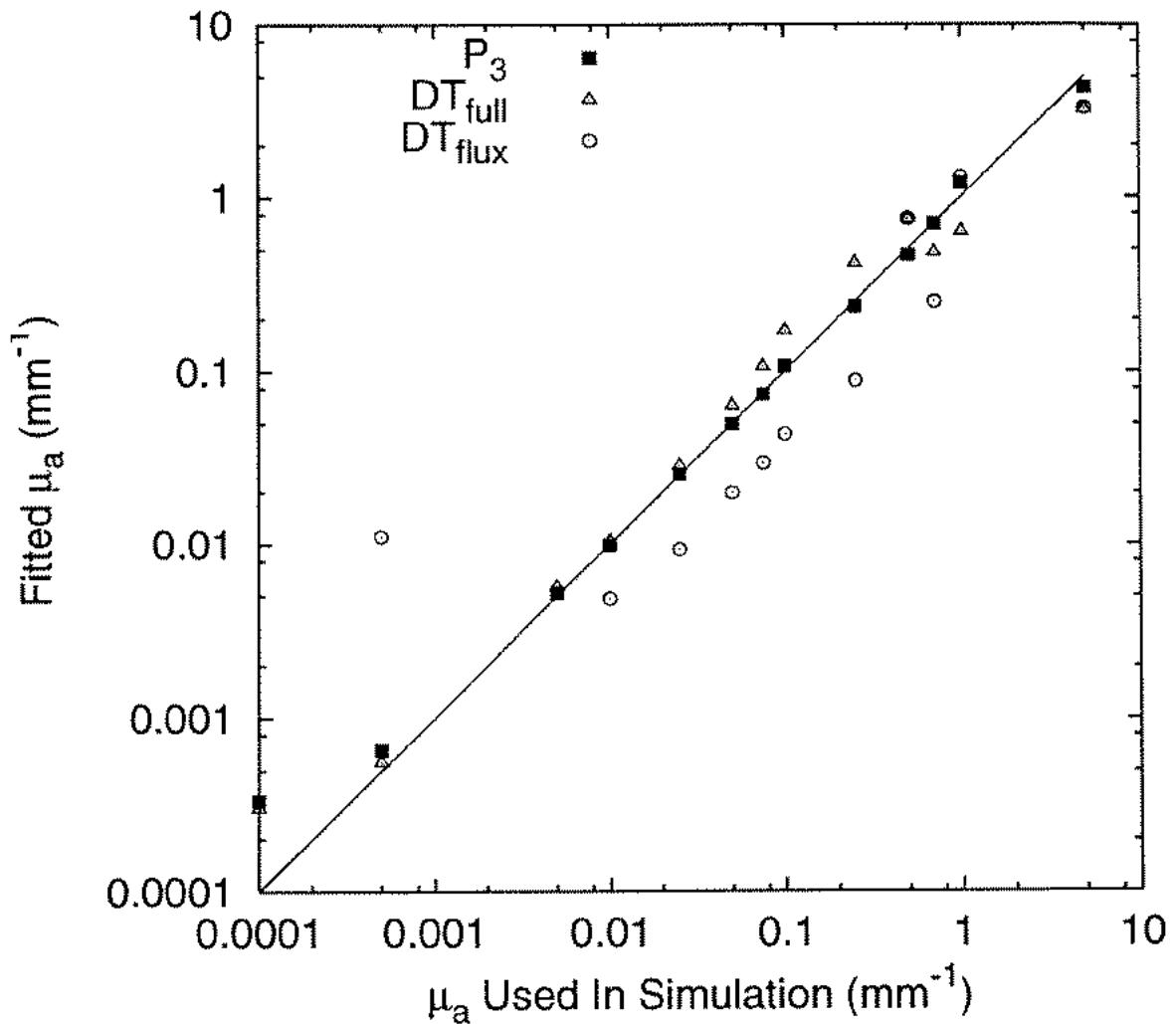


Figure 3.8 Values of μ_a returned from fits to a series of index-mismatched Monte Carlo data sets. In the simulations, μ_s' was equal to 1.00 mm^{-1} and μ_a ranged from 0.0001 mm^{-1} to 5.0 mm^{-1} . The diagonal line indicates the line of exact agreement between fitted and actual absorption coefficients. The open circles represent the DT_{full} solution with $\rho_{\text{min}}=1.65 \text{ mm}$, the open triangles represent the DT_{flux} solution with $\rho_{\text{min}}=1.65 \text{ mm}$, and the solid squares represent the P_3 solution with $\rho_{\text{min}}=0.45 \text{ mm}$.

occurs at $\mu_a=0.75 \text{ mm}^{-1}$. The DT_{flux} solution exhibits significant inaccuracy in the reconstructed value of μ_a throughout the full range of investigation and also exhibits several transitions between under- and overestimation of the absorption coefficient. Interestingly, in the range of absorption coefficients most commonly encountered in near-IR spectroscopy of tissue ($0.01 \leq \mu_a \leq 0.05 \text{ mm}^{-1}$), the DT_{flux} solution consistently underestimates μ_a , but the relative change in μ_a from sample to sample is correctly determined, as evidenced by the slope of the line connecting the fitted μ_a values in this range. This suggests that the DT_{flux} solution, while inaccurate in an absolute sense, may still give reasonable estimates of changes in optical properties of scattering media where diffusion theory is most often implemented. In contrast to the diffusion theory expressions, the P_3 expression gives optical properties which are accurate to 10% or better for $0.005 \leq \mu_a \leq 0.700 \text{ mm}^{-1}$. Not surprisingly, the P_3 expression exhibits the same apparent lower limit of detectability in μ_a . However, the absorption coefficient is reconstructed by the P_3 expression accurately for transport albedos as small as 0.59, which is the approximate small-albedo limit for spectroscopy of tissue in the visible region of the spectrum.

Figure 3.9 demonstrates that the transport scattering coefficients reconstructed by the diffusion theory solutions also exhibit significant errors as the absorption coefficient increases beyond the range typically considered valid for optical diffusion. The DT_{diff} solution yields values of μ_s' accurate within 10% for $\mu_a \leq 0.025 \text{ mm}^{-1}$ but underestimates μ_s' for $\mu_a > 0.025 \text{ mm}^{-1}$, with the error in the fitted value becoming progressively larger for increasing μ_a . The DT_{flux} solution yields significant errors throughout the range of investigation. The P_3 solution, however, retains 10% accuracy or better for $\mu_a \leq 0.7 \text{ mm}^{-1}$, which is again encouraging with respect for the potential

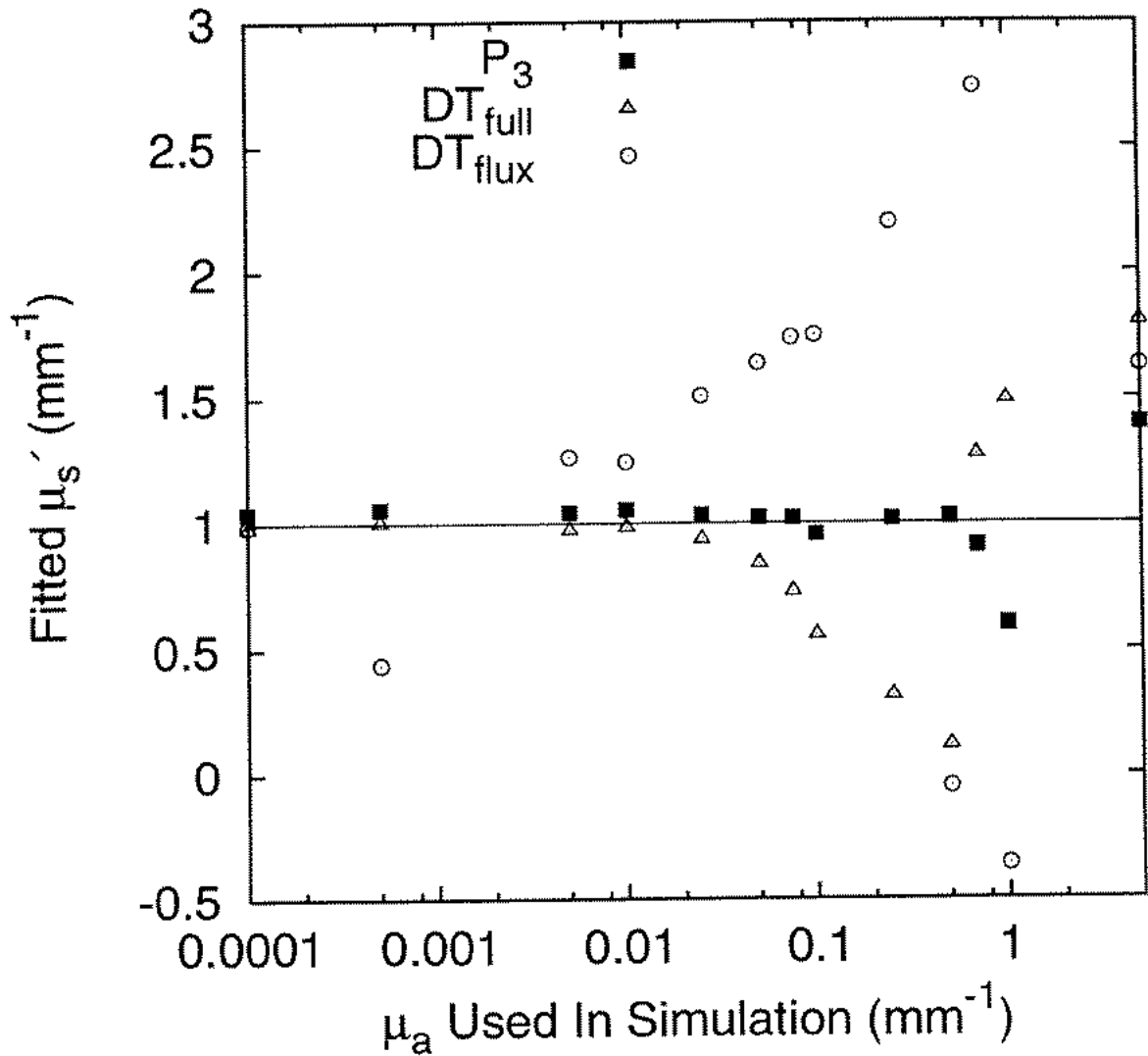


Figure 3.9 Fitted values of μ_s' returned from fits to a series of index-mismatched Monte Carlo data sets. In the simulations, μ_s' was equal to 1.00 mm^{-1} and μ_a ranged from 0.0001 mm^{-1} to 5.0 mm^{-1} . The horizontal line indicates the value of μ_s' used in the simulations. The open circles represent the DT_{full} solution with $\rho_{\text{min}}=1.65 \text{ mm}$, the open triangles represent the DT_{flux} solution with $\rho_{\text{min}}=1.65 \text{ mm}$, and the solid squares represent the P_3 solution with $\rho_{\text{min}}=0.45 \text{ mm}$.

for quantitative tissue spectroscopy in the visible spectral region.

3.2.2 Sensitivity to maximum source-detector separation

To investigate the maximum source-detector separation required for accurate quantitation of optical properties, a series of fits was again made to Monte Carlo simulated data, this time varying ρ_{\max} as well as ρ_{\min} . The highly absorbing medium ($\mu_a=0.5 \text{ mm}^{-1}$, $\mu_s'=1.0 \text{ mm}^{-1}$, and $n_{\text{rel}}=1.4$) was used for this series of fits. In this case, only a comparison between the DT_{full} and P_3 solutions was investigated, since the DT_{flux} solution has been demonstrated to be inaccurate for index-mismatched boundaries. For both the DT_{full} and P_3 solutions, ρ_{\min} was varied from 0.1 mm to 1.6 mm, and ρ_{\max} was varied from 3.0 to 7.0 mm. The results of this series of fits are depicted in Figure 3.10. The panels on the left-hand side of the figure are contours of constant fractional error in μ_s' (upper panel) and μ_a (lower panel) for the DT_{full} solution. The panels on the right-hand side present the same analysis for the P_3 solution. The legends at the bottom of the μ_a contour plots also apply to the corresponding μ_s' contour plots. In all cases, the solid linestyle denotes zero fractional error.

Several things are evident from Figure 3.10. First, for highly absorbing media, accurate quantitation of the absorption coefficient is possible in the P_3 approximation for fairly modest maximum source-detector separations ($\rho_{\max} \approx 4\text{-}5 \text{ mm}$), provided a first detection fiber is placed at $0.2 \leq \rho_{\min} \leq 0.6 \text{ mm}$. The valley of stability centered around ρ_{\min} is an important feature of this analysis. In contrast, the errors in the optical properties returned by the DT_{full} solution are larger than those returned by the P_3 solution, are very sensitive to the location of ρ_{\min} , and have different optimum values of ρ_{\min} for μ_a and μ_s' . Therefore, it is clear that the P_3 solution offers greater accuracy

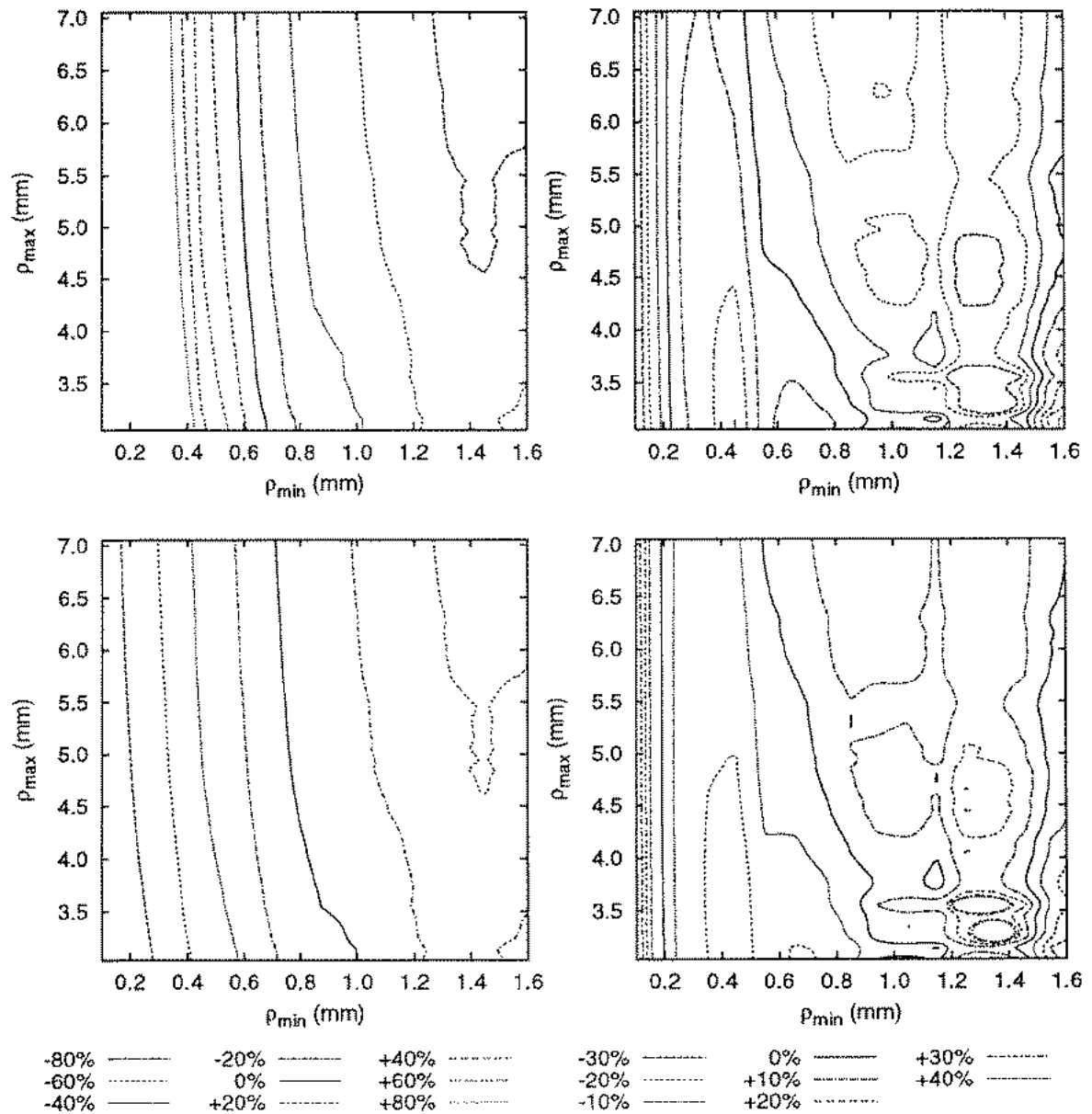


Figure 3.10 Contours of constant fractional error in μ_s' (upper panels) and μ_a (lower panels) obtained from fitting the DT_{full} (left-hand panels) and P_3 (right-hand panels) reflectance expressions with various values of ρ_{min} and ρ_{max} to Monte-Carlo reflectance data simulated for a medium with optical properties of $\mu_a=0.5 \text{ mm}^{-1}$, $\mu_s'=1.00$, and $n_{rel}=1.4$. The legends at the bottom of the μ_a contour plots also apply to the corresponding μ_s' contour plots. In all cases, the solid linestyle denotes zero fractional error.

for highly absorbing media, provided the approximations outlined in Chapter 2 are valid. In addition, the small maximum source-detector separations which are possible offer the potential for quantitative optical spectroscopy via endoscopy, since the largest available endoscope accessory channels are ~4-5 mm in diameter.

3.3 Broadband Steady-state Reflectance Spectrometer

3.3.1 Instrument

Our steady-state reflectance spectrometer is based on a design first proposed by Wilson et al. [2]. A schematic diagram of the instrument is given in Figure 3.11. White light from a 250 W quartz tungsten halogen bulb is coupled into a 400- μm diameter optical fiber (NA=0.22). Present coupling efficiency enables throughput of approximately 1.4-1.8 mW of optical power in a 10-nm bandpass in the wavelength range 550-850 nm. This source fiber is mounted in a circular probe containing nineteen 200- μm diameter detection fibers located at radial distances of 1.0 mm to 20.0 mm from the source fiber as shown in Figure 3.12. The source fiber and the nineteen detection fibers are arranged in a 2.0 cm diameter circle. At the center of this circular probe is mounted another 400- μm source fiber, which, because it is equidistant from all other fibers, can be used to calibrate the spectral response and throughput of the detection fibers. The flat surface of the probe is placed in contact with the surface of the phantom or tissue under investigation, allowing white light from the source fiber to be injected into the sample surface. The probe described here and illustrated in Figure 3.12 is used for collection of reflectance data from media with optical properties appropriate for diffusion theory. The probe used for measurements of reflectance from highly absorbing

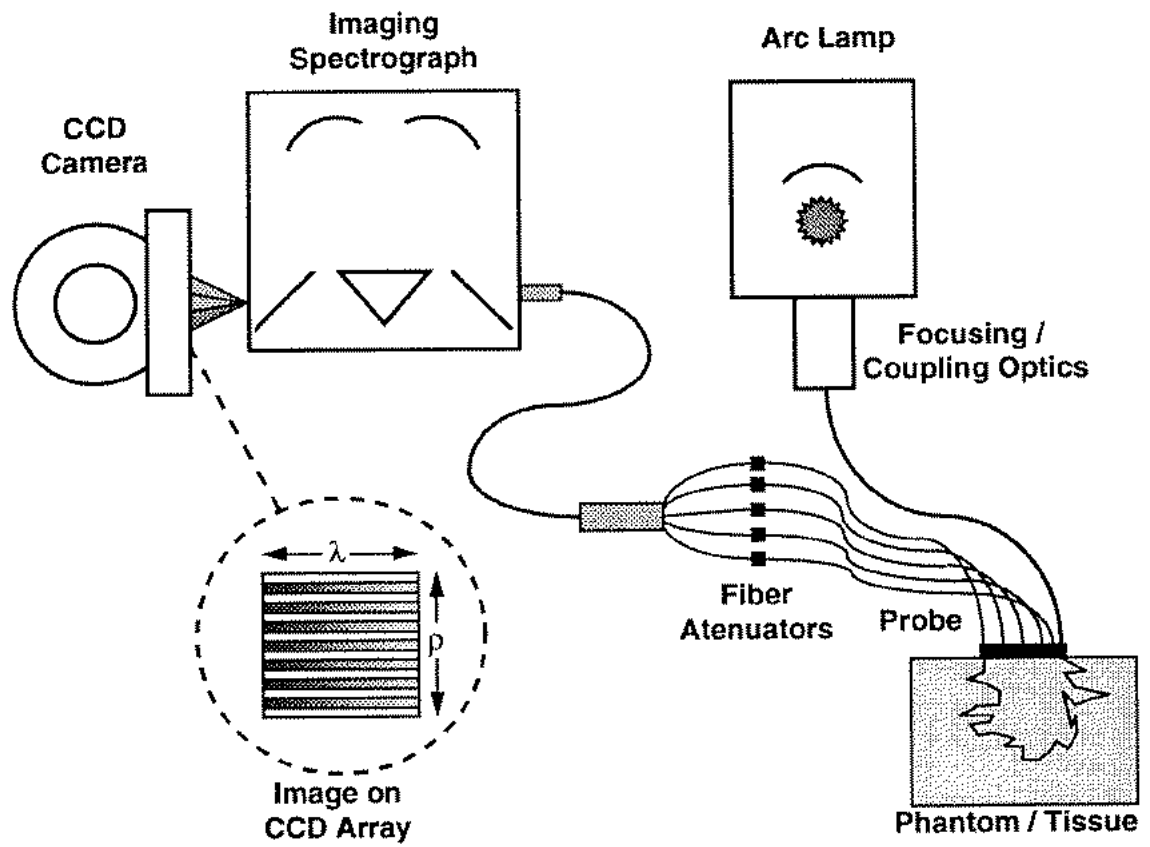


Figure 3.11 White-light, steady-state reflectance spectrometer.

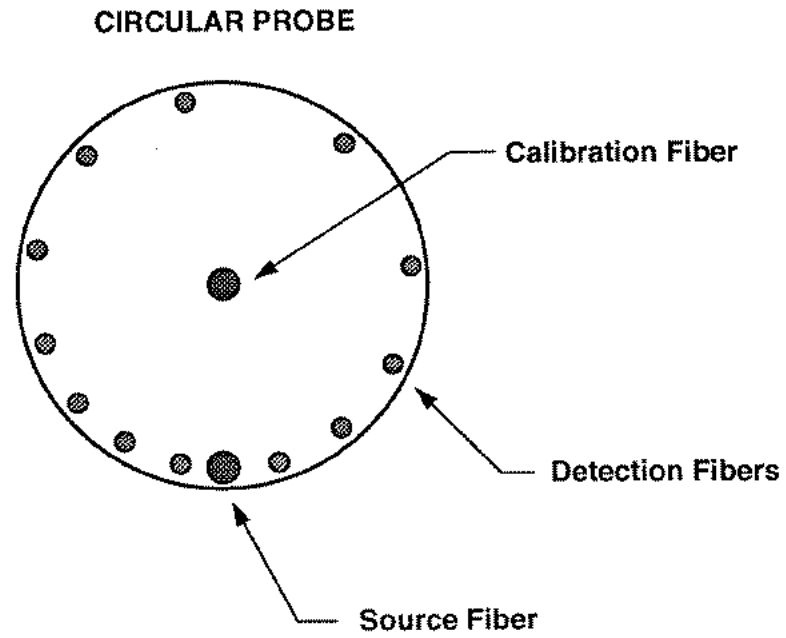


Figure 3.12 Circular probe for collection of reflectance data.

media is described in Section 3.5.1.

The reflectance probe is constructed of a black plastic material known as Delrin® (3M, St. Louis, MO). The refractive index of Delrin was not available from the manufacturer, but it is probably in the range of 1.4-1.5. The fact that a portion of the surface of the scattering medium contacts the probe surface and the remainder of the interface is open to air introduces an ambiguity in the proper choice for the internal reflection parameter A . For example, assuming the refractive indices of both tissue and Delrin® are 1.4, the “correct” value of A to use in reflectance data analysis is likely to be between 2.95, which is the theoretical value for $n_{rel}=1.4$, and 1.00, which is the theoretical value for an index-matched interface. This issue is investigated in Section 3.4.

Because a typical radially-resolved diffuse reflectance data set encompasses four to five decades of dynamic range and the effective dynamic range of the detector is only about two decades if shot noise in the detected signal is to be $\leq 4\%$, light from the detection fibers nearest the source fiber is passed through adjustable attenuators (OZ Optics, Carp, Ontario, Canada) to decrease the effective signal intensity from these fibers. The output of each attenuator is coupled to a corresponding 300- μm diameter transfer fiber which transmits the signal to a grating spectrograph. Unattenuated fibers are connected directly to their mating transfer fibers by SMA adapters.

The transfer fibers are gathered into a bundle that terminates in a ferrule. At the end of the ferrule the fibers are arranged in a row and positioned in the focal plane of a 0.275-m imaging spectrograph (Acton Research Corporation, Acton, Mass.). The spectrograph was modified slightly by the addition of several baffles in order to maximize stray light rejection. Presently, in the 400-650 nm wavelength range,

approximately 0.5% of the signal from any given fiber is present as stray light in the signal of the fibers to which it is immediately adjacent. This fiber-to-fiber crosstalk increases significantly in the near-IR, however, becoming as large as 4% at $\lambda=900$ nm. For this reason, it is necessary to correct data collected in the near-IR for fiber-to-fiber crosstalk.

The ends of the transfer fibers are imaged through a low-resolution, high-dispersion grating (300 l/mm) onto the surface of a liquid-nitrogen cooled, 512x512, 16-bit CCD camera (Princeton Instruments, Princeton, NJ). The dispersion of the grating and the useful flat field of the spectrograph are such that 170 nm of spectral information may be collected in a single acquisition. The signal at the detector is thus the spectrally-resolved diffuse reflectance collected at several distinct distances from the source fiber, oriented such that the signals from the individual optical fibers lie in non-overlapping regions of the CCD array perpendicular to the slit axis. Imaging of the fibers is 1:1 through the spectrograph, so the signal from a given 300- μm transfer fiber is distributed over approximately twelve 25- μm pixels along the axis of the spectrometer slit. To optimize the signal-to-noise ratio, regions of 9 pixels along the slit axis and 3 pixels along the wavelength axis are binned to create a single super-pixel. Pixel binning in the wavelength direction results in one diffuse reflectance data set every 0.96 nm, which is approximately the resolution of the instrument in its current configuration. The binned pixels are read from the CCD with the software provided by the manufacturer and later analyzed offline.

3.3.2 Data reduction

The first stage of data analysis constructs a diffuse reflectance curve for each of the

binned wavelengths obtained by the apparatus. To do this, the raw reflectance data must first be corrected for individual fiber throughput differences, the attenuator settings, and fiber-to-fiber crosstalk. Calibration data are acquired over the wavelength range of interest by injecting white light into a tissue-simulating phantom through the center fiber of the detector probe and collecting reflectance through each of the detection fibers. Since each detection fiber is equidistant from the center source fiber and the tissue-simulating phantom is presumed to be homogeneous, any differences in the spectra obtained in this configuration are due to individual variation in the detection fibers, variation of the throughput of the apparatus along different sections of the light path, variation in the degree of attenuation of individual detection fibers, or fiber-to-fiber crosstalk. It should be emphasized that the phantom is used in the calibration procedure only because it provides a convenient method for providing a uniform signal to each detection fiber. The technique described here is in no way dependent upon obtaining a calibration standard with known optical properties [3]. The throughput of the attenuators is typically adjusted to make the signal from the detection fiber nearest the source approximately 1% of the CCD dynamic range, which corresponds to ~4% shot noise. The level of attenuation decreases with increasing ρ , and fibers corresponding to $\rho \geq 15$ mm are usually not attenuated.

The degree of fiber-to-fiber crosstalk is wavelength-dependent, and, since the focal plane of the spectrograph is not perfectly flat, also depends on the exact location of the detected signal within the focal plane. For this reason, it is necessary to determine the fiber-to-fiber crosstalk for each individual detection channel for every wavelength setting of the spectrograph. This is accomplished by independently illuminating each fiber and measuring the fraction of the signal in the illuminated

fiber's CCD detection channel which is present in the detection channels of adjacent fibers. Using this pre-determined crosstalk data, the measured signal intensity in each detection channel can be expressed

$$\begin{pmatrix} I_{1_{meas}} \\ I_{2_{meas}} \\ I_{3_{meas}} \\ \vdots \\ I_{N_{meas}} \end{pmatrix} = \begin{pmatrix} 1 & CT_{21} & CT_{31} & \dots & CT_{N1} \\ CT_{12} & 1 & CT_{32} & \dots & CT_{N2} \\ CT_{13} & CT_{23} & 1 & \dots & CT_{N3} \\ \vdots & \vdots & \vdots & \ddots & \vdots \\ CT_{1N} & CT_{2N} & CT_{3N} & \dots & 1 \end{pmatrix} \begin{pmatrix} I_{1_{act}} \\ I_{2_{act}} \\ I_{3_{act}} \\ \vdots \\ I_{N_{act}} \end{pmatrix}, \quad (3.2)$$

where $I_{j_{meas}}$ is the measured signal intensity in detection channel j , CT_{ij} is the measured fractional crosstalk in detection channel j from a signal in detection channel i , $I_{j_{act}}$ is the actual signal (uncorrupted by the effects of crosstalk) in detection channel j , and N is the total number of detection channels. Although there are 19 separate detection channels used with our present diffuse reflectance probe, we have found that, for $\lambda < 900$ nm, it is only necessary to correct for the cross-talk from the 7 nearest neighbors to each detection channel. Thus, in practice, the crosstalk matrix in Equation 3.2 is 8-fold diagonal. The effects of cross-talk may therefore be corrected by computing

$$\mathbf{I}_{act}(\lambda) = (\mathbf{CT}(\lambda))^{-1} \mathbf{I}_{meas}(\lambda), \quad (3.3)$$

where \mathbf{I}_{act} is a vector of corrected signal intensities, \mathbf{CT} is the cross-talk matrix in Equation 3.2, and \mathbf{I}_{meas} is a vector of measured signal intensities. All parameters in Equation 3.3 are wavelength-dependent; a different cross-talk correction matrix is

required for each wavelength in the dataset.

One disadvantage of the crosstalk correction technique described here is that it makes the reduced data noisier than uncorrected data. This is because the thin, back-illuminated CCD we use for these measurements becomes increasingly transparent in the near-IR. Because of this, the detector acts as an imperfect etalon, and small thickness fluctuations across the surface of the chip create interference patterns which vary with wavelength and physical location on the detector. While these effects are normalized out in an uncorrected data set, the crosstalk correction process has the effect of combining signals from physically distinct regions of the detector, leading to small but noticeable fluctuations in the raw data. An additional post-correction data smoothing step would likely be valuable but has not yet been implemented.

In order to correct for the possibility of background light leakage through the system, a background data set is also acquired with no light coupled to the source fiber. While typical background levels are negligible, this procedure allows subtraction of any constant offset counts added to the analog-to-digital converter by the CCD controller in order to facilitate data acquisition.

After obtaining the reflectance, calibration, and background data sets, the diffuse reflectance curve, $R(\rho;\lambda)$, can be computed for each binned wavelength on the CCD from the following equation:

$$R(\rho;\lambda) = \frac{R_s(\rho;\lambda) - B}{R_c(\rho;\lambda) - B}, \quad (3.4)$$

where R_s is the crosstalk-corrected reflectance data set, R_c is the crosstalk-corrected calibration data set, B is the background signal which, in general, can vary across the

CCD, ρ is the source-detector separation and λ is the wavelength. The parameters ρ and λ correspond to binned locations parallel and perpendicular to the spectrometer slit axes, respectively, as illustrated in Figure 3.11. Uncertainties in the reflectance data computed by Equation 3.4 are determined by applying Poisson counting statistics to the raw CCD counts obtained in each measurement described above and propagating these uncertainties by conventional means [4]. We have found this calibration procedure to effectively eliminate systematic deviations due to variations in the throughput of the individual fibers, attenuator settings, and fiber-to-fiber crosstalk.

Finally, after calculating $R(\rho; \lambda)$ for all ρ and λ used in a given experiment, each radial reflectance curve generated at a particular wavelength is normalized to the diffuse reflectance from the detection fiber nearest the source fiber at that wavelength. By doing this, the experimental data are cast into a form suitable for analysis with Equation 3.1 as a fitting function.

The second stage of the data analysis involves successively fitting Equation 3.1 to each of the 170 normalized diffuse reflectance profiles in the manner described above in order to determine the absorption and transport scattering coefficients at each wavelength represented in the data set. Completing this fitting process and printing the results to a monitor typically takes 4 seconds or less on our 200 MHz Pentium Pro[®] microcomputer. In this manner, the absorption and transport scattering spectra are effectively reconstructed from the radially-resolved diffuse reflectance profiles.

3.4 Phantom studies

In this section, phantom studies designed to experimentally test each of the fitting

functions described in Section 3.1 are presented. The experiments described in Sections 3.4.1 and 3.4.3 were performed in the visible region of the spectrum, so no crosstalk correction was implemented for these studies. For the studies in Sections 3.4.1 and 3.4.2, a Levenberg-Marquadt nonlinear least squares algorithm adapted from Press et al. [5] was used to reconstruct optical properties from the normalized reflectance data. The Levenberg-Marquadt algorithm from the MATLAB® software package was used for the study in Section 3.4.3.

3.4.1 Partial diffusion theory solution

Although the DT_{flux} solution has been demonstrated to be the least accurate of the three expressions discussed in Section 3.1, it was the first published closed-form solution which led to straightforward separation of optical properties of scattering media. It was therefore the technique initially investigated in our laboratory.

A series of experiments was conducted in order to calibrate the instrument and determine its sensitivity to changes in sample absorption and scattering and to determine the range of optical properties for which accurate fits to the experimental data are possible. In these trials, optical phantoms were prepared which consisted of a scattering solution and known quantities of chromophore. The phantoms were prepared to simulate tissue scattering properties reported in the literature [6]. The porphyrin manganese meso-tetra (4-sulfanato-phenyl) porphine (MnTPPS) was used as an absorber because of its high water solubility and lack of fluorescence.

Absorption spectra of a phantom consisting of 1.25% Liposyn-II (Abbott Laboratories, North Chicago, IL) and varying concentrations of MnTPPS are shown in Figure 3.13. Data for each spectrum were collected over the wavelength range 510 nm

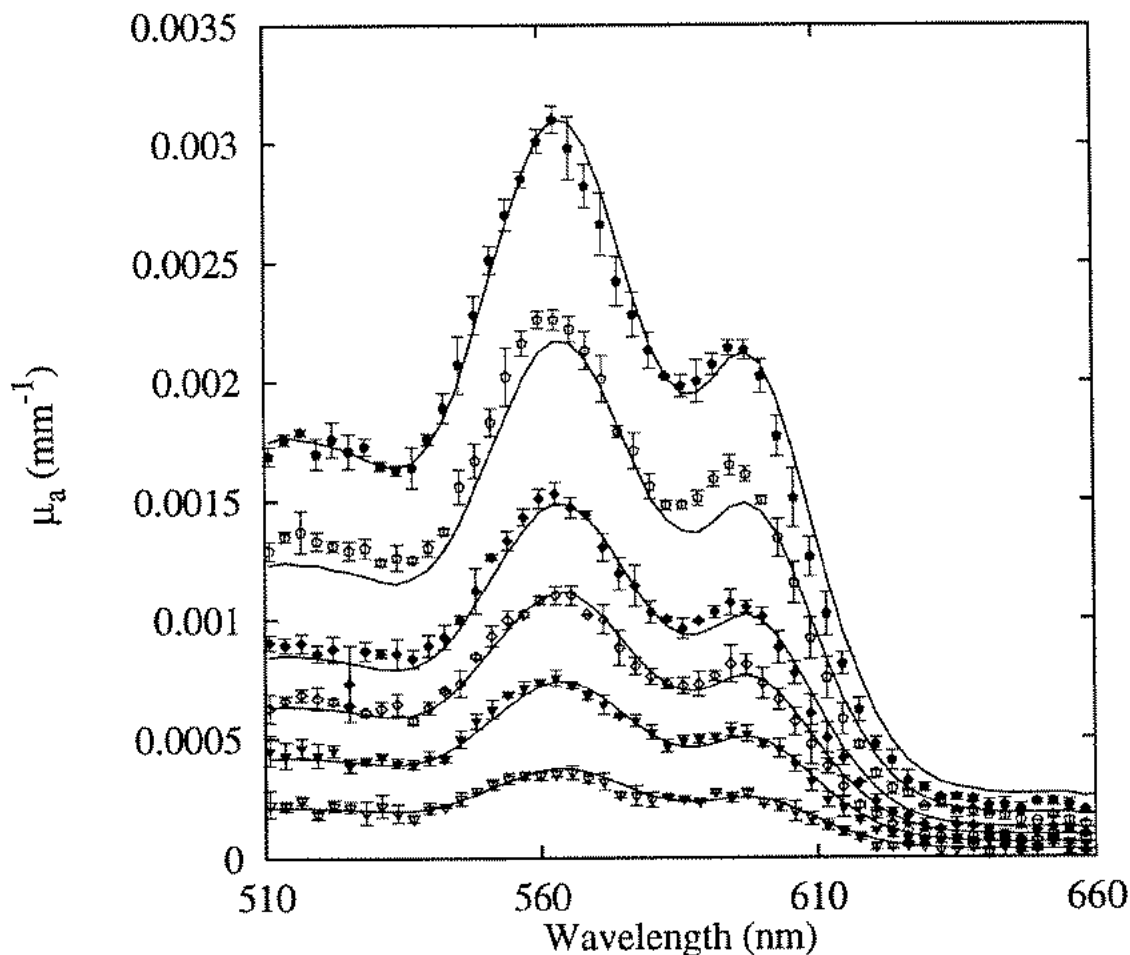


Figure 3.13 Background-subtracted absorption spectra (data points) of several concentrations of MnTPPS in 1.25% Liposyn-II reconstructed from diffuse reflectance measurements. The error bars represent the standard deviation of the fitted values of μ_a . The standard deviation in the diffuse reflectance data points used in the fitting algorithm resulted from assuming Poisson counting statistics to determine the uncertainty in the counts read from the CCD camera. The lines are absorption spectra from spectrophotometer measurements of non-scattering samples with amplitudes scaled to provide the best fit to the data. The single linear fitting parameter reveals the concentration of MnTPPS in the phantom. Actual concentrations of MnTPPS range from 0.15 μM to 1.25 μM .

to 670 nm in a single acquisition. The points are the absorption coefficients (μ_a) returned by fitting Equation 3.1 using the DT_{aux} solution with $A=1.00$ to radially-resolved diffuse reflectance measurements following subtraction of the background absorption of the lipid emulsion, which was obtained prior to the addition of MnTPPS. The error bars in Figure 3.13 represent the standard deviations of the fitted values of μ_a returned by the Levenberg-Marquadt fitting algorithm. Absorption spectra acquired from samples of MnTPPS in non-scattering aqueous solution in a conventional spectrometer were then fit to the data points with the amplitude of the spectrum as a linear fitting parameter. The solid lines in Figure 3.13 indicate the best fits of these “cuvette” spectra to the absorption coefficients calculated from diffuse reflectance measurements. If the concentration of the solution used to obtain the cuvette spectrum is known, then the fitting parameter enables one to determine the absolute concentration of MnTPPS in the phantom. This method was used to quantitatively evaluate the absorption coefficients returned by fitting Equation 3.1 to the diffuse reflectance data over the range of concentrations used in these experiments. A total of 34 measurements were made with MnTPPS concentrations ranging from 7.8 nM to 13.8 μM .

The accuracy of the MnTPPS concentration determined in this way is illustrated in Figure 3.14a - 14d. In these plots, the data points represent the concentration of MnTPPS in the phantom obtained by fitting the cuvette spectrum to the absorption spectra reconstructed from radial diffuse reflectance measurements. The solid lines indicate the actual MnTPPS concentration in the phantom as determined by the volume of 0.780 mM MnTPPS stock added to the phantom. The upper and lower lines indicate the limits of error in the actual concentration due to measurement

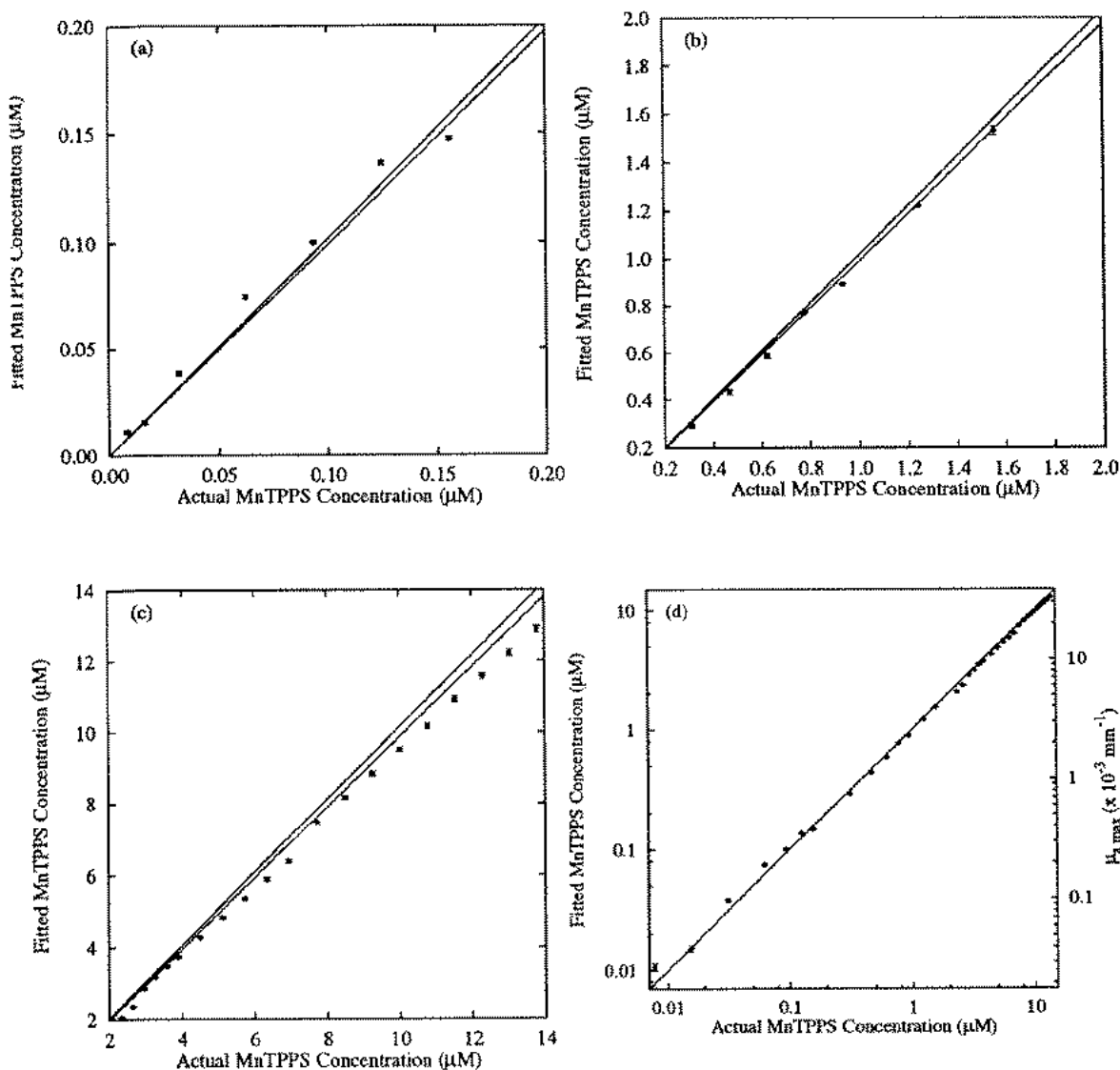


Figure 3.14 The actual (solid lines) and fitted (data points) concentrations of MnTPPS in a 1.25% Liposyn-II phantom. The upper and lower solid lines indicate the range of uncertainty in the actual MnTPPS concentration due to 1.0% uncertainties assigned to the micropipettes and graduated cylinders used to prepare the phantom. Fitted concentrations were determined by fitting “cuvette” spectra of MnTPPS to absorption spectra reconstructed from diffuse reflectance measurements. The maximum value of μ_a (at $\lambda \approx 560$ nm) in the reconstructed absorption spectra ranges from 2.5×10^{-5} to $2.5 \times 10^{-4} \text{ mm}^{-1}$ (panel a), 7.0×10^{-4} to $4.0 \times 10^{-3} \text{ mm}^{-1}$ (panel b), 5.0×10^{-3} to $3.5 \times 10^{-2} \text{ mm}^{-1}$ (panel c). Panel d illustrates the full range of concentrations used in the experiments.

uncertainties of 1.0% associated with the pipettes and graduated cylinders used in the phantom preparation.

The smallest concentrations, for which the fit is most inaccurate, correspond to changes in μ_a less than or equal to 0.0001 mm^{-1} above the background absorption of the Liposyn-II phantom near the 560 nm absorption maximum of MnTPPS (Figure 3.14a). This appears to be the approximate limit of the sensitivity of the current instrument to changes in μ_a and is in agreement with the Monte Carlo results presented in Section 3.1. After this threshold is exceeded, the returned concentration is quite accurate (Figure 3.14b). The first six points plotted in Figure 3.14b correspond to the absorption spectra illustrated in Figure 3.13. The maximum absorption coefficient for these spectra (at $\lambda \approx 560 \text{ nm}$) ranges from $\sim 0.0003 \text{ mm}^{-1}$ to $\sim 0.003 \text{ mm}^{-1}$. As the transport albedo decreases with the addition of absorber, there is a tendency for the fitted concentrations to become systematically low by approximately 10% relative to the actual concentration present in the phantom Figure 3.14c.

Recall that the Monte Carlo results presented in Figure 3.4 for $\mu_a = 0.01 \text{ mm}^{-1}$ and $\mu_s' = 1.00 \text{ mm}^{-1}$ indicated that the fitted value of μ_a was approximately 13% *high* for a minimum source-detector separation greater than approximately 1.0 mm. Experimentally, the returned value for μ_a is systematically low, a result which was obtained by fitting with Monte Carlo data which included reflectance from source-detector separations less than 1 mfp'. It is possible that this discrepancy may be explained by the fact that the source and detection fibers have finite diameters of 0.4 and 0.2 mm, respectively. In addition, the optical fibers have a numerical aperture of 0.22 rather than the idealized pencil beam assumed for the Monte Carlo simulations. These factors may combine to yield an effective minimum source-detection fiber

separation of less than 1.00 mm, thus placing our experiment in the regime where returned values for μ_a are systematically low. Of course, this is just one possible explanation. Another explanation might be based on the assumption of an index-matched boundary, which is certainly questionable. Our experience has been, however, that values of A other than 1.0 result in increased errors in the values of both μ_a and μ_s' returned by fitting the $DT_{0_{ux}}$ expression to reflectance data collected with our experimental probe.

When examined over the entire range of concentrations used in these experiments (Figure 3.14d), our data indicate that changes in the absorption coefficient relative to the subtracted background spectrum are determined to within 10% accuracy for transport albedos >0.983 , provided a threshold change in absorption over background of approximately 0.0001 mm^{-1} is exceeded. This correct estimation of the absorption coefficient relative to a constant background absorption is again consistent with the Monte Carlo results presented in Section 3.1.

Figure 3.15 illustrates the transport scattering spectra of the same phantom used to obtain the absorption spectra in Figure 3.13. As in the previous case, each scattering spectrum represents a fit of Equation 3.1 to a diffuse reflectance measurement made after the addition of a known quantity of MnTPPS to the phantom. Of course, one would not expect the scattering properties of the phantom to change when a relatively small amount of pure absorber is added to the system. In fact, as successive amounts of MnTPPS are added, the scattering spectrum is not significantly altered. Indeed, all of the spectra are within experimental uncertainty of one another (error bars have been omitted in order to increase the clarity of the plot).

In an effort to evaluate the quantitative accuracy of the scattering coefficients

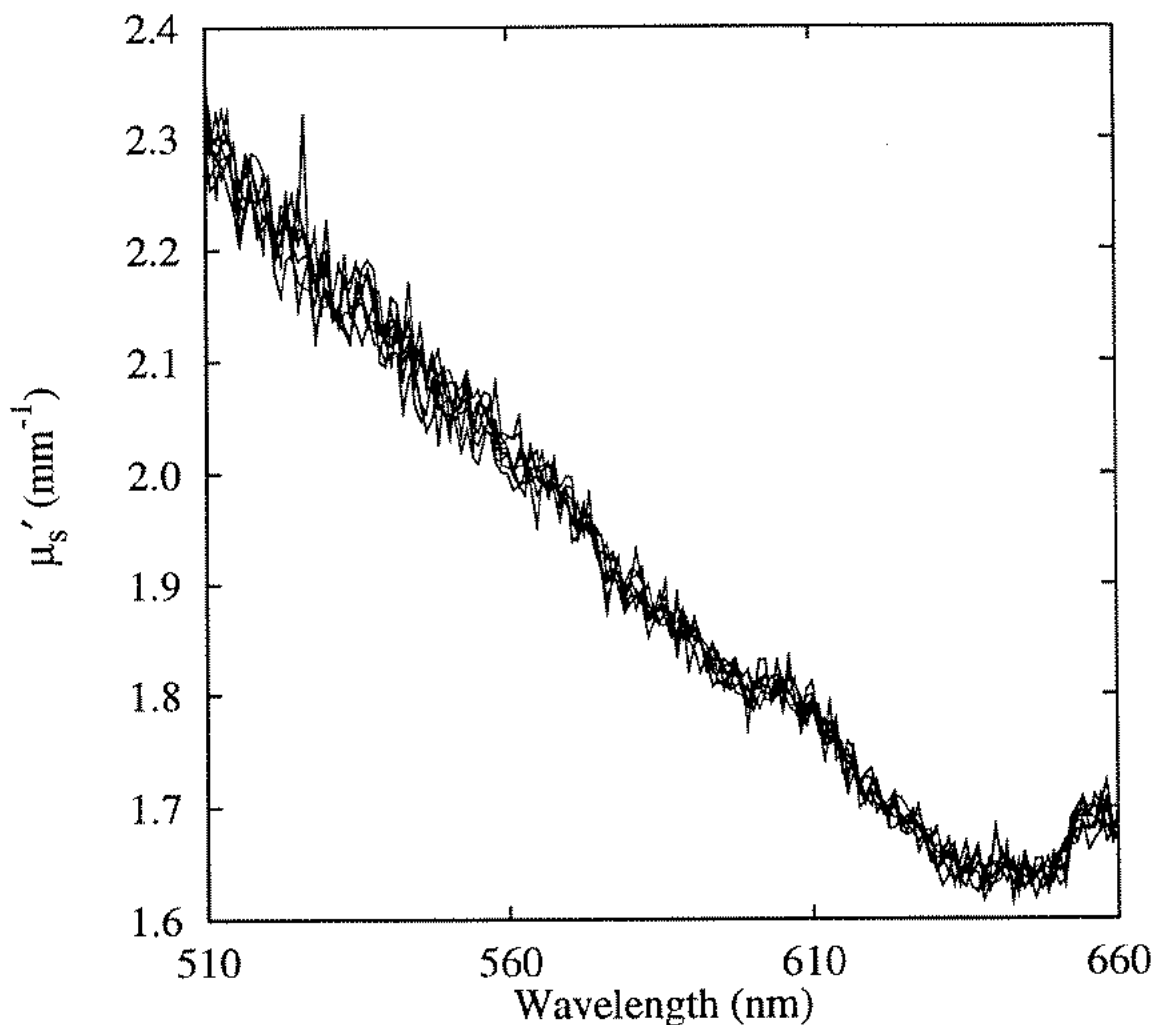


Figure 3.15 Scattering spectra of a 500-ml 1.25% Liposyn-II phantom determined by fitting Equation 3.1 to radially-resolved diffuse reflectance measurements. Each separate line represents the scattering spectrum after the addition of various concentrations of MnTPPS ranging from 0.15 μM to 1.25 μM . The spectra are all within one measurement standard deviation of one another.

returned by fitting the DT_{flux} solution to radially-resolved diffuse reflectance data, a series of phantoms was prepared consisting of 500 ml of distilled water and varying amounts of an aqueous suspension of 0.519 μm -diameter polystyrene microspheres (Duke Scientific, Palo Alto, CA). The density of scatterers was varied from $1.58 \times 10^{10} \text{ ml}^{-1}$ to $2.79 \times 10^{10} \text{ ml}^{-1}$ in these experiments. Figures 3.16a through 16d illustrate the transport scattering spectra predicted by Mie theory for four suspensions of 0.519- μm diameter non-absorbing spheres in the wavelength range of 500 - 825 nm, along with the measured values of μ_s' obtained from the phantom using our diffuse reflectance spectroscopy system. In Figure 3.16a, the experimental and theoretical spectra possess the same wavelength dependence and are in excellent quantitative agreement. This corresponds to the maximum density of scatterers used in this experiment. As the density of scatterers is decreased (Figures 3.16b - 16d), the fitted transport scattering coefficients become increasingly large with respect to the theoretical prediction.

It is possible that this may again be understood in terms of the minimum source-detector separation used in the acquisition and analysis of these data. For each of the panels in Figure 3.16, ρ_{min} was equal to 1.0 mm. In Figure 3.16a, the actual transport scattering coefficients are in the range of 0.75 - 1.0 mm^{-1} , corresponding to transport mean free paths of approximately 1.3 - 1.0 mm. Thus, since ρ_{min} is on the order of 0.75 - 1.0 mfp' one would expect the experimental data to yield the correct optical coefficients. As the density of scatterers decreases, the transport mean free path associated with the phantom becomes as large as 2.4 mm (Figure 3.16d). As a result, ρ_{min} becomes increasingly small with respect to the transport mean free path (as small as 0.4 mfp' in Figure 3.16d), and the transport scattering coefficient is correspondingly overestimated.

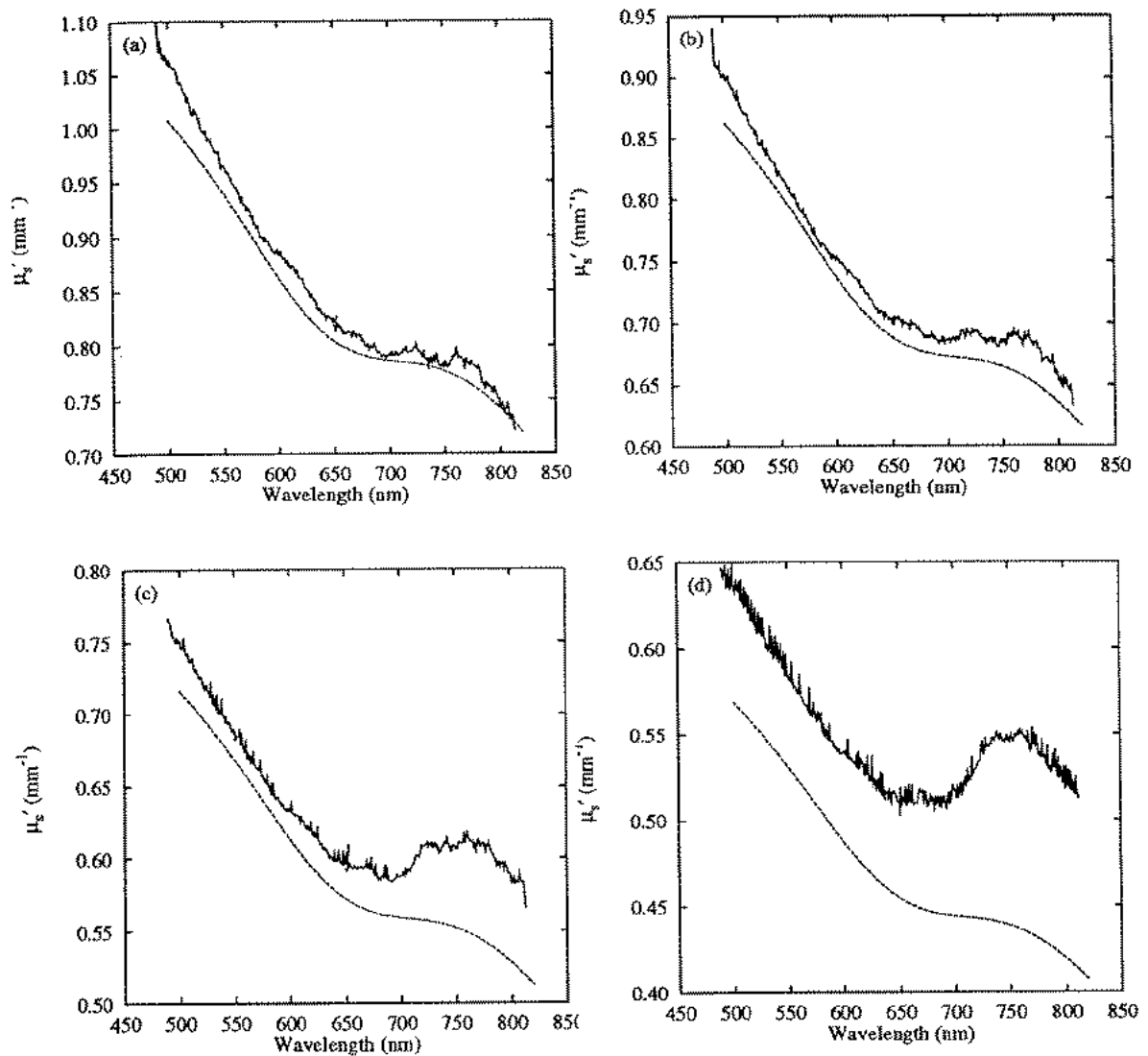


Figure 3.16 The scattering spectra of a phantom containing 500 ml H_2O and varying amounts of $0.519 \mu\text{m}$ -diameter polystyrene microspheres in aqueous suspension. The smooth lines indicate the transport scattering coefficient as predicted by Mie theory. Noisy lines are fitted values of μ_s' from experimental diffuse radial reflectance data. The density of scatterers decreases from $2.79 \times 10^{10} \text{ ml}^{-1}$ in panel (a) to $1.58 \times 10^{10} \text{ ml}^{-1}$ in panel (d).

3.4.2 Full diffusion theory solution

The tissue-simulating phantoms utilized in these studies were designed to examine the accuracy of the absorption and transport scattering spectra obtained from diffuse reflectance measurements in the near-infrared (~650-950 nm) spectral region. In these phantoms, 0.519 μm diameter polystyrene latex microspheres (Duke Scientific, Palo Alto, CA, USA) were added to 450 ml of distilled water to achieve a number density of 2.8×10^{10} spheres/ml. The transport scattering coefficient of the resulting suspension calculated by Mie theory ranged from $\sim 1.1 \text{ mm}^{-1}$ ($\lambda=650 \text{ nm}$) to $\sim 0.8 \text{ mm}^{-1}$ ($\lambda=950 \text{ nm}$). This scattering solution was placed in a cylindrical beaker 80 mm in diameter, resulting in a phantom depth of approximately 75 mm. Varying amounts of MnTPPS were subsequently added to these phantoms in order to compare the absorption spectrum reconstructed from reflectance measurements to the absorption spectrum of MnTPPS obtained from nonscattering solutions in a conventional spectrophotometer. A magnetic stirring rod was placed in the beaker, and the phantom was stirred continuously.

The solid line in Figure 3.17 is the absorption spectrum reconstructed using the DT_{full} solution from reflectance data obtained from a polystyrene sphere/distilled water phantom with no additional chromophores. The smooth dashed line in Figure 3.17 represents the absorption spectrum of water measured by Kou *et al.* [7]. It should be emphasized that this line indicates the absolute absorption coefficient of water and is not a fit. Since the phantom is 99.998% water by volume, one would expect its absorption spectrum to be nearly identical to that of water, and this is reflected in the experimental data. The uppermost dotted line in Figure 3.17 illustrates the results of fitting the same reflectance data to the DT_{flux} solution with $A=1.0$. Note that the shape of the water spectrum is reproduced with reasonable accuracy, but the absolute

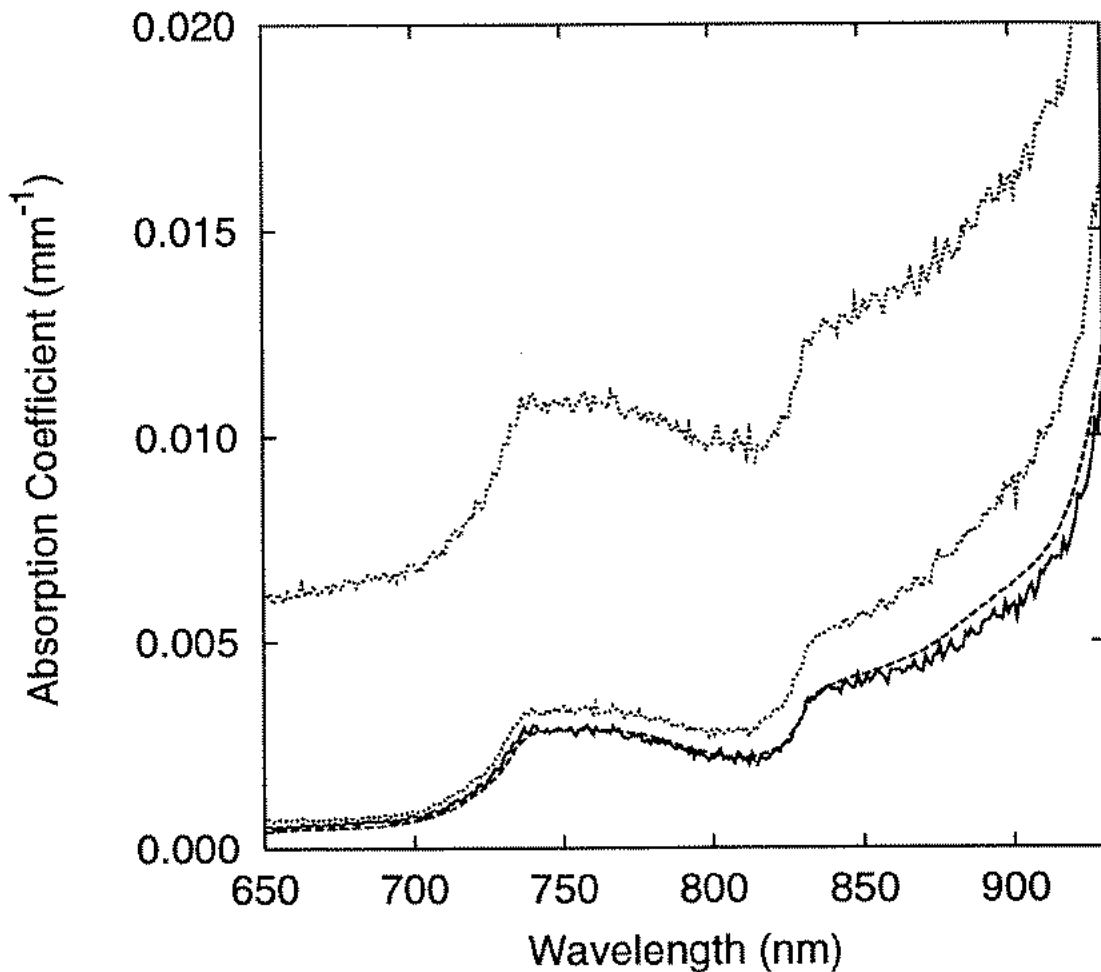


Figure 3.17 The absorption spectrum reconstructed by fitting the DT_{full} solution to reflectance measurements (solid line) of a tissue-simulating phantom comprised of $0.519 \mu\text{m}$ diameter polystyrene spheres diluted in distilled water to a density of 2.8×10^{10} spheres ml^{-1} . The smooth dashed line (---) is the absolute absorption spectrum of water (not a fit) as measured by Kou *et al.* The uppermost dotted line illustrates the results of fitting the same reflectance data (corrected for fiber-to-fiber crosstalk) with the DT_{full} solution using $A=1.0$. The lower dotted line illustrates the DT_{full} solution to the data before correcting for the effects of fiber-to-fiber crosstalk.

magnitudes of the fitted absorption coefficients are too large. The lower dotted line in Figure 3.17 illustrates the results of fitting the SDR data, uncorrected for the effects of fiber-to-fiber crosstalk, with the DT_{full} solution. As the crosstalk effects increase in severity in the NIR, the fitted values of μ_a deviate increasingly from the accepted absorption spectrum at longer wavelengths. Thus, use of the DT_{full} solution and crosstalk correction results in a significant increase in accuracy in the final absorption spectrum.

Figure 3.18 depicts transport scattering (upper panel) and absorption (lower panel) spectra reconstructed from the same set of reflectance data using various values of A . The value of A used in the fits varied from 2.52, which is the theoretical value for an air-water interface, to 1.00. Interestingly, the reconstructed scattering coefficient is more sensitive to A than is the absorption coefficient. The top noisy line in the upper panel is the scattering spectrum computed for $A=2.52$, and succeeding lines correspond to $A=2.0$, 1.5, and 1.0, respectively. The smooth line at the bottom is the scattering spectrum predicted by Mie theory. The spectrum computed with $A=1.00$ matches Mie theory most closely, but the scattering coefficients are still overestimated by approximately 15%. The reconstructed absorption spectra do not change significantly as A is varied. These spectra suggest that it may be best to assume an index-matched interface when performing reflectance spectroscopy with the current plastic probe.

As a second validation step, four aliquots of a concentrated aqueous solution of MnTPPS were added to the phantom, resulting in MnTPPS concentrations ranging from 10.8 to 43.6 μM . Diffuse reflectance data were collected after the addition of each successive aliquot. Figure 3.19 depicts the reconstructed absorption spectrum after subtraction of the background absorption (Figure 3.17). The lines in Figure 3.19 are

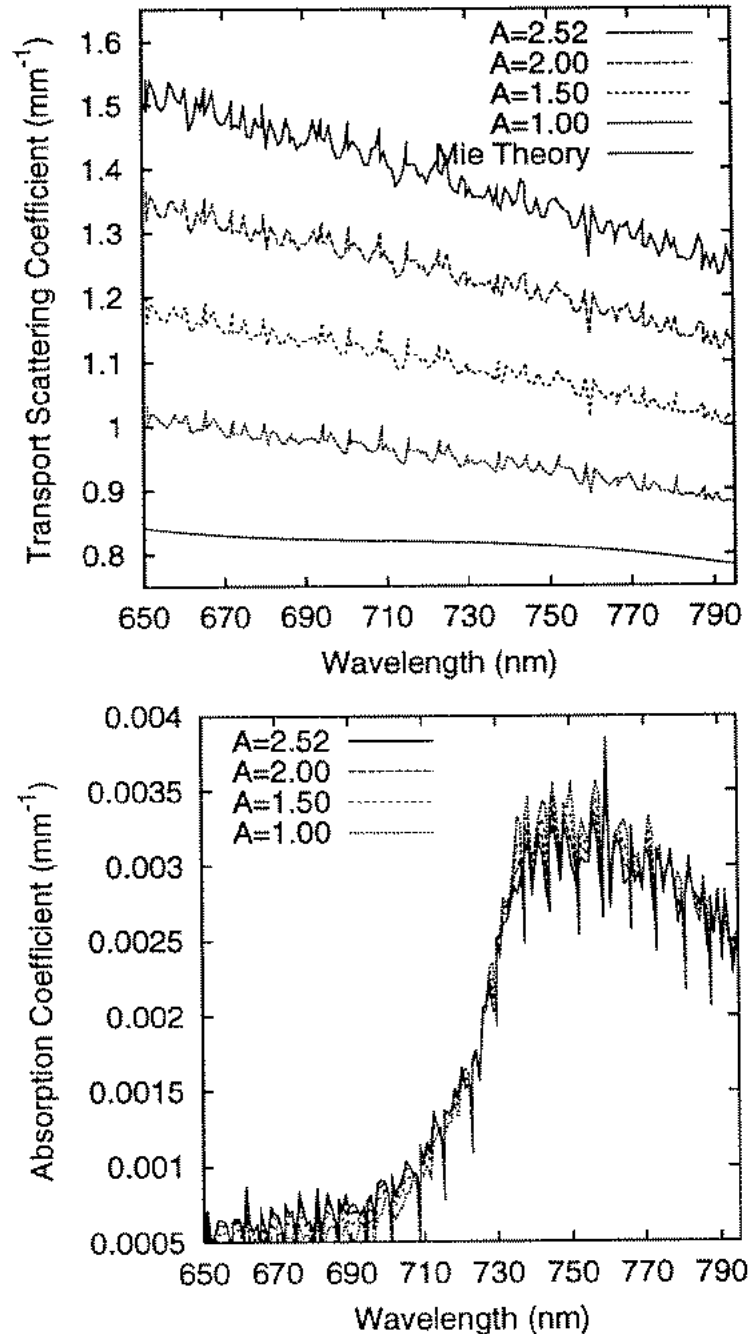


Figure 3.18 Transport scattering (upper panel) and absorption (lower panel) spectra reconstructed with the DT_{full} solution from reflectance measurements of a phantom comprised of $0.511 \mu\text{m}$ diameter polystyrene spheres diluted in distilled water to a density of 3.89×10^{10} spheres/ml. The value of the internal reflection coefficient (A) used in the fits varied from 2.52 (top noisy line in the upper panel) to 1.00 (bottom noisy line in the upper panel).

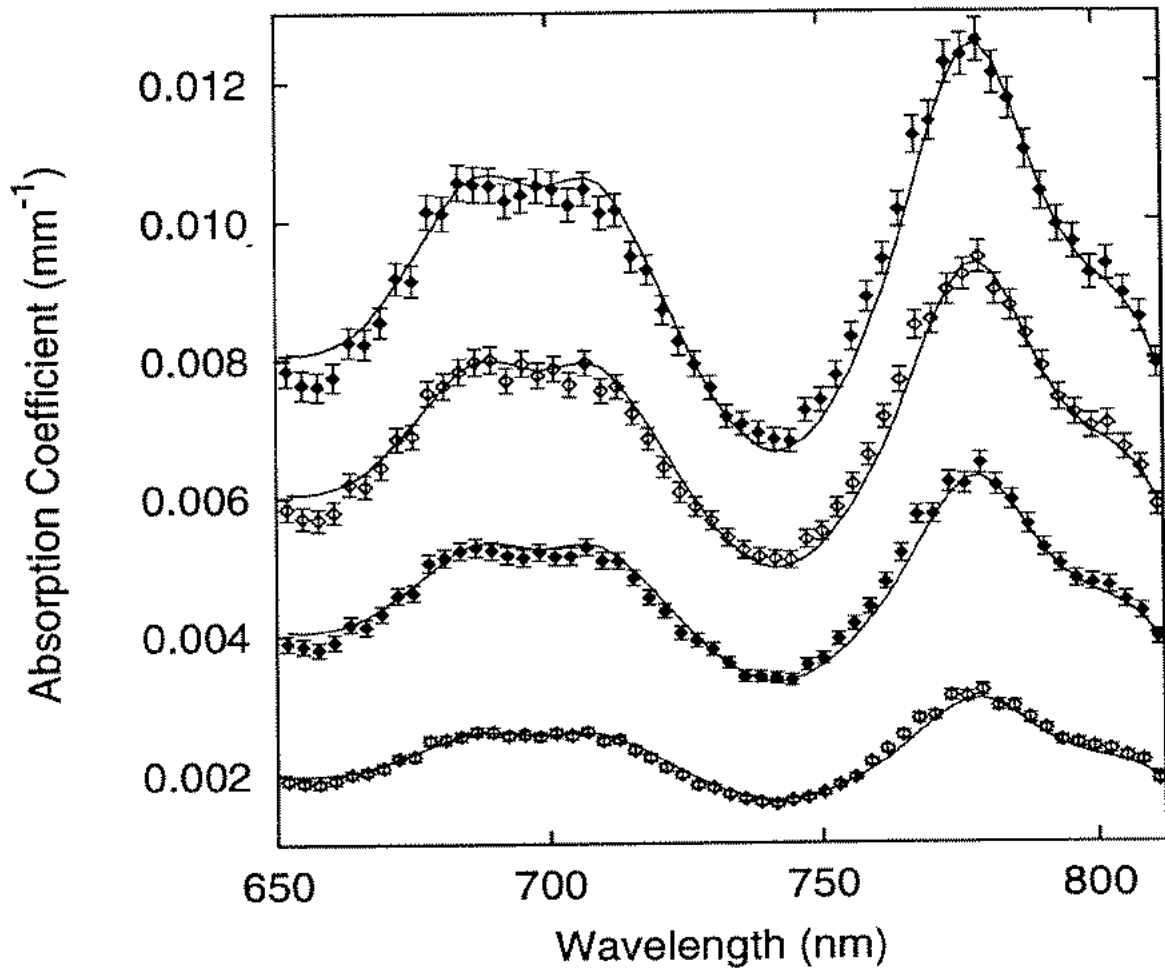


Figure 3.19 Absorption coefficients (data points) reconstructed from SDR measurements of a polystyrene sphere phantom ($\rho=2.8 \times 10^{10}$ spheres ml^{-1}) to which varying concentrations of MnTPPS were added. The absorption spectrum of the scattering phantom alone was measured prior to the introduction of MnTPPS and has been subtracted from these data. The spectra have been smoothed by averaging every three data points. The error bars on the averaged data points were obtained from propagation of the uncertainties in the fitted values of μ_a at each averaged wavelength. Solid lines are least squares fits of the MnTPPS absorption spectrum measured in a nonscattering solution in a conventional spectrophotometer to the background-corrected SDR spectra.

least-squares fits of the MnTPPS absorption spectrum measured in a nonscattering solution in a conventional spectrophotometer to the background-corrected SSDR spectra. The only parameter used in these fits was a linear scaling factor, which was used to determine the fitted MnTPPS concentration. The actual and fitted MnTPPS concentrations are presented in Table 3.1. It can be seen from these data that the reconstructed absorption spectrum matches the shape of the known absorption spectrum quite accurately and that the magnitudes of the fitted concentrations are accurate to within $\pm 4\%$.

3.4.3 P_3 solution

A final series of phantoms was designed to test the accuracy of the P_3 solution at low albedos. In this series of phantoms, MnTPPS was again used as an absorber in the $500 \text{ nm} \leq \lambda \leq 650 \text{ nm}$ wavelength region. The scatterers were $0.511 \mu\text{m}$ diameter polystyrene spheres diluted in 400 ml of distilled water to a number density of 3.2×10^{10} spheres/ml. Successive aliquots of MnTPPS were added to the phantom to achieve maximum absorption coefficients ranging from 0.01 mm^{-1} to 0.65 mm^{-1} .

The experimental probe used in these studies differed slightly from the probe described in Section 3.3.2. This probe consisted of a linear array of $100\text{-}\mu\text{m}$ diameter detection fibers arranged at distances of 0.43 mm to 9.53 mm from a $200\text{-}\mu\text{m}$ diameter source fiber. Since this probe did not contain a central calibration fiber, calibration data were obtained by illuminating the probe with light from an optical fiber terminated with a gradient index lens, which provided a beam with an intensity profile uniform to $\pm 0.5\%$ across the region which illuminated the probe. The calibration beam was passed through an optical diffusing plate placed directly in front of the linear

| Actual [MnTPPS] (μM) | Fitted [MnTPPS] (μM) |
|-----------------------------------|-----------------------------------|
| 10.8 ± 0.2 | 10.55 ± 0.03 |
| 21.6 ± 0.3 | 21.16 ± 0.06 |
| 32.4 ± 0.5 | 31.56 ± 0.09 |
| 43.6 ± 0.6 | 41.82 ± 0.12 |

Table 3.1 The actual and fitted concentrations of MnTPPS in the phantoms depicted in figure 2. The magnitudes of the fitted concentrations are accurate to within $\pm 4\%$.

detection array. The diffusing plate served to randomize the direction of the light incident on the linear array, analogous to the situation encountered during a reflectance measurement.

Sample absorption spectra reconstructed from a single measurement in this series are depicted in Figure 3.20. The solid line in Figure 3.20 indicates the actual phantom absorption spectrum computed from the “cuvette” spectrum of MnTPPS and the known MnTPPS concentration used in the phantom. The open circles indicate the absorption coefficients reconstructed from the reflectance data using the DT_{full} solution with $\rho_{min}=1.1$ mm and $\rho_{max}=3.75$ mm, which was the largest source-detector separation for which uncertainties in the reflectance data were less than approximately 10%. The solid squares indicate the absorption coefficients reconstructed from the P_3 solution with $\rho_{min}=0.43$ and $\rho_{max}=3.75$ mm. Similarly, in Figure 3.21, theoretical transport scattering spectra calculated from Mie theory (solid line), the transport scattering spectrum reconstructed using the DT_{full} solution (open circles) and P_3 solution (solid squares) are shown. Several interesting features are present. First, for absorption coefficients larger than approximately 0.1 mm^{-1} , the diffusion theory solution incorrectly inverts the shape and magnitude of the absorption and transport scattering spectra. This sharp transition in the magnitude and direction of error in the fitted optical properties in the diffusion theory solutions was illustrated in Section 3.2. It is evident here in the experimental data as well. Secondly, it can be seen that the absorption coefficients reconstructed from the P_3 solution are systematically low for $\lambda > 580$ nm, and are systematically high for $\lambda < 580$ nm. These errors are inverted in the scattering spectrum, where μ_s' is systematically high for $\lambda > 580$ nm and systematically low for $\lambda < 580$ nm. It is suspected that these deviations are again due to the approximate

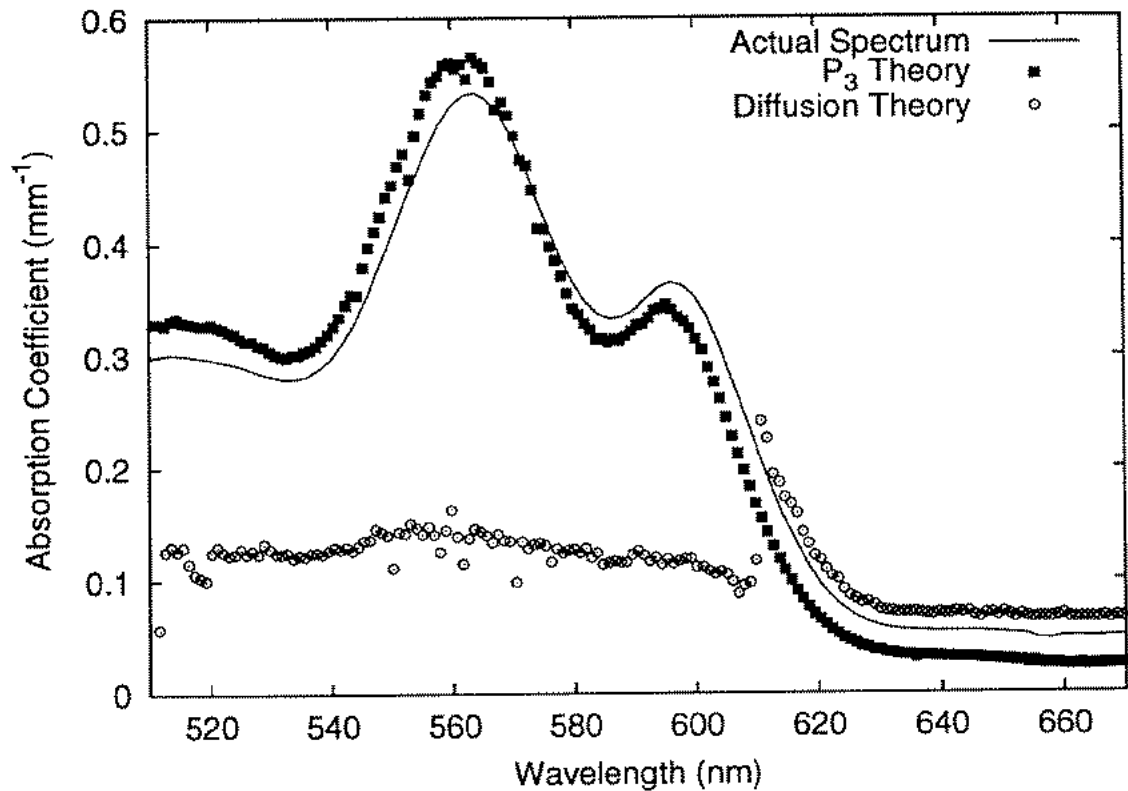


Figure 3.20 Absorption spectra reconstructed from a reflectance data collected from a phantom of MnTPPS in an aqueous suspension of 0.511 μm diameter polystyrene spheres. The solid line is the actual phantom absorption spectrum, computed from the “cuvette” spectrum of MnTPPS and the known MnTPPS concentration. The open circles are result from fitting the DT_{full} solution with $\rho_{\text{min}} = 0.432$ mm and $\rho_{\text{max}} = 3.75$ mm. The solid squares results from fitting the P_3 solution with identical values of ρ_{min} and ρ_{max} .

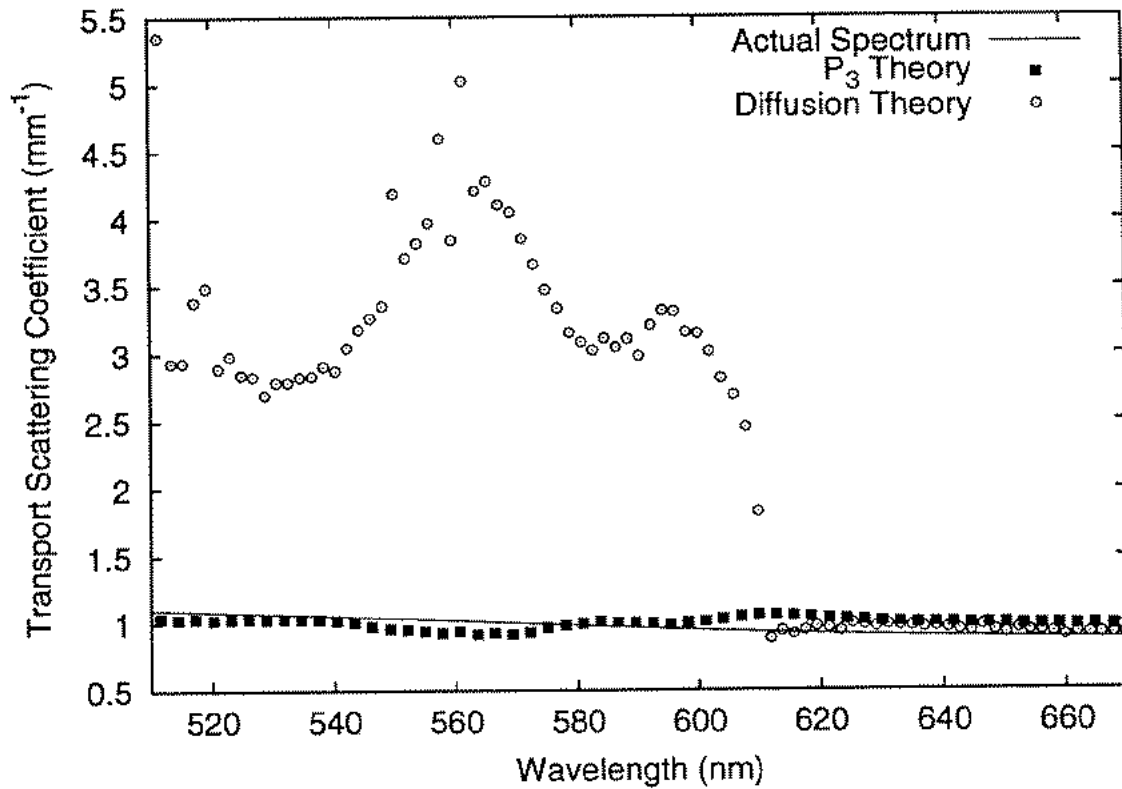


Figure 3.21 The theoretical transport scattering spectrum calculated from Mie theory (solid line) for the phantom described in Figure 3.20. The open circles are the transport scattering coefficients reconstructed using the DT_{full} solution and the solid squares are the transport scattering coefficients reconstructed using the P_3 solution.

nature of the P_3 fitting function implemented in this chapter, since we have observed this “crosstalk” between scattering and absorption coefficients in the past when the diffusion theory fitting function was not completely correct. A thorough evaluation of the full P_3 solution will be the subject of future investigations. It is also possible that these deviations result from inaccuracies in the values assigned to γ and δ . For the fits described here, $\gamma=1.85$ and $\delta=2.6$ were assumed; these values have been optimized for the Henyey-Greenstein phase function.

A summary of concentrations resulting from fits of the MnTPPS “cuvette” spectrum to absorption spectra reconstructed from reflectance measurements in this series of experiments is presented in Figure 3.22. The line indicates the actual MnTPPS concentration, the solid squares are the concentrations resulting from fits to absorption spectra reconstructed with P_3 theory, and the open circles are the concentrations resulting from fits to absorption spectra reconstructed with diffusion theory. The actual concentrations ranged from 4.2 – 251.0 mM, which correspond to maximum absorption coefficients of 0.01 – 0.65 mm^{-1} . For concentrations ≤ 10 mM, both theories gave concentrations in error by more than 15%. This is because the largest source-detector separation in the P_3 reflectance probe is ~ 9 mm, which is too small a source-detector separation to sufficiently resolve the small absorption coefficients present in these samples. For concentrations larger than 10 mM, the fitted P_3 concentrations are accurate to $\pm 11\%$, while the diffusion solution significantly underestimates ($5 \text{ mM} \leq [\text{MnTPPS}_{\text{actual}}] \leq 35 \text{ mM}$) or overestimates ($70 \text{ mM} \leq [\text{MnTPPS}_{\text{actual}}] \leq 115 \text{ mM}$) the concentration. For concentrations larger than 200 mM, which correspond to maximum absorption coefficients larger than 0.5 mm^{-1} , the P_3 solution is the only trustworthy estimator of the MnTPPS concentration, since the

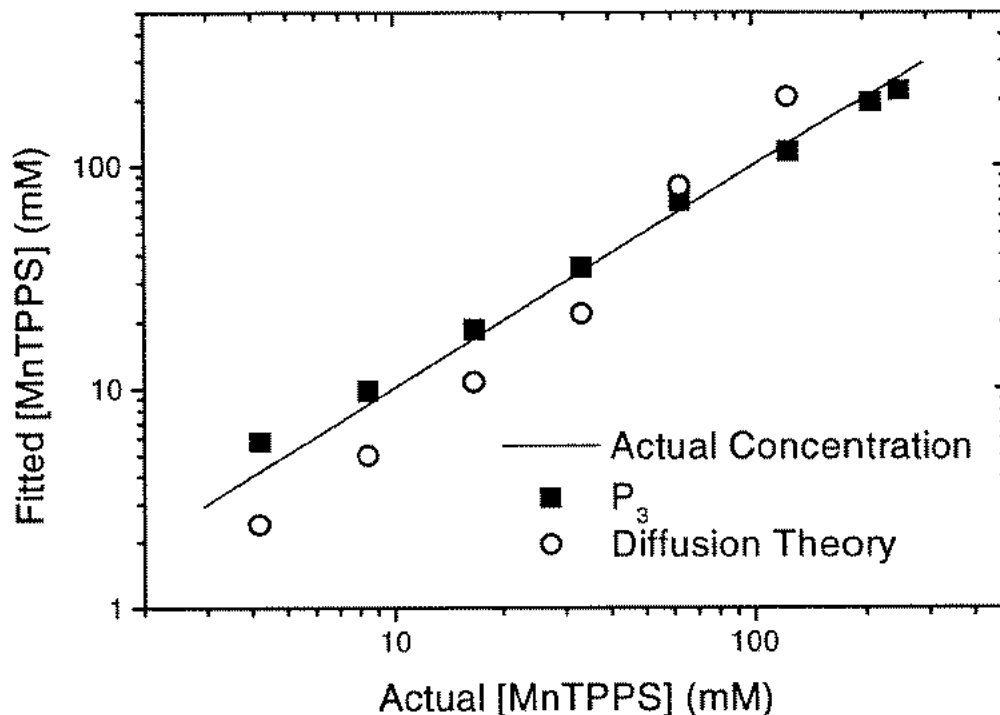


Figure 3.22 Concentrations resulting from fits of the MnTPPS “cuvette” spectrum to absorption spectra reconstructed from reflectance measurements of a phantom comprised of an aqueous suspension of polystyrene spheres and various concentrations of MnTPPS. The line indicates the actual MnTPPS concentration, the solid squares are the concentrations resulting from fits to absorption spectra reconstructed with P_3 theory, and the open circles are the concentrations resulting from fits to absorption spectra reconstructed with diffusion theory. The maximum absorption coefficient of the phantoms ranged from 0.01 mm^{-1} ($[\text{MnTPPS}] = 4.3 \text{ mM}$) to 0.6 mm^{-1} ($[\text{MnTPPS}] = 256.8 \text{ mM}$). There are no diffusion theory data points for the two largest concentrations because the diffusion theory spectra failed in the manner illustrated in Figures 3.20 and 3.21.

diffusion theory analysis fails in the catastrophic manner depicted in Figures 3.20 and 3.21.

3.5 Summary

The validation experiments described in this chapter have demonstrated that the DT_{full} solution is capable of reconstructing absorption and transport scattering coefficients of turbid media with accuracies of 10% or better when the transport albedo is greater than approximately 0.98. With the exception of the case of an index-matched boundary, the DT_{flux} solution has been shown to generate optical coefficients which are inaccurate and sensitive to the exact value of ρ_{min} . However, if the condition of an index-matched interface is assumed, the DT_{flux} solution can serve as an accurate indicator of changes in the absorption coefficient, again provided the transport albedo is greater than 0.98. In the case of small albedos, both diffusion theory solutions fail to yield accurate optical properties. The P_3 solution, however, returned fitted absorption and transport scattering coefficients which are accurate to $\pm 10\%$ for albedos as small as 0.59.

The sensitivity of the P_3 solution to the precise value of γ and δ is an issue which must be explored further. A more detailed investigation of the effects of the finite diameters and numerical apertures of the delivery and detection fiber optics on the reconstructed optical properties would also be interesting and potentially useful.

References

1. L.H. Wang, S.L. Jacques, and L. Zheng, "MCML - Monte Carlo modeling of light transport in multilayered tissues," *Comp. Meth. Prog. Biomed.* **47**, 131-146 (1995).
2. B.C. Wilson, T.J. Farrell, and M.S. Patterson, "An optical fiber-based diffuse reflectance spectrometer for non-invasive investigation of photodynamic sensitizers in vivo.," in *Future Directions and Applications in Photodynamic Therapy*, C. J. Gomer, ed., SPIE Institute Series, **IS6**, 219-232 (1990).
3. H.L. Liu, D.A. Boas, Y.T. Zhang, A.G. Yodh, and B. Chance, "Determination of optical properties and blood oxygenation in tissue using continuous NIR light," *Phys. Med. Biol.* **40**, 1983-1993 (1995).
4. P.R. Bevington, *Data Reduction and Error Analysis for the Physical Sciences* (McGraw-Hill, New York, 1996), Chapter 4.
5. W.H. Press, S.A. Teukolsky, W.T. Vetterling, and B.P. Flannery, *Numerical Recipes in C: The Art of Scientific Computing* (Cambridge University Press, Cambridge, UK, 1992), pp. 683-687.
6. A.J. Welch and M.J.C. van Gemert, *Optical-Thermal Response of Laser-Irradiated Tissue* (Plenum Press, New York, 1995), pp. 275-303.
7. L.H. Kou, D. Labrie, and P. Chylek, "Refractive indexes of water and ice in the 0.65 μm to 2.5 μm spectral range," *Appl. Opt.* **32**, 3531-3540 (1993).

CHAPTER 4

Quantitative Near-infrared Spectroscopy of Tissue-Simulating Phantoms Containing Erythrocytes and Mitochondria

4.1 Introduction

In vivo near infrared spectroscopy (NIRS) has attracted sustained interest as a technique for noninvasive monitoring of quantities such as oxyhemoglobin (HbO_2) and deoxyhemoglobin (Hb) concentration, hemoglobin oxygen saturation (SO_2), and the concentrations or redox states of other chromophores with appreciable NIR extinction, particularly water and cytochrome c oxidase [1-3]. As the field has evolved, various schemes have been developed and refined to analyze NIR reflectance or transmission data to correct for the effects of scatter. For example, optical diffusion theory may be employed to directly determine tissue transport scattering and absorption coefficients from time-resolved measurements of the remitted portion of a short (~ 1 ps) laser pulse [4-6]. These time-domain spectroscopic techniques have found wide applicability in laboratory research settings [7,8], and significant efforts are currently being directed toward development of time-resolved instruments for low-resolution tomographic imaging of intrinsic and exogenously administered sources of optical contrast. Despite the utility of time-domain methods, the technology involved is the most expensive of the

NIRS techniques and is perhaps the least easily adapted for routine clinical use.

Similarly, diffusion theory may be utilized to determine μ_a and μ_s' from phase and amplitude measurements of the reflectance originating from an incident intensity-modulated beam [9,10]. These frequency-domain techniques have also been widely used for *in vivo* spectroscopy [2,11,12], and commercial instruments for bedside monitoring are presently available. Present implementations of time- and frequency-domain measurements suffer, however, from the limitation of exploiting only a small number (2-6) of laser diodes, yielding at most 6 absorption coefficients from which to extract the desired chromophore concentrations. Typical instruments employ 4 discrete wavelengths, in principle allowing determination of HbO₂, Hb, water, and cytochrome c oxidase concentrations. Such a completely determined calculation is sufficient for monitoring of these species in the case of an ideal measurement, but in cases where data have a signal-to-noise ratio which precludes accurate quantitation of weakly absorbing species or are contaminated by the presence of other chromophores, a completely constrained system is of less value.

Continuous-wave transmission measurements such as those first used by Jöbsis and more recently refined by Delpy, Chance, and others, have traditionally functioned primarily as trend indicators because of the inability of these techniques to properly separate the effects of absorption and scattering in the attenuation measurement. Such continuous wave techniques can be used to quantitatively monitor μ_a provided the scattering spectrum is known *a priori*. In these cases, changes in the absorption coefficient are typically calculated using a modification of the Beer-Lambert law in which a differential pathlength factor (dpf) is introduced to account for the increased effective optical pathlength in tissue due to scattering [13]. Substantial effort has been directed toward time- and frequency-domain measurement of these correction factors

for various tissue types, particularly the adult and neonatal brain [14,15]. The low cost and ease of use of these continuous wave techniques has led to the development of a number of laser-diode based instruments which are now commercially available (e.g. NIRO 500®, Hamamatsu Photonics, Hamamatsu City, Japan; and Invos 3100®, Somanetics, Inc., Troy, MI, USA). The differential pathlength factors employed in the algorithms used by these instruments must be applied judiciously, however, since the tissue scattering coefficient is subject to patient-to-patient variability based on changes in such factors as temperature, water concentration, and glucose concentration [16-18]. More importantly, the dpf is also a nonlinear function of the absorption coefficient [3], a fact which can potentially lead to significant error in μ_a in cases of large changes in tissue blood volume or water content which may occur with hemorrhage or edema, respectively [19]. Clinicians have begun to publish studies in which these instruments are used [20-22], and in some cases, these studies closely approach the above limitations.

An ideal *in vivo* NIR spectroscopy instrument would utilize relatively straightforward and inexpensive technology to allow rapid measurement of tissue absorption and scattering spectra over a broad wavelength range, thus allowing the use of multivariate analysis techniques to more accurately ascertain the exact concentrations and species of contributing chromophores. This is of particular importance in situations where other hemoglobin species such as ferric hemoglobin, carboxyhemoglobin, or fetal hemoglobin may be present [23,24]. Broadband data would also be useful in instances where the chromophores contributing to the non-hemoglobin background spectrum are not known *a priori*, such as testing for the presence of exogenously administered photosensitizers [25,26].

Chapter 3 described the design and implementation of a steady-state, white-

light diffuse reflectance spectrometer for the determination of absorption and transport scattering spectra of highly scattering media in a tunable 164 nm spectral window. It was demonstrated that, using optical diffusion theory, both the scattering and absorption spectra of optically turbid media could be measured to 10% accuracy provided an appropriate range of source-detector separations (~ 1 -20 mm) was employed and the transport albedo was sufficiently large (≥ 0.983). In this chapter, steady-state diffuse reflectance spectroscopy (SSDRS) is used to measure the NIR absorption spectrum of tissue-simulating phantoms containing intact human red blood cells at various oxygen partial pressures (pO_2). These spectra are fitted with either a nonlinear least squares or a singular value decomposition (SVD) fitting algorithm to determine SO_2 . The accuracy of these SO_2 values is assessed by comparing the estimated saturations with those predicted by published parameters describing the hemoglobin oxygen dissociation curve for the experimental temperature and pH [33]. In addition, the ability of the SVD algorithm to reconstruct the low-level background absorption spectrum not originating from hemoglobin or water without *a priori* assumptions regarding its spectral features or absolute magnitude is investigated. This technique is used to reconstruct the absorption spectrum of a combination of weakly absorbing chromophores added to a scattering phantom containing red cells.

In many tissues, the most significant contributors to this non-hemoglobin absorbing background are mitochondrial cytochromes. The final section of this chapter presents preliminary measurements of phantoms containing erythrocytes and mitochondria. In the visible region of the spectrum, it is demonstrated that it is possible to reconstruct the absorption spectrum and oxidation status of mitochondrial cytochromes in the presence of physiologically relevant concentrations of hemoglobin.

4.2 Materials and Methods

4.2.1 Phantom Preparation

The tissue-simulating phantoms utilized in these studies were used to validate the absorption and transport scattering spectra obtained from diffuse reflectance measurements in the near-infrared (~650-950 nm) spectral region. In these phantoms, 0.519 μm diameter polystyrene latex microspheres (Duke Scientific, Palo Alto, CA, USA) were added to 0.9% saline buffered to pH=7.4 with 0.05 M Trizma (Sigma, St. Louis, MO, USA) to achieve a number density of 2.8×10^{10} spheres/ml. The transport scattering coefficient of the resulting suspension (calculated by Mie theory) ranged from $\sim 1.1 \text{ mm}^{-1}$ ($\lambda=650 \text{ nm}$) to $\sim 0.8 \text{ mm}^{-1}$ ($\lambda=950 \text{ nm}$). This scattering solution was placed in a cylindrical beaker 80 mm in diameter, resulting in a phantom depth of approximately 75 mm. Intact human erythrocytes were subsequently added to this scattering solution.

Red blood cells were prepared from blood drawn from healthy, non-smoking volunteers. The whole blood was washed with isotonic saline and centrifuged (2000 g), after which the supernatant was decanted. This process was repeated until the supernatant was clear (~3 times). Red cells were then added to each phantom to achieve a volume fraction of 1.6%, typical of physiologic conditions assuming a 4.0% blood volume and 40% hematocrit. In one case, a small concentration ($1.9 \times 10^{-3} \mu\text{l ml}^{-1}$) of India ink (Eberhard Faber, Inc., Lewisberg, TN, USA) was added to the phantom prior to the addition of red blood cells. The phantoms were deoxygenated by the addition of a trace amount (~1 cc) of dry bakers' yeast, allowing the phantom to gradually deoxygenate over a period of approximately 20-30 minutes. During the deoxygenation process, the phantom temperature was regulated to $37.0 \pm 0.5^\circ \text{C}$.

The oxygen partial pressure in the hemoglobin phantoms was continuously monitored with an oxygen-sensitive electrode (Microelectrodes, Inc., Londonderry, NH, USA). At the beginning of a given experiment, the electrode was calibrated in an air-saturated sample of the scattering phantom and in a sample of the phantom deoxygenated with $\text{Na}_2\text{S}_2\text{O}_4$. Oxygen partial pressure was then determined from the electrode current assuming a linear response. The calibration procedure was repeated at the end of an experiment as well to help control for electrode drift. During the experiment the electrode was placed approximately 5 mm below the surface of the phantom near the wall of the beaker to avoid interference with the diffuse reflectance measurement. The mixture was continuously stirred to minimize oxygen concentration gradients. There was no measurable change in pO_2 as a function of depth in the phantom.

4.2.2 Spectral Analysis Techniques

The broadband nature of the spectra recovered from our SSDRS measurement allows for a number of different multivariate analysis techniques, including conventional least-squares methods, principal component analysis, second derivative analysis, and others. In this work, we have analyzed our spectra using nonlinear least squares and singular value decomposition algorithms to extract estimates of the concentrations of various contributing chromophores. Both fitting algorithms were adapted from Press *et al.* [27].

4.2.2.1 Least squares fitting

In the case of least squares fitting, a linear combination of several known absorption spectra was fit to the phantom absorption spectrum reconstructed from SSDRS measurements in order to extract the concentrations of the various component species

as fitting parameters. A function of the form

$$\mu_a(\lambda) = [HbO_2]\epsilon(\lambda)_{HbO_2} + [Hb]\epsilon(\lambda)_{Hb} + [H_2O]\epsilon(\lambda)_{H_2O} \quad (4.1)$$

was fitted to the total SSDR absorption spectrum, $\mu_a(\lambda)$. In Equation 4.1, the quantities in square brackets are concentrations of oxy- and deoxyhemoglobin and water, and $\epsilon(\lambda)$ represents the molar extinction coefficients of these species at wavelength λ . Because the absorption spectrum of polystyrene is negligible in this wavelength region, the absorption spectrum of the scattering phantom alone is essentially that of water, which comprises more than 99.9% of the phantom volume.

Since the absorption spectrum of the scattering phantom may be measured prior to the introduction of additional chromophores, it is also possible to subtract this background spectrum prior to least-squares analysis. This is desirable, because the yeast adds a small but not negligible contribution to the background spectrum. In this case, the water contribution to Equation 4.1 is omitted from the fit. It should be emphasized that subtraction of the measured background is used only for validation of the reconstructed absorption spectrum and is not a necessary aspect of the analysis.

4.2.2.2 Singular value decomposition

A thorough development of SVD is beyond the scope of this discussion. Press *et al.* [27] and Hull and Foster [28] provide introductory discussions and references to more detailed treatments of this subject. In brief, SVD provides the best least-squares fit of a linear combination of basis spectra to a set of data while simultaneously minimizing ambiguous combinations of basis spectra which do not significantly contribute to the reduction of the χ^2 goodness-of-fit statistic. This is accomplished by a matrix inversion technique which eliminates the smallest “singular values” of the design matrix, the columns of which are proportional to the basis spectra. As illustrated in the uppermost

spectrum of Figure 4.8, the rms noise in absorption coefficients reconstructed from SSDRS measurements of phantoms containing hemoglobin is typically on the order of 2.5%. Thus, in the fits described here, singular values less than $0.025 S_{\max}$ are eliminated, where S_{\max} is the largest singular value of the design matrix. Because it is not generally possible to have *a priori* information regarding the exact magnitude and shape of the background absorption spectrum, we use SVD to fit the 164 nm SSDR absorption spectrum to a function of the form

$$\mu_a(\lambda) = \epsilon_{Hb}(\lambda)[Hb] + \epsilon_{HbO_2}(\lambda)[HbO_2] + \epsilon_{H_2O}(\lambda)[H_2O] + A_0 + \sum_{n=1}^m \left[B_n \cos\left(\frac{n\pi(\lambda-\lambda_i)}{\lambda_f-\lambda_i}\right) + C_n \sin\left(\frac{n\pi(\lambda-\lambda_i)}{\lambda_f-\lambda_i}\right) \right], \quad (4.2)$$

where the top line is identical to Equation 4.1, and the bottom line is an expansion of the absorption background not originating from hemoglobin or water as a linear superposition of sines and cosines. Here, m is the number of cosine and sine terms included in the expansion, A_0 , B_n , and C_n are the expansion coefficients, and λ_f and λ_i are the final and initial wavelengths in the data set.

Since oxy- and deoxyhemoglobin and water are presumed to be the dominant phantom chromophores in the near-infrared, the amplitudes of these basis spectra are weighted by a factor of 15 relative to the individual sine and cosine terms. These weighting factors are motivated by the fact that, in the spectral region of interest, the magnitude of absorption due to hemoglobin is roughly two times that of water and 30 times that originating from background chromophores. While the success of the algorithm depends on hemoglobin and water being appropriately weighted relative to the Fourier components, it is our experience that good results can be obtained if the exact values of the weighting factors deviate as much as 20% from those stated here. The algorithm can be made more robust by performing a preliminary two-component

least squares fit (*i.e.*, fitting a simple sum of the absorption spectra of oxy- and deoxyhemoglobin) to the full SSDRS absorption spectrum in order to obtain a crude initial estimate of SO_2 . This initial SO_2 estimate may then be used to more appropriately divide the total hemoglobin weighting factor (30) among the oxy- and deoxyhemoglobin contributions. In this case, the oxyhemoglobin weighting factor is $30 \cdot SO_2$ and the deoxyhemoglobin weighting factor is $30 \cdot (1-SO_2)$.

4.2.2.3 Computation and verification of hemoglobin oxygen saturation

After the phantom Hb and HbO₂ concentrations are determined from either of the above analysis techniques, it is straightforward to calculate SO_2 *via*

$$SO_2 = \frac{[HbO_2]}{[Hb] + [HbO_2]} \quad (4.3)$$

It is well known that the hemoglobin oxygen dissociation curve is sigmoidal in shape and may be expressed mathematically as

$$SO_2 = \frac{pO_2^n}{p_{50}^n + pO_2^n} \quad (4.4)$$

where pO_2 is the oxygen partial pressure, p_{50} is the oxygen partial pressure at which hemoglobin is 50% saturated, and n is a dimensionless parameter known as the Hill coefficient. By fitting Equation 4.4 to SO_2 values determined from SSDR spectra, n and p_{50} may be extracted as fitting parameters. These fitted values may then be compared to literature values for n and p_{50} for hemoglobin in the native chemical environment of the red cell and at the temperature and pH corresponding to experimental conditions. In this way, the validity of the SO_2 estimates determined from SSDRS data may be assessed.

4.3 Results and Discussion

4.3.1 Hemoglobin Reference Spectra

Accurate Hb and HbO₂ reference spectra are essential for quantitatively accurate assessment of SO₂ from *in vivo* NIRS measurements. Several NIR hemoglobin absorption spectra have been published in recent years, most notably those of Wray *et al.* [29] and Cope [30]. The Cope data are also tabularized by Matcher *et al.* [31]. In both of these reports, the hemoglobin was prepared from lysed red cells. It is possible that organic phosphates present in relatively high concentrations in the red cell may alter the hemoglobin absorption spectrum. It is also possible that chromophores other than hemoglobin present in red cells may contribute weakly to the cells' NIR absorption spectrum. For these reasons, we first compared our SSDR absorption spectra to those of Wray *et al.* and of Cope.

In Figure 4.1, reconstructed SSDR absorption spectra in the 650-950 nm spectral region are presented. The measured background absorption spectrum of the polystyrene sphere phantom (in the oxygenated case) or the polystyrene sphere+yeast phantom (in the deoxygenated case) has been subtracted from these data, and the spectra have been smoothed and the error bars assigned in the same manner described in Section 3.4. The solid lines in Figure 4.1 represent the best fit of the spectra of Cope to these data. The dashed line in Figure 4.1 represents the best fit of the oxyhemoglobin spectrum of Wray *et al.* to the SSDR spectrum corresponding to the oxygenated case. The inset is a magnification of the region near the isosbestic point of the two spectra, reported to be 798 nm by Wray *et al.* and Cope. It can be seen that while the SSDR spectrum for the deoxygenated case is in very good agreement with the results of Cope, the SSDR spectrum for the oxygenated case deviates from Cope's

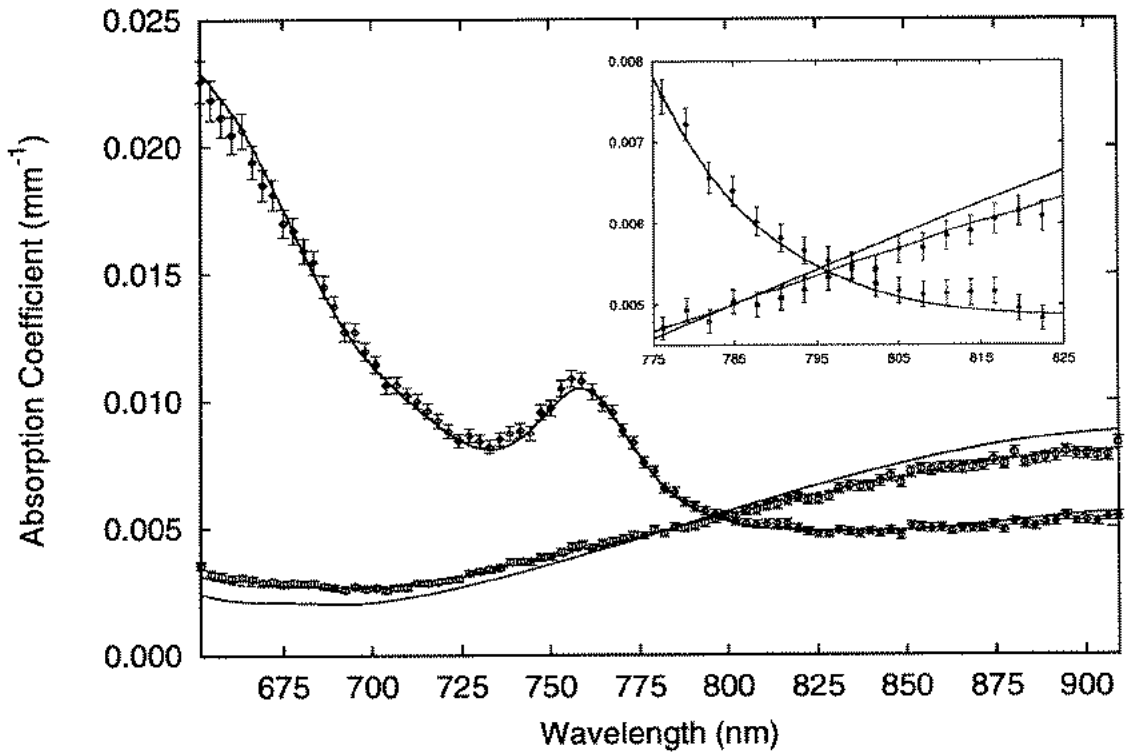


Figure 4.1 Absorption coefficients reconstructed from SSDRS measurements (data points) of a phantom comprised of polystyrene spheres and intact red blood cells. The volume fraction of red cells was 0.7%. The data have been smoothed and the error bars assigned as described in Section 3.4. Two cases are illustrated: air-saturated oxygen conditions (circles) and after full deoxygenation by addition of ~1 cc dry bakers' yeast (diamonds). The solid lines are the best fits of the oxy- and deoxyhemoglobin spectra of Cope (ref. [30]) to these data. The dashed line is the best fit of the oxyhemoglobin spectrum of Wray *et al.* (ref. [29]) to the SSDR absorption coefficients. The inset is a magnification of the region near the isosbestic point of the two spectra (reported to be 798 nm by both Cope and Wray *et al.*)

results but is in nearly exact agreement with the oxyhemoglobin spectrum of Wray *et al.* The deoxyhemoglobin spectrum of Wray *et al.* is nearly indistinguishable from that of Cope and is therefore not included in Figure 4.1. For this reason, in the following analysis where fits to SSDRS data are performed, we use the oxyhemoglobin spectrum of Wray *et al.* and the deoxyhemoglobin spectrum of Cope. It seems unlikely that a NIR absorbing chromophore is present in the red cell which would contribute an oxygen-dependent absorption spectrum having a magnitude comparable to the deviations shown in Figure 4.1, particularly since hemoglobin is known to comprise 92% of red cell solids [32]. Therefore, in the following discussion, we assume that the SSDR spectra in Figure 4.1 represent those of oxyhemoglobin and deoxyhemoglobin in the chemical environment of the red cell.

4.3.2 Spectroscopy of Erythrocytes; Verification of Reported Saturations

Figure 4.2 presents the results of several SSDRS measurements of a polystyrene spheres+red cell phantom which was deoxygenated by addition of yeast. The phantom was continuously deoxygenated over a period of ~20-30 minutes, and SSDR data were acquired as frequently as every 20 seconds. In these spectra, the measured background absorption spectrum of the spheres+yeast suspension has been subtracted from the SSDRS data. The bottommost spectrum corresponds to an oxygen partial pressure of 95 torr, and the uppermost spectrum corresponds to an oxygen partial pressure of 0.0 torr. The spectra reflect a well-defined isosbestic point near 800 nm, and excellent fits to the data are possible throughout the entire range of oxygen partial pressures. In Figure 4.3, the oxyhemoglobin, deoxyhemoglobin, and total hemoglobin concentrations reported by least-squares fits to the background-subtracted data are plotted as a function of the measured oxygen partial pressure in the phantom. Note that the total

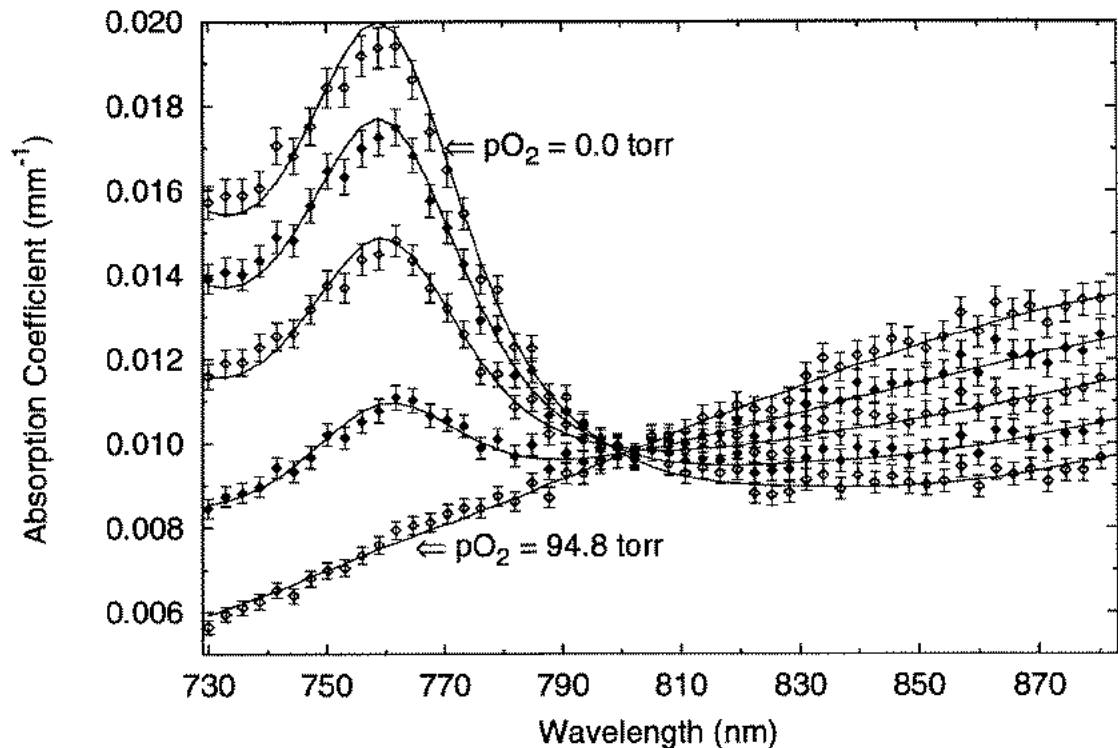


Figure 4.2 Background-corrected absorption spectra of a polystyrene sphere+red cell phantom in the 730-880 nm wavelength range. The volume fraction of red cells was 1.6%. The data have been averaged and the error bars assigned as described in Section 3.4. The phantom was deoxygenated by the addition of a small amount of dry bakers' yeast, and SSDRS data were collected throughout the deoxygenation process at intervals as frequent as every 20 seconds. Solid lines are best fits of a linear combination of the oxyhemoglobin absorption spectrum of Wray *et al.* (ref. [29]) and the deoxyhemoglobin spectrum of Cope (ref. [30]) to the SSDRS data.

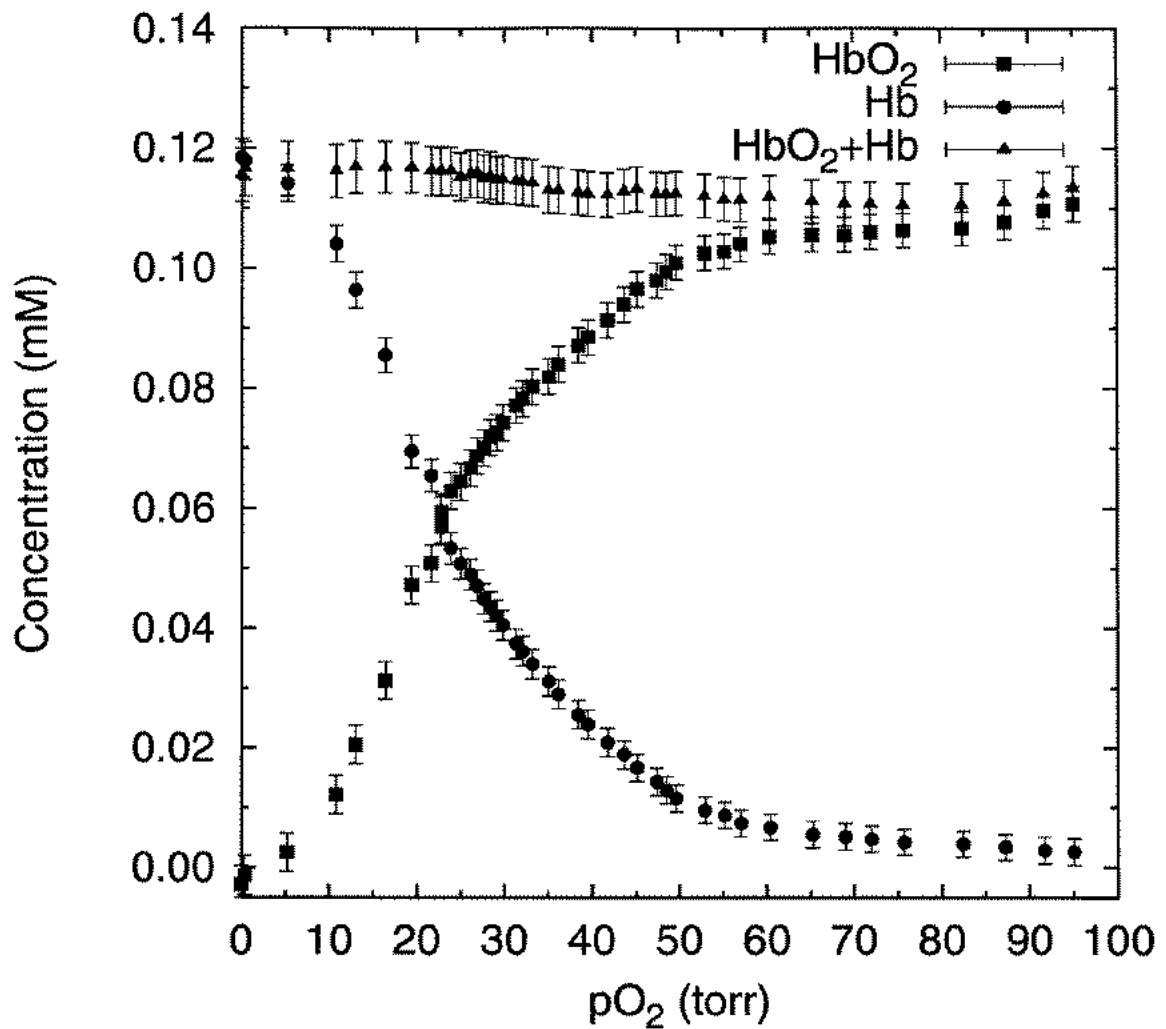


Figure 4.3 The concentrations of oxyhemoglobin (squares), deoxyhemoglobin (circles) and total hemoglobin (triangles) determined from the fits illustrated in Figure 4.2. The concentrations are plotted as a function of the oxygen partial pressure in the phantom, which was measured with an oxygen-sensitive electrode.

hemoglobin concentration remains constant to within $\pm 5\%$ over the full range of oxygen partial pressures.

In Figure 4.4 the concentrations indicated in Figure 4.3 are plotted as a function of the oxygen partial pressure in the phantom. The Hill parameters p_{50} and n were determined from these SO_2 values from a linear regression of $\log_{10}(SO_2/(1-SO_2))$ vs. $\log_{10}(pO_2)$ for all data points between $SO_2=20\%$ and $SO_2=80\%$, as described by Zwart *et al.* [33]. The results of this fit are $n=2.42\pm 0.05$, and $p_{50}=21.8\pm 0.9$ torr, in good agreement with the findings of Zwart *et al.* who reported $n=2.46\pm 0.05$ and $p_{50}=25.95\pm 1.43$ torr. The solid line in Figure 4.4 represents the oxygen dissociation curve which results from incorporating these parameters into Equation 4.4. Because the fits to the SSDR spectra are excellent and the Hill parameters agree well with literature values, this oxygen dissociation curve will serve as a reference for comparison to SO_2 values for spectra from this experiment computed with other algorithms.

The results of fitting Equation 4.1 to the SSDRS data without background subtraction are depicted in Figure 4.5, where the data points are the uncorrected values of μ_a reconstructed from SSDRS measurements. The data have been averaged and the error bars scaled as described above. The solid lines are the best fits of a linear combination of Hb, HbO₂, and water to these data. Note that incorporating the water spectrum into the fitting function allows excellent fits to the data over the full range of saturations. The oxygen dissociation curve resulting from these three-component fits to the SSDRS data is depicted in Figure 4.6. The fitted values of the Hill parameters for these data are $n=2.44\pm 0.05$ and $p_{50}=23.4\pm 1.0$ torr, and the solid line in Figure 4.6 results from substituting these values into Equation 4.4. The dashed line is the best fit line from Figure 4.4 reproduced for comparison. It can be seen that the oxygen dissociation curve obtained from this analysis is very similar to that obtained from a

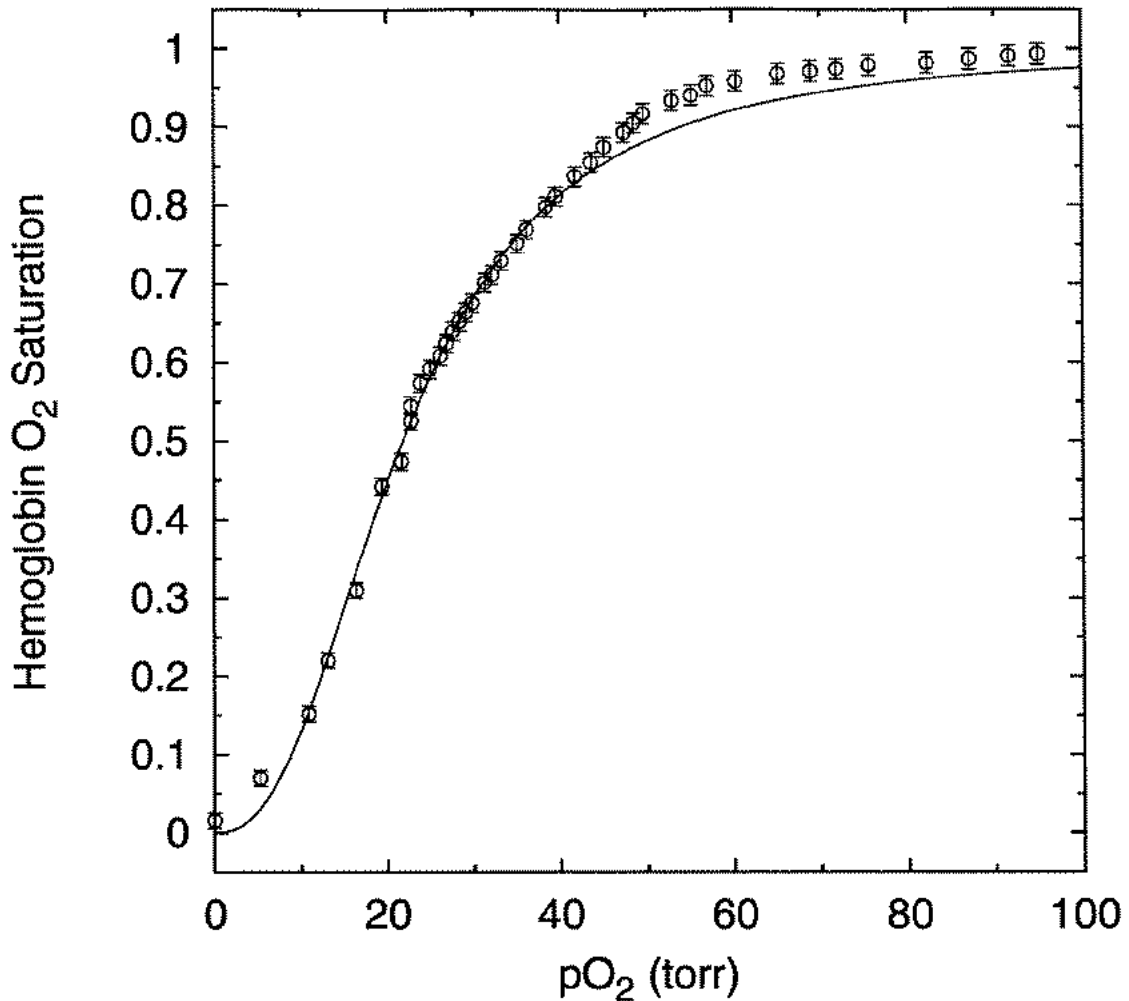


Figure 4.4 Hemoglobin oxygen saturations (determined from the concentrations in Figure 4.2) plotted as a function of oxygen partial pressure. This oxygen dissociation curve is characterized by the Hill coefficient (n) and p_{50} . Fitted values of these parameters were obtained from the slope and intercept returned by a linear regression of $\log_{10}(pO_2)$ vs. $\log_{10}(SO_2/(1-SO_2))$, using data points corresponding to saturations in the range of 20-80%. The fit returned values of $n=2.42\pm 0.05$ and $p_{50}=21.8\pm 0.9$ torr. The solid line is the dissociation curve which results from incorporating these parameters into Equation 4.4.

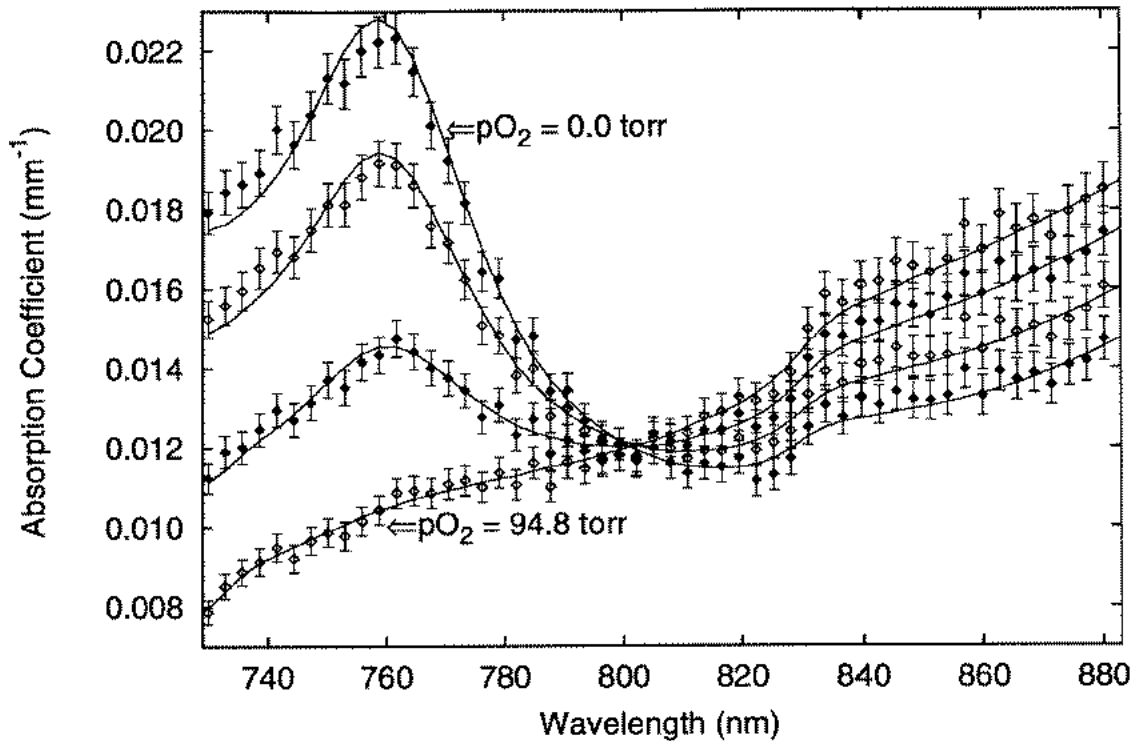


Figure 4.5 The same SDRS absorption spectra depicted in Figure 4.2 but without subtraction of the background absorption spectrum (essentially that of water). Solid lines are best fits of Equation 4.1 (including the contribution of water) to these data.

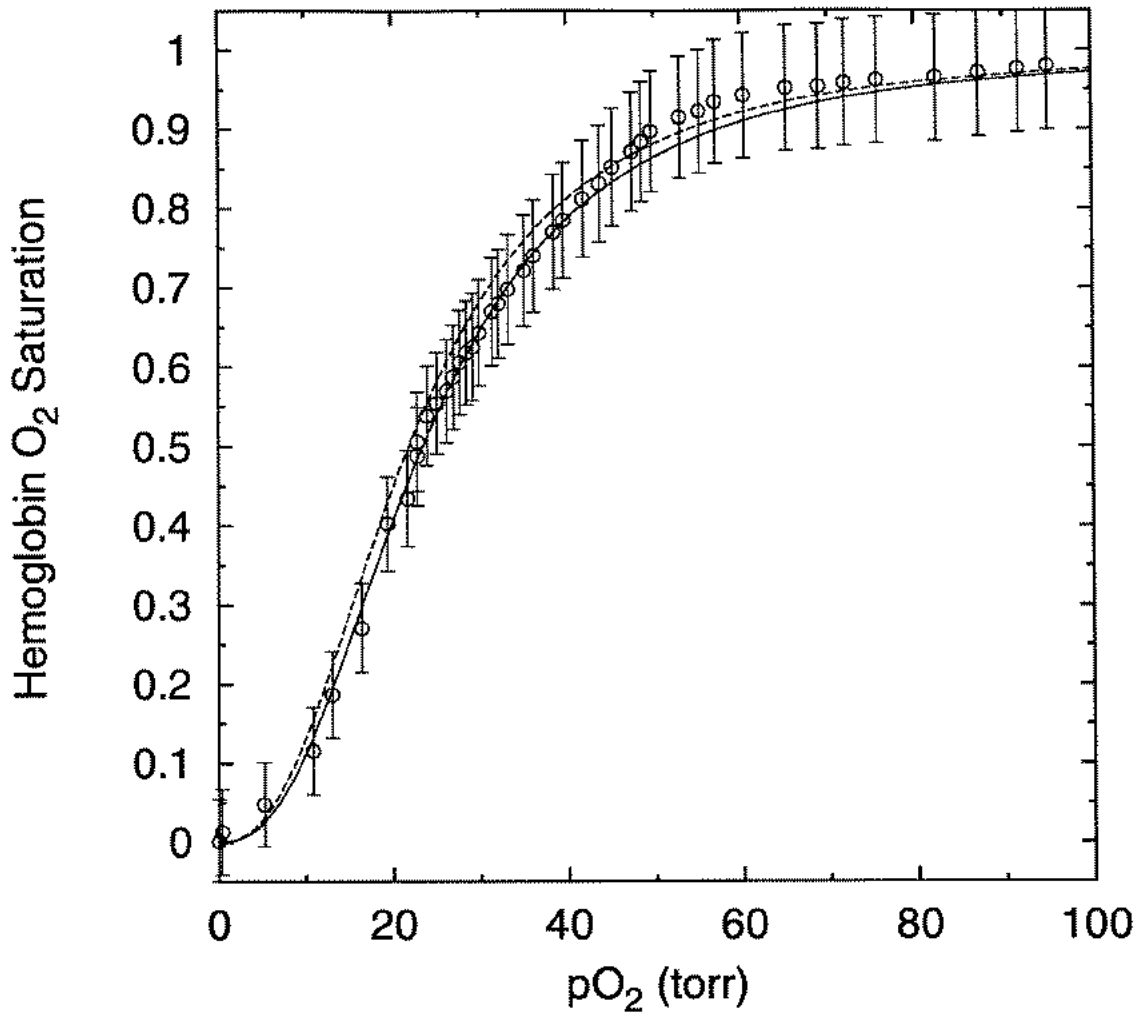


Figure 4.6 Hemoglobin oxygen saturations determined from fitted Hb and HbO₂ concentrations returned from the fits depicted in Figure 4.5 (fits which explicitly accounted for the absorption of water). Fitted values of the Hill coefficient (n) and p_{50} for these data were $n=2.44\pm 0.05$ and $p_{50}=23.4\pm 1.0$ torr. The solid line is the dissociation curve which results from incorporating these parameters into Equation 4.4. The dashed line is the dissociation curve from Figure 4.4. The fact that these lines are nearly identical is an indication that the effects of water absorption are being accounted for properly over the full range of oxygen saturations.

two-component fit to background-subtracted data, indicating that the algorithm is successfully determining the concentration of water in the phantom.

4.3.3 SVD Background Estimation

The SVD algorithm is useful for reconstructing spectra of chromophores whose contribution to the total absorption spectrum is small compared to more dominant chromophores such as hemoglobin and water in the near-infrared. In order to test the ability of SVD to reconstruct the non-hemoglobin background absorption spectrum, a spheres+red cell phantom was prepared as described above, but with a trace amount ($1.9 \times 10^{-3} \mu\text{l ml}^{-1}$) of India ink added to create an oxygen-independent “background” absorption. This background absorption spectrum is illustrated in Figure 4.7 where the data points are the SSDRS absorption coefficients after subtraction of the water spectrum. The shape and magnitude of this spectrum ($\mu_{a \text{ max}} \approx 0.0006 \text{ mm}^{-1}$) are suggestive of those which might be encountered with cytochrome c oxidase *in vivo*, assuming a concentration of 5 μM and an extinction coefficient of $3.0 \text{ mM}^{-1} \text{ cm}^{-1}$ at $\lambda=830 \text{ nm}$ in its oxidized form [34]. The phantom was then deoxygenated by addition of a small amount of dry bakers’ yeast. As the deoxygenation progressed, SSDR data were collected at approximately 40 different oxygen partial pressures ranging from ~100 torr to 0 torr.

Each reconstructed SSDR spectrum collected from this experiment was analyzed with Equation 4.2, using twenty Fourier components ($m=10$). This allows accurate modelling of background spectral features which are $\leq 17 \text{ nm}$ FWHM and excludes higher frequency noise in the SSDR spectrum from the modelled background spectrum. The hemoglobin weight factors used in the fit were derived from a preliminary saturation estimate obtained as described in the methods section. Figure 4.8 depicts

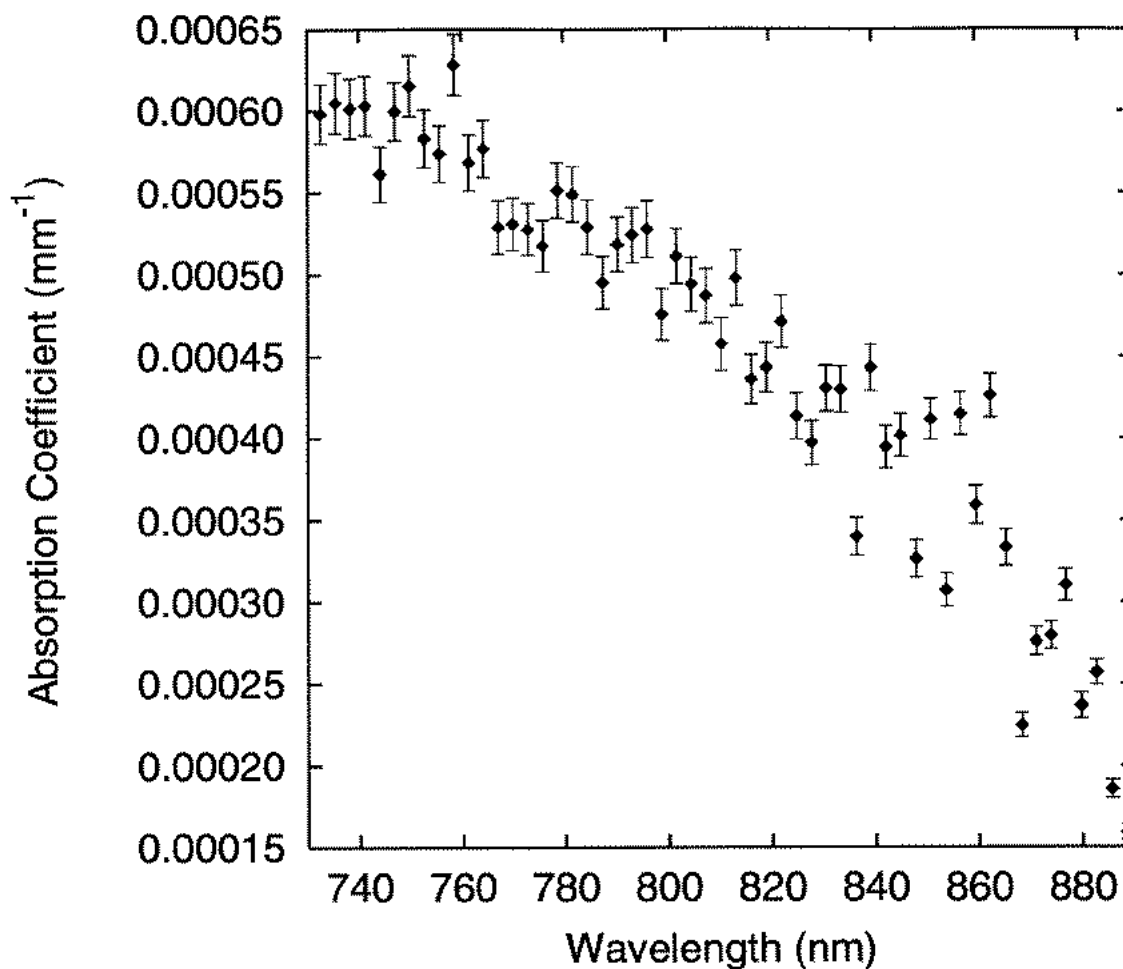


Figure 4.7 The absorption spectrum of a small amount of India ink added to a polystyrene sphere phantom. The ink provides an oxygen-independent “background” absorption spectrum having a shape and magnitude ($\mu_{a\max} \approx 0.0006 \text{ mm}^{-1}$) suggestive of those which might be encountered with cytochrome c oxidase *in vivo*.

the results of analyzing one of the intermediate spectra in this manner. In Figure 4.8, the noisy solid lines represent spectra reconstructed directly from SSDRS measurements, and the smooth dashed lines represent SVD estimates of the spectra of various contributing chromophores. The uppermost solid (dashed) lines in Figure 4.8 represent the measured (fitted) absorption spectrum of the phantom, including contributions from water, hemoglobin, and ink. The second noisy line from the top depicts the hemoglobin contribution to the phantom absorption spectrum, *i.e.*, the spectrum remaining after subtraction of the contributions of water and India ink, measured prior to the introduction of red cells. The corresponding dashed line indicates the SVD estimate of the oxy- and deoxyhemoglobin contributions to the measured spectrum, *i.e.*, the first two terms of Equation 4.2. The third noisy line from the top of Figure 4.8 represents the measured absorption spectrum of the phantom prior to the introduction of ink or red cells, which is essentially the absorption spectrum of water. The corresponding dashed line is the SVD estimate of the water contribution to the full absorption spectrum, *i.e.*, the third term of Equation 4.2. The bottommost noisy line indicates the absorption originating from ink, *i.e.*, the data depicted in Figure 4.7, and the corresponding dashed line represents the SVD estimate of the background absorption spectrum, *i.e.*, the bottom line of Equation 4.2. We observe that the approximate shape and magnitude of the background spectrum is reproduced in spite of the fact that no information was supplied to the algorithm regarding its amplitude or spectral features.

Figure 4.9 depicts the oxygen saturations (open squares) computed from the concentrations returned by the SVD analysis as a function of the oxygen partial pressure in the phantom. Fitting the Hill equation to these data in the manner described in section 4.3.2 returned values of $n=2.85\pm 0.03$ and $p_{50}=25.1\pm 0.5$ torr. The

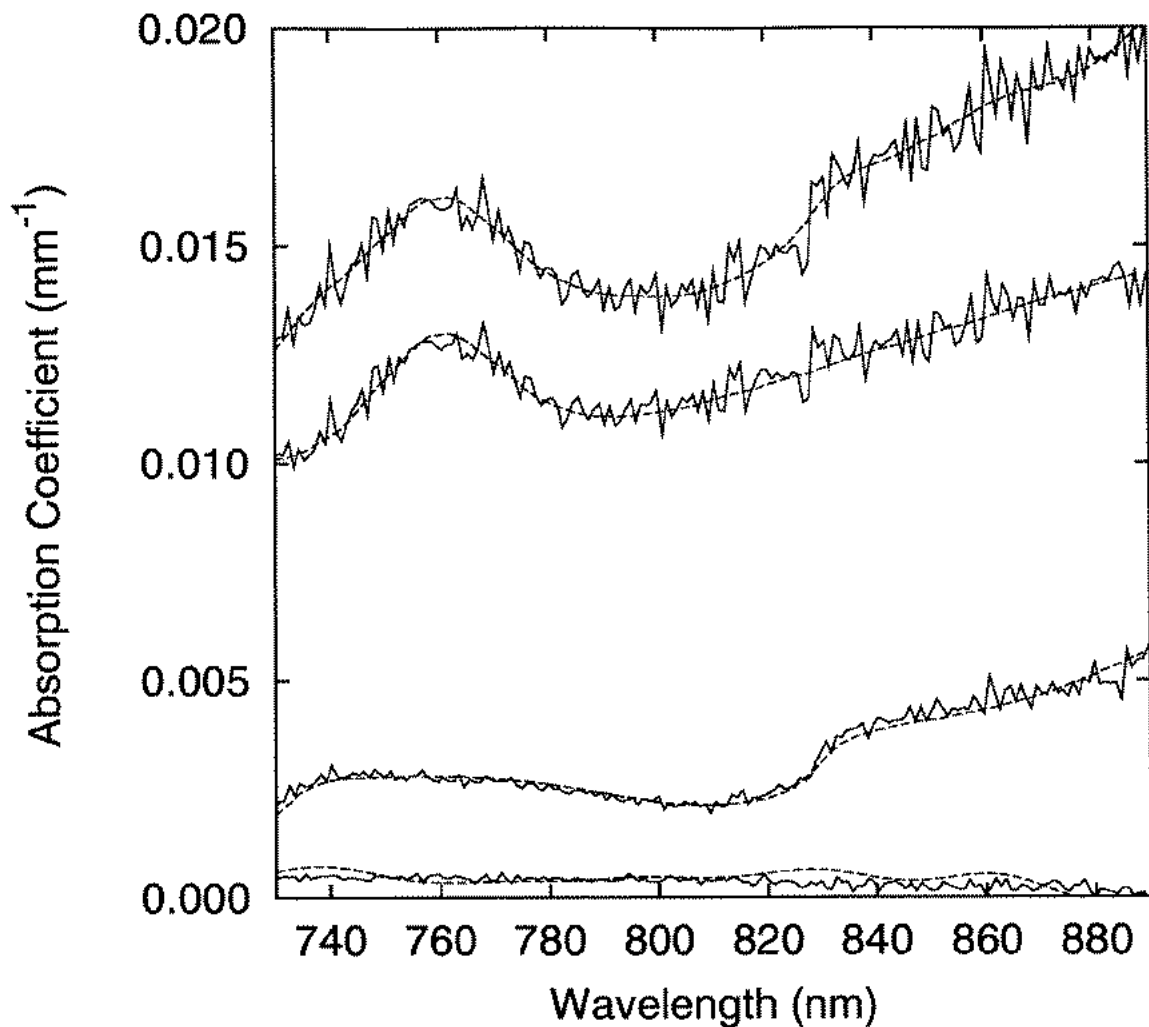


Figure 4.8 The SVD analysis of a single SSDR absorption spectrum from a polystyrene sphere phantom containing red cells and a small amount of India ink. The oxygen partial pressure was approximately 25 torr. The noisy solid lines represent spectra reconstructed directly from SSDRS measurements, and the smooth dashed lines represent SVD estimates of the spectra of various contributing chromophores. Refer to the text for a complete description of each contributing spectral component.

dashed line indicates the oxygen dissociation curve calculated from these parameters. For comparison, the saturations determined by least squares fits to background corrected spectra are also shown (solid circles). The best fit values of the Hill parameters for these data were $n=2.78\pm 0.04$ and $p_{50}=24.9\pm 0.5$ torr, and the solid line is the corresponding dissociation curve. The saturations returned by the SVD analysis are nearly identical to those determined by least squares fits to background corrected spectra, indicating the SVD algorithm is properly accounting for the presence of the India ink.

4.3.4 Comparison with discrete wavelength algorithms

A significant advantage of the SSDRS technique described here is the fact that a spectrum spanning a broad (164 nm) wavelength range is obtained in a single acquisition. This fact enables the least-squares and SVD algorithms to extract estimates of SO_2 which are more quantitatively accurate and less susceptible to errors caused by uncharacterized absorbers than SO_2 estimates returned by discrete wavelength techniques. To illustrate this, SO_2 values were calculated from our SSDR data with algorithms utilizing values of μ_a at two or three discrete wavelengths. These saturations are compared to those obtained from fits to full background-corrected SSDR spectra.

Under the assumption that Hb and HbO_2 are the only significant absorbers in the NIR, it is straightforward to show [8] that SO_2 may be calculated from the ratio of two absorption coefficients by the formula

$$SO_2 = \frac{\epsilon_{Hb}^{\lambda_1} - \epsilon_{Hb}^{\lambda_2} (\mu_a^{\lambda_1} / \mu_a^{\lambda_2})}{\left(\epsilon_{Hb}^{\lambda_1} - \epsilon_{HbO_2}^{\lambda_1} \right) + \left(\epsilon_{HbO_2}^{\lambda_2} - \epsilon_{Hb}^{\lambda_2} \right) (\mu_a^{\lambda_1} / \mu_a^{\lambda_2})}, \quad (4.5)$$

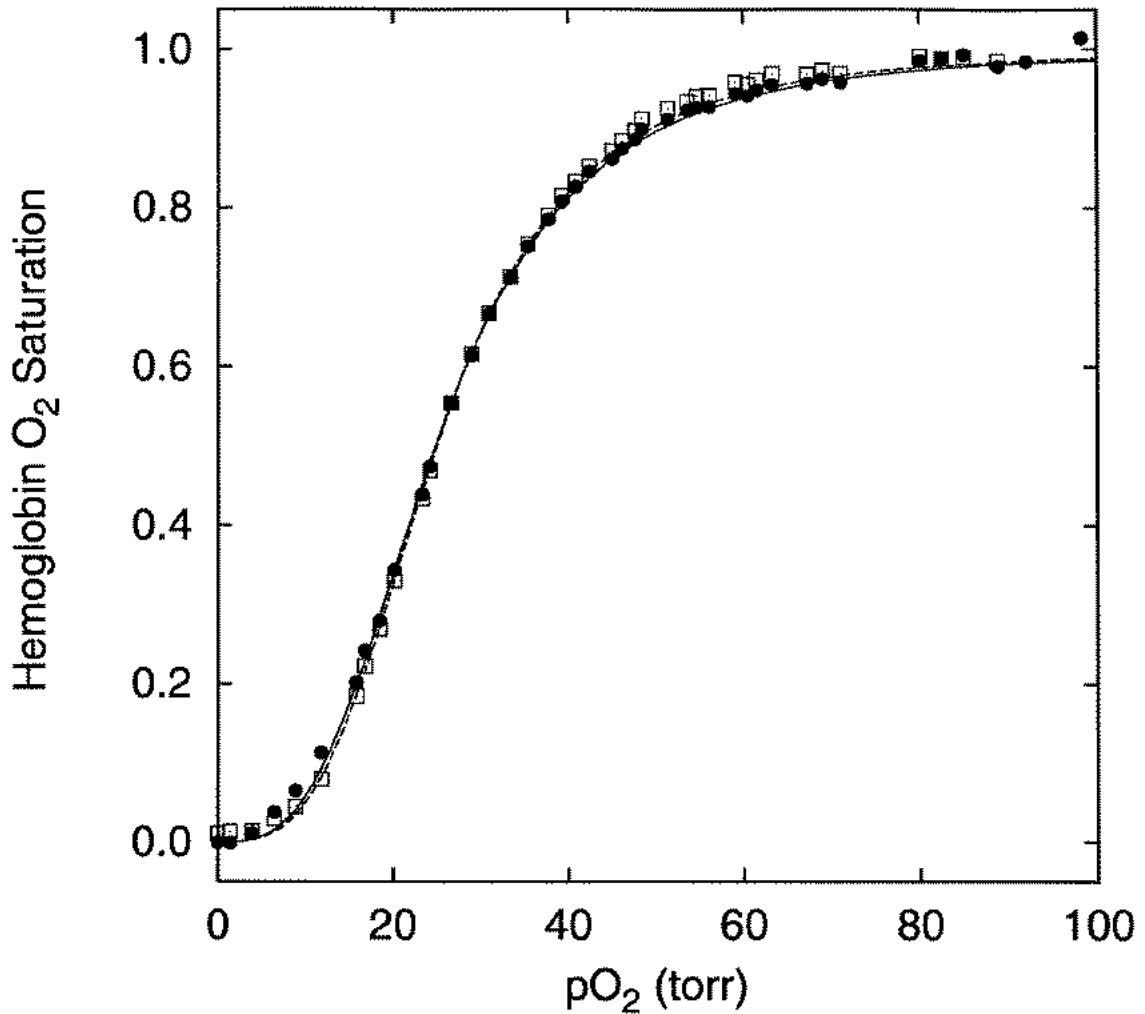


Figure 4.9 The hemoglobin oxygen saturations determined from least squares fits (solid circles) to background corrected absorption spectra reconstructed from SSDR measurements of a phantom comprised of polystyrene spheres, red cells, and a small amount of India ink. The solid line is the dissociation curve corresponding to fitted parameters for these data of $n=2.78\pm 0.04$ and $p_{50}=24.9\pm 0.5$ torr. The open squares are saturations returned from singular value decomposition analysis of the same spectra. The dashed line is the dissociation curve for these data corresponding to fitted parameters of $n=2.85\pm 0.3$ and $p_{50}=25.1\pm 0.5$ torr.

where λ_1 and λ_2 are the wavelengths of interest and ϵ_{HbO_2} and ϵ_{Hb} are the extinction coefficients of oxy- and deoxyhemoglobin. Two-wavelength techniques have been adopted fairly widely. For example, Franceschini *et al.* have recently studied the effect of water absorption on returned values for SO_2 using a frequency domain instrument operating at 715 and 825 nm [35]. The Runman® (NIM, Inc., Philadelphia, PA, USA) is a steady-state two-wavelength device which employs laser diodes at 760 and 850 nm. If three wavelengths are available, a system of three equations in three unknowns may be solved, allowing more accurate determination of SO_2 . In matrix notation, this system of equations may be represented by

$$\begin{pmatrix} [\text{Hb}] \\ [\text{HbO}_2] \\ [\text{H}_2\text{O}] \end{pmatrix} = \begin{pmatrix} \epsilon_{\text{Hb}}^{\lambda_1} & \epsilon_{\text{HbO}_2}^{\lambda_1} & \epsilon_{\text{H}_2\text{O}}^{\lambda_1} \\ \epsilon_{\text{Hb}}^{\lambda_2} & \epsilon_{\text{HbO}_2}^{\lambda_2} & \epsilon_{\text{H}_2\text{O}}^{\lambda_2} \\ \epsilon_{\text{Hb}}^{\lambda_3} & \epsilon_{\text{HbO}_2}^{\lambda_3} & \epsilon_{\text{H}_2\text{O}}^{\lambda_3} \end{pmatrix}^{-1} \begin{pmatrix} \mu_a^{\lambda_1} \\ \mu_a^{\lambda_2} \\ \mu_a^{\lambda_3} \end{pmatrix}, \quad (4.6)$$

where λ_1 , λ_2 , and λ_3 are the three wavelengths of interest. In the following analysis, the two-wavelength algorithm (Equation 4.5) is investigated for $\lambda=730$ and 825 nm and for $\lambda=760$ and 850 nm. The three-wavelength algorithm (Equation 4.6) is investigated using $\lambda=730$, 800, and 885 nm.

The results of analyzing the SSDRS data depicted in Figure 4.5 (obtained from a phantom containing spheres, water, and red cells) with these algorithms are illustrated in Figure 4.10. The fitted dissociation curve from Figure 4.4 is reproduced as a solid line for comparison. It can be seen that both two-wavelength algorithms estimate SO_2 reasonably well at large $p\text{O}_2$. The algorithm exploiting μ_a at 730 and 825 nm does not yield significant errors until the saturation falls below 50%, a result that is consistent with the findings of Franceschini *et al.* [35]. Both two-wavelength

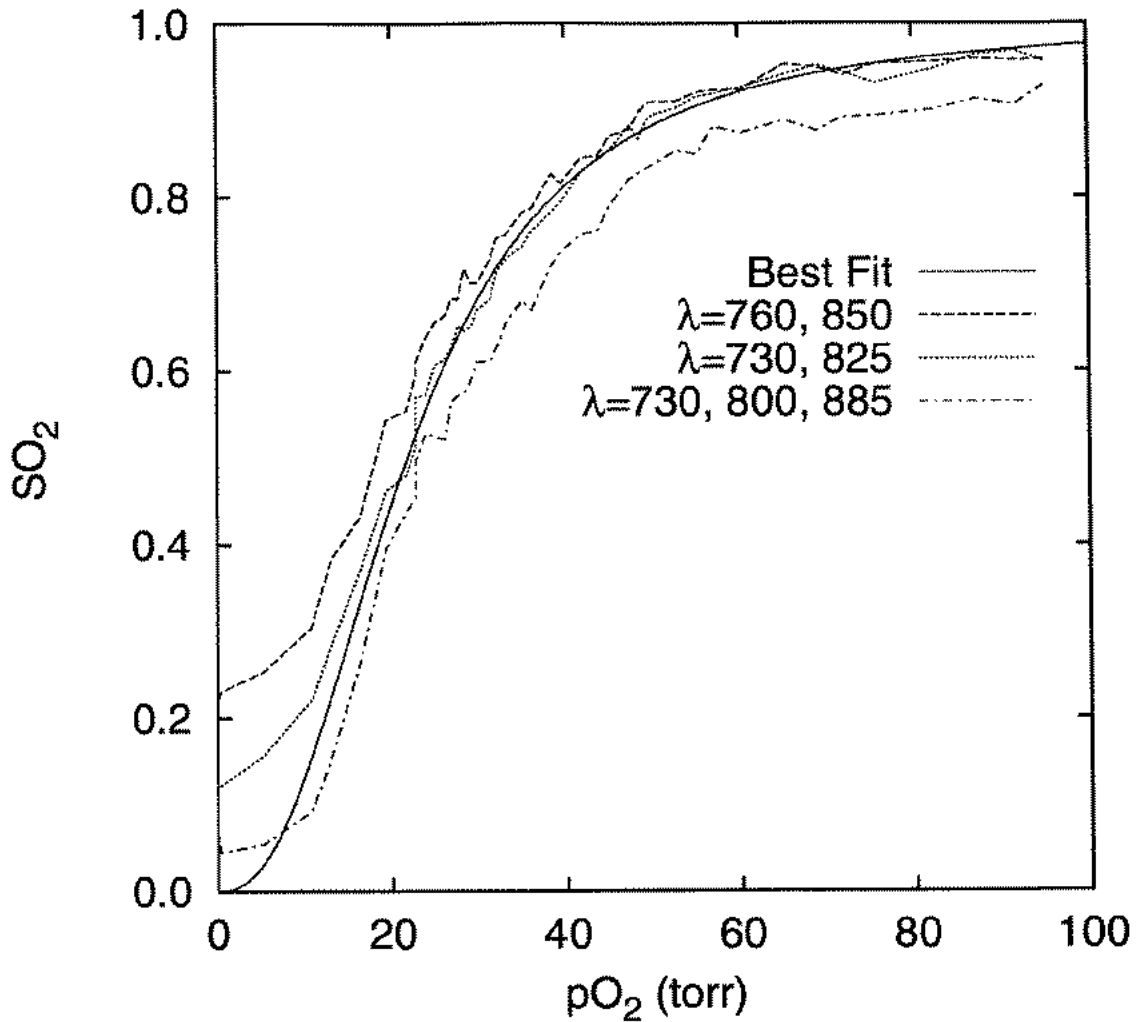


Figure 4.10 Hemoglobin oxygen saturations (SO_2) plotted as a function of pO_2 for the red cell phantom whose SSDR spectra are illustrated in Figure 4.5. SO_2 was computed by three different algorithms which utilize values of μ_a at either two or three discrete wavelengths. In the two wavelength cases, wavelengths of (760 and 850 nm) or (730 and 825 nm) were used. In the three wavelength case, wavelengths of 730, 800, and 885 nm were used. Algorithms are described in the text. The solid line is the fitted dissociation curve obtained from SO_2 values determined from least squares fits to background-corrected SSDR spectra (*i.e.*, the solid line from Figure 4.4).

algorithms produce SO_2 estimates which are in error by 10-20% at low oxygen tensions (0-5 torr). This is significant, since it is this range of pO_2 which is most critical in the context of ionizing radiation therapy and photodynamic therapy of cancer. These errors result from the fact that when only two wavelengths are utilized, the absorption of water is indistinguishable from a small amount of hemoglobin with $SO_2 = 76\%$ (in the case of $\lambda = 730$ and 825 nm) or 92% (in the case of $\lambda = 760$ and 850 nm). The three-wavelength algorithm most closely reconstructs the dissociation curve throughout the full range of pO_2 , although at large oxygen tensions (≥ 40 torr), it produces the largest deviations of the three algorithms. Since the only significant absorbers in this phantom were Hb, HbO_2 , and H_2O , the errors produced by the three-wavelength algorithm originate only from errors in the individual values of μ_a taken from the SSDR spectra.

The results of analyzing the SSDRS data depicted in Figure 4.8 (obtained from a phantom containing water, spheres, red cells, and India ink) are illustrated in Figure 4.11. In this case, all three algorithms produce significant errors at low pO_2 . Interestingly, the two-wavelength algorithm using μ_a at 730 and 825 nm produces the most accurate results in this region, while the three-wavelength algorithm produces the largest deviations. This results from the fact that, at the three wavelengths used in the analysis, the background ink spectrum may be best represented by a negative water and a positive oxyhemoglobin contribution. These results illustrate the fact that discrete wavelength techniques can yield potentially significant errors if a small amount of an uncharacterized absorber is present. For example, an optimized two-wavelength system would incorrectly correlate the presence of methemoglobin, which has an increased NIR absorption relative to HbO_2 and a pronounced peak at 630 nm, with decreased oxygen saturation and increased blood volume. The lack of validity of the assumption that absorbance changes are due only to Hb and HbO_2 would only

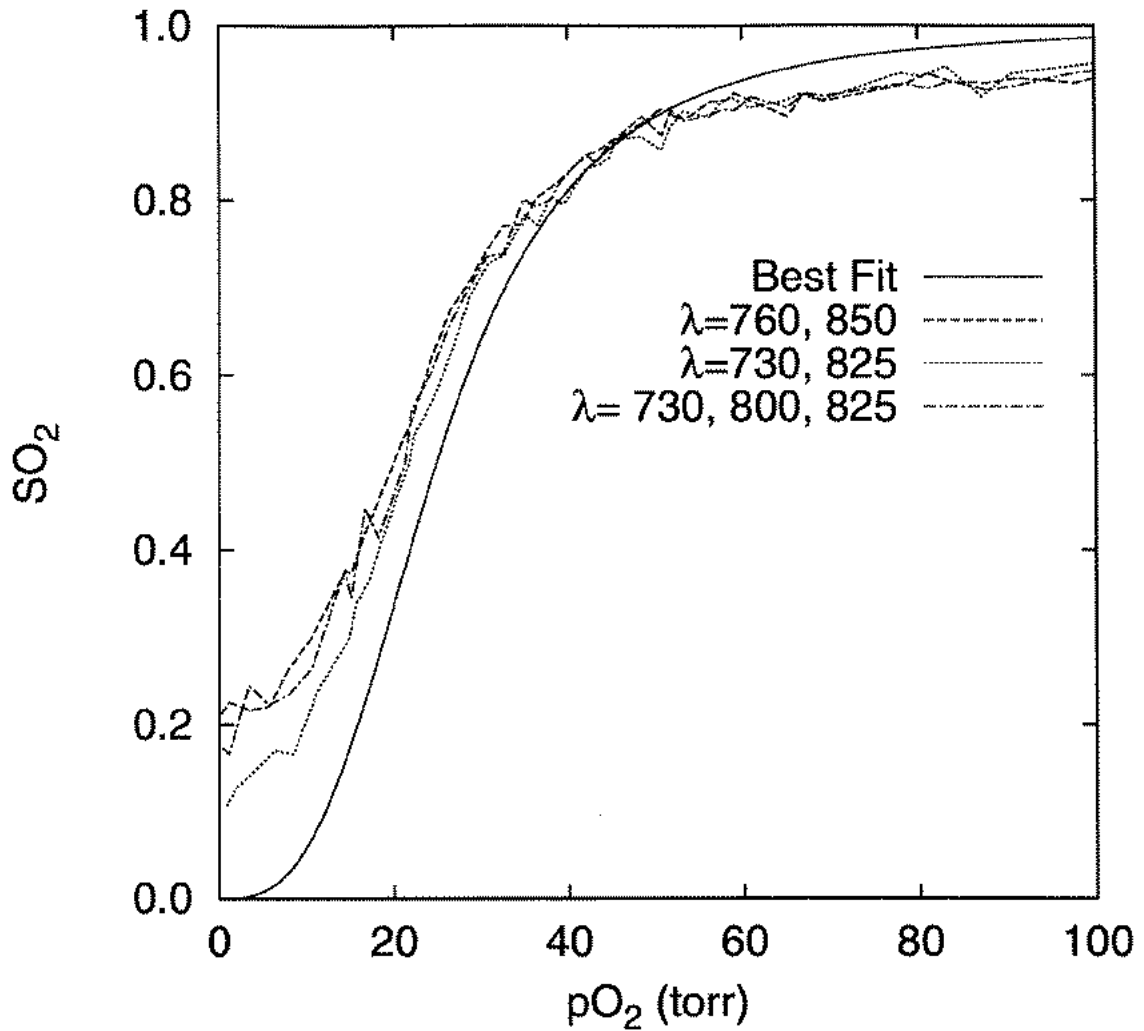


Figure 4.11 Hemoglobin oxygen saturations computed by the three algorithms described in Figure 4.10 for a phantom comprised of polystyrene spheres, red cells, and a small amount of India ink. The ink provides an oxygen independent “background” absorption spectrum, illustrated in Figure 4.7. The solid line is the fitted dissociation curve obtained from SO_2 values determined from least squares fits to background-corrected SSDR spectra (*i.e.*, the solid line from Figure 4.4).

become apparent when additional wavelengths were analyzed.

In addition to the possible presence of unanticipated chromophores, another challenging problem in tissue spectroscopy is sample-to-sample fluctuations in the absorption of certain chromophores arising from complex dependence on local environment. Wray *et al.* have suggested, for example, that *in vitro* cytochrome aa_3 extinction spectra may be unreliable and instead obtained the difference spectrum *in vivo* by replacing the blood with a fluorocarbon-based substitute which would not interfere with cytochrome aa_3 [29]. When such variability is likely, a broadband technique such as the implementation of SSDRS described here becomes an attractive option.

It is noted that the multiple source-detector separations required by the SSDR technique sample depths ranging from ~1 - 5 mm from the tissue surface. Thus SSDRS is an excellent choice for measurements near accessible surfaces, particularly when reasonably homogeneous optical properties in the corresponding probed volume can be expected. SSDRS is less suitable for probing deeper tissues, *e.g.*, noninvasive spectroscopic studies of the brain. The issue of tissue heterogeneity remains an important area of investigation for all methods of tissue spectroscopy [36,37], and the reconstruction of spatially varying tissue optical properties is an area of extreme interest within the medical optics community [38,39].

4.4 Spectroscopy of phantoms containing hemoglobin and mitochondria

The inner mitochondrial membrane and intermembrane space contain proteins which form the respiratory complexes of the electron transport chain. *In vivo*, passage of

electrons through the redox centers of this transport chain is coupled to oxidative phosphorylation, the process responsible for production of ATP and consumption of oxygen, which is the terminal electron acceptor [40]. Several of these proteins, called cytochromes, possess absorption spectra which depend on the oxidation state of their redox center, which in turn depends on the local availability of oxygen. Although several factors can contribute to the oxidation status of the cytochromes, their absorption spectra are at least partially sensitive to the local oxygen concentration. If quantitative cytochrome spectroscopy were possible in the presence of the more dominant absorption of hemoglobin, it would therefore provide a measure of sensitivity to *cellular* oxygenation. This is to be contrasted with hemoglobin spectroscopy, which is an indicator of *vascular* oxygenation. It is possible that processes which can induce rapid oxygen depletion, such as photodynamic therapy [41-43], may render some tissue regions hypoxic without significant perturbation of hemoglobin oxygen saturation in nearby vessels. Cytochrome spectroscopy is a particularly attractive approach for observation of such phenomena because the spectroscopic transitions do not occur until oxygen tensions are extremely low. For example, a p_{50} of 1.5 torr has been reported by Wilson et al. for cytochrome c in cultured neuroblastoma cells [44].

In order to assess the feasibility of cytochrome spectroscopy in the presence of hemoglobin, mitochondria were isolated from rabbit livers using a protocol published by Gibson et al. [45]. Briefly, livers were excised, placed on ice in 0.9% NaCl solution, weighed and minced with scissors. Four grams of tissue were placed in 10 ml of cold homogenization buffer containing 0.33 M sucrose, 1 mM dithiothreitol, 1 mM EGTA, 0.03% bovine serum albumin, and 100 mM KCl. Tissues were homogenized and centrifuged at 500 g for 15 minutes. The supernatant was then removed and centrifuged at 15,000 g for 30 minutes at 4° C. The resulting pellet was resuspended

in 8 ml of buffer, and the high-speed centrifugation was repeated. The final pellet was suspended in ~4 ml of buffer and stored at -70°C until use.

In order to obtain basis spectra for later analysis of mixed phantoms, mitochondria only were first placed in a scattering emulsion consisting of 330 ml of 0.9% Liposyn-II® (Abbott Labs, Chicago, IL) diluted with Trizma®-buffered saline (pH=7.1). The emulsion was deoxygenated by addition of yeast as described in the preceding sections. We have verified that the yeast absorption spectrum, which itself originates with cytochromes, does not change upon deoxygenation. Figure 4.12 depicts mitochondrial absorption spectra reconstructed from SSDR measurements in the near IR (upper panel) and visible (lower panel) for oxygen tensions of ~160 torr (oxidized spectra, solid lines) and 0 torr (reduced spectra, dashed lines). All of the measurements were conducted with mitochondrial concentrations that allowed diffusion-theory data analysis; the reconstructed absorption spectra from the visible have been scaled to align with the near IR absorption spectra. At least two interesting features are evident in these plots. First, the overall magnitude of the absorption coefficient increases by a factor of approximately 200 from $\lambda=850\text{ nm}$ to $\lambda=450\text{ nm}$. This represents approximately a 4-fold greater increase in overall extinction compared to hemoglobin for the same wavelengths. Thus, differentiation of cytochrome and hemoglobin absorption should be facilitated by moving to the visible region of the spectrum. In addition, the visible spectra exhibit more interesting spectral content than the near IR spectra, which are rather featureless by comparison. These maxima and minima should also allow easier differentiation of cytochrome and hemoglobin spectra in the visible.

Because the spectra depicted in Figure 4.12 are of mitochondria rather than individual isolated cytochromes, it is important to investigate whether they are indeed

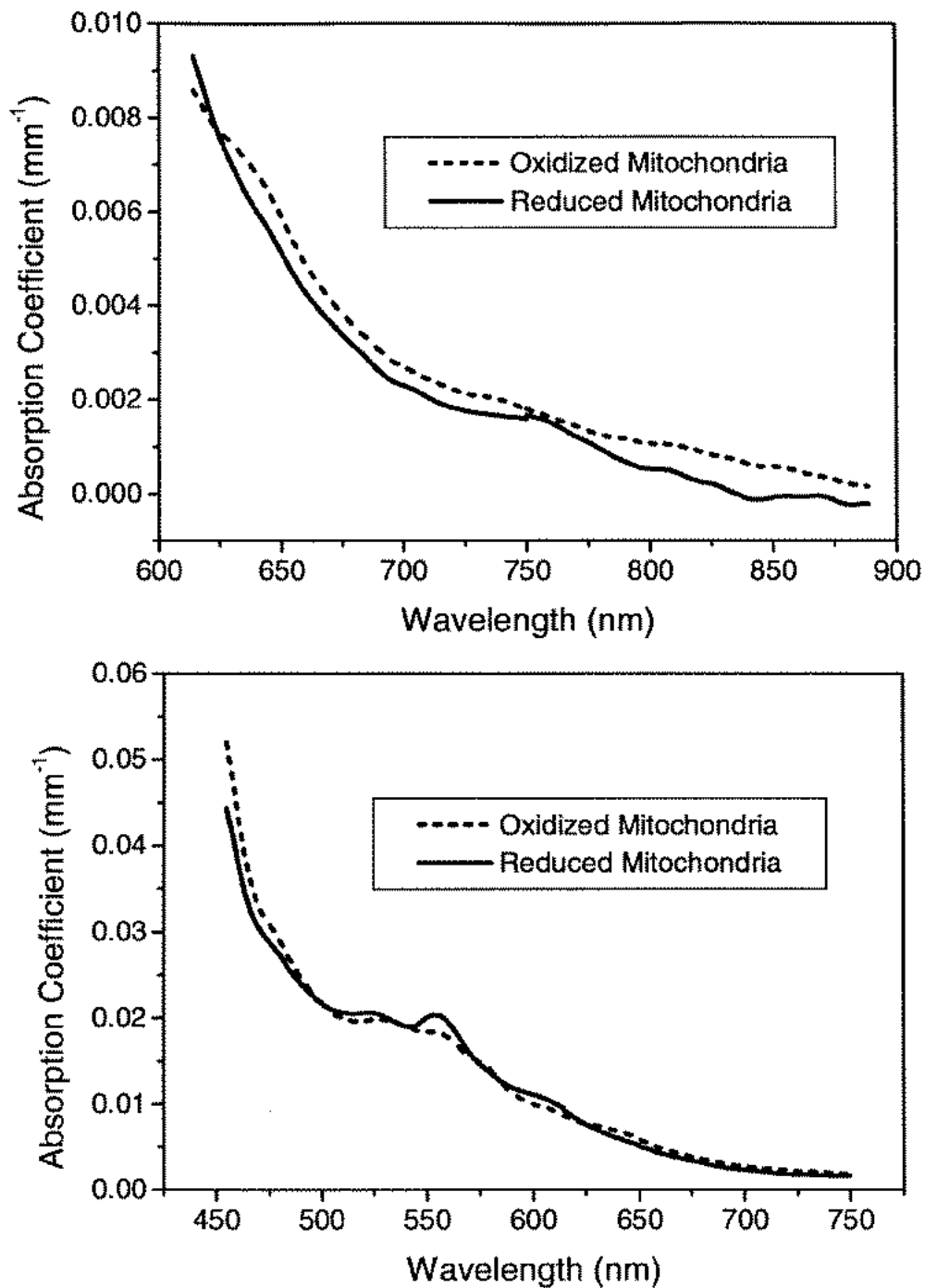


Figure 4.12 Absorption spectra reconstructed from steady-state diffuse reflectance measurements of mitochondria isolated from rabbit liver. The oxidized spectra were obtained at $pO_2 \approx 160$ torr, and the reduced spectra were obtained at $pO_2 = 0$ torr.

reasonable. One way of approaching this validation is to compare the difference (i.e., oxidized-reduced or reduced-oxidized) spectra obtained from SSDRS measurements with those obtained by others. A comparison of near IR difference spectra is provided in Figure 4.13, which depicts the SSDRS difference spectrum (upper panel) with the in-vivo near IR difference spectrum obtained by Cope in rat brain [1]. Cope's measurement involved exchange of the blood with a perfluorocarbon substitute followed by nitrogen asphyxiation. His difference spectrum was computed from near IR transmission measurements based on knowledge of differential pathlength factors for rat brain. Qualitative agreement exists between the two spectra. The SSDRS data are noisy because they result from subtraction of two crosstalk-corrected absorption spectra that are nearly equal in magnitude. A similar comparison of visible difference spectra is presented in Figure 4.14. The SSDRS difference spectrum is again shown in the upper panel, and the lower panel is the difference spectrum obtained by Chance for rat liver [46]. Again, the spectra are in good agreement. The labels on the plot from Chance identify the absorption bands (Greek letters) of the particular cytochromes (Latin letters) responsible for each peak in the difference spectrum.

To assess the potential for quantitative cytochrome spectroscopy in the presence of hemoglobin, mitochondria obtained from 5.33 g (3.94 cc) of rabbit liver were added to a 330 ml phantom consisting of 0.9% Liposyn-II diluted with Trizma®-buffered saline. Freshly-washed human red cells were then added to the phantom in a physiologically correct proportion to the original volume of liver tissue from which the mitochondria were extracted. Assuming typical values of 4% blood volume and 40% hematocrit, the red cell volume was determined by multiplying the volume of original liver tissue (3.94 cc) by a factor of 0.016, which gives 63 μ l. The volume of mitochondria was chosen in order to make the phantom optical properties suitable for analysis with

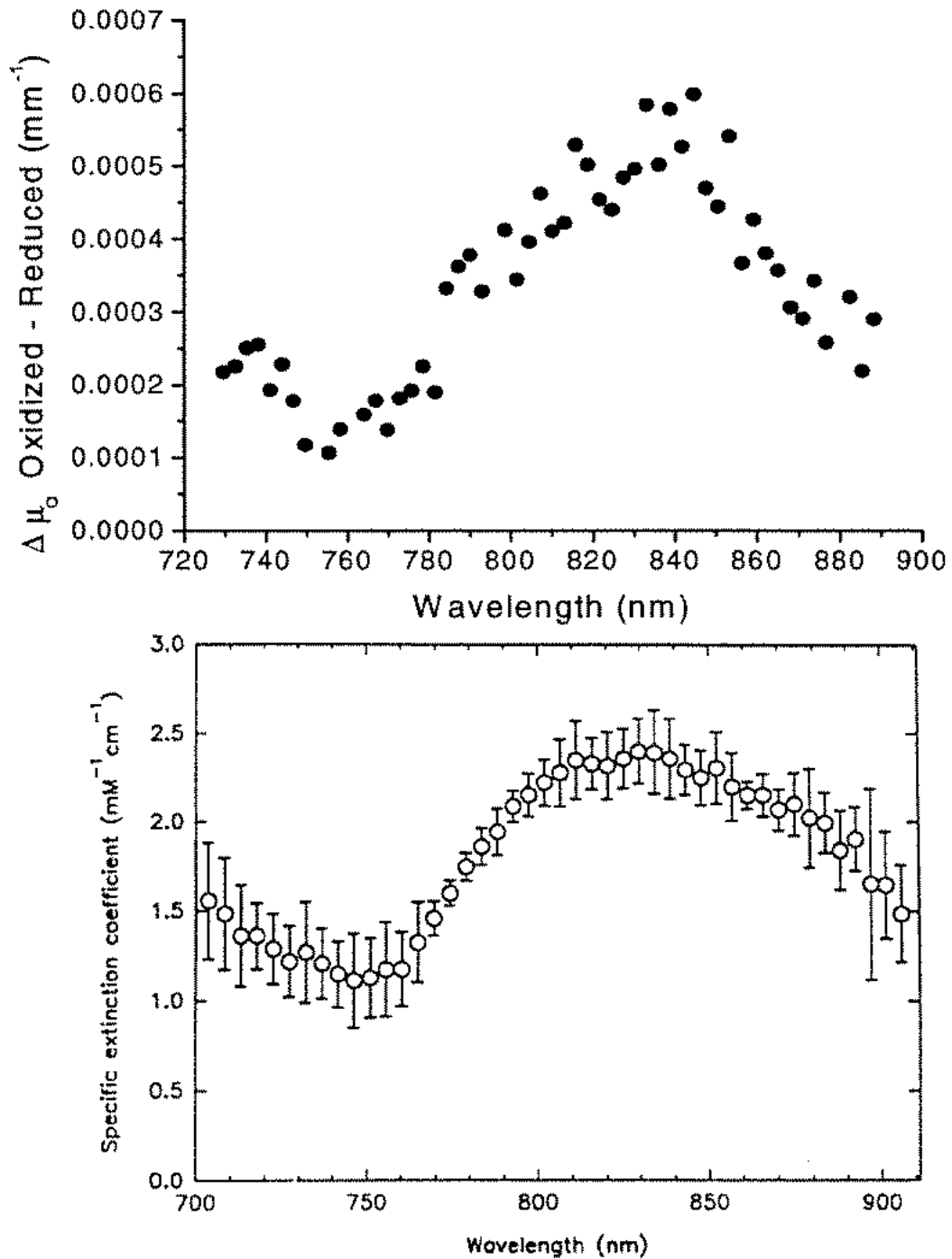


Figure 4.13 Near IR mitochondrial difference spectra. The upper panel is the difference spectrume of rabbit mitochondria reconstructed from steady-state diffuse reflectance measurements obtained at $p\text{O}_2=160$ torr and 0 torr, respectively. The lower panel is the in vivo difference spectrum of blood-free rat brain obtained by Cope [30].

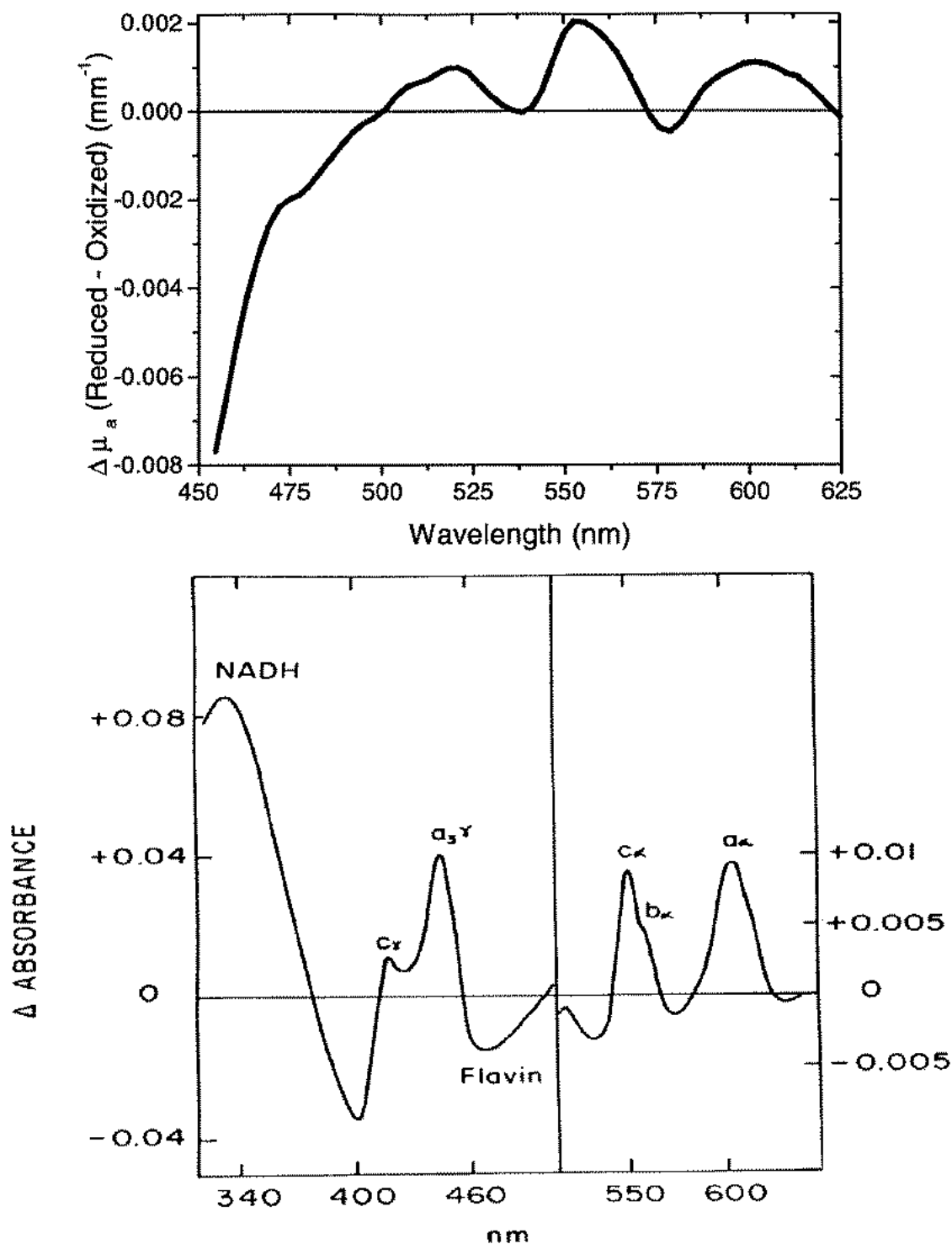


Figure 4.14 Difference spectra of rabbit liver mitochondria reconstructed from diffuse reflectance measurements (upper panel) and of rat liver (lower panel) in the visible region of the spectrum. The data in the lower panel are from Chance [46]. Labels on the lower panel indicate the cytochromes responsible for each spectral feature.

diffusion theory. Thus, these experiments were performed in the visible spectral region, but the optical properties were typical of tissue in the near IR. The phantom was deoxygenated in the manner described above, and SSDRS data were collected throughout the deoxygenation. A Clark-style oxygen microelectrode was used for measurement of pO_2 in order to minimize errors in the recorded oxygen tension resulting from electrode response time. The response time of these electrodes has been demonstrated to be ≤ 0.5 s. An SVD algorithm within the commercial software package Origin® was used to fit a sum of oxy- and deoxyhemoglobin and oxidized and reduced mitochondria basis spectra to the reconstructed SSDRS spectra. Concentrations of these species were extracted as fitting parameters.

Representative spectra from the mixed phantom are illustrated in Figure 4.15. The upper panel corresponds to $pO_2 \approx 160$ torr and depicts fully oxygenated/oxidized spectra. The lower panel corresponds to 0 torr and depicts fully deoxygenated/reduced spectra. The symbols are the SSDRS absorption coefficients after subtraction of the water background; at physiological hemoglobin concentrations, water absorption is entirely negligible in this wavelength range. The dotted lines are the SVD estimates of the hemoglobin contribution to the absorption spectrum, the dashed lines are the estimated mitochondrial contribution to the spectrum, and the solid lines are the sum of these two components. For the majority of the wavelength range, the hemoglobin absorption dominates that of the mitochondria by approximately a factor of 8.

The results of fitting SSDR absorption spectra collected for $0 \text{ torr} \leq pO_2 \leq 60 \text{ torr}$ are presented in Figure 4.16. The open circles squares depict the fitted concentrations of oxyhemoglobin (open symbols) and deoxyhemoglobin (filled symbols). The circles represent the fitted concentrations, in arbitrary units, of oxidized (open symbols) and reduced (filled symbols) mitochondria. It can be seen that the value of p_{50} for

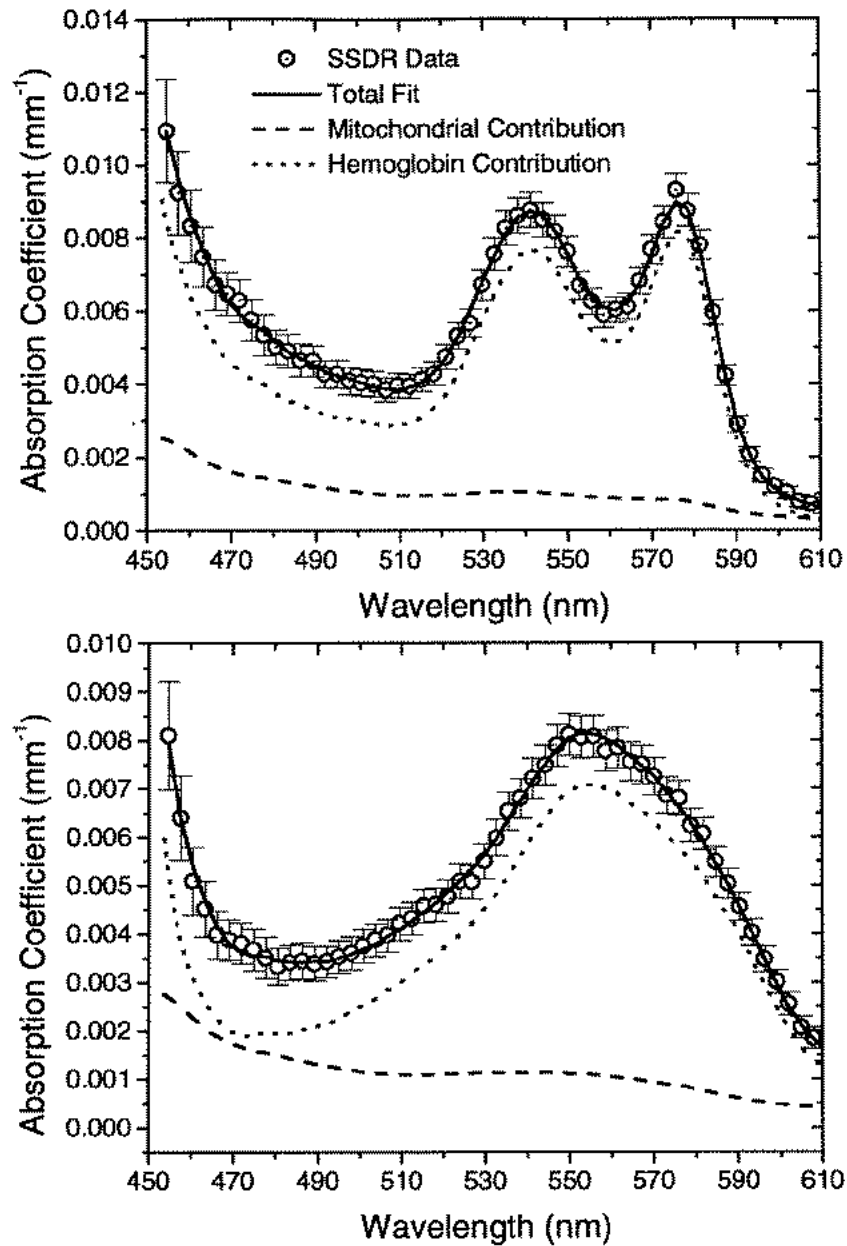


Figure 4.15 Absorption coefficients (\circ) reconstructed from SS DR measurements of a phantom comprised of mitochondria from 5.33 g of rabbit liver, 60 μ l of packed red blood cells, and 330 ml of 0.9% Liposyn-II diluted in Trizma-buffered saline. Data in the upper panel were acquired at $pO_2 \approx 160$ torr (fully oxygenated/oxidized), and data in the lower panel were acquired at $pO_2 = 0$ torr (fully deoxygenated/reduced). The dotted lines are the fitted hemoglobin contribution to the total spectrum, the dashed lines are the fitted mitochondrial contribution to the total spectrum, and the solid lines are the sum of the hemoglobin and mitochondrial contributions.

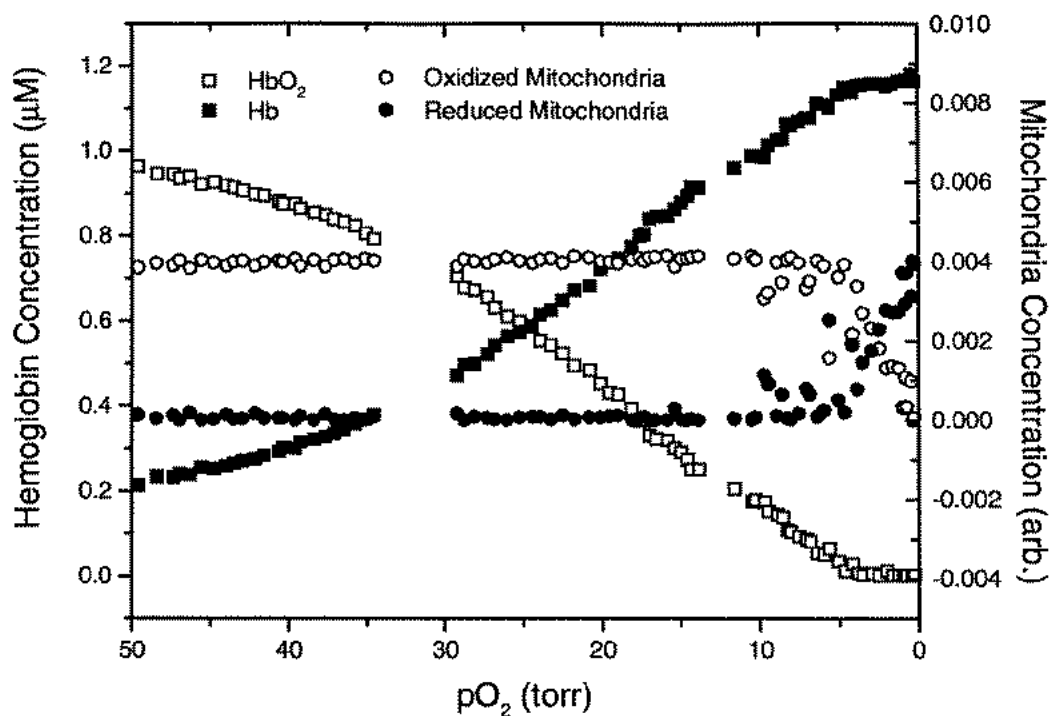


Figure 4.16 Fitted concentrations of oxy- and deoxyhemoglobin (open and filled squares, respectively) and oxidized and reduced mitochondria (open and filled circles, respectively) as a function of pO_2 in the phantom described in Figure 4.15. The oxygen tension was monitored with an oxygen electrode.

hemoglobin is approximately 25 torr, in agreement with the results of the preceding sections, and the mitochondrial p_{50} is approximately 2.5 torr, which is within measurement uncertainty of the value given by Wilson et al. [44]. Thus, it is reasonable to conclude that the mitochondrial absorption spectrum has been successfully isolated from the hemoglobin spectrum over the full range of oxygen partial pressures. This result is certainly encouraging with respect to the potential for in vivo cytochrome spectroscopy.

4.5 Conclusions

These studies demonstrate that SSDRS is an effective technique for monitoring hemoglobin oxygen saturation in highly scattering environments. By effectively decoupling the effects of scattering and absorption, quantitative spectroscopic studies are possible over a broad wavelength range in the NIR with signal integration times on the order of 1-5 seconds. This broadband capability offers significant advantages over discrete wavelength techniques, particularly when unknown, weakly absorbing species must be characterized. Of course, when it is possible to have *a priori* knowledge of the spectra of the various background chromophores, this information can be used to further constrain the fitting process. The relatively low cost and technical simplicity of the equipment involved makes this technique an excellent choice for spectroscopic applications where optical properties are to be measured at the surface of a turbid medium such as human tissue.

Preliminary measurements of mixed hemoglobin and mitochondria phantoms have also been presented. These results suggest that differentiation of hemoglobin and cytochrome absorption spectra in the visible is feasible provided a theoretical method

of quantitative spectroscopy in this wavelength range is available. The P_3 approximation developed and validated in Chapters 2 and 3 may be a useful approach to this problem.

References

1. M. Cope and D.T. Delpy, "System for long-term measurement of cerebral blood and tissue oxygenation on newborn infants by near-infrared transillumination," *Med. Biol. Eng. Comput.* **26**, 289-294 (1988).
2. R.A. Deblasi, S. Fantini, M.A. Franceschini, M. Ferrari, and E. Gratton, "Cerebral and muscle oxygen-saturation measurement by frequency-domain near-infrared spectrometer," *Med. Biol. Eng. Comput.* **33**, 228-230 (1995).
3. S.J. Matcher, M. Cope, and D.T. Delpy, "Use of the water absorption spectrum to quantify tissue chromophore concentration changes in near-infrared spectroscopy," *Phys. Med. Biol.* **38**, 177-196 (1993).
4. M.S. Patterson, B. Chance, and B.C. Wilson, "Time resolved reflectance and transmittance for the noninvasive measurement of tissue optical properties," *Appl. Opt.* **28**, 2331-2336 (1989).
5. A. Kienle and M.S. Patterson, "Improved solutions of the steady-state and the time-resolved diffusion equations for reflectance from a semi-infinite turbid medium," *J. Opt. Soc. Am. A* **14**, 246-254 (1997).
6. B. Chance, J.S. Leigh, H. Miyake, D.S. Smith, S. Nioka, R. Greenfeld, M. Finander, K. Kaufmann, W. Levy, M. Young, P. Cohen, H. Yoshioka, and R. Boretsky, "Comparison of time-resolved and time-unresolved measurements of deoxyhemoglobin in brain," *PNAS* **85**, 4971-4975 (1988).
7. B. Chance, S. Nioka, J. Kent, K. McCully, M. Fountain, R. Greenfeld, and G. Holtom, "Time-resolved spectroscopy of hemoglobin and myoglobin in resting and ischemic muscle," *Anal. Biochem.* **174**, 698-707 (1988).
8. E.M. Sevick, B. Chance, J. Leigh, S. Nioka, and M. Maris, "Quantitation of time-resolved and frequency-resolved optical spectra for the determination of tissue oxygenation," *Anal. Biochem.* **195**, 330-351 (1991).

9. M.S. Patterson, J.D. Moulton, B.C. Wilson, K.W. Berndt, and J.R. Lakowicz, "Frequency-domain reflectance for the determination of the scattering and absorption properties of tissue," *Appl. Opt.* **30**, 4474-4476 (1991).
10. B.W. Pogue and M.S. Patterson, "Frequency-domain optical absorption spectroscopy of finite tissue volumes using diffusion theory," *Phys. Med. Biol.* **39**, 1157-1180 (1994).
11. S.J. Madsen, E.R. Anderson, R.C. Haskell, and B.J. Tromberg, "Portable, high-bandwidth frequency-domain photon migration instrument for tissue spectroscopy," *Opt. Lett.* **19**, 1934-1936 (1994).
12. J.B. Fishkin, O. Coquoz, E.R. Anderson, M. Brenner, and B.J. Tromberg, "Frequency-domain photon migration measurements of normal and malignant tissue optical properties in a human subject," *Appl. Opt.* **36**, 10-20 (1997).
13. S.J. Matcher and C.E. Cooper, "Absolute quantification of deoxyhemoglobin concentration in tissue near-infrared spectroscopy," *Phys. Med. Biol.* **39**, 1295-1312 (1994).
14. A. Duncan, J.H. Meek, M. Clemence, C.E. Elwell, L. Tyszczuk, M. Cope, and D.T. Delpy, "Optical pathlength measurements on adult head, calf and forearm and the head of the newborn infant using phase-resolved optical spectroscopy," *Phys. Med. Biol.* **40**, 295-304 (1995).
15. P. van der Zee, M. Cope, S.R. Arridge, M. Essenpreis, L.A. Potter, A.D. Edwards, J.S. Wyatt, D.C. McCormick, S.C. Roth, E.O.R. Reynolds, and D.T. Delpy, "Experimentally measured optical pathlengths for the adult head, calf and forearm and the head of the newborn infant as a function of interoptode spacing," *Adv. Exp. Med. Biol.* **316**, 143-153 (1992).

16. J.T. Bruulsema, J.E. Hayward, T.J. Farrell, M.S. Patterson, L. Heinemann, M. Berger, T. Koschinsky, J. Sandahl-Christiansen, H. Orskov, M. Essenpreis, G. Schmelzeisen-Redeker, and D. Böcker, "Correlation between blood glucose concentration in diabetics and noninvasively measured tissue optical scattering coefficient," *Opt. Lett.* **22**, 190-192 (1997).
17. J.H. Torres, A.J. Welch, I. Cilesiz, and M. Motamedi, "Tissue optical property measurements - overestimation of absorption coefficient with spectrophotometric techniques," *Lasers Surg. Med.* **14**, 249-257 (1994).
18. B. Chance, H.L. Liu, T. Kitai, and Y.T. Zhang, "Effects of solutes on optical properties of biological materials - models, cells, and tissues," *Anal. Biochem.* **227**, 351-362 (1995).
19. C.D. Kurth and B. Uher, "Cerebral hemoglobin and optical pathlength influence near-infrared spectroscopy measurement of cerebral oxygen saturation," *Anesth. Analg.* **84**, 1297-1305 (1997).
20. P. Rhee, L. Langdale, C. Mock, and L.M. Gentilello, "Near-infrared spectroscopy: Continuous measurement of cytochrome oxidation during hemorrhagic shock," *Crit. Care Med.* **25**, 166-170 (1997).
21. F. Nomura, H. Naruse, A. duPlessis, T. Hiramatsu, J. Forbess, D. Holtzman, J.J. Volpe, R. Jonas, and M. Tsuji, "Cerebral oxygenation measured by near infrared spectroscopy during cardiopulmonary bypass and deep hypothermic circulatory arrest in piglets," *Pediatr. Res.* **40**, 790-796 (1996).
22. K.K. McCully, C. Halber, and J.D. Posner, "Exercise-induced changes in oxygen saturation in the calf muscles of elderly subjects with peripheral vascular disease," *J. Gerontol.* **49**, B128-B134(1994).
23. V. Pollard, D.S. Prough, A.E. DeMelo, D.J. Deyo, T. Uchida, and R. Widman, "The influence of carbon dioxide and body position on near-infrared spectroscopic assessment of cerebral hemoglobin oxygen saturation," *Anesth. Analg.* **82**, 278-287 (1996).

24. E.D. Speakman, J.C. Boyd, and D.E. Bruns, "Measurement of methemoglobin in neonatal samples containing fetal hemoglobin," *Clin. Chem.* **41**, 458-461 (1995).
25. B.C. Wilson, T.J. Farrell, and M.S. Patterson, "An optical fiber-based diffuse reflectance spectrometer for non-invasive investigation of photodynamic sensitizers in vivo.," in *Future Directions and Applications in Photodynamic Therapy*, C. J. Gomer, ed., **SPIE Institute Series, Volume IS6**, 219-232 (1990).
26. R.A. Weersink, J.E. Hayward, K.R. Diamond, and M.S. Patterson, "Accuracy of noninvasive in vivo measurements of photosensitizer uptake based on a diffusion model of reflectance spectroscopy," *Photochem. Photobiol.* **66**, 326-335 (1997).
27. W.H. Press, S.A. Teukolsky, W.T. Vetterling, and B.P. Flannery, *Numerical Recipes in C: The Art of Scientific Computing* (Cambridge University Press, Cambridge, UK, 1992), pp. 683-687.
28. E.L. Hull and T.H. Foster, "Noninvasive near-infrared hemoglobin spectroscopy for in vivo monitoring of tumor oxygenation and response to oxygen modifiers," in *Optical tomography and spectroscopy of tissue: Theory, instrumentation, model, and human studies II*, B. Chance and R. R. Alfano, eds., *Proc SPIE* **2979**, 355-364 (1997).
29. S. Wray, M. Cope, D.T. Delpy, J.S. Wyatt, and E.O.R. Reynolds, "Characterization of the near-infrared absorption spectra of cytochrome aa_3 and hemoglobin for the noninvasive monitoring of cerebral oxygenation," *Biochim. Biophys. Acta* **933**, 184-192 (1988).
30. M. Cope, "The development of a near infrared spectroscopy system and its application for non-invasive monitoring of cerebral blood and tissue oxygenation in the newborn infant," PhD dissertation (University College London, London, UK, 1991).
31. S.J. Matcher, C.E. Elwell, C.E. Cooper, M. Cope, and D.T. Delpy, "Performance comparison of several published tissue near-infrared spectroscopy algorithms," *Anal. Biochem.* **227**, 54-68 (1995).

32. R.B. Gunn, O. Frölich, "Methods and analysis of erythrocyte anion fluxes," in *Biomembranes Part T: Cellular and Subcellular Transport: Eukaryotic (Nonepithelial) Cells*, S. Fleischer and B. Fleischer, eds., Methods in Enzymology (Academic Press, New York, 198), pp. 76.
33. A. Zwart, G. Kwant, B. Oeseburg, and W.G. Zijlstra, "Human whole blood oxygen affinity - effect of temperature," *J. Appl. Physiol.* **57**, 429-434 (1984).
34. C.E. Cooper, S.J. Matcher, J.S. Wyatt, M. Cope, G.C. Brown, E.M. Nemoto, and D.T. Delpy, "Near-infrared spectroscopy of the brain - relevance to cytochrome-oxidase bioenergetics," *Biochem. Soc. Trans.* **22**, 974-980 (1994).
35. M.A. Franceschini, S. Fantini, A. Cerussi, B. Barbieri, B. Chance, and E. Gratton, "Quantitative spectroscopic determination of hemoglobin concentration and saturation in a turbid medium: analysis of the effect of water absorption," *J. Biomed. Opt.* **2**, 147-153 (1999).
36. A. Kienle, M.S. Patterson, N. Dognitz, R. Bays, G. Wagnieres, and H. van den Bergh, "Noninvasive determination of the optical properties of two-layered turbid media," *Appl. Opt.* **37**, 779-791 (1998).
37. M. Hiraoka, M. Firbank, M. Essenpreis, M. Cope, S.R. Arridge, Van derZee, and D.T. Delpy, "A Monte Carlo investigation of optical pathlength in inhomogeneous tissue and its application to near-infrared spectroscopy," *Phys. Med. Biol.* **38**, 1859-1876 (1993).
38. M.A. O'Leary, D.A. Boas, B. Chance, and A.G. Yodh, "Experimental images of heterogeneous turbid media by frequency-domain diffusing-photon tomography," *Opt. Lett.* **20**, 426-428 (1995).
39. H. Jiang, K.D. Paulsen, and U.L. Österberg, "Optical image reconstruction using DC data: simulations and experiments," *Phys. Med. Biol.* **41**, 1432-1498 (1996).
40. D. Voet and J.G. Voet, *Biochemistry* (John Wiley & Sons, New York, 1995), pp. 564-564.

41. M.G. Nichols and T.H. Foster, "Oxygen diffusion and reaction kinetics in the photodynamic therapy of multicell tumor spheroids," *Phys. Med. Biol.* **39**, 2161-2181 (1994).
42. T.H. Foster, D.F. Hartley, M.G. Nichols, and R. Hilf, "Fluence rate effects in photodynamic therapy of multicell tumor spheroids," *Cancer Res.* **53**, 1249-1254 (1993).
43. T.H. Foster and L. Gao, "Dosimetry in photodynamic therapy: oxygen and the critical importance of capillary density," *Radiation Research* **130**, 379-383 (1992).
44. D.F. Wilson, M. Erecinska, C. Drown, and I.A. Silver, "The oxygen dependence of cellular metabolism," *Arch. Biochem. Biophys.* **195**, 485-493 (1979).
45. S.L. Gibson and R. Hilf, "Photosensitization of mitochondrial cytochrome c oxidase by hematoporphyrin derivative and related porphyrins in vitro and in vivo," *Cancer Res.* **43**, 4191-4197 (1983).
46. B. Chance, "Spectrophotometry of intracellular respiratory pigments," *Science* **120**, 767-775 (1954).

CHAPTER 5

Carbogen-induced Changes in Rat Mammary Tumor Oxygenation Reported by Near-infrared Spectroscopy

5.1 Introduction

The use of commercial, needle-based oxygen sensitive electrode systems in human trials during the past decade has provided a wealth of new information regarding the role of tumor oxygen status in predicting survivability and local recurrence. Vaupel et al., for example, have shown that, in the breast, severe hypoxia is present only in malignant disease [1]. Further, the presence of hypoxia is not related to the stage or pathologic grade of the tumor, suggesting that even if these were determined from biopsy samples, no prediction regarding the presence or absence of radiation-therapy-limiting hypoxia could be made. Several studies in various anatomic sites have demonstrated a correlation between tumor hypoxia and response to treatment with ionizing radiation therapy [2-4]. In these studies, extreme hypoxia, as determined by analysis of pO_2 histograms obtained from measurements using polarographic needle electrodes, indicated poor prognosis. In addition to predicting local treatment failure, a recent report by Brizel et al. [5] suggested that hypoxia in primary soft tissue sarcomas was correlated with the probability of appearance of remote metastatic disease. Studies in cell culture support the suggestion that exposure to sustained hypoxia results in the

selection of malignant cells expressing aggressive phenotypes [6].

The sustained interest in tumor hypoxia has given rise to the introduction of various methods of improving tumor oxygenation. The use of hyperbaric oxygen was an early example [7], and it continues to be studied in laboratory animal systems and in human clinical trials [8,9]. Inhalation of high oxygen content gases such as carbogen has also been studied rather extensively [10-12]. Chemical agents such as nicotinamide, which is designed to modify tumor blood flow, have been used either alone [13] or together with carbogen inhalation [14] in an effort to sensitize tumor cells rendered hypoxic by more than one mechanism (i.e., chronic vs. acute). The combination of nicotinamide and carbogen in conjunction with accelerated radiotherapy is being evaluated currently in clinical trials in Europe [15]. Each of these methods has demonstrated some success in specific situations and tumor models, while none has emerged yet as being generally accepted in clinical practice.

The importance of hypoxia in predicting tumor response to ionizing radiation (and photodynamic) therapy and in possibly predicting the likelihood of metastases has stimulated great interest in improving techniques for clinical measurement of tumor oxygenation *in vivo*. These methods and others suitable only for laboratory use have been reviewed recently by Stone et al. [16]. While polarographic electrode systems have come to be viewed as a standard, their widespread, routine clinical acceptance may be limited by their invasiveness [15]. This may be especially important if tumor oxygenation is to be monitored repeatedly during the course of fractionated therapy.

Near infrared spectroscopy is among the noninvasive methods that are sensitive to some measure of tumor oxygenation. Specifically, because the absorption spectra of deoxy- and oxyhemoglobin are markedly different, the hemoglobin oxygen saturation may be determined from the tissue absorption spectrum, which may be reconstructed

from appropriate reflectance measurements. Successful spectroscopic determination of the HbO₂ saturation (SO₂) in the near infrared spectral region depends upon two things: (1) the ability to determine accurately the absorption spectrum in the presence of significant light scattering by tissue and (2) the ability to account properly for the contributions of chromophores other than hemoglobin in the measured tissue absorption spectrum. Chapters 3 and 4 described a continuous-wave diffuse reflectance spectrometer and data reduction scheme that address both of these criteria. Here, we describe the use of this spectroscopic method to obtain noninvasively the response of subcutaneous rat mammary adenocarcinomas to carbogen breathing. The technique is simultaneously sensitive to both the HbO₂ saturation and to the tumor hemoglobin concentration.

5.2 Materials and Methods

5.2.1 Spectroscopy

The reflectance probe for these measurements consisted of a linear array of twenty 200- μm core diameter detection fibers located at distances of 1.0 - 20.0 mm from the source fiber (see Figure 5.1). The probe calibration data was obtained in the manner described for the P₃ reflectance probe in Section 3.5.1. All other aspects of the instrumentation, reflectance data reduction, and error analysis for these experiments are as described in Sections 3.3 – 3.4. During a measurement, the probe was placed in contact with the skin overlying the tumor. Typical signal integration times for measurements described here were approximately 5 s.

The reflectance data were analyzed with the full solution to the photo-diffusion equation as described in Section 2.7.1. After determining the absorption and transport

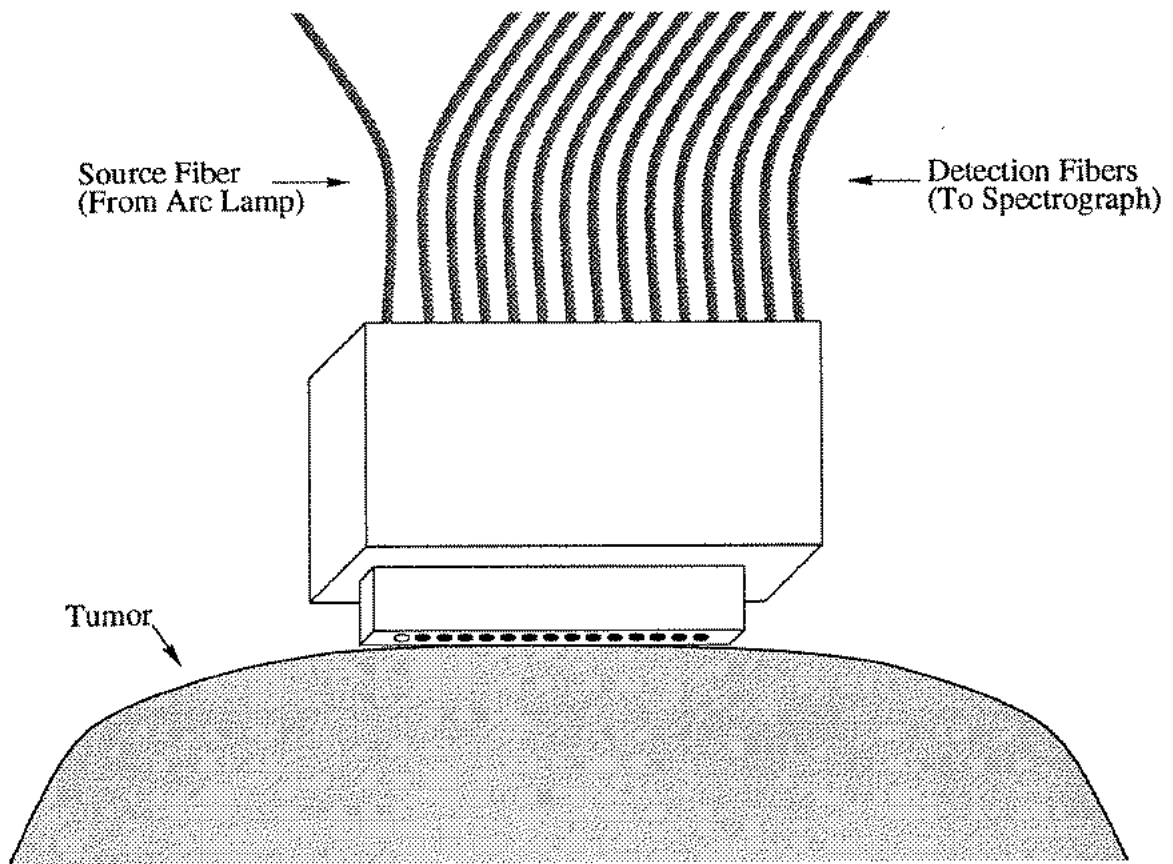


Figure 5.1: A schematic drawing of the optical probe in contact with the tumor surface. A total of 20 detection fibers are located at distances of 1.0 to 20.0 mm from the source fiber.

scattering spectra in this way, the tissue oxy- and deoxyhemoglobin concentrations, water concentration, and background absorption spectrum were determined using the singular value decomposition (SVD) algorithm described in Section 4.2.2.2.

5.2.2 Animals and Tumors

R3230 mammary adenocarcinomas were serially transplanted subcutaneously in the abdominal region of female Fischer rats (100 - 120 g). Tumor sections having dimensions of 1 mm x 1 mm x 3 mm were implanted using a sterile trochar technique [17]. Implantation of this rectangular tissue section produced ellipsoidal tumor volumes that were in general more viable at sizes suitable for spectroscopy than the hemispherical tumors that result from similarly transplanted 1 mm x 1 mm x 1 mm sections. Spectroscopy was performed when tumor dimensions were approximately 20 mm x 12 mm. Assuming an ellipsoidal geometry, these dimensions correspond to tumor volumes of approximately 1.5 cc. In order to immobilize the animal and to avoid stress associated with confinement, anesthetic (75 mg kg⁻¹ ketamine hydrochloride and 6 mg kg⁻¹ xylazene) was administered prior to data acquisition and was given in smaller doses (0.4 of initial) as needed (approximately every 20 min). Carbogen (5% CO₂, 95% O₂) or air was administered via a nose cone at a flow rate of 3 liters min⁻¹. Animal care was conducted according to guidelines established by the University Committee on Animal Resources at the University of Rochester.

5.3 Results

Figure 5.2 shows representative absorption spectra reconstructed from diffusion theory analysis of diffuse reflectance measurements made on the skin surface directly over an

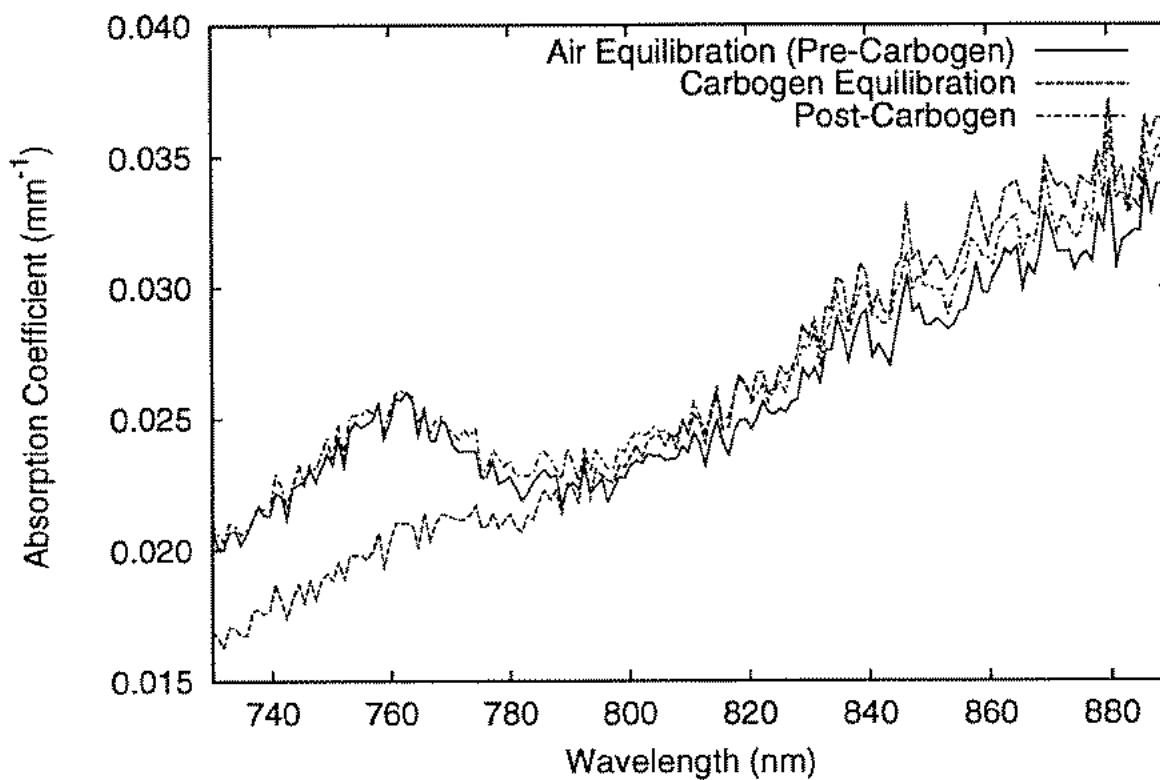


Figure 5.2: Absorption spectra reconstructed from diffuse reflectance measurements performed on an R3230AC tumor prior to carbogen delivery (—), during maximum response to carbogen (---), and upon restoration of equilibrium after carbogen was stopped (- - -).

R3230AC tumor in a living, anesthetized animal. Three cases are presented corresponding to (i) the animal breathing room air, (ii) during carbogen inhalation, and (iii) several minutes after the cessation of carbogen administration. The characteristic deoxyhemoglobin peak near 760 nm was evident in all spectra recorded from tumors during inhalation of room air (solid line in Fig 4.2). With the onset of carbogen breathing, the amplitude of this peak rapidly decreased, and the qualitative appearance of the spectrum reflected a larger oxyhemoglobin contribution (dashed line). At the end of carbogen delivery, the spectrum gradually returned to its baseline shape, however, the time required for this restoration was quite variable in different animals and was sometimes as long as 16 min.

Figure 5.3 shows results of applying the SVD analysis to the absorption spectra depicted in Figure 5.2. The spectrum in Figure 5.3a was obtained while the rat breathed room air, while that in Figure 5.3b was taken during carbogen inhalation. In both cases, the data points (with uncertainties) are the individual absorption coefficients obtained from analysis of the diffuse reflectance measurements. The solid lines are the SVD estimate of the absorption from hemoglobin (oxy- plus deoxyhemoglobin), while the dot-dashed lines are the estimates of the absorbing background. The dashed line through the data points represents the sum of all components of the fitted absorption spectrum. Thus, by separating the contribution of hemoglobin to the total absorption coefficient from that of the other chromophores, the method ensures that only the hemoglobin absorption is used in the calculation of the hemoglobin oxygen saturations. We note that at least in this particular case, the background absorption of the tumor remained approximately unchanged during carbogen administration.

Hemoglobin oxygen saturations determined from data recorded before, during,

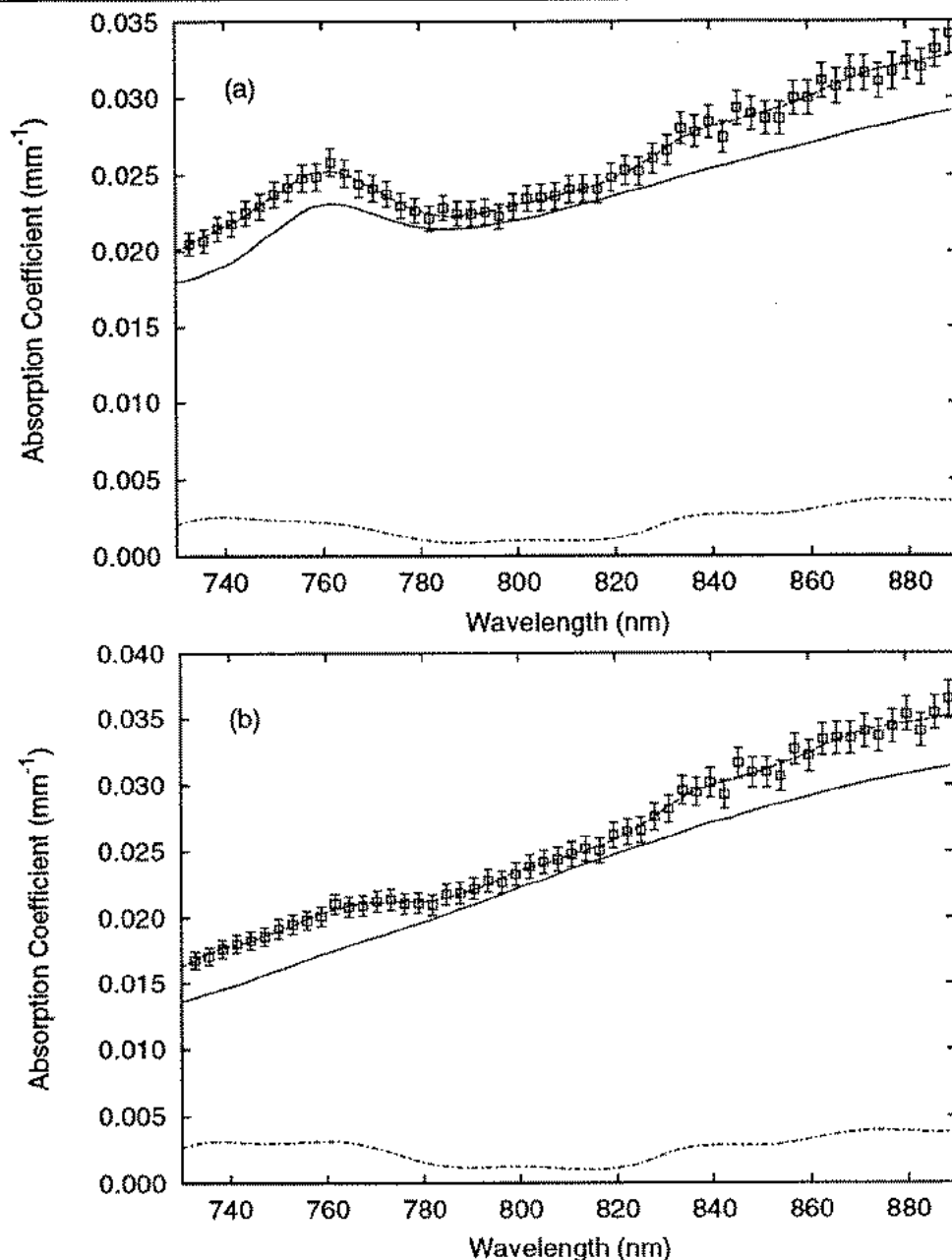


Figure 5.3: Results of the SVD analysis of two of the spectra shown in Figure 5.2. The symbols (\square) depict the absorption coefficients (μ_a) derived from the diffusion theory analysis of the diffuse reflectance measurements, the solid lines (—) depict the SVD estimate of the contribution resulting from hemoglobin (oxy- plus deoxy-), and the dot-dashed lines (— · —) show the SVD estimates of the tumor absorption that result from chromophores other than hemoglobin. The dashed line (---) represents the sum of the hemoglobin and background spectra. The spectrum in (a) was taken prior to carbogen; the spectrum in (b) was acquired during maximum response to carbogen.

and after carbogen inhalation are shown for a representative tumor in Figure 5.4a. The vertical, dotted line at time = 0 s indicates the beginning of carbogen breathing; the second vertical line indicates the end. Figure 5.4b shows separately the concentrations of Hb, HbO₂ and total hemoglobin ([Hb] + [HbO₂]) for the tumor over the same time course. In this case, the initial SO₂ was slightly greater than 0.75. With the onset of carbogen breathing, the saturation rose over a period of approximately 50 s to 0.97, where it remained very constant for the duration of administration. During the period after carbogen was stopped, the saturation remained at or near its highest level for 30 s, after which it gradually declined over the next 100 s until reaching an apparent equilibrium, which was slightly elevated with respect to the initial baseline value. This pattern is reflected in the concentrations of Hb (■) and HbO₂ (□) plotted in Figure 5.4b. In this tumor, the total hemoglobin concentration (●) remained approximately constant.

Although a possible mechanism for the observed increase in tumor oxygenation is an increased hemoglobin concentration, which might be expected in response to vasodilation or to the resumption of flow in acutely closed tumor blood vessels, our data demonstrate that such a mechanism was not responsible for the enhanced saturations. In Figure 5.5, we plot the maximum change in tumor SO₂ vs. the change in the total hemoglobin concentration for the 16 tumors in the study. The majority (10 of 16) of tumors showed a decreased hemoglobin concentration at the time corresponding to the peak oxygen enhancement. In three tumors the hemoglobin concentration remained approximately constant, while in three others, the concentration increased. Among all tumors, there was no correlation between the magnitude of the change in the hemoglobin concentration (either positive or negative) and the increase in the measured tumor SO₂.

The data in Figure 5.6 compare the maximum change in tumor SO₂ with the

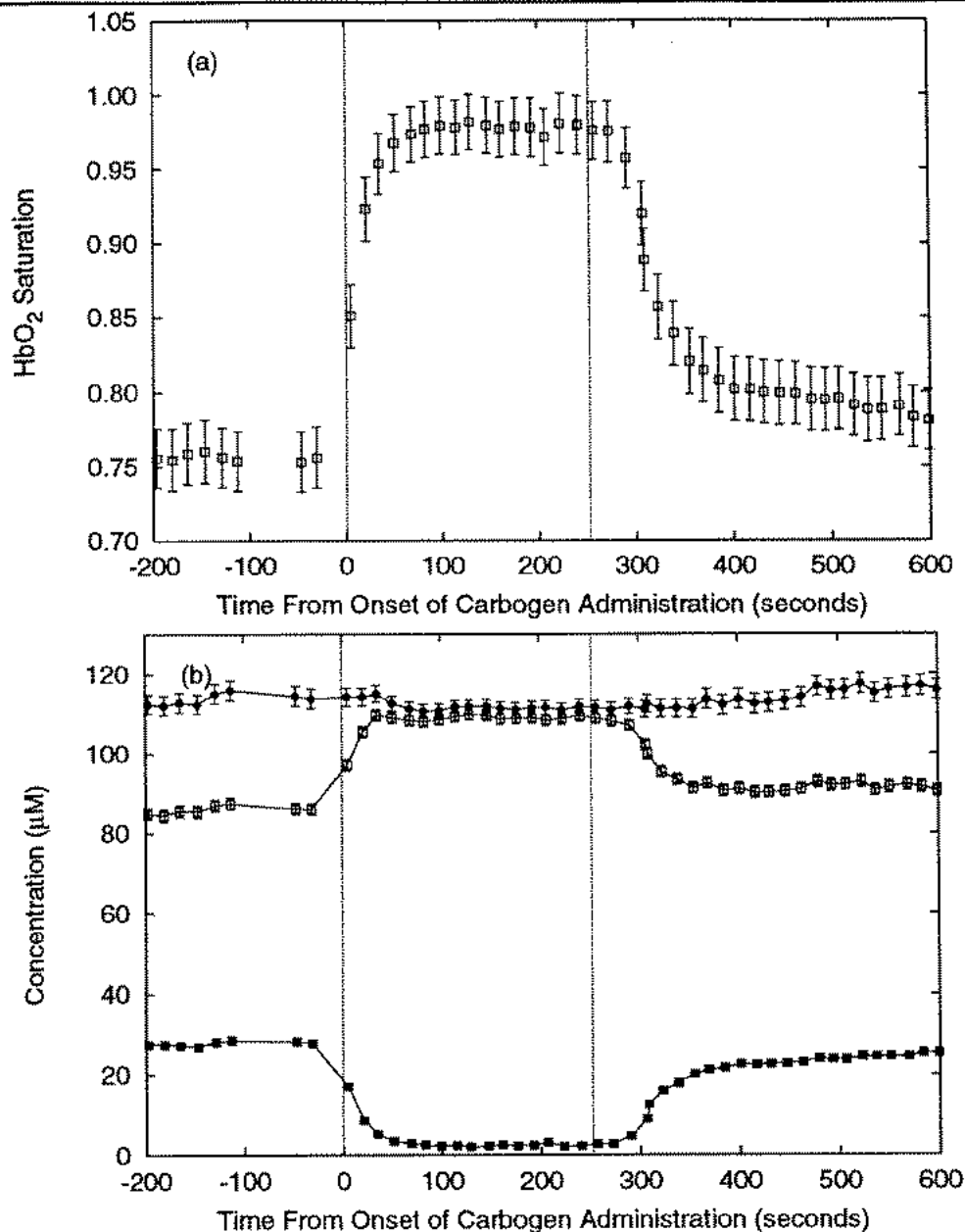


Figure 5.4: Hemoglobin oxygen saturation (a) and concentrations (b) of total hemoglobin (●), oxyhemoglobin (□), and deoxyhemoglobin (■) for a single R3230AC tumor before, during, and after carbogen breathing. The vertical line at time = 0 corresponds to the beginning of carbogen inhalation; the vertical line at the later time corresponds to the end.

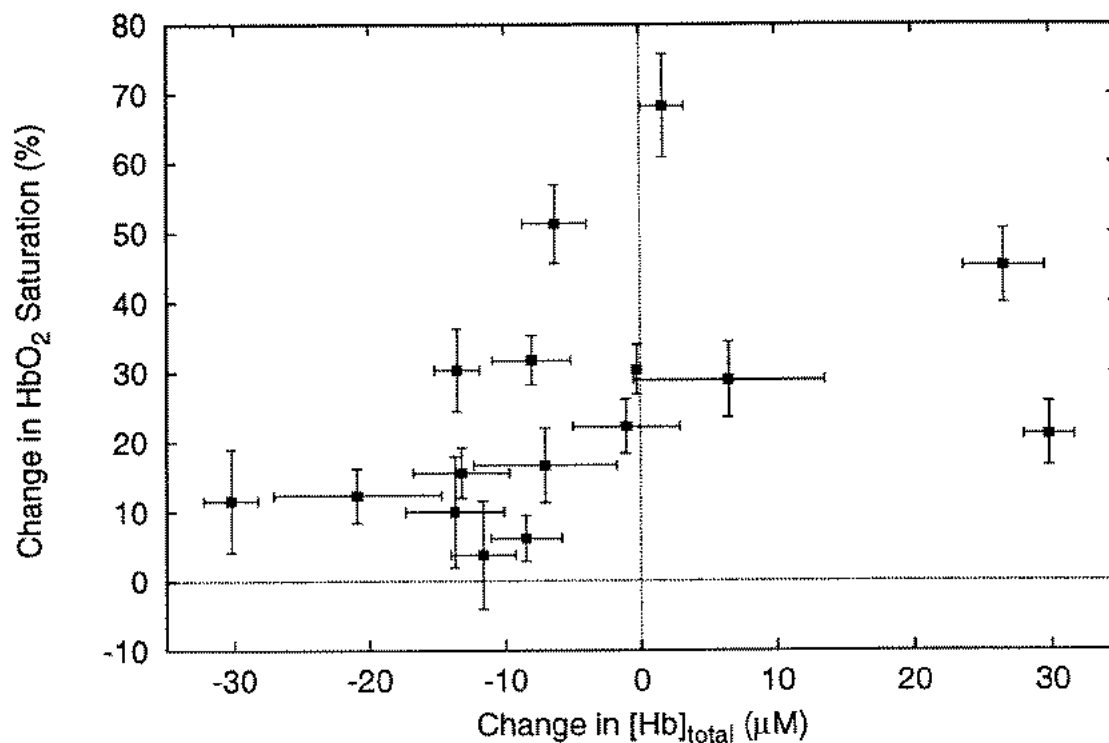


Figure 5.5: The carbogen-induced change in hemoglobin oxygen saturation (maximum saturation minus initial saturation) vs. the change in the total hemoglobin concentration (hemoglobin concentration at the time of maximum saturation minus initial concentration) for all tumors included in this study (n=16).

initial saturation measured immediately prior to carbogen administration. There appear to be roughly two subpopulations of tumors, one of which exhibits a greater degree of change in saturation than the other for a given initial SO_2 . Within each of these subpopulations, there is a trend toward a larger carbogen-induced change for tumors with lower initial saturation. Using a pH of 7.15 for the R3230AC tumor, which has been determined by Ceckler et al. from ^{31}P NMR spectroscopy measurements [18], and the Hill parameters n (2.46) and p_{50} (33.7 torr) corresponding to this pH [19,20], we fit an expression of the form

$$\Delta SO_2 = \frac{\left[\left(\frac{SO_{2init} P_{50}^n}{1 - SO_{2init}} \right)^{\frac{1}{n}} + \Delta pO_2 \right]^n}{P_{50}^n + \left[\left(\frac{SO_{2init} P_{50}^n}{1 - SO_{2init}} \right)^{\frac{1}{n}} + \Delta pO_2 \right]^n} - SO_{2init} \quad (5.1)$$

to the data in Figure 5.6 to find the average change in blood pO_2 (ΔpO_2) induced by carbogen. The derivation of this equation is presented in the Appendix. The fit of Equation 5.1 to the data is shown as the solid line in Figure 5.6, and the carbogen-induced change in pO_2 returned by the fit is 29.7 ± 6.6 torr.

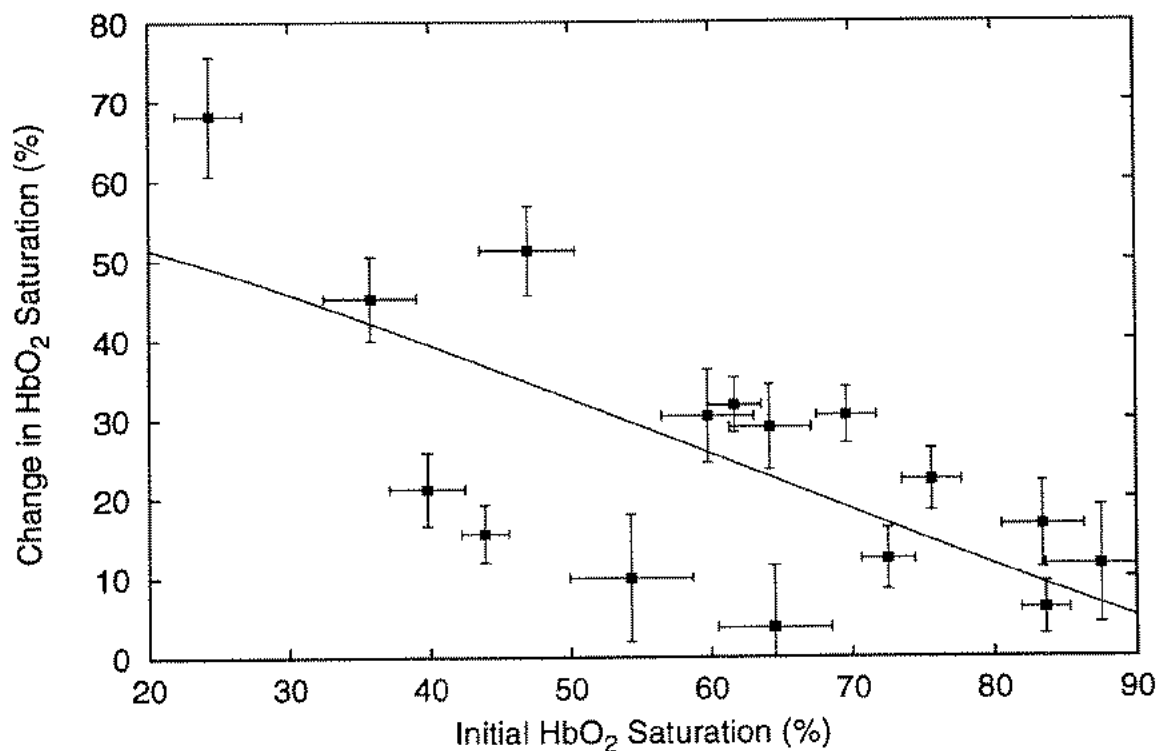


Figure 5.6: The maximum carbogen-induced change in hemoglobin oxygen saturation vs. the initial saturation for all tumors included in this study ($n=16$). The solid line is a fit of Equation 5.1 to these data. The fit yielded a carbogen-induced change in blood pO_2 of 29.7 ± 6.6 torr.

5.4 Discussion

Spatially-averaged tumor hemoglobin oxygen saturation (SO_2) and hemoglobin concentration are reported through noninvasive measurements of near infrared diffuse reflectance. The near-infrared measurement samples all vessels within the light field and thus reports an average that is presumably weighted by the relative arterial and venous volumes. In the series of experiments described here, the magnitude of the change in SO_2 induced by carbogen was highly variable, although in every tumor ($n = 16$) we observed some increase in saturation. The rate of increase in the saturation was relatively rapid, with the maximum SO_2 typically reached within 1 minute after carbogen breathing began. With the termination of carbogen administration, the return to baseline SO_2 was slower, sometimes taking as long as 15 minutes. The mechanism through which carbogen inhalation enhanced the SO_2 in this tumor model clearly did not involve increasing the total hemoglobin concentration, as would occur if, for example, the total tumor blood volume increased. Indeed, as is evident from the data shown in Fig. 4.5, in the majority of tumors, the total hemoglobin concentration decreased in response to carbogen breathing. This observation may be a consequence of the "steal effect", in which vasodilation in the normal circulation results in a loss of blood volume in the tumor, where physiological regulation is deficient or absent. Among the tumors that exhibited decreased hemoglobin volume, the extent of volume change was not related to the magnitude of the increase in the SO_2 (Figure 5.5).

The data suggest a relationship between the extent of the carbogen-induced change in saturation and the initial SO_2 of the tumor, with a tendency for the largest induced changes to occur in those tumors with the lowest initial saturations (Figure 5.6). Qualitatively, one way that this relationship can be understood is on the basis of

the shape of the hemoglobin-oxygen dissociation curve (the Hill curve). At the lower oxygen partial pressures where the Hill curve is roughly linear, an increase in partial pressure will give rise to a corresponding increase in the SO_2 . At higher partial pressures where the slope of the Hill curve becomes more gradual, the same increase in blood oxygen content will produce a lesser effect on the saturation. With respect to the magnitude of this dependence, the data presented in Figure 5.6 also suggest that there may be two subpopulations of tumors in our study. This finding could be a result of the sensitivity of the Hill curve to pH [19,21], although we have no direct evidence to support this interpretation. In more acidic environments, hemoglobin more readily releases oxygen at a given oxygen partial pressure. Thus, a particular tumor's pH will influence the extent to which an induced change in blood pO_2 will be reflected in an increased SO_2 . Our observations may be explained either by differences in the initial pH in subpopulations of these tumors or by differences in the response to CO_2 in these subpopulations.

In addition to the variability in the extent of the carbogen-induced change in tumor SO_2 , the data presented in Figures 4.5 and 4.6 show that the initial (pre-carbogen) SO_2 and the carbogen-induced change in total hemoglobin concentration also varied significantly for the 16 tumors in this study. The reasons for this pronounced heterogeneity are not clear. There was no obvious relationship between initial SO_2 and tumor volume (data not shown). Although the initial anesthetic dose administered to the animals was constant, some variation in the time between injection of anesthetic and the diffuse reflectance measurements was inevitable. The need for smaller subsequent injections to sustain chemical restraint was also variable among animals, and it is possible that one or the combination of these anesthetic-related effects was responsible for some of the observed variability in the data. We note, however, that

investigators using other techniques have also reported significant intratumor and intertumor heterogeneity in SO_2 within the same tumor type ([22], and references therein). Clearly, a detailed appreciation of the physiological information available from near infrared spectroscopy is not yet available, and studies designed to further this understanding appear to be warranted. Comparisons of tumor SO_2 determined in vivo using near infrared spectroscopy with similar determinations made using cryospectroscopy [22] would be particularly relevant, in that the latter technique provides hemoglobin saturations in individual vessels in frozen tumor sections.

As we have implemented the technique, near infrared spectroscopy (NIRS) provides a measure of the average hemoglobin SO_2 and therefore of the average response to oxygen modifiers such as carbogen in the volume of tissue sampled by the optical probe. It is possible to consider approaches to low resolution imaging of tissue optical properties using near infrared light, which in principle may allow spatially resolved determinations of tumor SO_2 [23]. Whether or not this spectroscopy will be a clinically useful predictor of tumor response to oxygen-dependent interventions such as ionizing radiation therapy and photodynamic therapy remains to be determined. Nevertheless, the method possesses attractive features that make it potentially useful as a research tool and eventually perhaps in some clinical settings. NIRS is completely noninvasive, thereby making it suitable in situations where it is desirable to perform repeated measurements on the same tumor, for example, during a course of fractionated radiation therapy. Its noninvasive character also means that it does not perturb tissue oxygen, either by oxygen consumption or by induction of bleeding, and it is likely to be well tolerated by patients. The method reports hemoglobin oxygen saturation directly, which will likely be useful in discerning mechanisms of action of various modifiers of tumor oxygenation. Recently, for instance, Robinson et al. [24,25]

have described changes in gradient-echo magnetic resonance images in response to carbogen breathing in animal tumor models. The magnetic resonance signal from flowing blood may be influenced by its deoxyhemoglobin content or by its degree of saturation (i.e., incomplete restoration of equilibrium) from repetitive radiofrequency pulses. Thus, from an enhanced signal in a gradient echo MR image alone it is in general not possible to distinguish between a decreased deoxyhemoglobin concentration and a reduction in the saturation of the MR signal as a result of increased blood flow velocity (without a change in deoxyhemoglobin) through the region of interest [24]. Because NIRS is capable of determining the SO_2 independent of hemodynamic changes, it could be useful in resolving ambiguities like this one. NIRS provides good temporal resolution, with signal acquisition times on our system of approximately 5 s. Finally, the instrumentation required to perform the steady-state form of diffuse reflectance spectroscopy is relatively inexpensive and can be as portable as an ultrasound system, thereby making it possible to consider measurements in the clinic immediately prior to or during therapy.

Of course, the method is not without its own limitations, especially in its current form. Although significantly reduced optical absorption of water and of hemoglobin in the near infrared spectral region (650 - 900 nm) enables light to penetrate several centimeters in tissue, it is unlikely that NIRS will be useful in the quantitative evaluation of hemoglobin saturation in tumors residing far from a surface that is accessible to an optical fiber probe. Further, the particular form of analysis that we have adopted assumes spatially homogeneous optical properties. This assumption, however, is not fundamental to the approach. Very recent work by other investigators has demonstrated diffusion theory based expressions that are capable of extracting optical properties of layered structures, provided that the thickness of the upper layer

in contact with the optical probe is not too thick [26]. Another limitation imposed by the diffusion theory approximation to light transport is that, in order to recover accurate values of the absorption coefficients, relatively large (approximately 15 mm) separations are required between the optical fiber that delivers light to the tissue and the most remote detection fiber. Although this requirement precludes the use of this technique on smaller tumors at present, it is not fundamental to the optical method and may be relaxed using other theoretical approaches. Investigation of suitable alternatives is an active area of research in several laboratories.

The need for improved methods of monitoring tumor oxygenation in patients continues to be recognized [15,27]. Even with its current limitations, the ability of NIRS to determine SO_2 noninvasively and to monitor changes induced by carbogen inhalation is sufficiently encouraging that its use could be considered in several anatomic sites where hypoxia has been recognized as a significant factor influencing the resistance of tumors to ionizing radiation therapy. These sites include the cervix, head and neck, superficial regions of the breast, and superficial soft tissue in the extremities.

Appendix

The Hill equation describing the hemoglobin-oxygen dissociation curve is written,

$$SO_2 = \frac{pO_2^n}{p_{50}^n + pO_2^n} \quad (5.2)$$

where SO_2 is the hemoglobin oxygen saturation, pO_2 is the oxygen partial pressure, p_{50} is the oxygen partial pressure at which the SO_2 is 0.5, and n is the Hill coefficient. The pH of the R3230AC tumor is approximately 7.15, as determined by Ceckler et al. using

^{31}P NMR spectroscopy [18]. The Hill coefficient, n , and the p_{50} corresponding to this pH are 2.46 and 33.7 torr, respectively [19,20]. In our experiments we measure the initial SO_2 (prior to carbogen delivery), which we denote $\text{SO}_{2\text{init}}$, and the final SO_2 after full equilibration on carbogen, which we denote here as SO_{2f} . The change in saturations, ΔSO_2 , is written simply as

$$\Delta\text{SO}_2 = \text{SO}_{2f} - \text{SO}_{2\text{init}}. \quad (5.3)$$

Writing SO_{2f} in terms of the corresponding $p\text{O}_{2f}$ through Equation 5.2, this becomes

$$\Delta\text{SO}_2 = \frac{p\text{O}_{2f}^n}{p_{50}^n + p\text{O}_{2f}^n} - \text{SO}_{2\text{init}}. \quad (5.4)$$

The $p\text{O}_{2f}$ is the sum of the initial $p\text{O}_2$ and the carbogen-induced change, $\Delta p\text{O}_2$. Expressing the initial $p\text{O}_2$ in terms of the initial SO_2 through Equation 5.2, we can write $p\text{O}_{2f}$ as,

$$p\text{O}_{2f} = \left(\frac{\text{SO}_{2\text{init}} p_{50}^n}{1 - \text{SO}_{2\text{init}}} \right)^{\frac{1}{n}} + \Delta p\text{O}_2. \quad (5.5)$$

Substitution of the right hand side of Equation 5.5 into Equation 5.4 yields

$$\Delta\text{SO}_2 = \frac{\left[\left(\frac{\text{SO}_{2\text{init}} p_{50}^n}{1 - \text{SO}_{2\text{init}}} \right)^{\frac{1}{n}} + \Delta p\text{O}_2 \right]^n}{p_{50}^n + \left[\left(\frac{\text{SO}_{2\text{init}} p_{50}^n}{1 - \text{SO}_{2\text{init}}} \right)^{\frac{1}{n}} + \Delta p\text{O}_2 \right]^n} - \text{SO}_{2\text{init}}, \quad (5.6)$$

which is the function that is fit to the data in Figure 5.6 to extract the carbogen-induced change in blood pO_2 , ΔpO_2 .

References

1. P. Vaupel, K. Schlenger, C. Knoop, and M. Höckel, "Oxygenation of human tumors: evaluation of tissue oxygen distribution in breast cancers by computerized O_2 tension measurements," *Cancer Res.* **51**, 3316-3322 (1991).
2. P. Okunieff, M. Hoeckel, E.P. Dunphy, K. Schlenger, C. Knoop, and P. Vaupel, "Oxygen tension distributions are sufficient to explain the local response of human breast tumors treated with radiation alone," *Int. J. Radiat. Oncol. Biol. Phys.* **26**, 631-636 (1993).
3. M. Höckel, C. Knoop, K. Schlenger, B. Vorndran, E. Baußmann, M. Mitze, P.G. Knapstein, and P. Vaupel, "Intratumoral pO_2 predicts survival in advanced cancer of the uterine cervix," *Radiother. Oncol.* **26**, 45-50 (1993).
4. D.M. Brizel, G.S. Sibley, L.R. Prosnitz, R.L. Scher, and M.W. Dewhirst, "Tumor hypoxia adversely affects the prognosis of carcinoma in the head and neck," *Int. J. Radiat. Oncol. Biol. Phys.* **38**, 285-289 (1997).
5. D.M. Brizel, S.P. Scully, J.M. Harrelson, L.J. Layfield, J.M. Bean, L.R. Prosnitz, and M.W. Dewhirst, "Tumor oxygenation predicts for the likelihood of distant metastases in human soft tissue sarcoma," *Cancer Res.* **56**, 941-943 (1996).
6. T.G. Graeber, C. Osmanian, T. Jacks, D.E. Housman, C.J. Koch, S.W. Lowe, and A.J. Giacca, "Hypoxia-mediated selection of cells with diminished apoptotic potential in solid tumours," *Nature* **379**, 88-91 (1996).
7. R.H. Thomlinson, "An experimental method for comparing treatments of intact malignant tumours in animals and its application to the use of oxygen in radiotherapy," *Br. J. Cancer* **14**, 555-576 (1960).
8. D.M. Brizel, S. Lin, J.L. Johnson, J. Brooks, M.W. Dewhirst, and C.A. Piantadosi, "The mechanisms by which hyperbaric oxygen and carbogen improve tumour oxygenation," *Br. J. Cancer* **75**, 1120-1124 (1995).

9. P.A. VouÛte, A.J. van der Kleij, J. DeKraker, C.A. Hoefnagel, M.M.C. Tiel-van Buul, and H. VanGennip, "Clinical experience with radiation enhancement by hyperbaric oxygen in children with recurrent neuroblastoma stage IV," *Eur. J. Cancer* **31A**, 596-600 (1995).
10. P.L. Olive and W.R. Inch, "Effect of inhaling oxygen/carbon dioxide mixtures on oxygenation and cure by X-rays of the C3HBA mouse mammary carcinoma," *Radiology* **106**, 673-678 (1973).
11. R.P. Hill and R.S. Bush, "Dose fractionation studies with a murine sarcoma under conditions of air or carbogen (95% O₂ + 5% CO₂) breathing," *Int. J. Radiat. Oncol. Biol. Phys.* **2**, 913-919 (1977).
12. C. Grau, M.R. Horsman, and J. Overgaard, "Improving the radiation response in a C3H mouse mammary carcinoma by normobaric oxygen or carbogen breathing," *Int. J. Radiat. Oncol. Biol. Phys.* **22**, 415-419 (1992).
13. M.R. Horsman, D.J. Chaplin, and J.M. Brown, "Tumor radiosensitization by nicotinamide: a result of improved perfusion and oxygenation," *Radiation Research* **118**, 139-150 (1989).
14. A. Rojas, "ARCON: accelerated radiotherapy with carbogen and nicotinamide," *Br. J. Radiol.* **24**, 174-178 (1999).
15. M. Saunders and S. Dische, "Clinical results of hypoxic cell radiosensitization from hyperbaric oxygen to accelerated radiotherapy, carbogen, and nicotinamide," *Br. J. Cancer* **74**, S271-S278(1996).
16. H.B. Stone, J.M. Brown, T.L. Phillips, and R.M. Sutherland, "Oxygen in human tumors: correlations between methods of measurement and response to therapy," *Radiation Research* **136**, 422-434 (1993).
17. R. Hilf, I. Michel, C. Bell, J.J. Freeman, and A. Borman, "Biochemical and morphological properties of a new lactating tumour line in the rat," *Cancer Res.* **25**, 286-299 (1965).

18. T.L. Ceckler, S.L. Gibson, S.D. Kennedy, R. Hilf, and R.G. Bryant, "Heterogeneous tumour response to photodynamic therapy assessed by in vivo localised ^{31}P NMR spectroscopy," *Br. J. Cancer* **63**, 916-922 (1991).
19. A. Zwart, G. Kwant, B. Oeseburg, and W.G. Zijlstra, "Oxygen dissociation curves for whole blood, recorded with an instrument that continuously measures pO_2 and SO_2 independently at constant T, pCO_2 , and pH," *Clin. Chem.* **28**, 1287-1292 (1982).
20. A. Zwart, G. Kwant, B. Oeseburg, and W.G. Zijlstra, "Human whole blood oxygen affinity - effect of temperature," *J. Appl. Physiol.* **57**, 429-434 (1984).
21. R.E. Benesch and R. Benesch, "The mechanism of interaction of red cell organic phosphates with hemoglobin," *Adv. Protein. Chem.* **28**, 211-237 (1974).
22. B.M. Fenton, R.F. Raubertas, and D.J. Boyce, "Quantification of micro-regional heterogeneities in tumour oxygenation using intravascular HbO_2 saturations," *Radiation Research* **141**, 49-56 (1995).
23. R.M. Danen, Y. Wang, X.D. Li, W.S. Thayer, and A. Yodh, "Regional imager for low-resolution functional imaging of the brain with diffusing near-infrared light," *Photochem. Photobiol.* **67**, 33-40 (1998).
24. S.P. Robinson, L.M. Rodrigues, A.S.E. Ojugo, P.M.J. McSheehy, F.A. Howe, and J.R. Griffiths, "The response to carbogen breathing in experimental tumor models monitored by gradient-recalled echo magnetic resonance imaging," *Br. J. Cancer* **75**, 1000-1006 (1997).
25. S.P. Robinson, F.A. Howe, and J.R. Griffiths, "Non-invasive monitoring of carbogen-induced changes in tumor blood flow and oxygenation by functional magnetic resonance imaging," *Int. J. Radiat. Oncol. Biol. Phys.* **33**, 855-859 (1995).
26. A. Kienle, M.S. Patterson, N. Dognitz, R. Bays, G. Wagnieres, and H. van den Bergh, "Noninvasive determination of the optical properties of two-layered turbid media," *Appl. Opt.* **37**, 779-791 (1998).

27. M. Höckel, B. Vorndran, K. Schlenger, E. Baußmann, and P.G. Knapstein, "Tumor oxygenation: a new predictive parameter in locally advanced cancer of the uterine cervix," *Gynecol. Oncol.* **51**, 141-149 (1993).

CHAPTER 6

Localization of Luminescent Inhomogeneities in Turbid Media with Spatially Resolved Measurements of CW Diffuse Luminescence Emittance

6.1 Introduction

The potential use of near infrared (NIR) radiation for diagnostic medical imaging has generated a significant volume of research in recent years [1,2]. Many of these efforts involve the use of theoretical models based on the diffusion theory of light transport in tissue in order to reconstruct maps of the local optical absorption or transport scattering coefficients [3-5]. These approaches are particularly useful when inherent absorption contrast is high, as in recent reports of NIR imaging of neonatal brain hemorrhage [6]. The photophysical properties of tissue fluorescence (*i.e.*, the fluorescence spectrum, quantum yield, and lifetime) may also provide useful sources of intrinsic optical contrast. Certain features of the autofluorescence spectrum of the breast [7], colon [8], bronchus [9], and cervix [10] have been shown to be suppressed or elevated in malignant tissues relative to their normal counterparts. In addition, an increase in fluorescence lifetime of endogenous fluorophores in certain lesions has been observed [11]. While these properties make autofluorescence an excellent tool for superficial imaging applications, optical imaging of inclusions at more remote depths

(~5-50 mm) requires radiation within the “therapeutic window” (approximately 650-950 nm), where most endogenous fluorophores absorb/fluoresce weakly. In these cases, administration of a luminescent agent may provide contrast not achievable with other methods.

The possibility of using exogenously administered fluorescent or phosphorescent dyes as contrast agents for optical imaging has been recognized and studied by several groups. This potential has spawned research to develop new candidate tumor-seeking fluorescent molecules with relatively high selective tumor accumulation (tumor to normal tissue ratios on the order of 10:1) and low photodynamic action [12-14]. Other researchers have begun to synthesize phosphorescent probes with significant extinction in the 630-700 nm wavelength region and emission maxima well into the near-infrared [15]. These types of contrast agents are of particular interest since fluorescence and phosphorescence lifetime imaging may provide information about physiological and biochemical status in addition to anatomic location of disease [16-18]. Some recently reported experimental and modeling work using time-resolved and frequency-domain methods in tissue-simulating phantoms suggests that it may be possible to image fluorescent inhomogeneities under conditions that are relevant to important clinical situations such as mammography. Wu *et al.* utilized the measured rise-time of fluorescence induced by femtosecond excitation pulses as an indicator of the depth of fluorescent sources buried as deep as 60 mm in a medium with a mean free path of 4.0 mm [19]. Hutchinson *et al.* [17], O’Leary *et al.* [18], and Paithankar *et al.* [20] have performed computational studies demonstrating the possibility of fluorophore lifetime imaging in the frequency domain. Boas *et al.* [21] and O’Leary *et al.* [22] demonstrated the possibility of reconstructing the origin of a diffuse photon density wave emitted by an embedded object in a turbid medium irradiated by an amplitude

modulated excitation beam. Knüttel *et al.* were able to identify the lateral position of an embedded fluorescent object with measurements of the shift in the null plane produced by two interfering sources of diffuse photon density waves [23]. Recently, Li *et al.* have evaluated detection limits of frequency- and time-domain techniques for imaging fluorophore concentration and lifetime [24].

This chapter describes a continuous wave (cw) method for localizing a source of luminescence buried deep within a scattering medium. In this method, spatially-resolved measurements of the cw luminescence emittance are analyzed using an approximate diffusion theory Green's function to reconstruct the origin of the emission. The Green's function is a generalization of theoretical models described in Chapter 2.

The experiments reported here were performed with small, point-like luminescent sources under conditions of ideal partitioning of the luminescent species into the targetted region. This approach was adopted to test rigorously the limitations of the theoretical Green's function under investigation. The eventual reconstruction of extended sources of luminescence will require the incorporation of this Green's function into a full imaging algorithm which models the attenuation of the excitation beam and allows for the convolution of the Green's function over a generalized source distribution. An example of such an algorithm applied to cw luminescence optical tomography has recently been published by Chang *et al.* [5]. In more realistic situations where luminescent contrast agent partitioning is not ideal, the approximately exponential attenuation of the excitation beam may result in background luminescence which greatly exceeds the signal from all but the most shallow target inhomogeneities. This situation is studied theoretically in section 6.5. While this limitation may preclude the practical clinical implementation of the method in those situations where contrast is based solely on preferential uptake and/or retention of a luminescent contrast agent,

other approaches which exploit physiological contrast are particularly well suited to this imaging method. Two such approaches are described in section 6.6.

6.2 Theory

In section 2.5, a Green's function satisfying the diffusion-theory extrapolated-boundary condition was developed for the emittance from an isotropic point source at depth z_0 in a semi-infinite turbid medium. That function may be expressed

$$E(\rho; z_0) = C_\phi \psi(\rho; z_0) + C_j j_z(\rho; z_0) \quad , \quad (6.1)$$

where

$$\psi(\rho, z=0; z_0) = \frac{1}{4\pi D} \left(\frac{\exp(-\mu_{eff} r_1)}{r_1} - \frac{\exp(-\mu_{eff} r_2)}{r_2} \right) \quad , \quad (6.2)$$

and

$$j_z(\rho, z=0; z_0) = \frac{1}{4\pi} \left[z_0 \left(\mu_{eff} + \frac{1}{r_1} \right) \frac{\exp(-\mu_{eff} r_1)}{r_1^2} + \left(z_0 + 2z_b \right) \left(\mu_{eff} + \frac{1}{r_2} \right) \frac{\exp(-\mu_{eff} r_2)}{r_2^2} \right] \quad . \quad (6.3)$$

In these equations, r_1 and r_2 are distances from an observation point on the surface of the medium ($r=\rho$, $z=0$) to the buried source and a negative image source, respectively, and z_b is the extrapolated boundary position ($z_b=2AD$, where A is the internal reflection coefficient). This geometry is reproduced in Figure 6.1. For a detector having a 180° acceptance angle, assuming an air/tissue refractive index mismatch of 1.4 ($A=2.95$), $C_1=0.1178$ and $C_2=0.3056$. If an optical fiber with refractive index 1.46 and numerical aperture 0.22 is used for detection, $C_\phi=0.0062$ and $C_j=0.0184$.

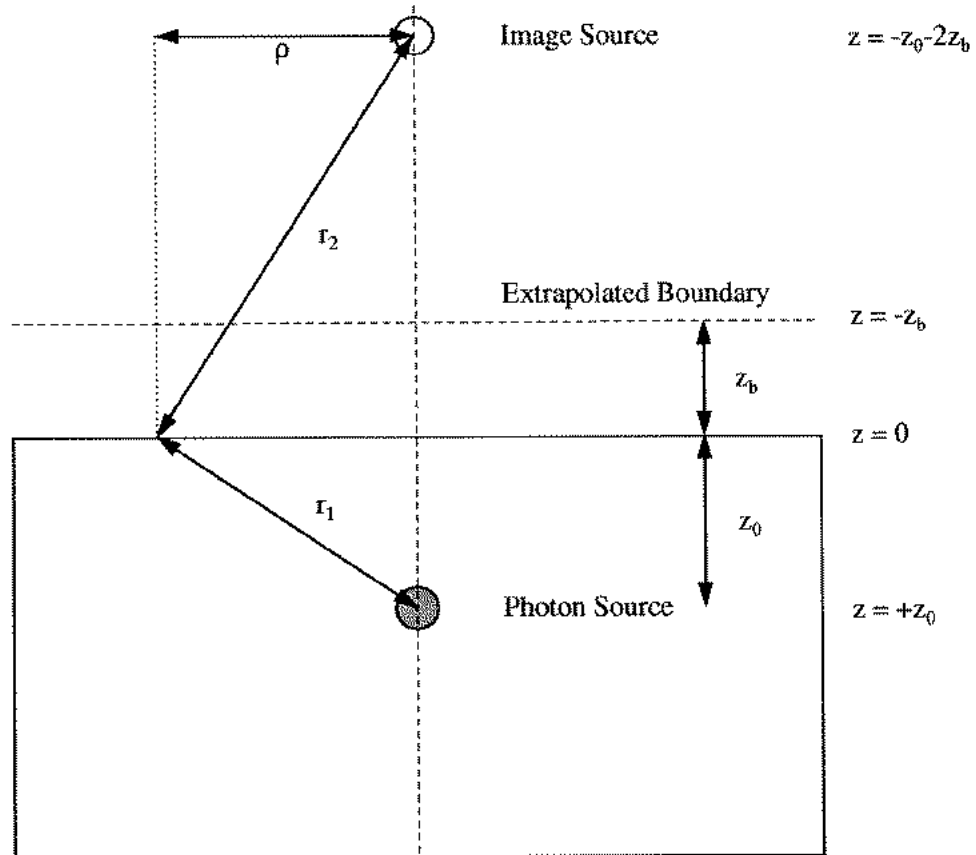


Figure 6.1 Dipole approximation for the emittance due to an isotropic point source at depth z_0 in an optically turbid semi-infinite medium. The image source is located at a position such that the fluence extrapolates to zero on a fictitious boundary.

In chapters 2-5, Equation 6.1 was used to analyze the *reflectance* $R(\rho)$ resulting from an incident pencil beam (modelled as an isotropic source at a depth of $z_0 = 1/\mu_s'$). More generally, Equation 6.1 describes the diffuse *emittance* $E(\rho)$ at the surface of a scattering medium from a point source located at any arbitrary depth z_0 . In both cases, the theoretical expressions may be fit to experimental data to extract z_0 and μ_{eff} as fitting parameters. In the reflectance analysis, these values may then be used to determine the optical properties μ_a and μ_s' , since the source depth is a known function of these parameters. In this chapter the emittance formulation is considered, which allows for the determination of μ_{eff} as well as the depth of a photon source at an arbitrary location in the medium. It has been convenient in these studies to normalize the data to the diffuse emittance measured at a known radial distance, ρ_{norm} , from the source. We therefore fit the expression

$$E_{\text{norm}}(\rho; z_0) = \frac{E(\rho; z_0)}{E(\rho_{\text{norm}}; z_0)} \quad (6.4)$$

to the experimental data, where the numerator is the function described in Equation 6.1 and the denominator is the function described in Equation 6.1 evaluated at $\rho = \rho_{\text{norm}}$. This eliminates the need to determine an overall scaling factor.

6.3 Experimental Methods and Results

Experiments were performed on a tissue simulating phantom consisting of a large tank (14.5 cm x 29.5 cm x 15.5 cm) filled with Liposyn-II (Abbott Labs, North Chicago, IL) diluted with distilled water to a lipid volume fraction of 0.9%. A small concentration (3.7 μM) of the nonfluorescent, water soluble dye manganese meso-tetra (4-

sulfonatophenyl) porphine (MnTPPS) (Porphyrin Products, Logan, UT) was added to the Liposyn in order to increase the absorption coefficient to a value typical of biological tissue at the wavelengths of interest. The fluorescent source was a 6.0 mm diameter spherical glass bulb containing the tumor-localizing fluorophore Nile Blue A (NBA) [25,26] diluted in the aqueous scattering emulsion to a concentration of 15.0 μM . The bulb was fixed to a micropositioner, which was used to adjust its position within the phantom. Distances are reported to the center of the spherical bulb.

The optical properties of the phantom were measured by steady-state diffuse reflectance spectroscopy. The transport scattering coefficient of the phantom was 0.97 mm^{-1} at the excitation wavelength (630 nm) and decreased to 0.87 mm^{-1} near the fluorescence maximum of Nile Blue A (~680 nm). The absorption coefficient of the phantom was 0.0016 mm^{-1} at both wavelengths, yielding an effective attenuation coefficient of 0.066 mm^{-1} at 680 nm. The absorption coefficient of the fluorescent source was determined by optical absorption measurements of identically diluted nonscattering samples in a conventional spectrophotometer. At 630 nm, the absorption coefficient of the NBA-containing target was 0.22 mm^{-1} .

A schematic diagram of the experimental apparatus is presented in Figure 6.2. Continuous wave 630 nm excitation light was produced by a standing wave dye laser pumped with an argon-ion laser (Coherent Inc., Irvine, CA). The output of the dye laser was filtered with a bandpass filter (D620/40, Chroma Technology, Battleboro, VT) to reject off-resonance dye fluorescence. The beam was then lens-coupled to an optical fiber terminated with a gradient index (GRIN) lens (General Fiber Optics, Fairfield, NJ), which provided a slowly diverging ($\text{NA} \approx 0.1$) beam with a uniform profile. The beam was recollimated by a second lens to a diameter of approximately 2.0 cm, resulting in a fluence rate at the surface of approximately 160 mW/cm^2 . The excitation

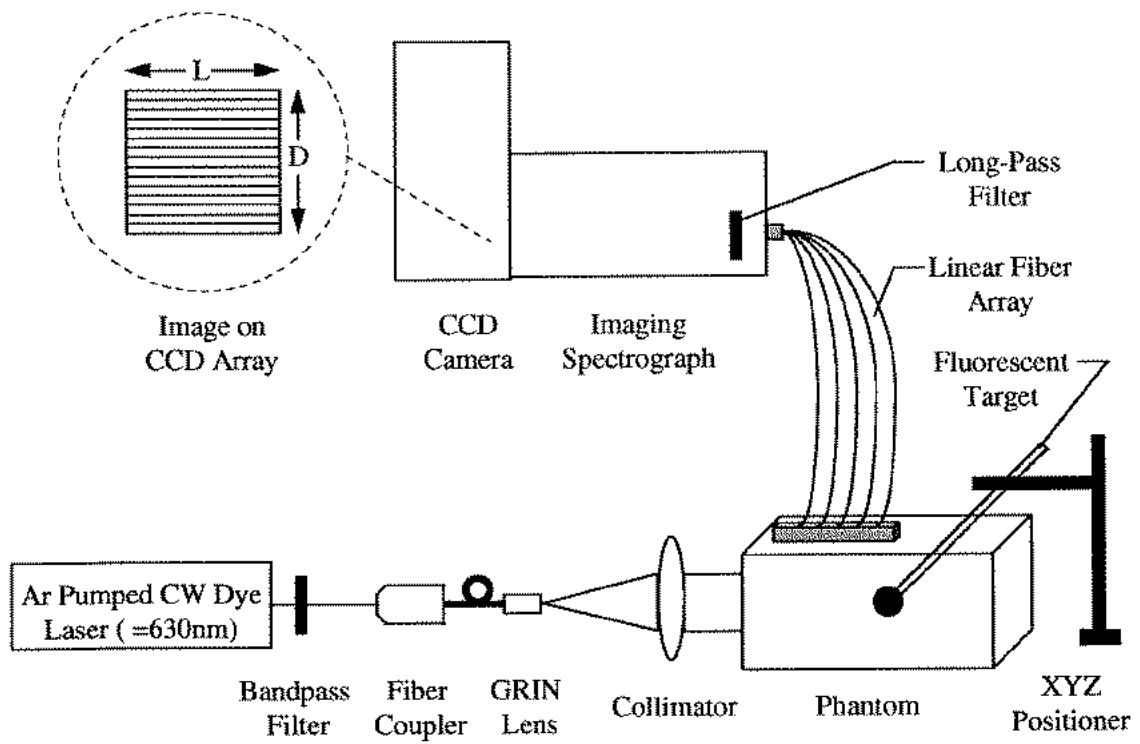


Figure 6.2 Experimental apparatus for fluorescence excitation and detection.

beam was incident from the side of the phantom, and the fluorescent target was positioned approximately 25 mm from this side of the tank.

Fluorescence detection was accomplished with a linear array of fourteen, 200 μm diameter fibers separated from one another by known distances and spanning a distance of approximately 50 mm along the surface of the phantom. The index of refraction of the fiber core was 1.46 and the numerical aperture was 0.22. The detection fiber array was positioned on the top surface of the phantom, with the ends of the fibers in mechanical contact with the phantom surface. The distal ends of the detection fibers were gathered into a row and placed in the focal plane of a 0.275 m imaging spectrograph (Acton Research Corporation, Acton, MA). The fiber ends were imaged through a low resolution, high dispersion grating (300 g/mm) onto the surface of a liquid nitrogen cooled, 512x512, 16 bit CCD camera (Princeton Instruments, Princeton, NJ). The signal at the detector is therefore the spectrally-dispersed fluorescence emittance collected at 14 known positions on the surface of the phantom, oriented such that the signals from the individual detection fibers lie in non-overlapping regions of the CCD array perpendicular to the axis of the spectrograph entrance slit. Rejection of excitation light was enhanced by placing a long-pass filter (Schott, RG 660) in the optical path of the spectrograph. Signal in the wavelength range 670-690 nm was collected in a single bin on the CCD, requiring integration times ranging from 10 seconds for source depths of 6.6 mm to 245 seconds for source depths of 44.6 mm. The dark current of the detector is negligible on these time scales.

Although no NBA was added to the tissue simulating phantom into which the fluorescent target was placed, Raman-shifted excitation light produced a background signal in the wavelength region of the NBA fluorescence maximum. This background signal was dominated by a Raman line associated with the lipids in the scattering

emulsion ($\sim 1050 \text{ cm}^{-1}$), but a significantly weaker water line ($\sim 3350 \text{ cm}^{-1}$) also contributed. For source depths of 10 mm, the Raman background was on the order of 15% of the total signal in the region of interest on the CCD array. When sources as deep as 50 mm were used, the background levels reached 95% or more of the full 16 bits of dynamic range available at the detector. For this reason, all measurements reported here have been background-corrected. The background was measured by removing the spherical fluorescent source and sampling the signal reaching the detector under otherwise identical experimental conditions.

Representative experimental data are plotted in Figure 6.3, where the data points are measured values of the diffuse fluorescence emittance, with $\rho_{\text{norm}} = 3.43 \text{ mm}$ (the position of the first detection fiber). Error bars were assigned by applying Poisson counting statistics to the background-corrected fluorescence signal binned on the CCD but are not shown since they are smaller than the data points in all cases. For the three data sets illustrated in Figure 6.3, the source was positioned at depths of $z_0 = 39.6 \text{ mm}$, 14.6 mm , and 6.6 mm . Equation 6.4 was fit to these data using a Levenberg-Marquardt nonlinear least squares fitting algorithm [27]. These fits are depicted by the solid lines in Figure 6.3. In all fits to experimental data, μ_{eff} and the source depth (z_0) were extracted as fitting parameters, and the extrapolated boundary position was held fixed at $z_b = 2.00 \text{ mm}$. This value deviates from the exact theoretical value for z_b (2.26 mm) and was chosen in order to demonstrate the insensitivity of the method to small errors in the estimated value for z_b . The results of fitting a complete series of experimental data are summarized in Figure 6.4, where the fitted values for z_0 (data points) are plotted as a function of the actual depth of the source. The solid line is the line of exact agreement between actual and fitted values. The data indicate that sources residing at depths up to 40 mm were located with an accuracy of 1.0 mm or

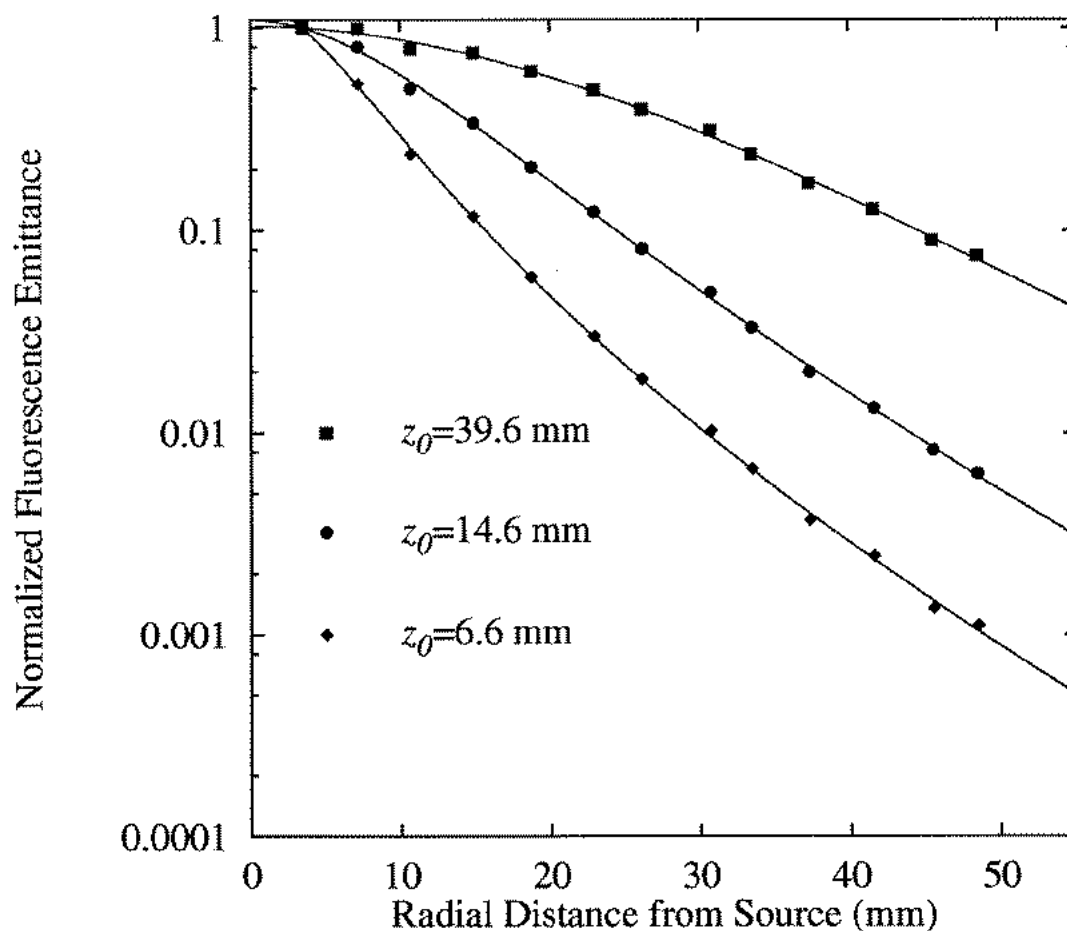


Figure 6.3 Representative experimental diffuse fluorescence emittance data (symbols) and best fits of Equation 6.4 to the data (lines). The actual source depths are indicated on the plot. The best fit values of z_0 were 40.6 ± 2.6 , 14.3 ± 0.3 , and 6.9 ± 0.1 mm, respectively. Error bars were assigned by applying Poisson counting statistics to the background-corrected fluorescence signal binned on the CCD but are not shown since they are smaller than the symbols in all cases.

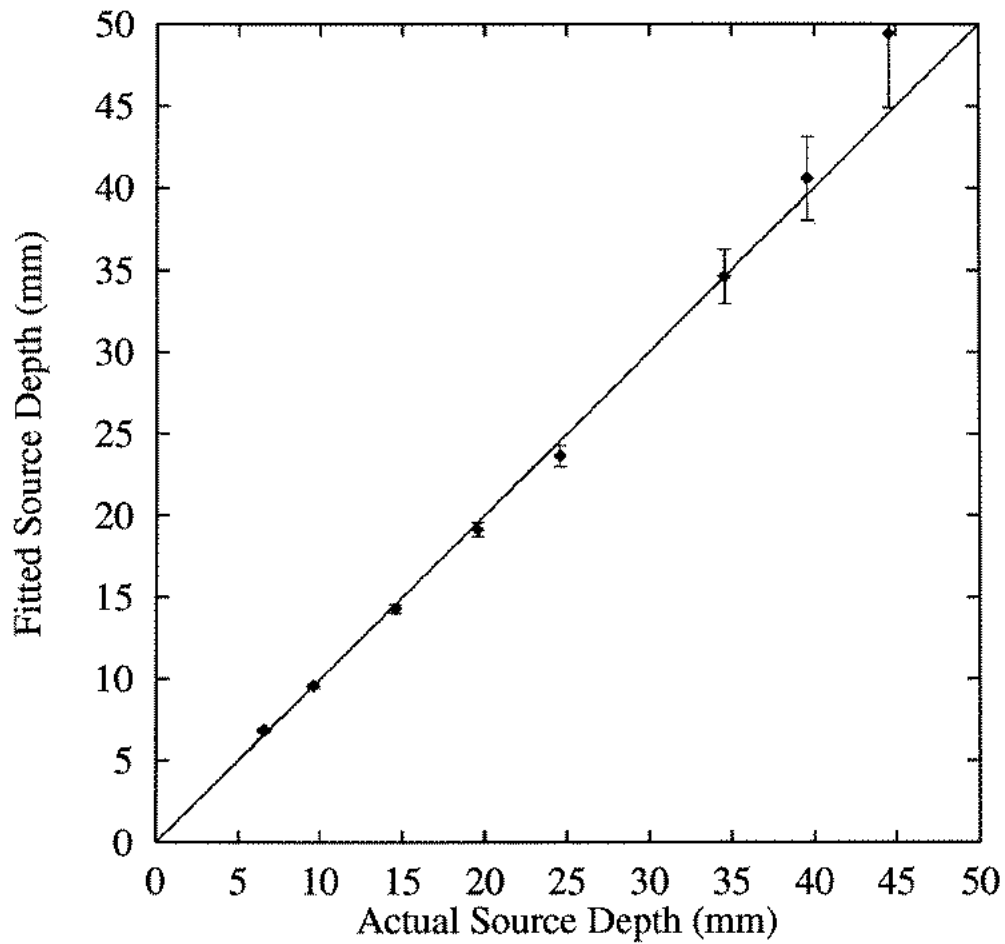


Figure 6.4 Values of z_0 obtained from fitting Equation 6.4 to experimental diffuse fluorescence emittance data. In the fits, z_b was held constant at 2.00 mm, and μ_{eff} and z_0 were extracted as fitting parameters. The solid line is the line of exact agreement between actual and fitted values.

better. The values of μ_{eff} returned from these fits are plotted in Figure 6.5, where the dotted line indicates the measured value of μ_{eff} at 680 nm (0.066 mm^{-1}). These data show that μ_{eff} is overestimated by approximately 10-15% relative to the measured value. The data plotted in Figures 6.4 and 6.5 are summarized in Table 6.1. We found the fitting algorithm to be robust with respect to the initial seed values supplied for the fitted parameters. In general, initial seeds which were within an order of magnitude of the actual value of z_0 or μ_{eff} resulted in fits which converged to identical solutions. Fitting techniques and related issues are discussed in detail in Section 6.4.

As a preliminary test of this method's ability to resolve multiple sources, a second experiment was conducted in which two identical 10 mm diameter fluorescent sources were placed in the phantom. One source was located at a depth of 9.5 mm directly under the first detection fiber, and the second was located at a depth of 10.0 mm at a radial distance of 23.0 mm from the first source. The detection fibers were oriented normal to the phantom surface, and the ends were in mechanical contact with the liquid. The tips of the fibers were located on a line connecting the points directly above the centers of the two sources. Since one of the sources was located closer to the excitation beam axis than the other, the excitation intensity at each source is not identical, and therefore the relative magnitude of each source's contribution to the emittance signal is different. The experimental fluorescence emittance data (arbitrarily normalized to the emittance at $\rho=4.19 \text{ mm}$) are depicted in Figure 6.6. A function of the form

$$F(\rho; z_{0_1}, z_{0_2}) = \alpha E(\rho; z_{0_1}) + \beta E(\rho - r_{\text{sep}}; z_{0_2}) \quad (6.5)$$

was fit to the data, where F is the diffuse fluorescence emittance, E is the function described by Equation 6.4, z_{0_1} and z_{0_2} are the two source depths, A and B are linear

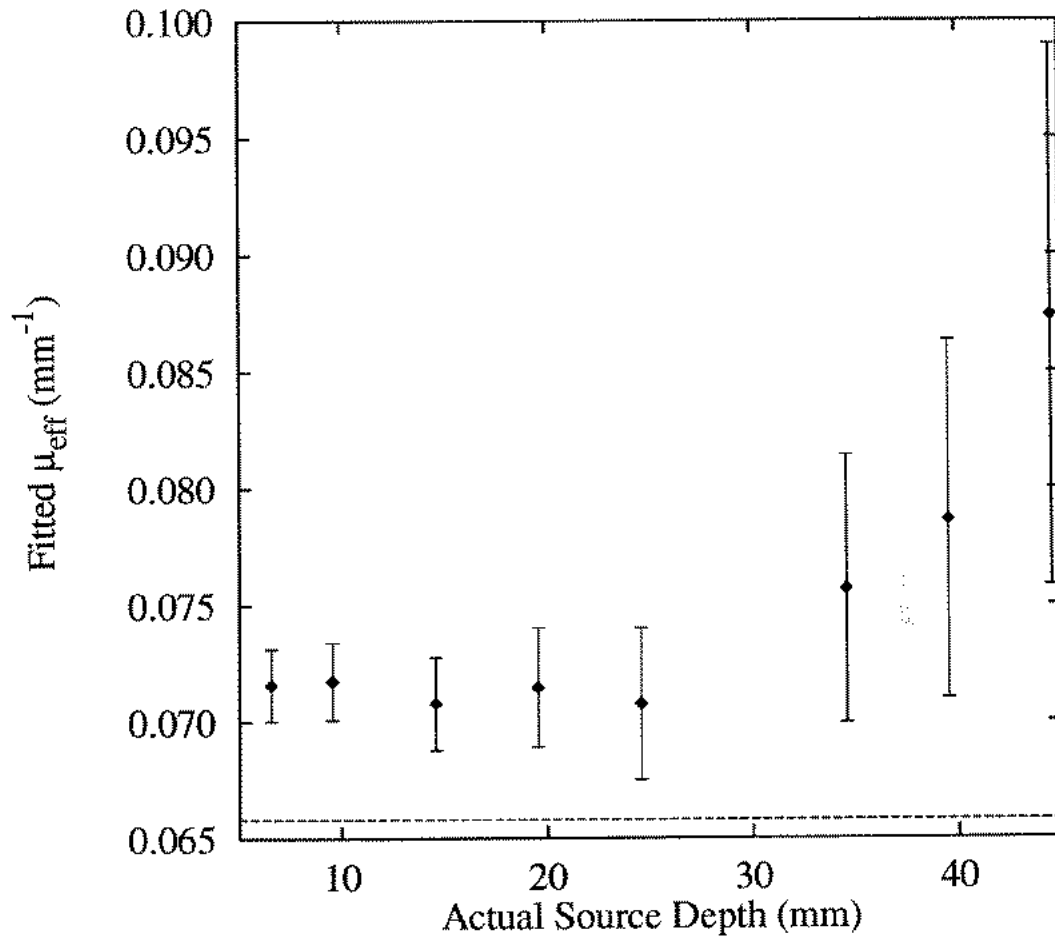


Figure 6.5 Values of μ_{eff} obtained from fitting Equation 6.4 to experimental diffuse fluorescence emittance data. In the fits, z_b was held constant at 2.00 mm, and μ_{eff} and z_0 were extracted as fitting parameters. The dotted line indicates the measured value of μ_{eff} at 680 nm (0.066 mm^{-1}).

| Trial | Actual z_0 (mm) | Fitted z_0 (mm) | Abs. Error in z_0 (mm) | Actual μ_{eff} (mm^{-1}) | Fitted μ_{eff} ($\times 10^{-2} \text{mm}^{-1}$) | % Error in μ_{eff} |
|-------|----------------------|----------------------|-----------------------------|---|--|----------------------------------|
| 1 | 6.57 | 6.85 ± 0.1 | 0.28 | 0.066 | 7.2 ± 0.2 | 9.1 |
| 2 | 9.57 | 9.57 ± 0.2 | 0.00 | 0.066 | 7.2 ± 0.2 | 9.1 |
| 3 | 14.57 | 14.27 ± 0.3 | -0.30 | 0.066 | 7.1 ± 0.2 | 7.8 |
| 4 | 19.57 | 19.14 ± 0.4 | -0.43 | 0.066 | 7.1 ± 0.3 | 7.8 |
| 5 | 24.57 | 23.65 ± 0.7 | -0.92 | 0.066 | 7.1 ± 0.3 | 7.8 |
| 6 | 34.57 | 34.60 ± 1.6 | 0.03 | 0.066 | 7.6 ± 0.6 | 15.2 |
| 7 | 39.57 | 40.59 ± 2.6 | 1.02 | 0.066 | 7.9 ± 0.8 | 19.7 |
| 8 | 44.57 | 49.43 ± 4.5 | 4.86 | 0.066 | 8.7 ± 1.2 | 31.8 |

Table 6.1 Actual and fitted values of z_0 and μ_{eff} for the experimental data depicted in Figures 6.3, 6.4, and 6.5.

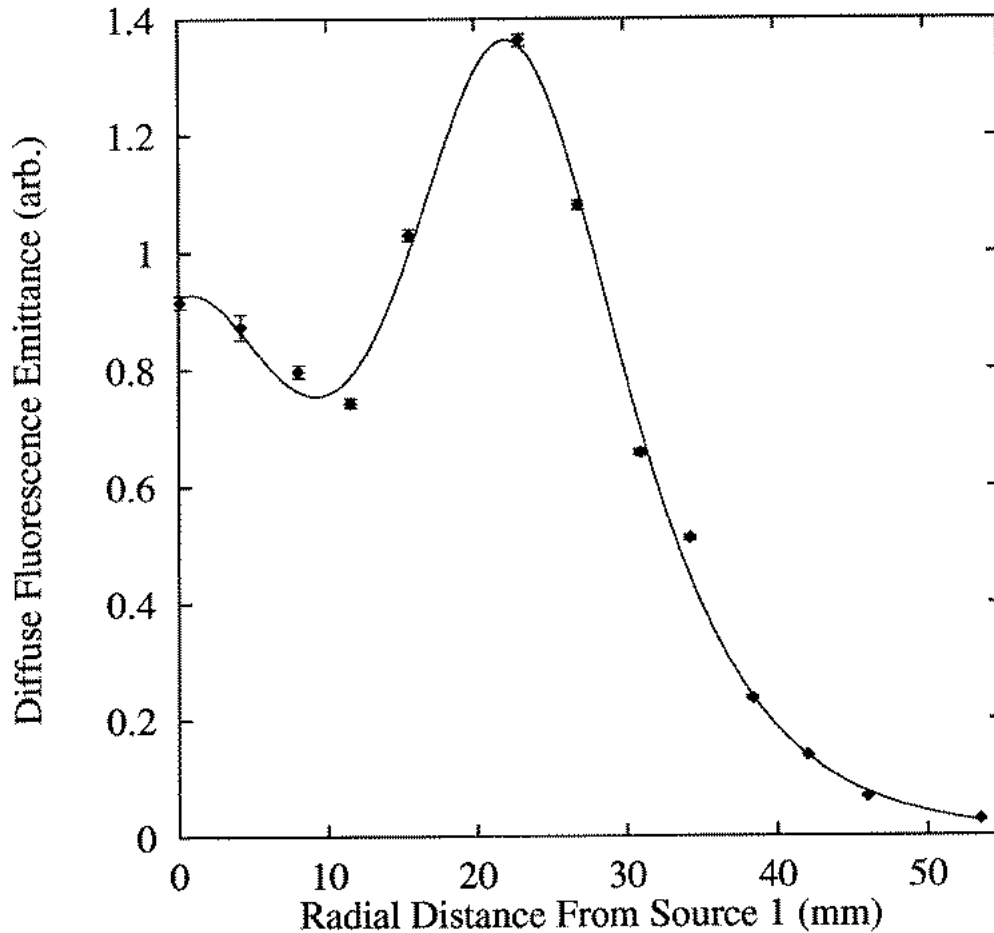


Figure 6.6 Experimental fluorescence emittance data (points) for two 10 mm diameter sources at positions of $(z_{01} = 9.5 \text{ mm}, \rho_1 = 0.0 \text{ mm})$ and $(z_{02} = 10.0 \text{ mm}, \rho_2 = 23.0 \text{ mm})$. The data are normalized to the emittance at $\rho = 4.19 \text{ mm}$ (chosen arbitrarily). The line is the best fit of Equation 6.5 to the data. The fit returned values of $z_{01} = 11.7 \pm 0.5 \text{ mm}$, $z_{02} = 11.9 \pm 0.2 \text{ mm}$, $r_{\text{sep}} = 22.4 \pm 0.1 \text{ mm}$, $\alpha = 114 \pm 11$, and $\beta = 186 \pm 13$. The increased error in these fitted source depths relative to those reported for localization of a single source results in part from the larger diameter of the spherical bulbs used to contain the fluorescent targets in the multiple source experiment. The larger diameters lead to decreased uniformity in the excitation light distribution at the targets. Uniform illumination was assumed in the fitting algorithm.

scaling parameters, and r_{sep} is the distance separating the sources. The line in Figure 6.6 represents the best fit of Equation 6.5 to these data. The fit returned values of $z_{0_1} = 11.7 \pm 0.5$ mm, $z_{0_2} = 11.9 \pm 0.2$ mm, $r_{\text{sep}} = 22.4 \pm 0.1$ mm, $\alpha = 114 \pm 11$, and $\beta = 186 \pm 13$.

6.4 Monte Carlo Evaluation of the Fitting Algorithm

To test the expected accuracy of source depths returned by fitting Equation 6.4 to fluorescence emittance data and to investigate the sensitivity of these fits to errors in the initial estimates of μ_{eff} and the diffusion coefficient D , a series of Monte Carlo data sets was generated to mimic the emittance due to an isotropic source residing at depths ranging from 1 to 50 mm. The medium used in the simulations was a 150 mm thick slab having optical properties of $\mu_a = 0.01$ mm⁻¹, $\mu_s = 6.67$ mm⁻¹, $g = 0.85$ ($\mu_s' = 1.00$ mm⁻¹, $\mu_{\text{eff}} = 0.174$ mm⁻¹, $D = 0.330$ mm), and $n = 1.4$ ($A = 2.95$). Photon packets were propagated according to the variance reduction algorithm of Wang *et al.* [28], and the emittance was scored in 0.5 mm-wide concentric annular rings centered over the isotropic source. The standard error in the emittance signal was also scored as the simulations progressed in order to estimate accurately the uncertainty in the emittance at each annular ring. The number of packets propagated in each simulation was chosen to achieve an uncertainty in the emittance comparable to that of the photon shot noise limitation inherent in the experimental detector. The number of photon packets ranged from 5.5×10^5 for $z_0 = 1.00$ mm to 13.0×10^6 for $z_0 = 50.0$ mm.

In order to evaluate the sensitivity of least-squares fitting algorithms to the source depth (z_0) when Equation 6.4 is used as a fitting function, the χ^2 goodness-of-fit statistic was computed from Equation 6.4 for each of the Monte Carlo data sets over a range of values for z_0 and μ_{eff} . In these calculations, the extrapolated boundary position

(z_b) was taken to be 1.95 mm (the value determined by the Monte Carlo simulation parameters), and every fourth radial point from $\rho=0$ mm to $\rho=54$ mm was included, simulating a detection fiber spacing of 2 mm. The results of these calculations are depicted in Figure 6.7, where the inverse of χ^2 is plotted as a function of the values of μ_{eff} and z_0 used for the calculation. Calculations for source depths of 1.0 mm (panel a), 10.0 mm (panel b), and 50.0 mm (panel c) are shown. These plots demonstrate that a well-defined global minimum in χ^2 exists for the full range of source depths investigated in these simulations. Although the trough surrounding the χ^2 minimum in parameter space becomes increasingly wide as the source depth is increased, no local minima appear when the uncertainties in the emittance are small enough to mimic the shot noise limit of the detector. Figure 6.7 also reveals that, except for extremely small source depths, the values of μ_{eff} and z_0 corresponding to the χ^2 minimum are coupled. Except for the case of $z_0=1.0$ mm, if either μ_{eff} or z_0 are fixed in the fitting process, it is not possible to determine the value of the other parameter corresponding to the global minimum in χ^2 . For this reason, it is necessary to allow both μ_{eff} and z_0 to vary as fitting parameters.

An important question that arises when examining Figure 6.7 is that of the sensitivity of the location of the global χ^2 minimum to the exact value of the extrapolated boundary position (z_b). If the location of the global minimum changes dramatically for small changes in z_b , then accurate source localization will require accurate *a priori* knowledge of z_b . Since the theoretical position of the extrapolated boundary is given by $z_b=2AD$, the accuracy of the extrapolated boundary position is governed by the accuracy with which the diffusion coefficient D is determined, assuming A is known. Because accurate *a priori* knowledge of the diffusion coefficient is not always possible or convenient, this uncertainty represents a potential source of

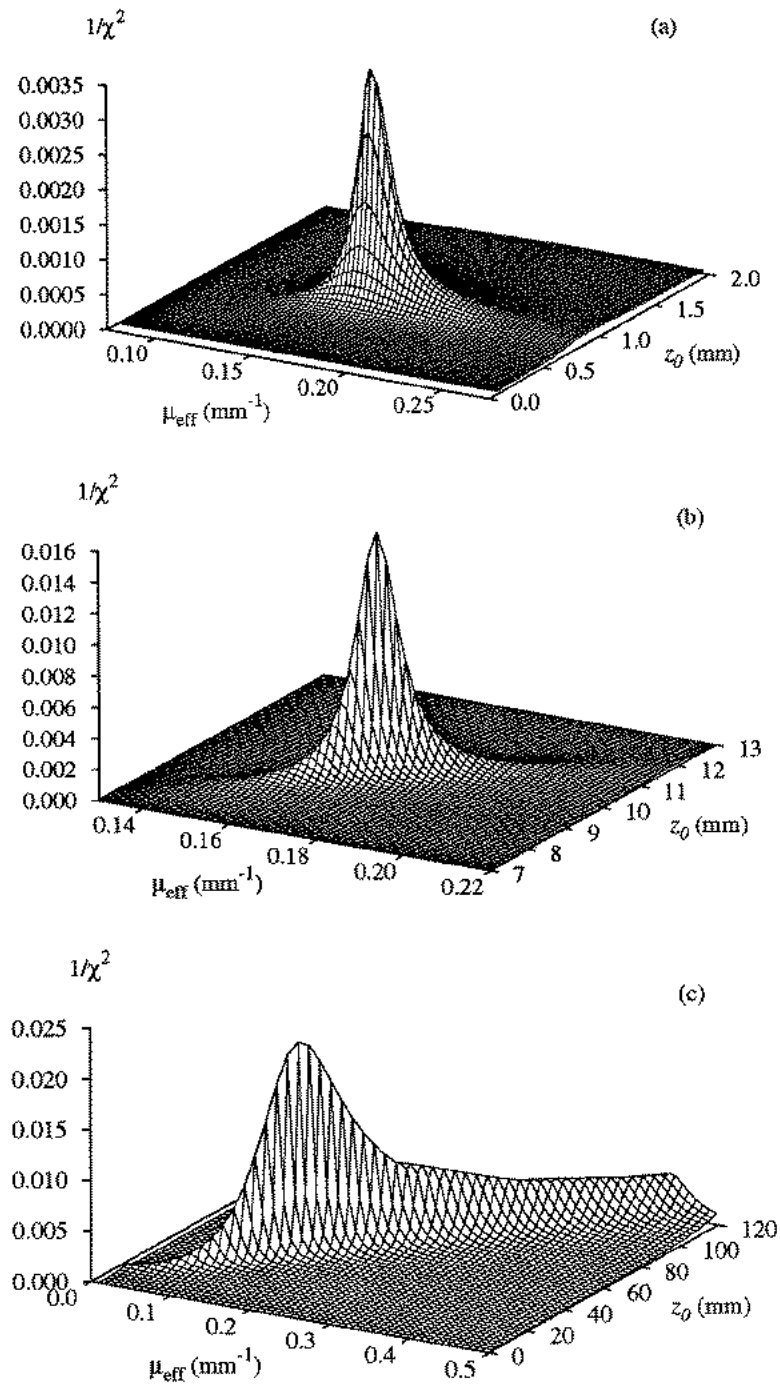


Figure 6.7 Inverse of the χ^2 goodness-of-fit statistic calculated with Equation 6.4 for Monte Carlo diffuse emittance data simulating isotropic point sources at depths of (a) $z_0 = 1.0$ mm, (b) $z_0 = 10.0$ mm, and (c) $z_0 = 50.0$ mm. The x and y axes represent the values of μ_{eff} and z_0 used in the calculation of χ^2 . In the calculations, z_b was assumed to be 1.95 mm.

error in the fitting process. This point is illustrated in Figure 6.8, where contours of constant χ^2 are shown as a function of μ_{eff} and z_0 for the Monte Carlo data set simulating a source depth of $z_0=10.0$ mm. The panels in Figure 6.8 depict the results obtained for three different extrapolated boundary positions: $z_b=0.1$ (panel a); $z_b=1.00$ mm (panel b); and $z_b=1.95$ mm (panel c). The horizontal line in each plot represents the exact value of z_0 used in the simulation (10.0 mm), and the vertical line represents the exact value of μ_{eff} used in the simulation (0.174 mm^{-1}). The solid contour connects points for which $\chi^2=100$. Subsequent line styles represent $\chi^2=500, 1000, 5000, 1 \times 10^4, 5 \times 10^4, 1 \times 10^5, \text{ and } 1 \times 10^6$, respectively. It can be seen that the position of the χ^2 minimum changes as a function of the assumed position of the extrapolated boundary. In this case, the most accurate source depths would be obtained by fixing z_b at 1.00 mm in the fitting process.

To examine the error in the reconstructed source depth resulting from uncertainty in the extrapolated boundary position, Equation 6.4 was fit to the Monte Carlo data using a Levenberg-Marquardt nonlinear least squares fitting algorithm. In these fits, z_0 and μ_{eff} were extracted as fitting parameters while z_b was held fixed at various prescribed values. Forty fits were conducted on each Monte Carlo data set, with z_b held fixed at values ranging from zero (*i.e.*, placing the extrapolated boundary on the physical boundary, the so-called “zero boundary condition”) to 1000.0 mm (*i.e.*, placing the extrapolated boundary nearly infinitely far away). A detection fiber spacing of 2 mm was again assumed.

The results of these fits are shown in Figures 6.9 and 6.10. In Figure 6.9, the percent error in the returned value for z_0 is plotted as a function of the value at which z_b was held fixed in each fitting procedure (bottom axis). Representative cases of $z_0 = 1, 2, 5, 10, \text{ and } 50$ mm are illustrated. For reference, the value of the diffusion

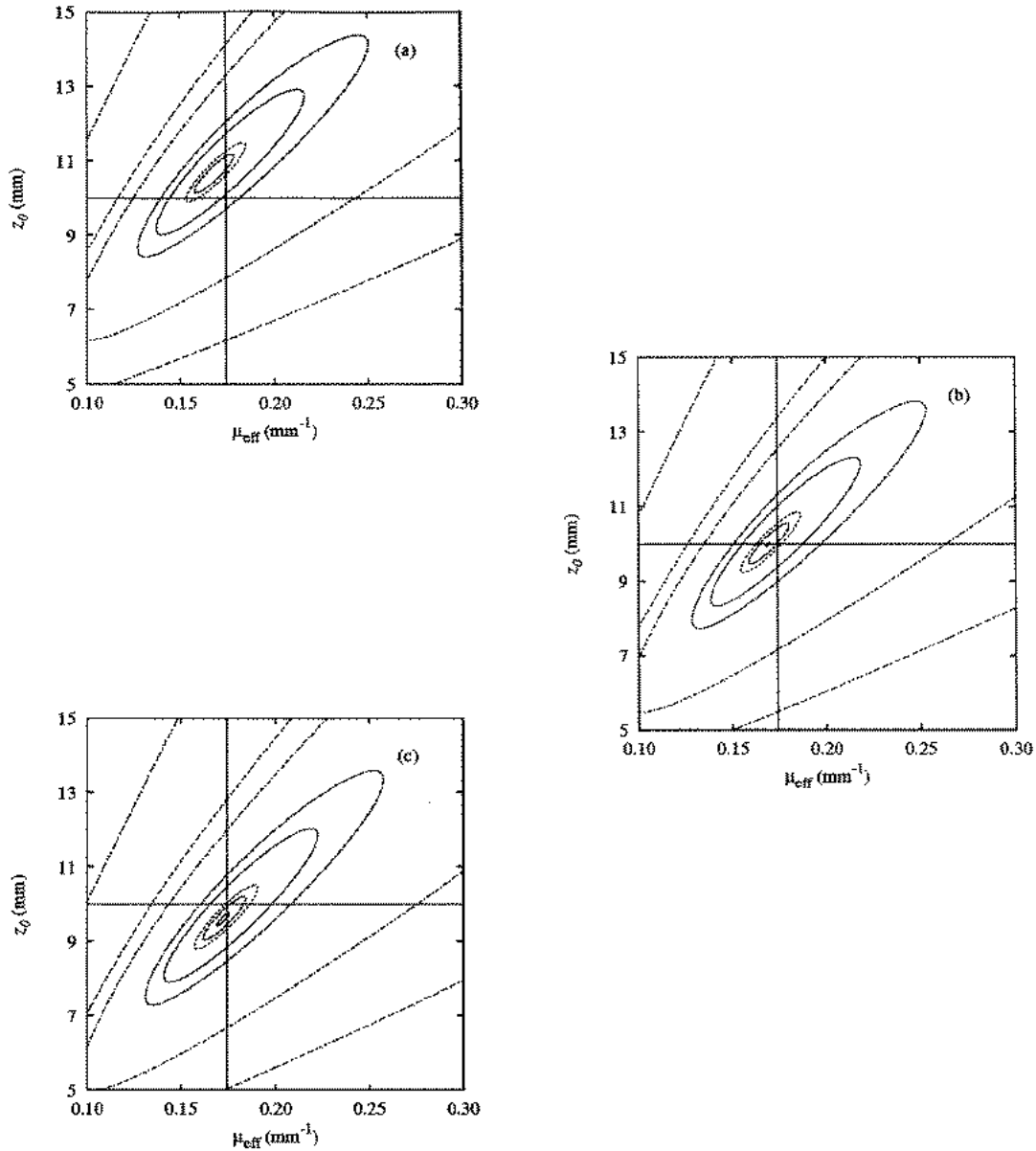


Figure 6.8 Contours of constant χ^2 computed by Equation 6.4 for Monte Carlo diffuse emittance data simulating an isotropic source depth of $z_0=10.0 \text{ mm}$. The x and y axes represent the values of μ_{eff} and z_0 used in the calculation of χ^2 . In the calculations, z_b was assumed to be 0.1 mm (panel a), 1.0 mm (panel b), or 1.95 mm (panel c). The horizontal lines represent the value of z_0 used in the simulation (10.0 mm), and the vertical lines represent the value of μ_{eff} used in the simulation (0.174 mm^{-1}). The solid contour connects points for which $\chi^2=100$. Subsequent line styles represent $\chi^2=500, 1000, 5000, 1 \times 10^4, 5 \times 10^4, 1 \times 10^5, \text{ and } 1 \times 10^6$, respectively.

coefficient corresponding to a given value of z_b (*i.e.*, $D=z_b/2A$) is shown on the top axis. The dashed vertical line represents the actual diffusion coefficient used in the simulations ($D=0.33$ mm, corresponding to $z_b=1.95$ mm). Only the range of z_b for which the error in z_0 is a rapidly changing function of z_b is shown; as z_b approaches the largest value used in the tests (1000.0 mm), the error in z_0 approaches the error obtained for the case of $z_b=0$. While the most significant errors occurred for the cases of $z_b=0$ and $z_b \approx \infty$, the error in the returned value of z_0 is confined to $\pm 5\%$ for source depths of 10 to 50 mm over nearly the entire examined range of extrapolated boundary positions. For source depths of 1.0 to 5.0 mm, the error in the returned source depth was greater for the extreme values of z_b (as high as 173% for $z_0=1.0$ mm), but demonstrated a broad minimum for extrapolated boundary positions in the range $1.0 \text{ mm} \leq z_b \leq 25.0 \text{ mm}$ ($0.17 \leq D \leq 4.24$ mm). In fact, for $1.0 \text{ mm} \leq z_b \leq 25.0 \text{ mm}$, the absolute error in the fitted value of z_0 was less than 1 mm for all of the simulated data sets. Therefore, excellent depth resolution is possible even if there is a large error in the value assigned to z_b (or D). Furthermore, since the magnitude of D is determined primarily by the transport scattering coefficient, if μ_s' can be estimated to within 50%, errors in z_0 will be minimized. The horizontal bracket in Figure 6.9 indicates the range of z_b corresponding to estimates of μ_s' which are accurate to within $\pm 50\%$. In addition, since the slope of the error curve is more gradual for values of z_b which are larger than the theoretically correct boundary position, it is advisable to favor larger values when z_b must be estimated.

In Figure 6.10, the error in the fitted value for z_0 is plotted against the fitted value of μ_{eff} for each of the fixed extrapolated boundary positions used in the series. The cases of $z_0 = 1, 2,$ and 5 mm are shown, but similar behavior was noted for all source depths. Each data point in Figure 6.10 represents the results of a fit corresponding to

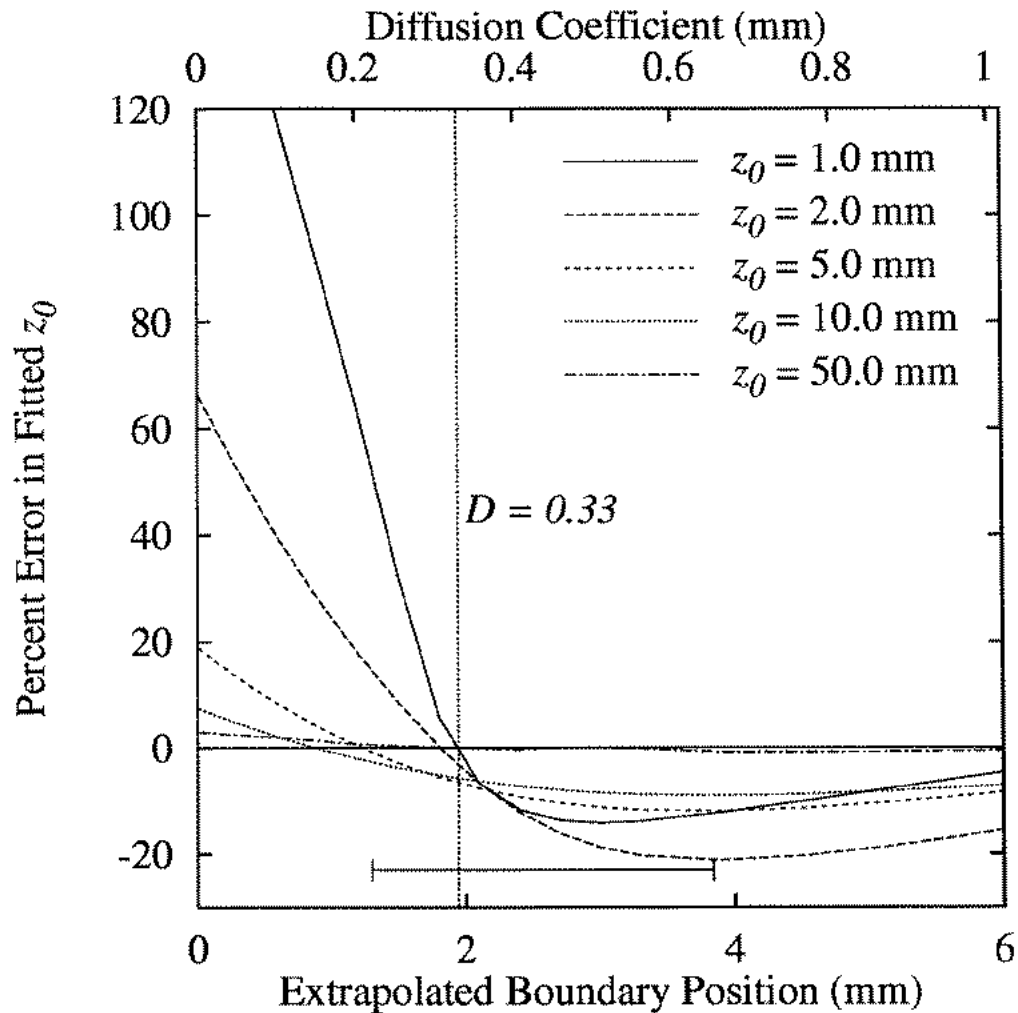


Figure 6.9 Results of a series of fits to Monte Carlo data in which z_b was held fixed at values ranging from zero to 1000.0 mm. The error in the returned value for z_0 is plotted as a function of the value at which z_b was held fixed during the fitting procedure (bottom axis). The corresponding value of the diffusion coefficient (D) is shown on the top axis. The vertical line indicates the diffusion coefficient used in the simulations (0.33 mm). The horizontal bracket at the bottom indicates the range of z_b corresponding to estimates of μ_s' which are accurate to within $\pm 50\%$. Only the range of z_b for which the error in z_0 changes rapidly is shown.

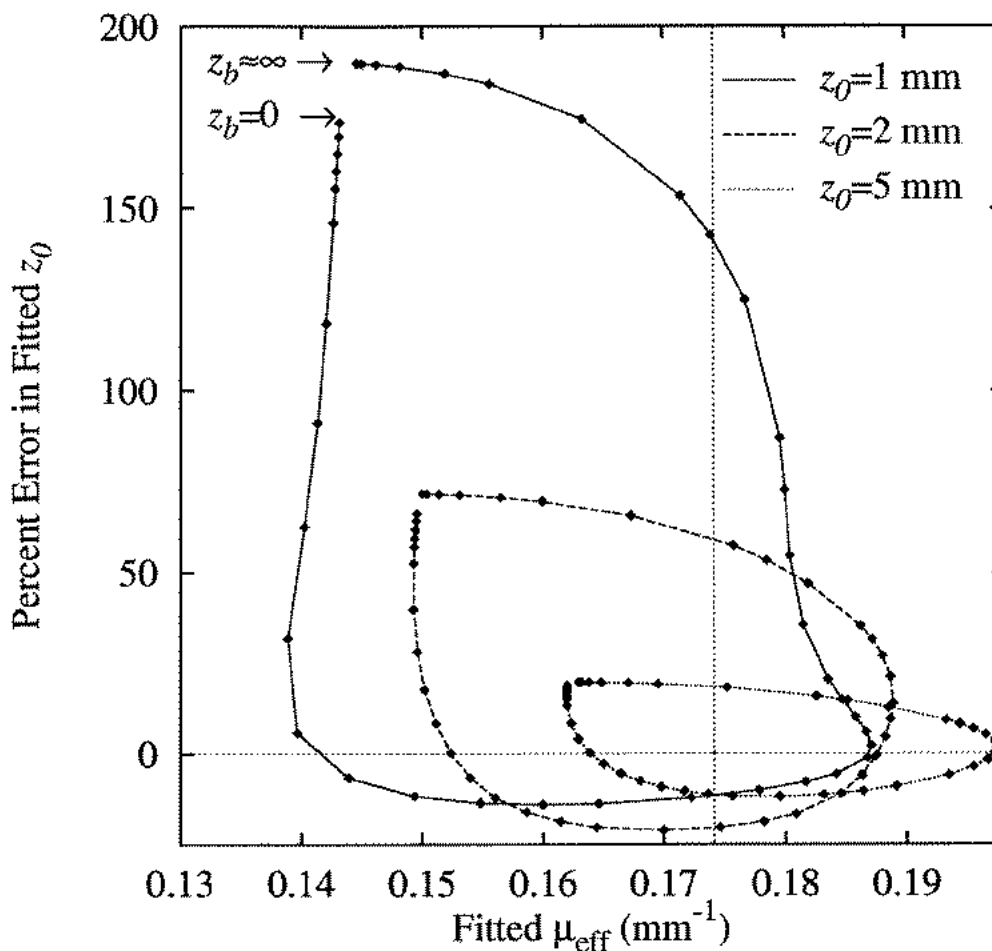


Figure 6.10 The error in the fitted value for z_0 plotted as a function of the fitted value of μ_{eff} for each of 40 fixed extrapolated boundary positions z_b ranging from zero to 1000.0 mm. The cases of $z_0=1, 2,$ and 5 mm are shown, but similar behavior was noted for all source depths. Each data point represents the results of a fit corresponding to a different fixed value of z_b . The values returned for $z_b=0$ and $z_b=\infty$ are indicated on the plot for the case of $z_0=1$ mm, and the endpoints are similar for the other cases. As the extrapolated boundary position (z_b) is increased, the data points proceed in a counter-clockwise fashion.

a different, fixed value of z_b . The values returned for $z_b=0$ and $z_b \approx \infty$ are indicated on the plot for the case of $z_0=1$ mm (the endpoints are similar for the other cases). As the extrapolated boundary is moved further away from the physical boundary, the returned values for z_0 and μ_{eff} proceed in a counter-clockwise fashion. The dotted vertical line indicates the value of μ_{eff} used in the simulations (0.174 mm^{-1}). It is interesting to note that as the extrapolated boundary position approaches infinity, the fitted z_0 and μ_{eff} parameters approach values similar to those obtained for the case of $z_b = 0$. This behavior can be understood by considering Equations 6.2 and 6.3. If z_b is set equal to zero in Equation 6.3, then for a given value of ρ , the values of r_1 and r_2 will be equal, making the two terms in Equation 6.3 identical. For $z_b=0$, the fluence described by Equation 6.2 is zero. Thus, to within a multiplicative constant, the emittance described by Equation 6.1 for $z_b=0$ is equivalent to the expression for the z-component of the flux of a single emitter. The emittance described by Equation 6.1 for the case of $z_b \approx \infty$ is equal to the *sum* of the fluence and the z-component of the flux for a single emitter. Because of this, the fitted values of μ_{eff} and z_0 for these two cases will be identical to the extent that the fluence and the flux terms are in constant proportion to one another for the entire sampled range of ρ . This is precisely the requirement of the partial-current diffusion theory boundary condition, which specifies that at the boundary, $\psi = -2A_j$. While this condition is minimally satisfied for small source depths (for which the relative magnitudes of the fluence and the flux terms change significantly from $\rho=0$ to $\rho=54$ mm because of non-diffuse light present in regions corresponding to small ρ), it is more nearly satisfied with increasing z_0 . This is evidenced in Figure 6.10 by the fact that, as z_0 is increased, the gap between the points corresponding to the extreme values of z_b decreases.

We have observed that the fitted values for z_0 and μ_{eff} returned by the algorithm

we have implemented are stable with respect to the initial seed value used for μ_{eff} . When the seed value for μ_{eff} was varied from 0.0174 mm^{-1} (one tenth the value used in the simulations) to 1.74 mm^{-1} (ten times the value used in the simulations), the fitting algorithm converged on the same parameter values depicted in Figures 6.9 and 6.10 (data not shown). This robust property of the fitting function, in conjunction with the relative insensitivity to the precise position of the extrapolated boundary, permits accurate reconstruction of source depths even when no *a priori* information is available regarding the optical properties of the medium.

These Monte Carlo experiments demonstrate that, when using Equation 6.4 as a fitting function, it is possible to obtain depth estimates accurate to within 1 mm for sources buried at depths ranging from 1 mm to 50 mm when the extrapolated boundary position is fixed at a constant value. This is true even if initial estimates of the medium's optical properties (*i.e.*, μ_{eff} and D) are in error by an order of magnitude or more. These conclusions are consistent with the experimental results presented in the preceding section.

6.5 Limitations Imposed by Background Luminescence

The experiments described in the preceding sections were conducted under conditions of ideal partitioning of the luminescent agent into the region of interest. This is not representative of the scenario *in vivo* where, under optimal conditions, the target to background uptake ratio is likely to be on the order of 10:1, a value reported recently by Woodburn *et al.* for the photosensitizer lutetium texaphyrin [14]. The contribution of non-specifically localized lumiphore to the total emittance signal must therefore be assessed in order to determine the practical limitations of the technique

described here.

In this section, we determine the emittance from a semi-infinite medium with a uniformly distributed lumiphore assuming steady-state, plane-wave illumination. This constant background signal is then superimposed on the emittance signal calculated by Monte Carlo simulations as described in Section 6.4 from a small spherical inclusion located at various depths. Equation 6.4 is then fitted to this “contaminated” emittance signal to determine the degree of error introduced in the fitted source depth. In this manner, a lower bound can be determined for the effective target to background contrast required for accurate localization of a source at a given depth.

Consider a semi-infinite scattering medium having a uniformly distributed lumiphore and a luminescence quantum yield ϕ . For notational simplicity and in accordance with the experimental measurements described in Section 6.3, assume that the medium optical properties at the absorption and emission wavelengths are identical. Assuming plane wave irradiation at the surface with an incident fluence rate F_0 , the fluence rate at depth z is written [29]

$$\psi(z) = (A_1 + F_0) \exp(-\mu_t z) + A_2 \exp(-\mu_{eff} z) , \quad (6.6)$$

with A_1 and A_2 given by:

$$A_1 = \frac{-3 F_0 (\mu_s \mu_t' + g \mu_s \mu_t)}{\mu_t^2 - \mu_{eff}^2} , \quad (6.7)$$

$$A_2 = \frac{-A_1 (3 \mu_t' + 2 \mu_t) - 6 F_0 \mu_s g}{3 \mu_t' + 2 \mu_{eff}} .$$

The luminescence emittance resulting from this excitation light distribution is

determined by integrating the Green's function for the emittance due to a plane source at depth z over the entire semi-infinite space, weighting the source intensity according to the fluence rate given by Equation 6.6. The fluence rate must be multiplied by a scale factor of $\phi\mu_a dz$ to obtain the amount of excitation light which is absorbed and subsequently re-radiated. The result is [30]

$$E = \mu_c \phi C \left[\frac{A_1 + F_0}{\mu_t + \mu_{eff}} + \frac{A_2}{2\mu_{eff}} \right], \quad (6.8)$$

where $C=3\mu_t/(3\mu_t' + 2\mu_{eff})$.

We may compare the strength of this constant background emittance with that originating from a spherical luminescent inclusion located at depth z_0 . The luminescence emitted at the surface of the inclusion will be a fraction of the incident fluence (given by Equation 6.6). That fraction is given by

$$\frac{L_{emitted}}{\Psi_{incident}} = \phi \exp(-\mu_{a_{incl}} r_{incl}) \quad (6.9)$$

where r_{incl} is the radius of the inclusion and $\mu_{a_{incl}}$ is the absorption coefficient within the inclusion.

Figure 6.11 depicts the ratio of the maximum emittance originating from a 6 mm diameter spherical inclusion ($E_{max \text{ inc.}}$) to the emittance originating from nonspecifically localized lumiphore (E_{bulk}) as a function of the depth of the inclusion (z_0). The background luminescence was calculated from Equation 6.8, the inclusion emittance was calculated from Equation 6.1 (at $\rho=0$, the location of maximum emittance), and the luminescence intensity at the surface of the inclusion was normalized to the value specified by Equation 6.9. Optical properties of $\mu_a=0.01 \text{ mm}^{-1}$,

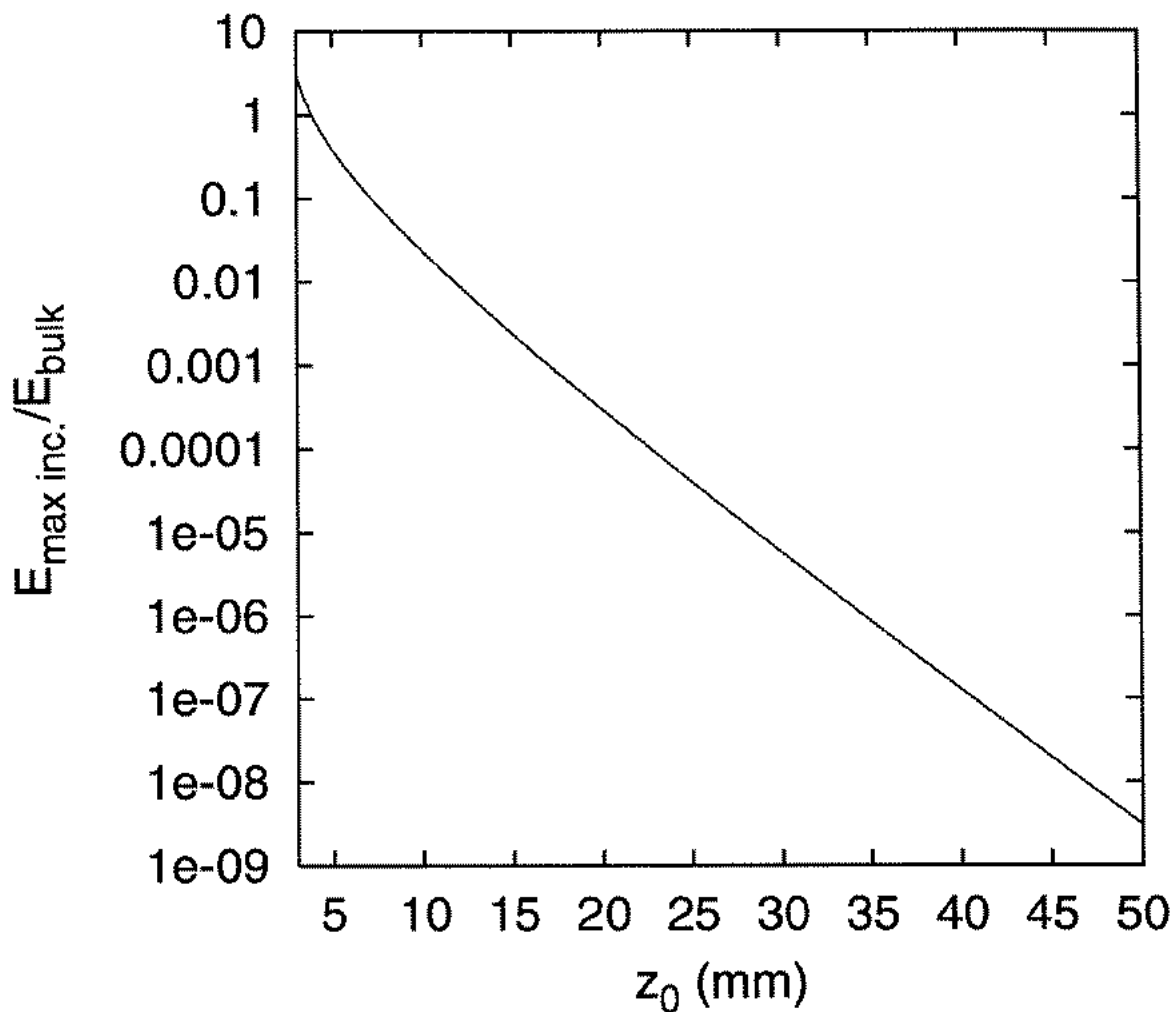


Figure 6.11 The ratio of the maximum emittance from a luminescent spherical inclusion ($E_{\max \text{ inc.}}$) buried at a depth z_0 in a semi-infinite turbid medium to the emittance originating from non-specifically localized lumiphore within the medium (E_{bulk}). The optical properties at the absorption and emission wavelengths are $\mu_a=0.01 \text{ mm}^{-1}$, $\mu_s=6.67 \text{ mm}^{-1}$, and $g=0.85$, and plane-wave illumination is assumed. The diameter of the inclusion is 6 mm, and the target:background uptake ratio is 10:1.

$\mu_b = 6.67 \text{ mm}^{-1}$, and $g = 0.85$ (identical to those used in the Monte Carlo simulations) were assumed, and $\mu_{a,inc}$ was taken to be 0.1 mm^{-1} (10:1 target to background uptake ratio). Index-matched boundary conditions were assumed for these calculations, but the order of magnitude of $E_{\text{max inc.}}/E_{\text{bulk}}$ will not change when an index mismatch is present at the boundary. Except for the most superficial source depths, the emittance from the inclusion is completely dominated by the emittance from the bulk medium. In addition, for $\rho > 0$ (off the axis of symmetry), the situation worsens considerably. Under conditions of realistic target to background uptake ratios, it is clear that mechanisms which provide significant additional contrast must be exploited for this localization technique to be considered practical.

To determine the effective target to background contrast required for accurate source localization, constant background signals of various amplitudes were superimposed on the Monte Carlo data described in the previous section. The data were then renormalized to the total signal at $\rho = 0$, and Equation 6.9 was fitted to the background-contaminated Monte Carlo data to extract the apparent source depth. Figure 6.12 illustrates representative background-contaminated data for source depths of 5 mm (panel a) and 25 mm (panel b). Four cases are illustrated in each panel: the original data ($E_{\text{bulk}} = 0$) and background-contaminated data for $E_{\text{max inc.}}/E_{\text{bulk}} = 10^3, 10^5$, and 10^7 . Fitted source depths and associated errors for these values of $E_{\text{max inc.}}/E_{\text{bulk}}$ are presented in Table 6.2 for simulated source depths of $1 \text{ mm} \leq z_0 \leq 25 \text{ mm}$. Table 6.2 also indicates the *effective* target to background contrast represented by each value of $E_{\text{max inc.}}/E_{\text{bulk}}$. For example, Figure 6.11 indicates that, under conditions of cw plane-wave irradiation, $E_{\text{max inc.}}/E_{\text{bulk}}$ for a 6 mm diameter spherical inclusion at $z_0 = 25 \text{ mm}$ is approximately 10^4 . In order to increase $E_{\text{max inc.}}/E_{\text{bulk}}$ to 10^3 (the minimum value illustrated in Figure 6.12), an *effective* target to background contrast of 10^7 is required.

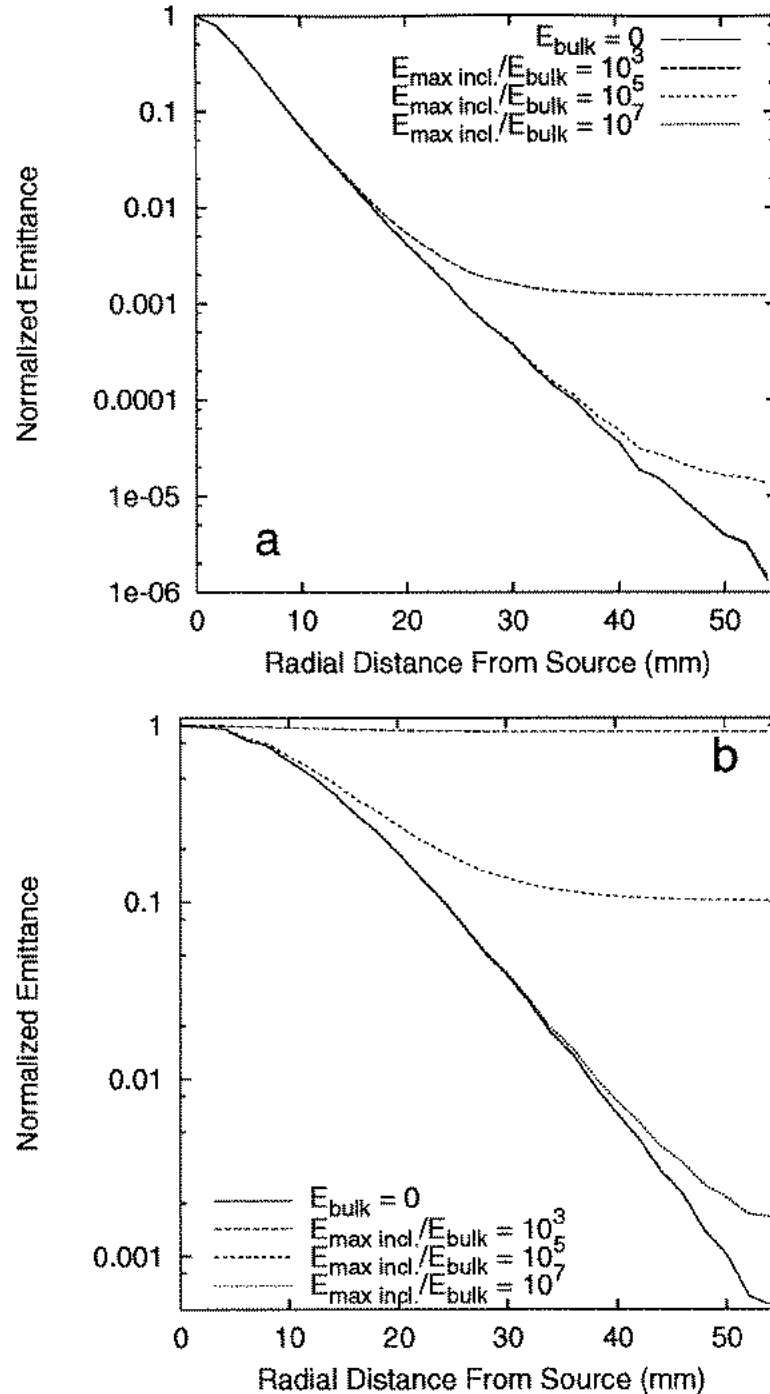


Figure 6.12 Simulated luminescence emittance data from point sources buried at $z_0=5$ mm (a) and $z_0=25$ mm (b) in a semi-infinite turbid medium ($\mu_s=0.01 \text{ mm}^{-1}$, $\mu_a=6.67 \text{ mm}^{-1}$, $g=0.85$) with superimposed background luminescence. The data were generated by adding a constant offset luminescence to the Monte Carlo data described in Section 6.3 and then renormalizing the data to the signal at $\rho=0$. Data are presented according to the ratio of the maximum point source emittance ($E_{\text{max incl.}}$) to the background emittance (E_{bulk}). The bottommost line in each panel corresponds to $E_{\text{bulk}}=0$.

| Actual z_0 | $E_{\max \text{ inc.}} / E_{\text{bulk}} = 10^3$ | | | $E_{\max \text{ inc.}} / E_{\text{bulk}} = 10^5$ | | | $E_{\max \text{ inc.}} / E_{\text{bulk}} = 10^7$ | | | $E_{\text{bulk}} = 0$ | | |
|-----------------|--|---------------|----------------|--|---------------|----------------|--|---------------|----------------|-----------------------|---------------|----------------|
| | Fitted z_0 | Abs. Error | Eff. Contr. | Fitted z_0 | Abs. Error | Eff. Contr. | Fitted z_0 | Abs. Error | Eff. Contr. | Fitted z_0 | Abs. Error | Eff. Contr. |
| 5 | 2.6 | -2.4 | 10^3 | 3.6 | -1.4 | 10^5 | 3.8 | -1.2 | 10^7 | 4.5 | -0.5 | ∞ |
| 10 | 6.5 | -3.5 | 10^4 | 6.7 | -3.3 | 10^6 | 8.4 | -1.6 | 10^8 | 9.0 | -1.0 | ∞ |
| 15 | 21.5 | +6.5 | 10^5 | 7.2 | -7.8 | 10^7 | 13.6 | -1.4 | 10^9 | 14.3 | -0.7 | ∞ |
| 20 | 33.6 | +13.6 | 10^6 | 5.1 | -14.9 | 10^8 | 17.7 | -2.3 | 10^{10} | 19.1 | -0.9 | ∞ |
| 25 | 50.6 | +25.6 | 10^7 | 15.5 | -9.5 | 10^9 | 19.9 | -5.1 | 10^{11} | 25.2 | +0.2 | ∞ |

Table 6.2 Actual and fitted values of z_0 for the background-contaminated emittance data depicted in Figure 6.12. The absolute error in the fitted source depth is also reported. $E_{\max \text{ inc.}}$ denotes the maximum emittance from the buried spherical inclusion (at $\rho=0$), and E_{bulk} denotes the emittance from non-specifically localized lumiphore. Cases of $E_{\text{bulk}} = 0$ (the original, uncontaminated data) and $E_{\max \text{ inc.}} / E_{\text{bulk}} = 10^3$, 10^5 , and 10^7 are shown. For a given source depth, the effective contrast is the value of $E_{\max \text{ inc.}} / E_{\text{bulk}}$ for the simulated data (shown in the top row of the table) divided by the value of $E_{\max \text{ inc.}} / E_{\text{bulk}}$ from Figure 6.11.

Table 6.2 indicates that sources as deep as 20 mm are localized with approximate accuracies of $\pm 10\%$ or ± 1 mm (whichever is greater) for $E_{\text{max inc.}}/E_{\text{bulk}} \geq 10^7$ (effective contrasts of 10^7 to 10^{11}). Judging from the level of contamination still present at large ρ for this background level (Figure 6.12), it is also likely that an additional order of magnitude in $E_{\text{max inc.}}/E_{\text{bulk}}$ would yield significantly improved fits for the 25 mm source depth.

6.6 Discussion and Conclusions

It is interesting to note that the center of the single spherical source is located with an accuracy of ± 1 mm when the source itself is 6 mm in diameter. This is because, to within a multiplicative constant, the diffuse emittance of a uniformly irradiated spherical luminescent source of any diameter is identical to that produced by a point source located at the center of the sphere [31]. In the experiments conducted with a single, 6.0 mm-diameter fluorescent source, the spherical inclusion was sufficiently small that the intensity of the excitation light at the outer surface of the sphere was reasonably uniform. In the case of the experiment that localized two inhomogeneities, the diameter of each source was 10.0 mm. Since the attenuation of the excitation beam by the bulk medium varies more significantly over this length scale, it is reasonable to expect increased error in the reported source depth. In fact, the source depths in this case were overestimated by approximately 2 mm. In the future, this work will be extended to the development of a complete imaging algorithm. This will allow for the forward propagation (attenuation) of the excitation beam and convolution of the Green's function evaluated in this report over an arbitrary source distribution. The assumption of uniform excitation will then be unnecessary.

While the background Raman signal discussed previously imposed a limit on the maximum source depths from which signals could be recovered under these specific experimental conditions, it is likely that *in vivo* measurements may not be as adversely affected by Raman scattering. Contrast agents may exist which possess Stokes shifts such that the luminescence emission maximum does not lie within the spectral region most severely contaminated by tissue Raman scattering. In addition, the irradiation wavelength may also be tuned to move Raman interference out of the wavelength region sampled by the detector. Finally, since the efficiency of the Raman scattering process decreases as the fourth power of the wavelength, as new luminescent probes are developed possessing significant extinction at longer wavelengths, the contribution of Raman scattering to the background light will diminish. These observations do, however, illustrate the potential importance of considering the Raman scattering spectrum of tissue for determining candidate fluorophores for *in vivo* luminescence imaging. At the present time, a far more significant obstacle to this and other methods attempting to optically localize buried sources of fluorescence from exogenously administered contrast agents is that of the specificity (tumor to normal tissue contrast) of currently available tumor-seeking dyes. The problem of background fluorescence has recently been considered by others in the context of time- [32] and frequency-domain [20,22] and steady-state [5] imaging methods.

An encouraging potential application of these methods is the use of oxygen-quenched phosphorescence to image centers of hypoxia in tissue. Several investigators have already published elegant studies in which the large phosphorescence yields of certain metalloporphyrins are exploited to provide two-dimensional maps of local oxygen tension in superficial layers of tumors and normal tissues [16,33,34]. These maps are based on the fact that phosphorescence from these molecules is readily

quenched by ground state molecular oxygen ($^3\text{O}_2$), and therefore the phosphorescence lifetime is dependent on local $^3\text{O}_2$ concentration. Under steady-state irradiation, the triplet population, $[T]$, of the phosphorescent probe is given by $[T] = \phi_t I_a / (k_p + k_{ot} [^3\text{O}_2])$, where ϕ_t is the quantum yield of triplet formation, I_a is the rate of photon absorption by the ground state of the probe, k_p is the intrinsic rate of decay of the triplet state, and k_{ot} is the bimolecular rate at which the triplets are quenched by $^3\text{O}_2$. Using well-known literature values [35] for the triplet state rate constants ($k_p=1250 \text{ s}^{-1}$, $k_{ot}=1.85 \times 10^9 \text{ M}^{-1}\text{s}^{-1}$) and assuming an oxygen concentration in well perfused normal tissue of approximately $100 \mu\text{M}$, one finds that the triplet state concentration in severely hypoxic regions exceeds that found in oxygenated normal tissue more than 100 - fold even when the phosphor exhibits no selectivity for the tumor. Of course, when there is some preferential tumor accumulation of the phosphorescent contrast agent the signal contrast is correspondingly more favorable. On the basis of these simple considerations, it is evident that the hypoxic tumor/normal tissue contrast is significantly higher for this case than it is for the case in which tumor detection and localization relies on preferential uptake/retention of a fluorophore. This intrinsically higher contrast makes possible the optical imaging of hypoxic tumor regions which reside at depths where fluorescently labelled tumors would not be detectable because of fluorescence originating from nonspecifically localized fluorophore. To our knowledge, this technique has not yet been extended to the problem of reconstructing accurately the 3-dimensional spatial origins of phosphorescence signals from relatively thick ($\sim 3\text{-}5 \text{ cm}$) tissues such as the compressed breast.

It is also possible that significantly enhanced hypoxia "weighting" of the detected signal may be obtained by gating signal acquisition to begin at times which are delayed with respect to the end of a brief pulse of excitation light. This may be appreciated by

considering the time-dependent phosphorescence signal, $S(t)$, which is, $S(t) \propto \phi_t I_a \exp(-t/\tau)$, where ϕ_t and I_a were defined above as the triplet yield and rate of photon absorption, respectively, t is the time, and τ is the phosphorescence lifetime. The rate of phosphorescence decay, $1/\tau$, is the sum of contributions from the intrinsic rate, k_p , and the oxygen quenching term, $k_{qt} [O_2]$. Using the typical porphyrin rates cited above, the phosphorescence lifetime in well oxygenated ($\sim 100 \mu\text{M}$) normal tissue is approximately $5 \mu\text{s}$, while in severely hypoxic ($\sim 0.1 \mu\text{M}$) tumor regions the lifetime approaches $700 \mu\text{s}$. This pronounced oxygen dependence creates favorable conditions for preferential detection of phosphorescence signals from hypoxic areas. For example, with a temporal gate of $60 \mu\text{s}$ and a $750 \mu\text{s}$ integration time, the ratio of the signals from hypoxic and well oxygenated regions receiving identical excitation intensities is 10^7 . Extending the gate to $100 \mu\text{s}$ with the same integration time increases this signal contrast to more than 10^{10} . This extraordinary contrast is accomplished with only negligible loss of signal from the phosphor in the hypoxic region. At $100 \mu\text{s}$, for example, the signal from a severely hypoxic ($0.1 \mu\text{M}$) tumor region is still 87% of its maximum value.

The high contrast that is available through temporally delayed data acquisition makes it a very promising candidate for detecting and imaging hypoxic tumors using the spatially-resolved diffuse luminescence emittance technique described here, particularly in optically accessible regions such as the breast. For example, Table 6.2 demonstrates that with an effective contrast of 10^{10} , 6-mm diameter spherical inclusions as deep as 15 mm were localized with 10% accuracy. The 20 mm source depth was recovered to within 2.3 mm. These tissue thickness are approximately one-half the thickness of a compressed breast.

In summary, these studies have demonstrated the experimental ability to

localize sources of luminescence buried as deep as 40 mm with an accuracy of 1.0 mm or better. This resolution can be achieved without *a priori* knowledge of the optical properties of the medium. Monte Carlo studies have been presented which suggest that when the luminescence emittance signal is shot-noise limited, sources buried as deep as 50 mm (the deepest sources modelled in these studies) can be localized with similar accuracy.

References

1. *Optical Tomography and Spectroscopy of Tissue: Theory, Instrumentation, Model, and Human Studies II*, B. Chance and R. R. Alfano, eds., Proc. SPIE **2979**, (1997).
2. "Advances in Optical Imaging and Photon Migration," R. R. Alfano and J. G. Fujimoto, eds., Vol. 2 of OSA Trend in Optics and Photonics Series (Optical Society of America, Washington, DC, 1996).
3. J.C. Hebden and D.T. Delpy, "Enhanced time-resolved imaging with a diffusion model of photon transport," *Opt. Lett.* **19**, 311-313 (1994).
4. M.A. O'Leary, D.A. Boas, B. Chance, and A.G. Yodh, "Experimental images of heterogeneous turbid media by frequency-domain diffusing-photon tomography," *Opt. Lett.* **20**, 426-428 (1995).
5. J.W. Chang, H.L. Graber, and R.L. Barbour, "Luminescence optical tomography of dense scattering media," *J. Opt. Soc. Am. A* **14**, 288-299 (1997).
6. D.A. Benaron, J.P. VanHouten, W.F. Cheong, E.L. Kermit, and R.A. King, "Early clinical results of time-of-flight optical tomography in a neonatal intensive care unit," in *Optical Tomography, Photon Migration, and Spectroscopy of Tissue and Model Media: Theory, Human Studies, and Instrumentation*, B. Chance and R. R. Alfano, eds., **Proc. SPIE 2389**, 582-596 (1995).
7. R.R. Alfano, A. Pradhan, G.C. Tang, and S.J. Wahl, "Optical spectroscopic diagnosis of cancer and normal breast tissues," *J. Opt. Soc. Am. B* **6**, 1015-1023 (1989).
8. R.M. Cothren, R. Richards-Kortum, M.V. Sivak, M. Fitzmaurice, R.P. Rava, G.A. Boyce, M. Doxtader, R. Blackman, T.B. Ivanc, G.B. Hayes, M.S. Feld, and R.E. Petras, "Gastrointestinal tissue diagnosis by laser-induced fluorescence spectroscopy at endoscopy," *Gastrointest. Endosc.* **36**, 105-111 (1990).
9. J. Hung, S. Lam, J.C. LeRiche, and B. Palcic, "Autofluorescence of normal and malignant bronchial tissue," *Lasers Surg. Med.* **11**, 99-105 (1991).

10. A. Mahadevan, M.F. Mitchell, E. Silva, S. Thomsen, and R.R. Richards-Kortum, "Study of the fluorescence properties of normal and neoplastic human cervical tissue," *Lasers Surg. Med.* **13**, 647-655 (1993).
11. Andersson-Engels, S., Johansson, J., Svanberg, K., and Svanberg, S. "Fluorescence imaging and point measurements of tissue - applications to the demarcation of malignant tumors and atherosclerotic lesions from normal tissue," *Photochem. Photobiol.* **53**, 807-814. (1991).
12. E. Reddi, A. Segalla, G. Jori, P.K. Kerrigan, P.A. Liddell, A.L. Moore, T.A. Moore, and D. Gust, "Carotenoporphyrins as selective photodiagnostic agents for tumors," *Br. J. Cancer* **69**, 40-45 (1994).
13. T. Takemura, S. Nakajima, and I. Sakata, "Tumor-localizing fluorescent diagnostic agents without phototoxicity," *Photochem. Photobiol.* **59**, 366-370 (1994).
14. K.W. Woodburn, Q. Fan, D.R. Miles, D. Kessel, Y. Luo, and S.W. Young, "Localization and efficacy analysis of the phototherapeutic lutetium texaphyrin (PCI-0123) in the murine EMT6 sarcoma model," *Photochem. Photobiol.* **65**, 410-415 (1997).
15. S.A. Vinogradov and D.F. Wilson, "Metallotetrabenzoporphyrins - new phosphorescent probes for oxygen measurements," *J. Chem. Soc. Perkin Trans. 2*, 103-111 (1995).
16. S.A. Vinogradov, L.W. Lo, W.T. Jenkins, S.M. Evans, C. Koch, and D.F. Wilson, "Noninvasive imaging of the distribution in oxygen of tissue in vivo using near-infrared phosphors," *Biophys. J.* **70**, 1609-1617 (1996).
17. C.L. Hutchinson, J.R. Lakowicz, and E.M. Sevick-Muraca, "Fluorescence lifetime-based sensing in tissues: a computational study," *Biophys. J.* **68**, 1574-1582 (1995).
18. M.A. O'Leary, D.A. Boas, X.D. Li, B. Chance, and A.G. Yodh, "Fluorescence lifetime imaging in turbid media," *Opt. Lett.* **21**, 158-160 (1996).

19. J. Wu, Y. Wang, L. Perelman, I. Itzkan, R.R. Dasari, and M.S. Feld, "Three-dimensional imaging of objects embedded in turbid media with fluorescence and Raman spectroscopy," *Appl. Opt.* **34**, 3425-3430 (1995).
20. D.Y. Paithankar, A.U. Chen, B.W. Pogue, M.S. Patterson, and E.M. Sevick-Muraca, "Imaging of fluorescent yield and lifetime from multiply scattered light reemitted from random media," *Appl. Opt.* **36**, 2260-2272 (1997).
21. D.A. Boas, M.A. O'Leary, B. Chance, and A.G. Yodh, "Scattering and wavelength transduction of diffuse photon density waves," *Phys. Rev. E* **47**, R2999-R3002(1991).
22. M.A. O'Leary, D.A. Boas, B. Chance, and A.G. Yodh, "Reradiation and imaging of diffuse photon density waves using fluorescent inhomogeneities," *J. Luminesc.* **60-1**, 281-286 (1994).
23. A. Knüttel, J.M. Schmitt, R. Barnes, and J.R. Knutson, "Acousto-optic scanning and interfering photon density waves for precise localization of an absorbing (or fluorescent) body in a turbid medium," *Rev. Sci. Instrum.* **64**, 638-644 (1993).
24. X.D. Li, M.A. O'Leary, D.A. Boas, B. Chance, and A.G. Yodh, "Fluorescent diffuse photon density waves in homogeneous and heterogeneous turbid media: Analytic solutions and applications," *Appl. Opt.* **35**, 3746-3758 (1996).
25. M.R. Lewis, H.A. Sloviter, and P.P. Golland, "In vivo staining and retardation of growth sarcomata in mice," *Anat. Rec.* **95**, 89-96 (1946).
26. L. Cincotta, J.W. Foley, T. MacEachern, E. Lampros, and A.H. Cincotta, "Novel photodynamic effects of a benzophenothiazine on 2 different murine sarcomas," *Cancer Res.* **54**, 1249-1258 (1994).
27. W.H. Press, S.A. Teukolsky, W.T. Vetterling, and B.P. Flannery, *Numerical Recipes in C: The Art of Scientific Computing* (Cambridge University Press, Cambridge, UK, 1992), pp. 683-687.
28. L.H. Wang, S.L. Jacques, and L. Zheng, "MCML - Monte Carlo modeling of light

- transport in multilayered tissues," *Comp. Meth. Prog. Biomed.* **47**, 131-146 (1995).
29. A. Ishimaru, *Wave Propagation and Scattering in Random Media* (Oxford University Press, Oxford, UK, 1997), pp. 182-183.
 30. J. Wu, M.S. Feld, and R.P. Rava, "Analytical model for extracting intrinsic fluorescence in turbid media," *Appl. Opt.* **32**, 3585-3595 (1993).
 31. M.G. Nichols, "Transport of Oxygen and Light in Model Tumor Systems," PhD dissertation (University of Rochester, Rochester, NY, 1996).
 32. J. Wu, L. Perelman, R.R. Dasari, and M.S. Feld, "Tomographic detection of fluorophores embedded in tissue-like phantom," in *Advances in Optical Imaging and Photon Migration*, R.R. Alfano and J.G. Fujimoto, eds., Vol. 2 of OSA Trends in Optics and Photonics Series (Optical Society of America, Washington, DC, 1996), pp. 116-118.
 33. D.F. Wilson and G.J. Cerniglia, "Localization of tumors and evaluation of their state of oxygenation by phosphorescence imaging," *Cancer Res.* **52**, 3988-3993 (1992).
 34. W.L. Rumsey, J.M. Van derKooi, and D.F. Wilson, "Imaging of phosphorescence: a novel method for measuring oxygen distribution in perfused tissue," *Science* **241**, 1649-1651 (1988).
 35. M.A.J. Rodgers, *The photoproperties of porphyrins in model biological environments* (Libreria Progetto Editore, Padova, Italy, 1985), pp. 21-35.

CHAPTER 7

Conclusions

Chapters 1-5 of this thesis described several methods for noninvasive measurement of the optical properties of highly scattering media. These techniques involve analysis of the intensity of the reflectance emitted from a semi-infinite scattering medium at multiple prescribed distances from a narrow, collimated beam normally incident upon the medium's surface.

It has been demonstrated that the diffusion approximation to the Boltzmann radiative transport equation, which is generally valid when the transport scattering cross-section dominates the absorption cross-section by a factor of approximately 100 or more, can be used to accurately model the optical fluence in a homogeneous infinite medium at source-detector separations larger than approximately 1 transport mean free path. Boundary conditions which may be applied at the interface between scattering and non-scattering media and which are consistent with the diffusion approximation were also described. Analytical expressions for the reflectance emitted from semi-infinite media were developed using these boundary conditions. These expressions were fitted to experimental reflectance data in order to extract the medium absorption and transport scattering coefficients, and accuracies of 10% or better were achieved.

In situations where the optical absorption coefficient is comparable in magnitude

to the transport scattering coefficient, diffusion theory is no longer valid. Under these conditions, it has been demonstrated that the P_3 approximation to the radiative transport equation, combined with appropriate boundary conditions, can accurately model the reflectance originating from a collimated beam at source-detector separations as small as 0.25 transport mean free path. Analytical reflectance expressions derived from the P_3 approximation were used to analyze experimental reflectance data collected at small (≤ 3 mm) source-detector separations from highly absorbing semi-infinite media. The absorption and transport scattering coefficients thus obtained were demonstrated to be accurate to within 10% for transport albedos as small as 0.59.

In Chapter 6, a technique for localizing a buried source of luminescence in a semi-infinite turbid medium using continuous-wave excitation was described. This technique exploited a diffusion-theory expression for diffuse luminescence emittance which was a direct outgrowth of the work presented in Chapters 1-5. It was demonstrated that a small spherical luminescent inclusion buried in a semi-infinite, non-luminescent tissue-simulating phantom could be localized to 1.0 mm accuracy for sources of luminescence as deep as 40 mm. A theoretical analysis of the effects of non-specifically localized lumiphore was also presented, and the results of that analysis indicated that sources as deep as 15 mm could potentially be localized to 1.0 mm accuracy if an effective target-to-background contrast level of 10^9 could be realized. One mechanism for providing such a level of contrast was proposed.

The techniques described in this thesis were developed in the context of a search for noninvasive methods of determining the optical properties of biological tissue. During the time required to complete this work, the field of biomedical optics has continued to evolve at a rapid pace. As this evolution continues, miniaturized probes which are capable of the localized measurements required for optical biopsy and which

are appropriate for endoscopic applications will likely become increasingly commonplace. It is hoped that the methods described here will find application in the analysis of clinical data collected from such diagnostic systems.